INFORMATION TO USERS

This manuscript has been reproduced from the microfilm master. UMI films the text directly from the original or copy submitted. Thus, some thesis and dissertation copies are in typewriter face, while others may be from any type of computer printer.

The quality of this reproduction is dependent upon the quality of the copy submitted. Broken or indistinct print, colored or poor quality illustrations and photographs, print bleedthrough, substandard margins, and improper alignment can adversely affect reproduction.

In the unlikely event that the author did not send UMI a complete manuscript and there are missing pages, these will be noted. Also, if unauthorized copyright material had to be removed, a note will indicate the deletion.

Oversize materials (e.g., maps, drawings, charts) are reproduced by sectioning the original, beginning at the upper left-hand corner and continuing from left to right in equal sections with small overlaps.

ProQuest Information and Learning
300 North Zeeb Road, Ann Arbor, MI 48106-1346 USA
800-521-0600

UMI®

NOTE TO USERS

Page(s) not included in the original manuscript are unavailable from the author or university. The manuscript was microfilmed as received.

7-9,94

This reproduction is the best copy available.

UMI®

MODELLING TWO-PHASE FLOW-EXCITED FLUIDELASTIC INSTABILITY IN HEAT EXCHANGER TUBE ARRAYS

by

Paul Feenstra, M. Eng.

A Thesis
Submitted to the School of Graduate Studies
in Partial Fulfilment of the Requirements
for the Degree of
Doctor of Philosophy

McMaster University
August 2000

MODELLING TWO-PHASE FLOW-EXCITED FLUIDELASTIC INSTABILITY IN HEAT EXCHANGER TUBE ARRAYS

Doctor of Engineering 2000
(Mechanical Engineering)

McMaster University
Hamilton, Ontario

Title: Modelling Two-Phase Flow-Excited Fluidelastic Instability in Heat Exchanger Tube Arrays

Author: Paul A. Feenstra, M. Eng. (Mechanical)
McMaster University

Supervisors: Dr. R.L. Judd
Dr. D.S. Weaver

Number of Pages: xv, 198

Abstract

This thesis reports on the investigation of flow induced vibration in heat exchanger tube arrays. This work is in support of nuclear steam generator design, where attention is focussed on the tubes in the upper U-bend region which are subjected to cross-flow, and are therefore most susceptible to the destructive effects of flow-induced vibration. While this topic has received plenty of attention by researchers since the late 60's, the present investigation involves a two-phase flow which most studies did not consider until much later. Results for this study are reported for a dynamically scaled model tube array in a parallel triangular layout, with a pitch over diameter ratio of P/D = 1.44, mounted in a clamped-free arrangement. This tube bundle was subjected to single and two-phase cross-flows of refrigerant R-11. The results were analysed to determine the critical velocity for fluidelastic instability, the magnitude of the turbulence buffeting force, and the nature of the two-phase flow, such as the actual void fraction and flow regime.

The main motivation of this work is to present experimental results on fluidelastic instability, the mechanism that usually causes the most damaging vibrations, and to make comparisons with other data on the basis of non-dimensional similitude parameters to determine the effect of using different fluid mixtures to simulate the actual steam-water flow in the steam generator. A new method is proposed for calculating the average fluid density and equivalent flow velocity of the two-phase fluid, using a newly developed void fraction model which accounts for the difference in velocity between the gas and liquid phases. The fluidelastic data of several researchers, who used a variety of fluids, is re-examined using this new void fraction model and the results show a remarkable difference in trend between two common flow regimes, bubbly and intermittent flow. The latest flow regime map, developed by other researchers for predicting the two-phase flow regimes in the shell-side cross-flows in tube bundles, was applied to the fluidelastic results. This analysis showed that the sudden change in stability behavior which appeared in various data sets were directly related to a predicted change in flow regime from bubbly to intermittent flow. The data corresponding to the bubbly flow regime showed no significant deviation from the trend established by Connor's theory. However, the data

corresponding to the intermittent flow regime showed a significant decrease in stability which was independent of mass-damping parameter. It is believed that the velocity fluctuations that are inherent in the intermittent flow regime are responsible for causing the instability to occur at a lower flow velocity than would normally occur for steady flow.

The two-fluid model used in the fluidelastic data analysis was developed by the present author from experimental measurements of void fraction in the horizontal tube bundle using the gamma densitometer. The development of this model is described in detail, and it is demonstrated that it agrees well with experimental void fraction measurements in air-water mixtures and two-phase R-113 for cross-flows in horizontal tube arrays over a sufficiently wide range of pitch mass flux, quality and P/D ratios. This void fraction model will allow researchers and designers to obtain better estimates of void fraction in the shell side flow in applications such as kettle reboilers and the U-bend region of nuclear steam generators than with the customarily used homogeneous equilibrium model. This will result in better estimates of average fluid density and average velocity of two-phase upward cross-flow through horizontal tube bundles.

Measurements of the damping effect of two-phase flows were obtained in the present study and are presented and compared with previous data using an existing analysis technique. Damping measurements showed that the tube damping peaks at about 75% to 80% HEM void fraction, and decreases at lower and especially higher void fraction. This is in reasonable quantitative agreement with air-water and R-22 data of other researchers.

The turbulence buffeting response of the tubes was measured and from this the non-dimensional spectrum of turbulent forces was determined and compared with existing data. In single phase flow, the data of the present study appears to plot higher than the extensive data points of Taylor *et al.* (1996), but are mostly within the upper bound determined by Taylor and Pettigrew (1999). In two-phase flow, the turbulent forces were analysed according to the new data reduction method of deLangre and Villard (1998). The present results compared agreeably with other data and plotted below the upper bound proposed by deLangre and Villard, which lent support to their analysis method.

Acknowledgements

The author would like to thank the following people for their contribution to this work:

Ron Lodewyks, Dave Schick, Jim McLaren and Joe Verhaeghe for their excellent technical help, as well as my supervisors Dr. D.S. Weaver and Dr. R.L. Judd for their help in guiding the research.

Special thanks are also due to Dr. M. Shoukri for graciously allowing me the use of the gamma densitometer.

Thanks also to work colleagues and F.I.V. members: Alex Gidi, Michael Morgenroth, Harland Mackenzie, Ming Li, Don Song, Michael Bardeleben, Marwan Hassan for interesting discussions and good times.

Table of Contents

Appendices

List of Figures

List of Tables

Nomenclature

a_n - mode shape correlation coefficient
A - Upstream cross sectional area of test section {m^2}
C_D - drag coefficient
C_L - lift coefficient
C_m - Added mass coefficient
Cap - Capillary number
d_e - effective tube diameter (used for flow regime calculations) {m}
D - tube diameter {m}
D_e - effective tube diameter (used for damping calculations) {m}
D_w - empirical void length (used for two-phase turbulence buffeting calculations){m}
$e(x)$ - relative error in variable x
f - frequency {Hz}
f_a - frequency of tube vibrating in air {Hz}
f_n - natural frequency {Hz}
f_R - reduced frequency (fD/V_p)
F_R - Froude number
G_p - pitch mass flux {kg/m^2s}
h_G - gas phase enthalpy {kJ/kg}
h_L - liquid phase enthalpy {kJ/kg}
h_{LG} - vapourization enthalpy {kJ/kg}
Δh - enthalpy rise of fluid through heater {kJ/kg}
H_1 - head reading on main sub-loop orifice plate {in Hg}
H_2 - head reading on cooling sub-loop orifice plate {in Hg}
J - joint acceptance
K - fluidelastic instability constant (a.k.a. Connors' constant)
L - tube length {m}
L_s - length scale (= 1.0 m)
L_c - modal joint acceptance {m}
m - tube mass per unit length including added mass {kg/m}
m_h - hydrodynamic mass (added mass) {kg/m}
m_R - mass ratio of tube to displaced fluid

m_t - tube mass per unit length {kg/m}
$\dot{m}$ - mass flow rate {kg/s}
M - total tube mass including added mass {kg}
N - photon count in two phase flow
N^* - photon count in two phase flow at reference temperature
N_G - reference photon count in gas
N_L - reference photon count in liquid
p_o - force scale factor (used for two-phase turbulence force measurements) {N}
P - tube pitch {mm}
P_{sat} - saturated pressure {N/m^2}
Q_T - total flow rate through pump {m^3/s}
Q_1 - volumetric flow rate through main sub-loop {m^3/s}
Q_2 - volumetric flow rate through cooling sub-loop {m^3/s}
Re - Reynolds number
Ri - Richardson number
R_F - cross correlation spectrum
S_F - power spectral density of flow excitation (N/m)^{2}s
S_y - power spectral density of tube response (N/m)^{2}s
S - velocity ratio (U_G/U_L)
Sn - gamma ray sensitivity {%}
S_t - Strouhal number based upon pitch velocity
T_1 - fluid temperature in test section {°C}
T_2 - fluid temperature at heater entrance {°C}
U_G - gas phase velocity {m/s}
U_{GS} - superficial gas phase velocity {m/s}
U_{GS}^* - non-dimensional superficial gas phase velocity
U_L - liquid phase velocity {m/s}
U_{LS} - superficial liquid phase velocity {m/s}
V - flow velocity {m/s}
V_{eq} - equivalent two-phase pitch flow velocity based upon the void fraction model {m/s}
V_p - pitch flow velocity based on the Homogeneous Equilibrium Model {m/s}
V_u - upstream flow velocity {m/s}
V_R - reduced velocity based upon pitch velocity (V_p/fD)
x - flow quality
$\dot{x}$ - instantaneous tube velocity in the x direction {m/s}
$\dot{y}$ - instantaneous tube velocity in the y direction {m/s}
y_{rms} - r.m.s. tube amplitude (at the free end) {% dia.}
$y(s)$ - tube amplitude at position s {m}
α - void fraction measured by radiation absorption or predicted with the void fraction model
α_H - homogeneous void fraction
γ - coherence function of fluid forces
δ - logarithmic decrement of damping ($2\pi\zeta$)
δ_a - logarithmic decrement of damping in vacuo (or air) ($2\pi\zeta_a$)
ζ - damping ratio

ζ_{TP} - two-phase flow component of damping ratio
$(\zeta_{TP})_D$ - normalized two-phase flow component of damping ratio
ζ_s - structural component of damping ratio (a.k.a. damping ratio in air)
ζ_v - viscous component of damping ratio
σ - surface tension {N/m}
$\sigma(z)$ - mode shape function
λ_c - correlation length of random forces along tube length {m}
μ - fluid dynamic viscosity {kg/ms}
ν - fluid kinematic viscosity {m^2/s}
ρ - fluid density {kg/m^3}
ρ_H - fluid density based upon HEM model {kg/m^3}
ρ - fluid density based upon RAD void fraction or predicted from void fraction model {kg/m^3}
ρ_G - gas phase density {m/s}
ρ_L - liquid phase density {m/s}
ρ_{LC} - liquid phase density at reference temperature {m/s}
$\sigma(s)$ - modal displacement of tube at location s
$\phi(f)$ - spectral density of fluctuating forces per unit tube length {N^2s/m^2}
$\Phi^0_E(f)$ - reference equivalent spectrum
$[\Phi_F(f_R)]_e$ - equivalent dimensionless forcing spectrum (E.D.F.S.)

CHAPTER 1

Introduction

Flow induced vibration is a relatively new field of study which examines the problems of elastic structures that vibrate when subjected to a flow. Typical examples of these problems are galloping of electrical transmission lines, flutter of aircraft wings and bridge decks, vibrations of thin aircraft panels in the wake of jet blasts, and vibrations of heat exchanger tube arrays. Traditionally, flow induced vibration was not considered in the design of these structures because, in the past, generous safety factors were utilized to handle static loads and this was usually sufficient to take care of oscillating loads. However, in cases where improved performance could be only be obtained by making parts lighter and structures more flexible, as in aircraft components, or by increasing the flow velocity and reducing pressure drop, as in heat exchangers, then flow induced vibration became a limiting factor.

Active study of flow induced vibration in heat exchanger tube arrays started in the mid 1960's which, for the western nations, was an economically booming period marked by an ever increasing demand for household consumer products, most of which were electrically driven. This coincided with a rapidly increasing demand for electricity by industry and consumers which fueled the development and construction of nuclear power plants. In Canada, AECL (Atomic Energy of Canada Limited) developed the CANDU (Canada Deuterium Uranium) reactor plant which utilizes natural uranium as fuel and heavy water as the coolant and moderator. A schematic of the CANDU power system is shown in Figure 1.1. Currently, there are 22 CANDU reactors in Canada and 10 reactors are operating or under construction in Argentina, Korea, Pakistan, Romania, India and China.

In order to meet the ever increasing demand for electricity, designers saw it necessary to build larger and more efficient power plants, because even small percentage increases in plant efficiency would result in significant fuel savings. Increasing the efficiency of a heat exchanger, which is an

integral part of any power plant, typically requires increasing the overall heat transfer coefficient and decreasing the pressure drop of the flow. This can be accomplished by increasing the throughput of flow, minimizing the diameter and wall thickness of the tubes and by minimizing the number of tube supports. However, this approach pushes the design towards lighter and more flexible tubes, thereby making them more susceptible to flow induced vibration. Figure 1.2 is a partial illustration of a typical recirculating type nuclear steam generator used in CANDU power stations. Figure 1.3 is a photograph of a nuclear steam generator, taken during fabrication at Babcock and Wilcox Canada, which shows the long tube spans of the U-bend region. The U-bend region of the steam generator, where the tubes are subjected to steam-water cross flow, is the tube region most vulnerable to the occurrence of vibration damage. The outer tube spans in this region are most susceptible since the tube supports are furthest apart and hence the stiffness is the lowest. Figure 1.4 and 1.5 are photographs of damaged tubes that were pulled from a nuclear steam generator. Table 1.1 provides a summary of reported steam generator problems worldwide, while Table 1.2 provides details of steam generator defects resulting in tube plugging. Green and Hetsroni (1995) provide an extensive review of PWR steam generators, covering a wide variety of topics including thermal-hydraulic analysis, tube fretting and wear, and a survey of steam generator problems reported worldwide.

As a result of these problems, a great deal of research has been undertaken to study the fluid structure interaction in tube arrays. Since the problem most often involves separated flows of high Reynolds numbers, research relies heavily on experimental studies. This usually involves the use of small scale models of tube arrays designed to achieve geometric and dynamic similarity with the prototype array. Initially, researchers investigated the simplest cases of a single tube or tube row in single-phase cross-flow. Gradually, as the level of understanding grew, so did the scope of the research. Studies have now covered all of the various tube bundle configurations, a wide range of tube frequencies, fluid to structure mass ratios and various fluids including two phase fluids such as air-water, Freon-water, various two phase refrigerants such as R-11 and R-12, and in a few cases steam-water has been used.

In the case of single phase flow, the state of knowledge is fairly well developed for predicting the vibration amplitude of a tube for a given cross flow velocity, and a number of computer codes have been developed as reported by Frick *et al.* (1984). In addition, empirical stability diagrams have been

generated to predict the onset of fluidelastic instability, the most damaging form of flow-induced vibration, which can be found in Weaver and Fitzpatrick (1988), Paidoussis (1982) Chen (1984), and Schroder and Gelbe (1999). Empirical maps of the power spectrum of fluid forces have also been developed to predict the tube response to turbulence buffeting as given by Axisa *et al.* (1990).

In many types of tube and shell heat exchangers however, boiling of the liquid occurs and hence the working fluid consists of two-phase gas and liquid flow. This type of flow requires special consideration since the effects of fluid damping and virtual mass have been found to be different than in single phase flow. The determination of cross-flow velocity and average fluid density also requires special consideration due to the complicated interaction between the gas and liquid phases. As a result, significantly more research has been undertaken in the last few years to study the fluid structure interaction in two phase flow, mostly in support of nuclear steam generator and fuel bundle design.

In a previous thesis by the present author, Feenstra (1993), an experimental study was performed to study fluidelastic instability in the U-bend region of nuclear steam generators. A two phase flow loop was designed and commissioned specifically for this purpose (see Dam, 1990), which uses refrigerant R-11 as the working fluid. That study focused mainly on the determination of critical velocities for the onset of fluidelastic instability. The primary interest was to compare the results with those of Pettigrew *et al.* (1989), who did similar research using air-water, to see the effect of using two component (air-water) mixtures as opposed to using one component (liquid-vapour) mixtures to model the actual steam-water mixtures in a nuclear steam generator. It was postulated that the tube vibration could induce local pressure changes in the vicinity of the tube surface which could induce vapour bubble collapse or liquid flashing. Such a scenario cannot occur in two component air-water flows as readily as in single component liquid-vapour flows such as R-11. It was found that the R-11 data showed slightly lower stability threshold than the air-water data. However, damping data was lacking and since both excitation and damping mechanisms may be sufficiently different in these two types of flows to have a noticeable effect on the vibration amplitude of the tubes, more work was needed to complete the comparison.

The main objective of the present study is to generate new data and new analysis tools for fluidelastic instability in two-phase flows. Thus, more accurate estimates of average fluid density and critical flow velocity can be obtained than by using the traditional homogeneous equilibrium model

(HEM) for two-phase flows. The ultimate goal is to give designers of nuclear steam generators and other heat exchanger equipment better design tools for predicting and avoiding tube damage due to flow-induced vibrations. The following new analysis tools are presented: 1. A new map for predicting the flow regime in the shell-side cross-flow of heat exchangers which is shown to corroborate the present author's observations. 2. A new model for predicting void fraction is developed, which will give designers a means of predicting the average density of two-phase flows more accurately than with the HEM. 3. New measurements of the damping effect of two-phase flows are presented and compared with previous data.

A brief outline of the thesis is as follows: In Chapter 2, a literature survey of previous experimental studies is presented, which covers fluidelastic instability, turbulence buffeting and vortex shedding in heat exchanger arrays. In Chapter 3, the theoretical framework of two vibration mechanisms for tube excitation, namely random vibrations and fluidelastic instability, is presented along with a literature survey of analytical prediction models for fluidelastic instability. In Chapter 4, the concept of physical modeling is discussed, specifically for scaling the fluid-structure interaction in the prototypical steam generator down to a model study which can be done practically in the laboratory. This analysis discusses the advantages of modeling the two-phase steam-water flow using Refrigerant 11 rather than using a two component mixture such as air-water. It also explains the assumptions made in modeling the complex tube geometry and support conditions in the steam generator using a cost effective apparatus. Chapter 5 describes the apparatus, the experimental procedure, the data analysis method and an error analysis. Chapter 6 discusses flow regimes and compares the present author's observations with the latest predictive map, which was used to help explain the somewhat unusual outcome of the fluidelastic data analysis (Chapter 8). Chapter 7 presents the results of a new model for predicting void fraction of a two-phase cross-flow in a tube array, which was developed by the present author. In Chapter 8, the fluidelastic instability data obtained in this study is compared with data of other researchers for single and two-phase flow. The two-phase flow data is given new examination using the afore-mentioned slip model and flow regime analysis. In Chapters 9 and 10, results are presented for two-phase damping and turbulence buffeting measurements respectively, and comparison is made with other data. Finally, conclusions and future recommendations are made in Chapter 11.

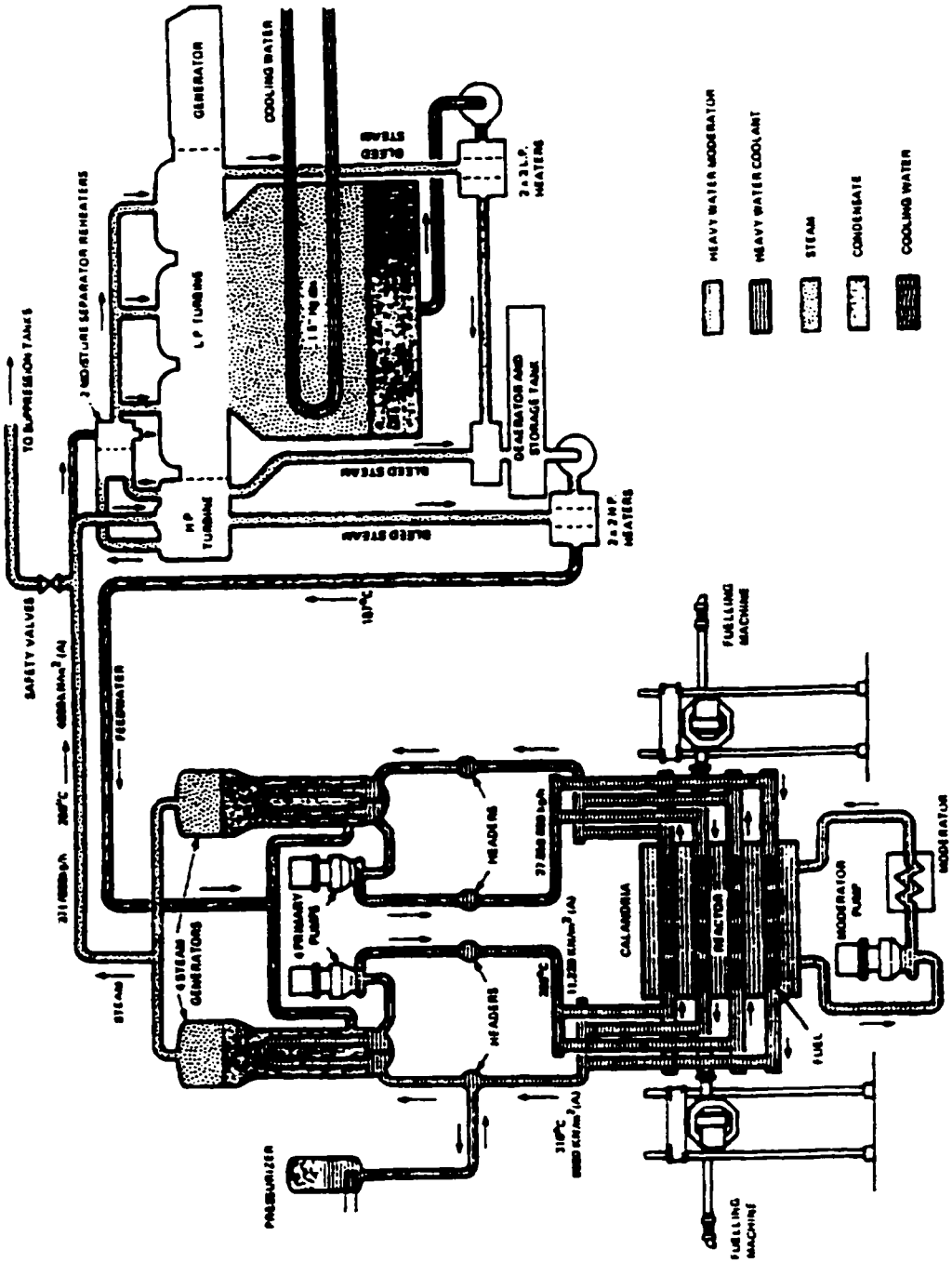

Figure 1.1 CANDU nuclear power system

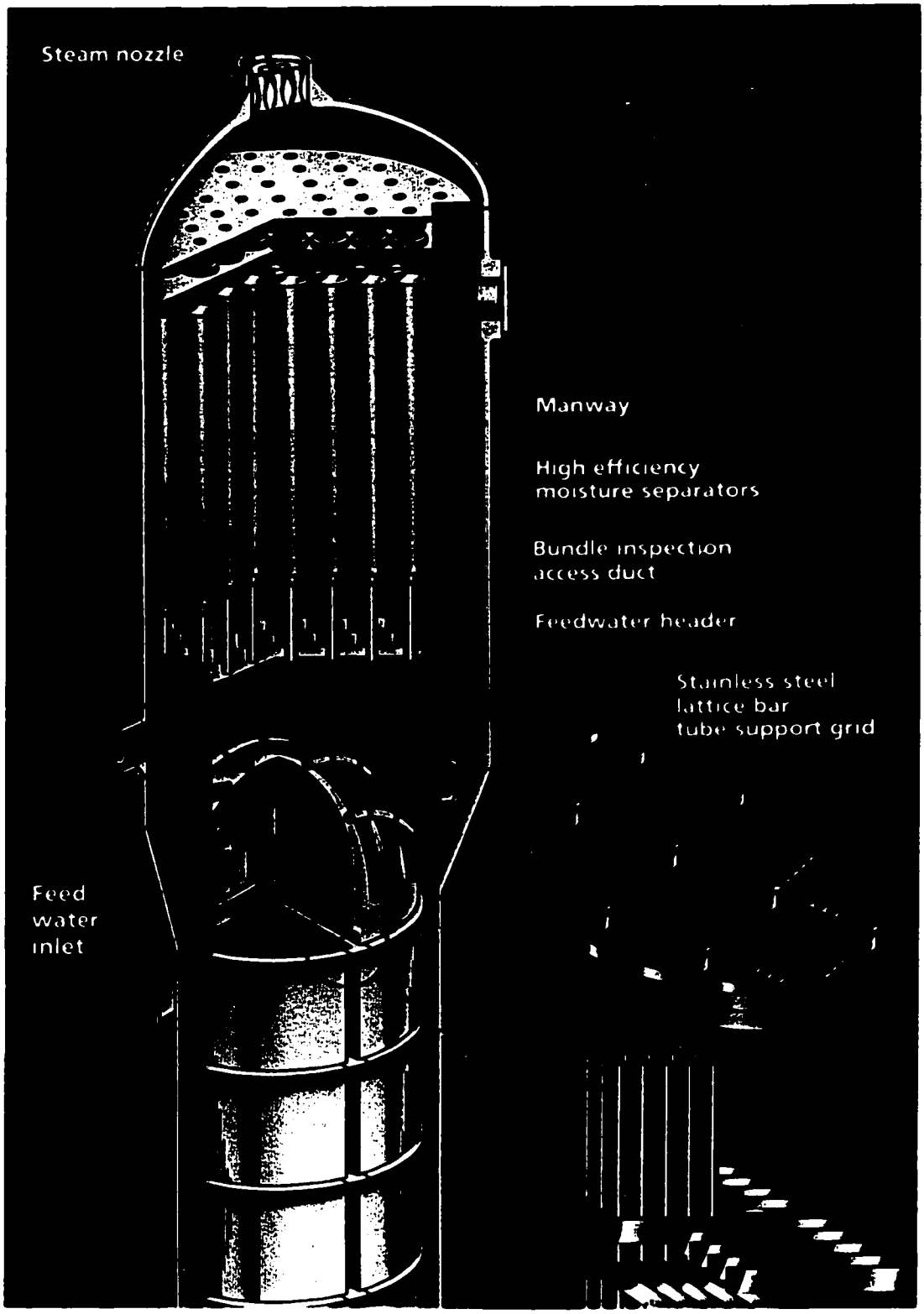

Figure 1.2 Partial illustration of a recirculating type nuclear steam generator. Babcock and Wilcox.

NOTE TO USERS

Page(s) not included in the original manuscript are unavailable from the author or university. The manuscript was microfilmed as received.

7-9

This reproduction is the best copy available.

UMI®

Table 1.1 Units reporting steam generator problems worldwide.*

Reported problem	1977	1982	1992
Total units	52	99	205
Denting			
Tube support corrosion	15	30	34
Tube-sheet corrosion	6	12	50
Tubing corrosion			
Wastage	19	28	39
Pitting	0	3	14
ID cracking	1	22	90
OD SCC/IGA	6	22	74
Mechanical damage			
Fretting	9	15	117
Fatigue cracking	3	4	10
Impingement	0	2	9
No reported problems	26	32	33

OD SCC = outer diameter stress corrosion cracking, IGA = inter-granular attack

* Source: Green & Hetsroni (1995).

Table 1.2 Reported causes of steam generator tube defects resulting in plugging (worldwide)*

Cause	Percentage of tubes plugged				
Year	1987	1988	1989	1990	1991
Primary side SCC	35.8%	40	36.6	43.2	22.1
Secondary side SCC/IGA	30	25.3	35.4	28.9	60.9
Pitting	7.1	6.8	6.5	1.6	2.0
Phosphate wastage	1.3	1.1	1.1	0.8	0.5
Denting	0.6	0.5	1.7	2.3	0.7
Thinning	1.1	0.14	0.1	0.5	0.04
Erosion-corrosion	2.3	1.0	1.2	0.6	0.5
Fretting	8.5	7.0	10.5	17.7	5.2
Fatigue	0.8	0.8	0.2	0.06	0.09
Mechanical Damage	0.4	0.2	0.05	0.85	0.8
Metallurgical examination	0.4	0.2	0.05	0.85	0.7
Undetermined	0.8	0.35	0.09	0.06	0.07
Other	11.3	16.8	6.4	3.3	7.2
Total number of tubes plugged	*5614*	*6583*	*5708*	*7688*	*10,208*
Percentage of tubes plugged	*0.19*	*0.21*	*0.18*	*0.23*	*0.30*

SCC = stress corrosion cracking, IGA = inter-granular attack

* Source: Nuclear Engineering International, Jan. 1995, Vol. 40, No. 486, pp. 18-22.

CHAPTER 2

Review of Flow-Induced Vibrations in Heat Exchangers

2.0 Introduction

Flow-induced vibrations research on heat exchanger tube arrays has typically focussed on orientations of tubes subjected to cross-flow rather than parallel-flow, because the former scenario was found to be far more susceptible to vibration damage. It is generally accepted that 3 mechanisms of excitation can cause tube vibrations, and these are physically distinct. These are turbulence buffeting, fluidelastic instability, and vortex shedding. These mechanisms fall into the categories of forced vibrations, self excited vibrations and self controlled vibrations respectively. These are equilibrium, eigenvalue and mixed problems respectively, which result in steady state, stability and resonance phenomena (Weaver, 1992). Figure 2.1 illustrates schematically how these three excitation mechanisms affect the amplitude response of a flexible tube in an array subjected to cross-flow. A fourth possible mechanism is acoustic resonance, which occurs in gas flows when vortex shedding or a shear layer instability of the flow through the array coincides with an acoustic mode in the shell of the heat exchanger. This phenomenon creates considerable noise which can lead to fatigue damage of the shell and discomfort to the plant personnel due to the high noise level.

Fluidelastic instability is the excitation mechanism which has the greatest potential for short term damage to heat exchangers, and thus it has received the most attention in research. With this excitation, a coincidence between the fluid forces and the tube motion occurs, and the tubes receive energy from the flow, which results in oscillations. The amplitude of these oscillations will grow until the tube is able to dissipate this energy through damping. Typically, the vibration amplitudes grow rapidly after the flow velocity exceeds a critical threshold level. Determining this threshold velocity has been the primary goal of most of the research to date. If these large oscillations are allowed to persist by operating the heat exchanger above the critical threshold velocity, tube damage will be the likely outcome, from fretting wear at the supports, by clashing with neighbouring tubes or by fatigue.

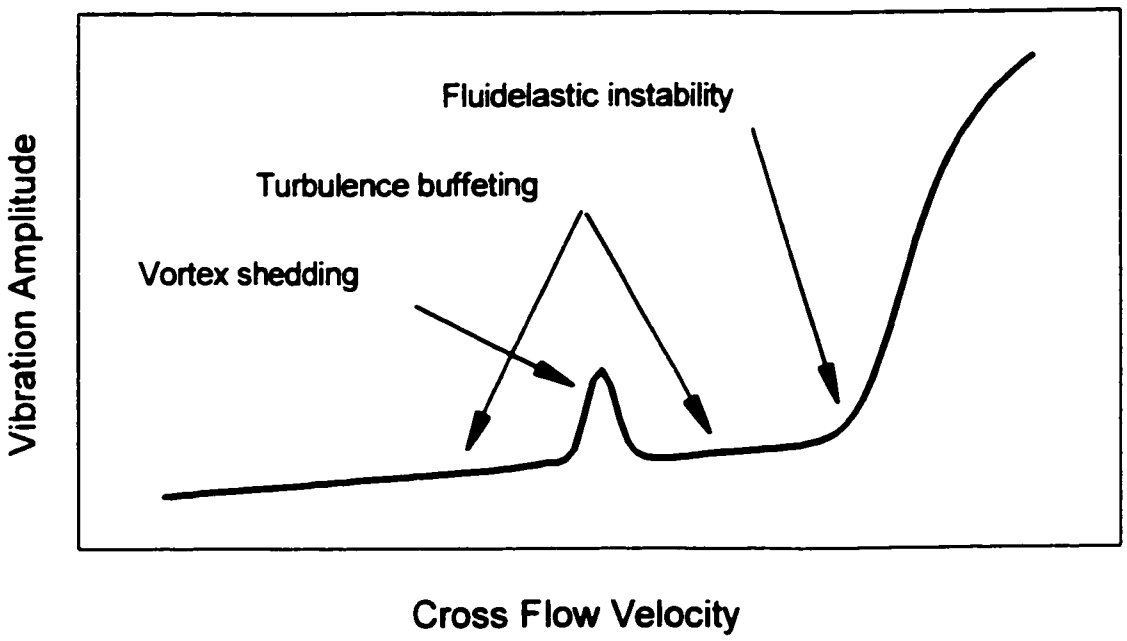

Figure 2.1 Idealized amplitude response of a tube array subjected to cross flow of fluid.

Fluidelastic instability has been studied extensively using both experimental and theoretical techniques, and excellent reviews have been written by Paidoussis (1982), Chen (1984, 87), Weaver and Fitzpatrick (1988), and Pettigrew and Taylor (1991). The most recent review of experimental studies of fluidelastic instability is by Pettigrew *et al.* (1998). Experiments done to study the problem have concentrated mainly on developing maps to predict the critical flow velocity at which instability would occur for various array geometries and structural parameters of the tubes. These maps can be found in Blevins (1990), Weaver and Fitzpatrick (1988) as shown in Figure 2.2, Chen (1984) as shown in Figure 2.3 and Schroder and Gelbe (1999). Theoretical studies have also been undertaken to predict the threshold of fluidelatic instability, which provide a more fundamental understanding of the phenomenon. A review of theoretical studies of fluidelastic instability is provided by Price (1995).

2.1 Fluidelastic Instability in Tube Arrays - Historical Development

In 1966, Roberts studied the fluid jets issuing from the gap between cylinders in a tube row, and found that they would coalesce with one of the neighbouring jets. This fluid jet pairing would alternately switch between one neighbour and the other in synchronism with the cylinder motions resulting in an abrupt change in drag on alternate cylinders. Roberts suggested that it was the jet

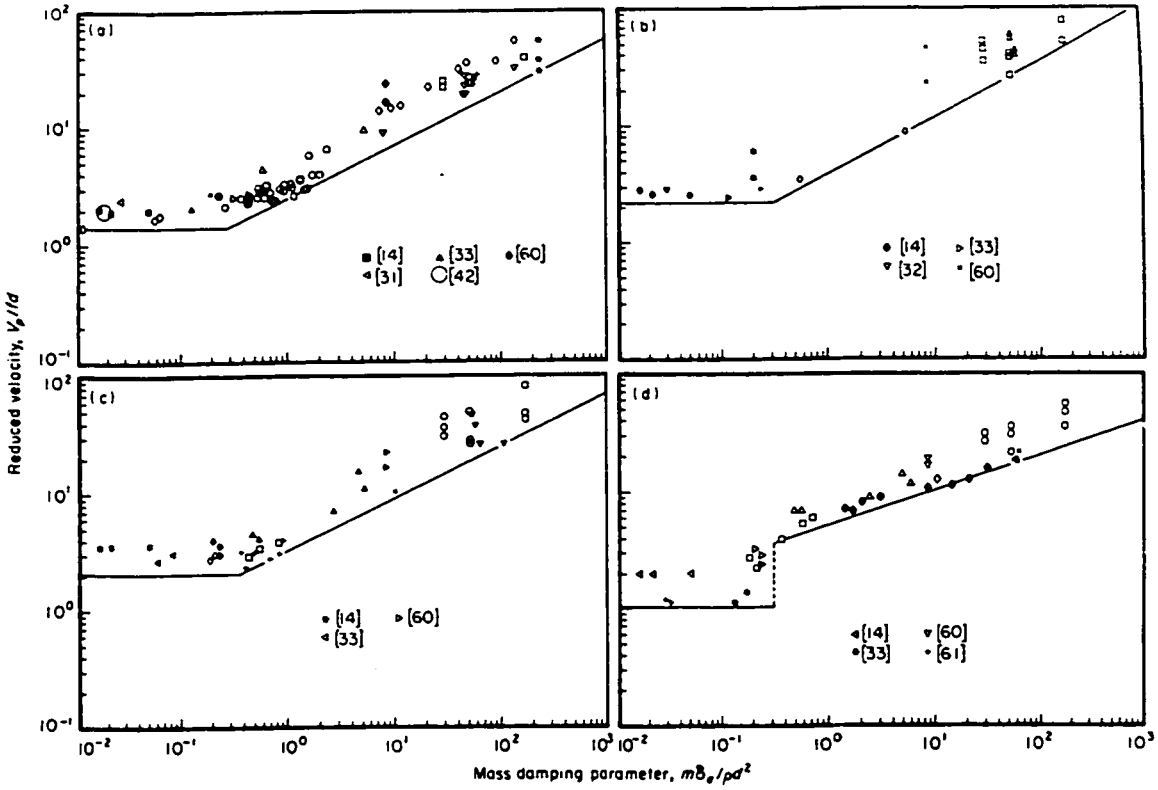

Figure 2.2 Stability diagram showing critical flow velocities for fluidelastic instability for (a) square arrays, (b) rotated square arrays, (c) normal triangular arrays, (d) parallel triangular arrays. Drawn from Weaver and Fitzpatrick (1988).

switching that caused the tubes to vibrate and proposed a semi-empirical analytical model to explain the vibrations. He predicted that tube instability would only occur when the dimensionless velocity, $V_p/f_nD > 12$ approximately, which would allow enough time for the jet switching to occur.

Connors (1970) studied a single row of flexible cylinders subject to cross-flow. He speculated that the forces and the tube displacement were interdependent and proposed a quasi-static semi-empirical analytical model to explain the self excited oscillations:

$$\frac{V_p}{f_n D} = 9.9\left[\frac{m\delta}{\rho D^2}\right]^{0.5} . \qquad (2.1)$$

Though its applicability was intended for a single tube row only, this equation became accepted by designers who applied it to multi-row tube bundles. Blevins (1974) mathematically formalized the

model and extended it to deal with arrays of tubes. He suggested that the form of Eqn. (2.1) should be applicable for cylinder arrays except the constant, 9.9 needed to be changed to some other constant, K, to be determined by theory or experiment,

$$\frac{V_p}{f_n D} = K\left[\frac{m\,\delta}{\rho D^2}\right]^{0.5} . \qquad (2.2)$$

A significant amount of research was undertaken in single phase flows to determine K for various array geometries and P/D ratios. However, large differences were found so that, as a design guideline, researchers defined a minimum value, K_{min}, which was conservative for design purposes and covered the various tube array geometries and the common P/D ratios.

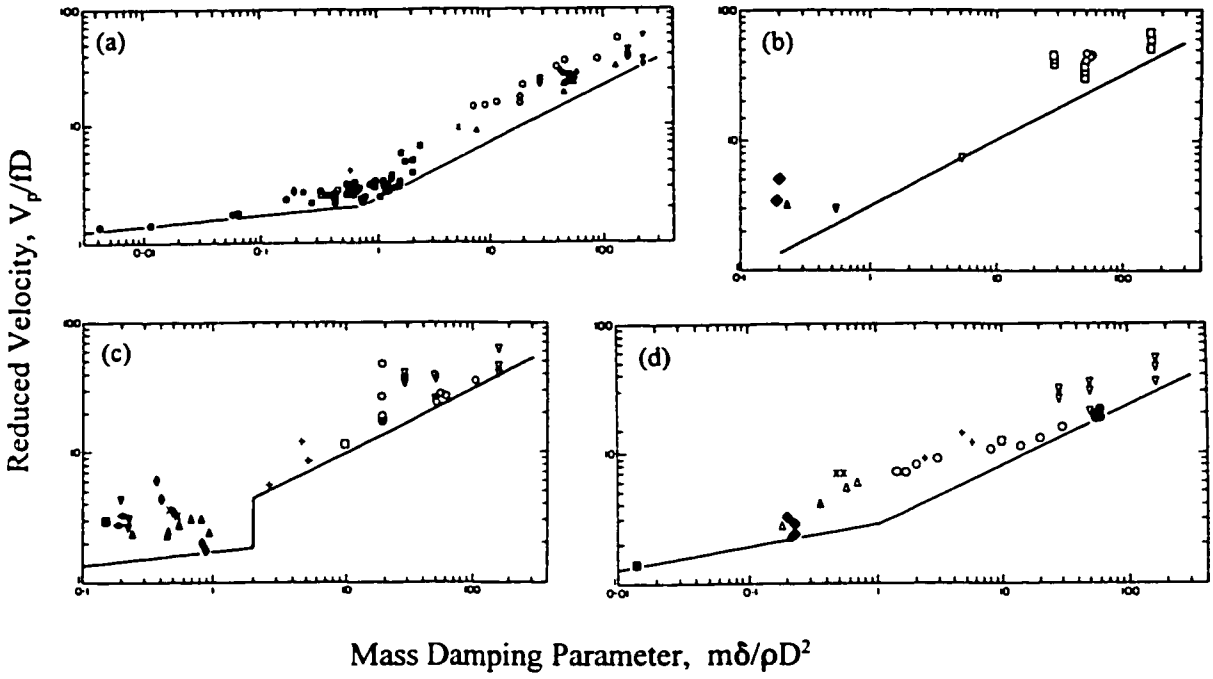

Figure 2.3 Stability diagrams showing critical flow velocities for fluidelastic instability for (a) square arrays, (b) rotated square arrays, (c) normal triangular arrays, (d) parallel triangular arrays. Drawn from Chen (1984).

A consequence of Connors/Blevins theory was that it predicted that a flexible tube in a rigid array would not go unstable, which was supported experimentally by Blevins (1974) and Price & Päidoussis (1987). However, Weaver and Lever (1977) systematically studied the effect of detuning adjacent tubes in a parallel triangular array (P/D = 1.375) so that their natural frequencies were different and compared the results to Blevins' theory. Their work showed that a single flexible tube in a rigid array would go unstable at essentially the same flow velocity as a fully flexible array. The implication of these findings was that neither Roberts' time lag mechanism nor Connors' displacement mechanism were correct by themselves.

Using dimensional analysis, Blevins (1990) showed that the onset of instability is governed by the following dimensionless groups: reduced velocity, mass ratio, damping, Reynolds number, upstream turbulence, tube spacing, and array pattern. He expressed these parameters as a power function of each group in the relationship below,

$$\frac{V_p}{f_n D} = C\left[\frac{m}{\rho D^2}\right]^a (2\pi\zeta)^b \left(\frac{P}{D}\right)^c \left(\frac{UD}{\nu}\right)^d \left(\frac{u'}{U}\right)^e . \qquad \textbf{(2.3)}$$

When large amounts of data were analyzed, Blevins found that instability was only weakly related to Reynolds number, array spacing and geometry. Individual studies of the effect of upstream turbulence on instability were contradictory. Hence, the critical velocity data were fitted to the simpler relationship,

$$\frac{V_p}{f_n D} = K\left[\frac{m\delta}{\rho D^2}\right]^a , \qquad \textbf{(2.4)}$$

where the coefficients "K" and "a" were obtained by fitting experimental data for various array geometries, different fluids etc. The data points plotted in Figures 2.2 and 2.3 were obtained from many experimental measurements of critical velocity from a variety of sources for P/D ratios. The experimental data for critical flow velocity are not always in agreement, and conservative boundary lines between safe and unsafe operating regions are drawn as a guide to designers. Reasons for the scatter in the data are proposed by Chen (1984): 1. Different parameters are used by different researchers. Some use in vacuo values for frequency and damping while others use in flow or in still

fluid values. 2. The flow velocity is not defined in a consistent manner. 3. Critical flow velocity is defined differently - some use a maximum amplitude while others use a criteria based upon the slope of the high amplitude part of the curve at the point where it intersects the velocity axis. 4. The fluid mechanical aspects of the instability are hidden within the coefficient K.

2.2 Review of Fluidelastic Instability in Single Phase Flows

Most of the experimental studies of flow-induced vibration in tube arrays have been performed in single phase fluids such as air or water. Most of this work was primarily designed to study fluidelastic instability, which is the most dangerous mechanism of vibration. These efforts led to a better understanding of the excitation mechanisms active in producing the instability of tubes and helped in the development of theoretical models. This body of work is reviewed first because it lays the groundwork for the subsequent studies in two-phase flows.

While the Connors/Blevins formula (eqn. 2.2) has gained wide acceptance, experiments have showed that the theoretical basis for the model was not correct. Weaver and Lever (1977) studied a rotated triangular array with P/D =1.375 subjected to a cross-flow of air. They found that de-tuning of neighbouring tubes did not have a monotonic stabilizing effect as expected from Blevins' theory (1974). Weaver and Grover (1978) performed wind tunnel studies on a parallel triangular array of P/D = 1.375. They observed a sharp instability threshold in the first two rows where the dominant mode of vibration was in the transverse direction. The first few rows of tubes had the lowest stability threshold and were therefore most critical. In addition, the critical velocity was found to be the same for the fully flexible array as for the rigid array with one flexible tube. These findings and those of Blevins *et al.* (1981) and Southworth and Zdravkovich (1975) disproved the previously held belief that the displacement of neighbouring tubes was required for fluidelastic instability to occur.

Chen and Jendrzejczyk (1981) performed experiments in water with 12 different tube arrays to test tube spacing, mass ratio, damping and detuning effects. In their analysis they confirmed that detuning of neighbouring tubes had a beneficial effect on stability, but only up to a 10% frequency difference, which agreed with the findings of Weaver and Lever (1977). They also found that, in the range of practical interest, geometry and tube spacing had little effect on the critical flow velocity. Damping, however, had a profound effect on tube response. Large tube damping suppressed the peaks

in the amplitude response and resulted in the critical flow velocity being sharply defined. For low values of damping, vibration amplitudes were high in the sub-critical velocity range and the critical flow velocity was not well defined.

Weaver and Yeung (1983) studied the effect of incident flow direction in a square array of tubes in water. The effect on critical flow velocity was not entirely clear, except that the 25° orientation of the tube rows with respect to the flow direction had a critical flow velocity that was about 50% higher than the 0° and 45° orientation. This result implied that studies performed on the 0° (normal square) array and the 45° (rotated square) array would be conservative. Figure 2.4(a) shows the change in stability threshold as the array is rotated from the normal square configuration in increments of 0, 10 and 20 degrees, while Figure 2.4(b) compares the amplitude response of a normal square and a rotated square array. The figures reveal the lumpy nature of the tube response in liquid cross flow, which sometimes makes it difficult to determine precisely the critical flow velocity.

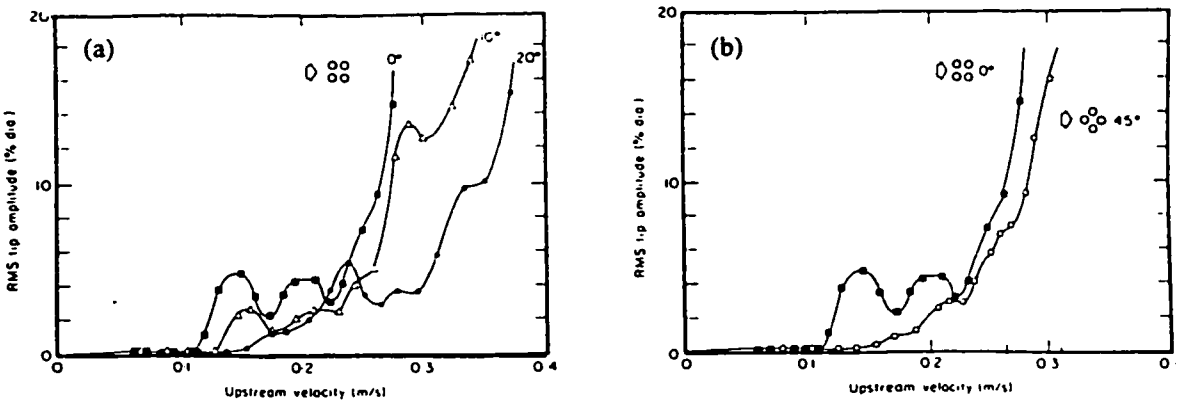

Figure 2.4 Amplitude response curves for various incident flow directions. Weaver and Yeung (1983).

Weaver and Koroyannakis (1983) studied the effect of asymmetric stiffness in the response of a flexible tube bundle in water cross flow. Eight cases were studied with up to 57% difference between streamwise and transverse frequencies. This arrangement was contrived to simulate the difference between in-plane and out-of-plane natural frequencies of U-tube heat exchangers. They found that asymmetric stiffness increased the stability threshold by 20% over the symmetric case, and

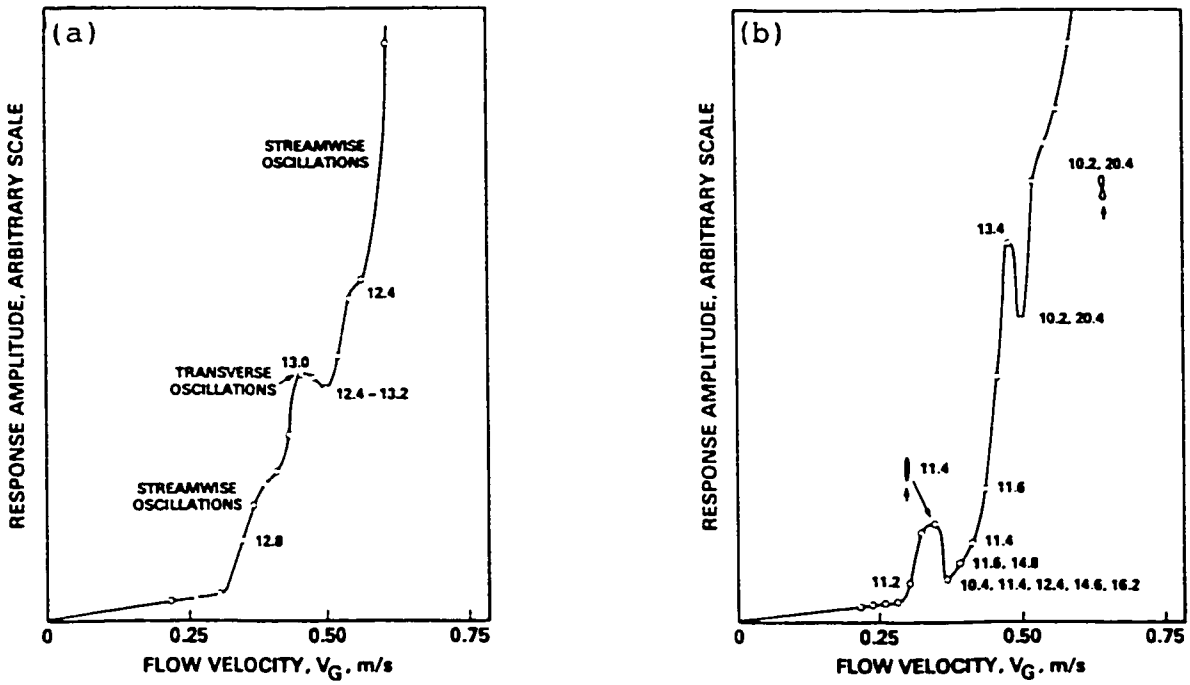

Figure 2.5 Amplitude response curves for a fully flexible tube bundle in water cross-flow, (a) symmetric stiffness, (b) asymmetric stiffness $f_T/f_S = 1.57$. Weaver and Koroyannakis (1983).

that it was independent of the magnitude of the asymmetry or its orientation to the flow direction. Figure 2.5 gives a comparison of the response for two cases. These figures show that the critical flow velocity is roughly the same for the case of symmetric and asymmetric stiffness. Two characteristics of the tube bundle response in water flows is evident in these figures; one is the lumps in the amplitude response below critical velocity and the other is the post instability undulations which coincide with a frequency shift and a change in vibration mode.

Price and Kuran (1991) performed experiments on a rotated square array with a relatively large pitch (P/D = 2.12), and found this array to be stable when one flexible tube was subjected to cross-flow. They also found that when three or more nearest neighbours were flexible and positioned in the first few rows, fluidelastic instability was possible. This was in agreement with theoretical analyses which predicted that instability in this array is a fluid-stiffness controlled mechanism, which requires fluid coupling between at least two adjacent flexible cylinders.

Austermann and Popp (1995) studied a single flexible tube subjected to air cross-flow in various geometries and P/D ratios. Using eddy current dampers, they were able to vary the mass-damping parameter of the flexible tube from about 12 to 500, which allowed greater flexibility of their bundle to exploring fluidelastic instability. Their apparatus allowed them to adjust the equilibrium position of the flexible tube to test how imperfections in geometrical layout affected tube stability. They compared their results for fluidelastic instability with results for fully flexible arrays and found sensitivity to geometric disturbances was greater for smaller P/D ratios.

Romberg and Popp (1998) studied the effect of upstream turbulence on the stability of a flexible tube in a bundle in a cross-flow of air. The intensity and length scale of the upstream turbulence was varied by a turbulence grid placed at variable positions in front of the tube array. They found that increasing the upstream turbulence intensity resulted in an increased stabilization for a single flexible tube when positioned in the first few rows. For the fully flexible array, varying the upstream turbulence had a negligible effect on stability.

2.3 Review of Fluidelastic Instability in Two Phase Flows

In the last two decades, researchers in heat exchanger vibration have begun to focus their attention on the tube bundle response in two-phase flow. This type of flow exists in many shell and tube heat exchangers such as condensers, evaporators, re-boilers and nuclear steam generators. Much of the research to this date has been focussed on the U-bend region of nuclear steam generators, where cross-flow of steam and water occurs. This part of the steam generator is susceptible to fluidelastic instability because of the long spans and low stiffness of the outer tubes. Due to the complicated nature of two-phase flow, there are many more aspects which need to be explored than in single-phase flow. As a result of these concerns, the data base for two-phase fluidelastic vibration has been expanding, and new studies are constantly being published. Figure 2.6 gives a comparison of some of the published data in two-phase flow for fluidelastic instability on a stability diagram, for various array geometries and P/D ratios of a number of researchers. The following section looks at some of the research done to date in cross-flow and outlines the unique difficulties with scaling parameters and data analysis in two phase flow.

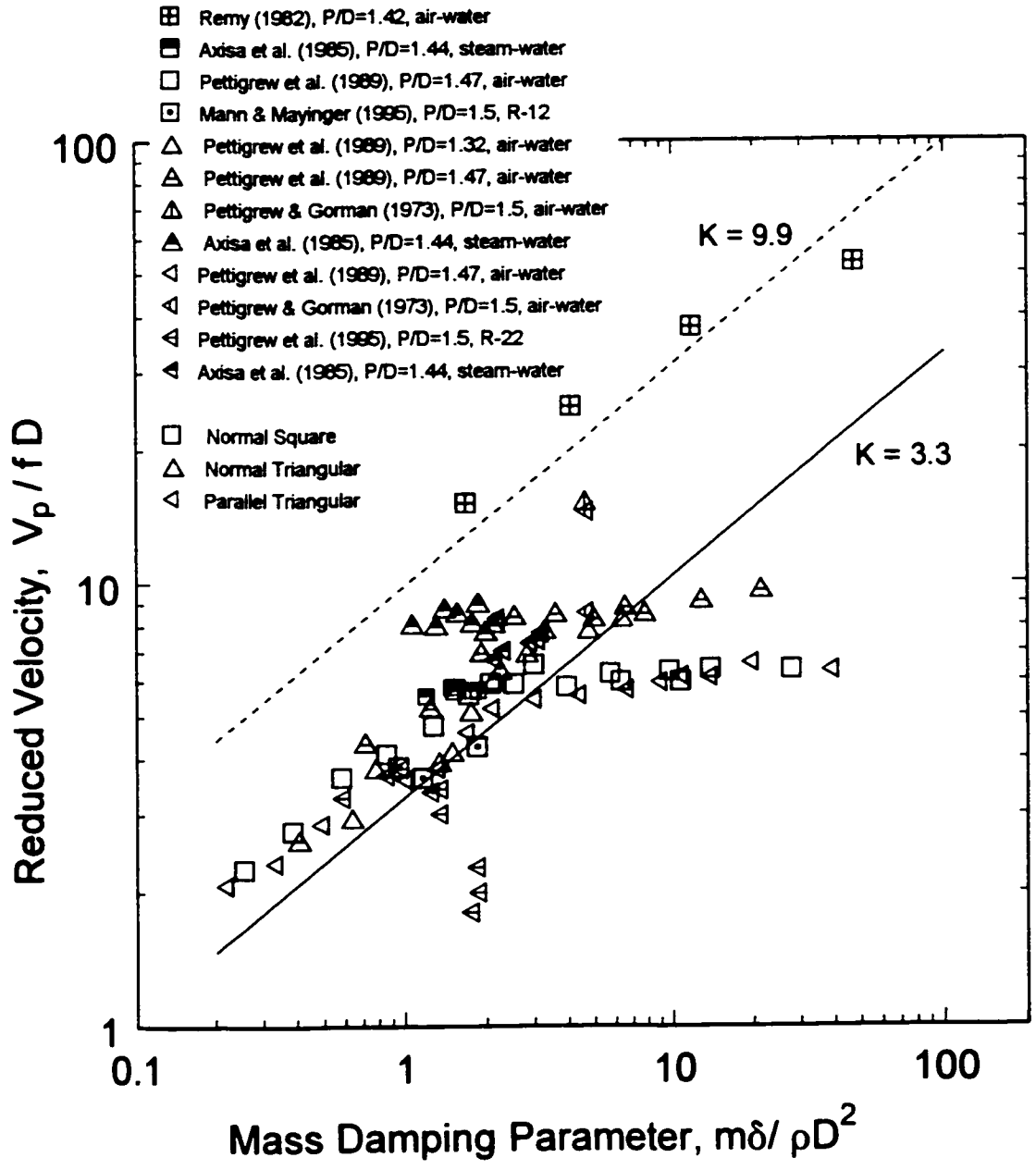

Figure 2.6 Critical velocities for fluidelastic instability obtained from experiments in two-phase flow.

Heilker and Vincent (1981) performed cross flow experiments in which they compared tube bundle response in single-phase water flows and two-phase air-water flows. They plotted their amplitude response in terms of a fluid pressure, $P_f = \rho V_G^2/2g$ because they believed it was intuitively correct that the tube response would be linearly proportional to the dynamic head and because it facilitated comparison of displacement caused by fluid of different densities. They found that the

incident flow direction had a significant bearing on the sensitivity of the array to vibration, where the parallel triangular orientation was most critical. Vortex shedding was not observed in any of the two-phase tests nor in the triangular array in single-phase flow. Their criteria for the onset of fluidelastic instability was tube impacting for small P/D ratios and rattling in the supports for large P/D ratios. These criteria differed from those used by most other researchers who defined the critical flow velocity as the point where the amplitude response takes a sharp upward turn, or where the amplitude exceeds a certain level, or a combination of both. Unless the post instability response is very high, using impacting as a criteria would lead to overly high estimates of critical flow velocity. This may explain why these authors obtained a rather high instability coefficient of K = 5.0 while Pettigrew *et al.* (1989) obtained values of K = 3.3 to 4.0. Damping values were obtained in two-phase flow using the half power band-width method. Unfortunately, the authors did not tabulate their results but rather plotted the calculated parameters on the stability diagram, so that their damping data was not made available.

Axisa *et al.* (1983) were the first to present results on fluidelastic instability in both air-water and steam-water cross-flow. A normal square tube bundle of P/D = 1.44 was tested and it was found that using air-water to simulate steam-water was reasonable for fluidelastic instability. Subsequently the study was extended to include parallel triangular, normal triangular and normal square arrays of P/D = 1.44 in steam-water cross-flow in Axisa *et al.* (1985). Nakamura *et al.* (1986a) has also reported data on fluidelastic instability in air-water cross-flow and steam-water cross-flow (1986b).

Pettigrew *et al.* (1989) published a series of papers which outlined their extensive program of study in tube arrays subjected to two-phase air-water cross-flow. Experimental results were presented for the four standard tube arrays (ie., normal and parallel triangular arrays, normal and rotated square arrays) and for pitch over diameter ratios of P/D = 1.32 and 1.47. The test bundles were subjected to air-water mixtures to simulate realistic mass fluxes and vapour qualities corresponding to void fractions from 5 to 99%. The effects of hydrodynamic mass, damping, fluidelastic instability, and turbulence induced excitation were reported.

Feenstra (1993) and Feenstra *et al.* (1995) were one of the first to report results on fluidelastic instability in cross-flow using a single component mixture of two-phase gas and liquid flow using refrigerant R-11, which represented a closer approximation to the density ratio of steam-water than the commonly used air-water mixtures. The fluidelastic results obtained were slightly less conservative

than the air-water results of Pettigrew *et al.* (1989b) when plotted on a stability diagram. Through the use of a gamma densitometer, the authors showed that the actual void fraction of the flow was considerably lower than that predicted by the often used homogeneous equilibrium model, and that this could have implications on data analysis and comparison with other works. In a latter paper, Feenstra *et al.* (1996) demonstrated how the fluidelastic data analysis could be performed on previously obtained data in two-phase flow, where the means to measure void fraction were not available, through the use of a empirical void fraction model. At that time however, the only void fraction models for tube bundle flows were highly empirical and were found to be not generally applicable to fluids different from those in which the data were generated.

Pettigrew and Knowles (1992) studied the effect of void fraction, tube frequency and surface tension on tube damping. A two phase flow field was simulated by filling a cylinder with water and bubbling air up from the bottom. A flexible tube was mounted concentrically in the cylinder and plucked to obtain the log-decrement vibration trace. Unfortunately it was not possible to exceed 25% void fraction due to limitations of the apparatus. The results showed that damping increased linearly with void fraction. A chemical surfactant added to the water allowed the surface tension to be reduced by 50%. The results were not wholly consistent but it appeared that damping increased with surface tension. The overall conclusion on damping was that design guidelines for damping of heat exchanger tubes would have to wait, because more investigation was required to unravel the complexity of the relationships.

In a more recent review paper, Pettigrew and Taylor (1994) discuss the two predominant excitation mechanisms in two-phase flow, fluidelastic instability and turbulence buffeting, where both axial and cross-flows are treated. Measurements and empirical models for hydrodynamic mass and damping were also presented.

Pettigrew et al. (1995) performed experiments in cross-flow of a parallel triangular array using two-phase refrigerant 22, and reported information on turbulence buffeting, damping and fluidelastic instability. They found damping to be highly dependent upon void fraction and that fluidelastic instability was dramatically affected by a change in two-phase flow regime. Mann and Mayinger (1995) performed experiments with a normal square tube bundle subjected to two-phase R-12 cross flow, which they operated at a pressure such that the density ratio of the Freon nearly replicated that

of the actual steam-water flow in a typical power plant. An optical probe was used to measure the local void fraction and thus they did not rely on the HEM. This device also allowed them to measure the fluctuations of void fraction in the flow lanes. By traversing across the bundle with their probe, they found that the local void fraction was higher in the wake zones behind the tubes, which was contrary to visual observations of Pettigrew and Taylor (1994) who observed predominantly liquid in these relatively stagnant zones. Delenne *et al.* (1997) presented data obtained from flow-induced vibration experiments on an in-line bundle subjected to two-phase water- Freon 13B1 cross-flow. Their results were analysed to derive the relationship between frequency, damping and vibration amplitude as a function of void fraction and mass flux. Attention was focussed on determining fluidelastic coefficients which could be used in theoretical models. Various two-phase fluid models were used to reduce the data, such as the HEM, the drift flux model by Zuber and Findlay (1965) and an empirical void fraction model developed by Schrage *et al.* (1988) from air-water cross flow measurements. Delenne *et al.* were one of the first to compare the applicability of the HEM with a more appropriate two-phase fluid model.

Up till now, two aspects of fluidelastic instability analyses have been lacking: One is a suitable void fraction model to more accurately predict the actual void fraction of the two-phase flow, since the commonly used homogeneous model was shown to be inaccurate. The other is a better means of predicting flow regime of the flow in tube arrays. Presently, researchers have relied on maps that did not cover a sufficient range of conditions or upon correlations that were generated for in-pipe flows but were not designed for shell-side flow through a tube bundle.

2.4 Review of Turbulence Buffeting in Tube Arrays

Turbulence induced vibration occurs because the tubes in the array act as turbulence generators and hence they are subjected to broad band turbulence buffeting at all flow velocities and in every conceivable situation. The tubes extract energy from the flow in a narrow spectrum corresponding to the fluid coupled natural frequencies of the cylinders. The vibration amplitudes resulting from this excitation mechanism are small, usually of little concern. However, long term damage to the tubes may result from buffeting so that it has received some attention from researchers. Axisa *et al.* (1990) investigated random excitation of tube arrays in cross-flow of single-phase and

two-phase flows. They developed a theoretical framework which related the amplitude response of a flexible tube to the dimensionless forcing spectrum of the flow excitation according to physically relevant scaling parameters. From their single-phase data, they were able to develop an upper bound of the dimensionless force spectrum which could be used for design purposes. In the case of two-phase flows, the data did not collapse using scaling parameters developed for the single-phase data, and the authors concluded that they had insufficient data to proceed further. From their practical experience, they found that the resultant fluid forces were more accurately obtained by direct measurement using a rigid tube mounted on force transducers rather than by indirect measurement using the response from a flexible tube. Nevertheless, some interesting findings resulted from this work. Axisa *et al.* concluded that air-water and steam-water forces are of the same order of magnitude, which suggested that air-water flow was suitable to simulate steam-water flow. In addition, random forces were the same order of magnitude in single-phase flows as in two-phase flow, based upon the data obtained by using the homogeneous equilibrium model.

Taylor *et al.* (1988) measured the fluctuating forces induced by water and air-water cross flow on a single row of tubes with P/D ratios of 1.5 and 3. The monitored tube was mounted on force transducers which allowed for direct fluid force measurements. It was found that the single-phase force spectra were drawn together by the use of equation (2.5),

$$\Phi(f_R) = \frac{\phi(f)}{(\frac{1}{2}\rho_w V_p^2 D)^2} \frac{V_p}{D}, \qquad \textbf{(2.5)}$$

where the dimensional fluid force spectrum, $\phi(f)$, could be normalized to give the dimensionless form, $\Phi(f_R)$, which rendered the data useful in predicting the rms tube response. The dimensionless forces in two-phase air-water flow were found to be higher than for single phase water. The air-water force spectra however, varied with void fraction and did not draw together with the use of equation (2.5) and no alternative method was derived. In subsequent papers, Taylor (1992, 96) developed a method of reducing two-phase random excitation data by defining new scaling parameters which were deemed more appropriate in a two-phase flow. For example, the length scale was based upon a characteristic bubble diameter and the force scale was dependent upon flow regime. Other notable papers on

turbulence buffeting have been published by Pettigrew and Gorman (1977), who presented some of the earliest data, Blevins (1994), Kawamura *et al.* (1997) who performed experiments in steam-water parallel-flow, and Romberg and Popp (1997) who measured the pressure distribution axially and circumferentially along a tube which was specially equipped with local piezoelectric pressure sensors. Recently, De Langre and Villard (1998) assembled a database of turbulence buffeting measurements including direct and indirect force measurements in various two-phase fluids from various researchers. They attempted to scale the data according to the formalism that had worked for single-phase flows, but additional scaling factors were employed to obtain better collapse of the two-phase data. They found that gravity forces were important in determining the appropriate dimensionless spectra, but of lesser importance were dynamic pressure, viscosity and surface tension forces. The end result of their efforts, which were of practical importance, was the development of an upper bound of the random fluid force magnitudes in two-phase flow, as shown in Figure 2.7, which could be used by designers to determine vibration amplitudes and help to predict long term wear of the heat exchanger tubes.

2.5 Review of Vortex Shedding in Tube Arrays

Vortex shedding can be a source of tube vibration in heat exchangers, but the intractable nature of this phenomenon has led some to speculate that it does not exist in tube arrays. It is typical for the amplitude response of tube arrays in liquid flow to exhibit a number of undulations in the amplitude response curve, which are sometimes associated with vortex shedding and sometimes associated with peaks in the turbulent energy spectrum coinciding with one of the fluid coupled natural frequencies. For arrays of cylinders, some prefer to call this phenomenon Strouhal periodicity, since it deviates considerably from the behaviour of a single cylinder. For staggered arrays, alternate vortex shedding from the first few tube rows is believed to be the source of flow periodicity, while for in-line arrays it is thought that symmetric or anti-symmetric jet instability is the source. In most cases, it is found that the first few tube rows of a bundle with a mass-damping parameter of less than unity are susceptible to Strouhal excitation. Deeper in the bundle, it is suppressed by turbulence induced by the tube array. Weaver (1993) provides a thorough review of the subject for cylindrical structures in cross flow.

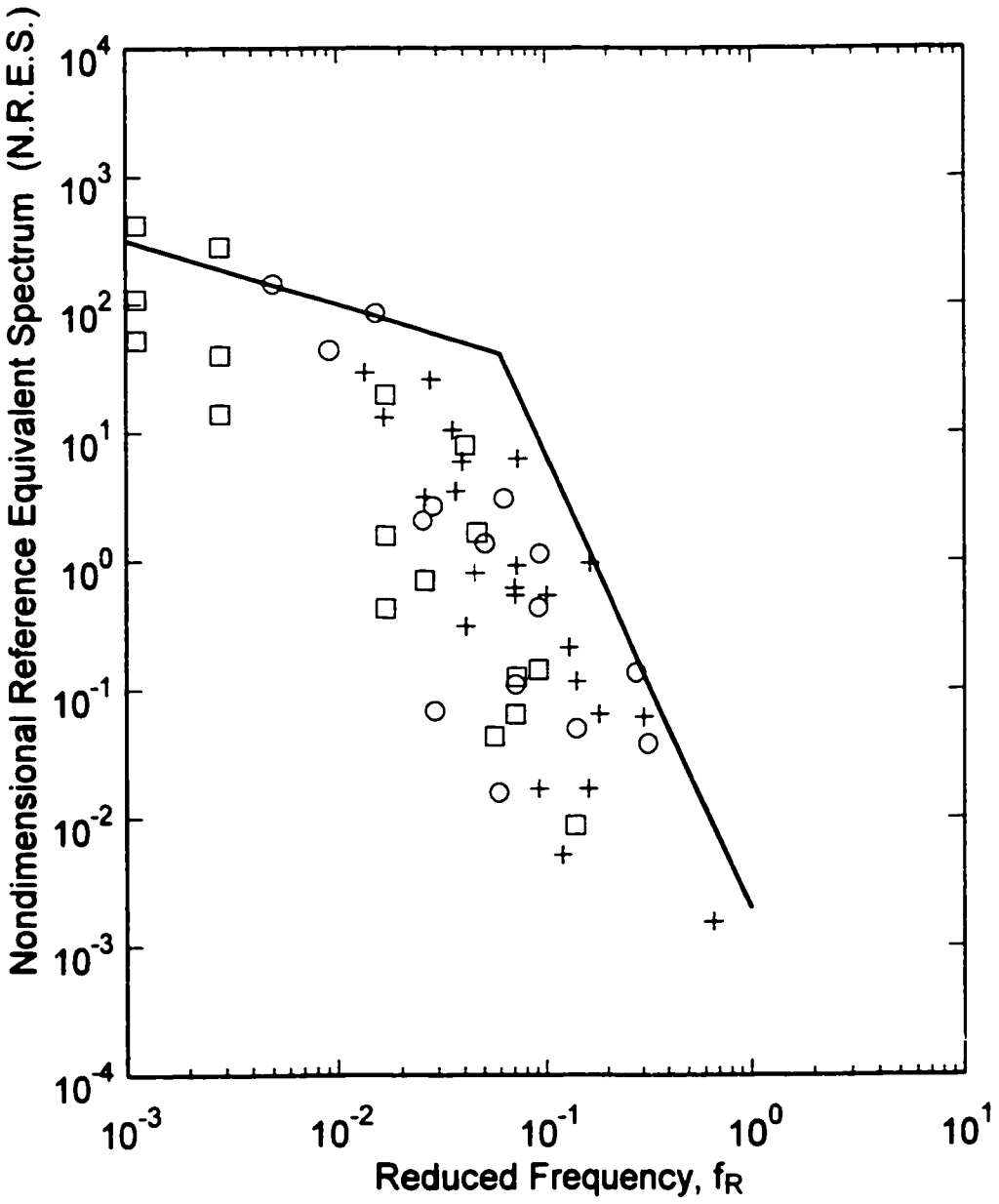

Figure 2.7 Reduced data for turbulence buffeting in two-phase flows. □ Steam-water data; ○ air-water data; + refrigerant data; ———— proposed upper bound. De Langre and Villard (1998).

Vortex shedding is characterized by the Strouhal number,

$$S_t = \frac{fD}{V}, \tag{2.6}$$

where f is the dominant frequency of the forcing spectrum and V is the flow velocity, usually taken as velocity in the minimum gap (ie., pitch velocity). Empirical work on this excitation mechanism hinges on determining the Strouhal number(s) for a given fluid structure interaction. This information is needed by designers who wish to avoid resonance between tube natural frequency and excitation frequency of the flow field.

The research to date indicates that Strouhal periodicity is possible in the first few rows of a tube array, but high upstream turbulence can suppress it. Deeper within tube arrays, Strouhal periodicity usually diminishes because of the turbulence generated by the tube array. However, it may persist depending upon the Reynolds number, cylinder geometry, mass ratio and vibration amplitude. Tube arrays with mass damping parameters of less than unity, (ie., liquid flows) are the most susceptible, while in gas flow, Strouhal periodicity acts as a source of noise. Resonance can be avoided if accurate Strouhal numbers are available for the given tube array and flow conditions. A considerable amount of research has gone into such predictions which has culminated in a series of Strouhal maps, one of which is adapted from Weaver and Fitzpatrick (1988) in Figure 2.8. This figure predicts a Strouhal number of 1.5 to 2.0 for a parallel triangular array with a pitch to diameter ratio of 1.44. Hence for a tube with a diameter of 6.35 mm and a natural frequency of 32 Hz in liquid R-11 flow, the flow upstream flow velocity at which resonance may occur is given by,

$$V_u = \frac{fD}{S_t} = \frac{32 * .00635}{1.75 \pm 14\%} = 0.12\ m/s \pm 14\% \tag{2.7}$$

which translates to a pitch velocity range of 0.33 m/s to 0.44 m/s.

In flow-induced vibrations experiments involving two phase flows, periodic phenomena such as Strouhal periodicity were generally not observed in the amplitude response of the flexible tubes (Axisa *et al.*, 1985, Pettigrew *et al.*, 1989, 1995 and Feenstra 1993.) This is likely because the presence of a second phase inhibits any organization of coherent structures in the wakes of the tubes.

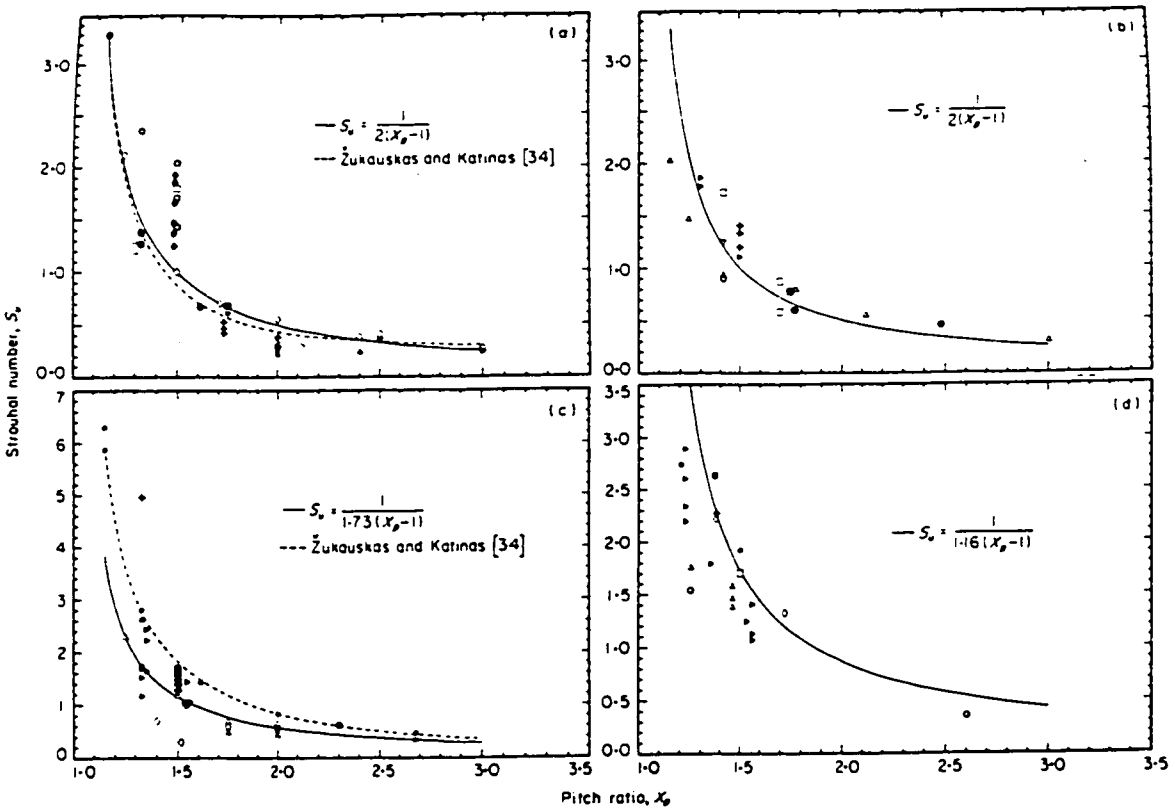

Figure 2.8 Strouhal number relationships for various array geometries. (a) square arrays, (b) rotated square arrays, (c) normal triangular arrays, (d) parallel triangular arrays. Weaver and Fitzpatrick (1988)

CHAPTER 3

Theoretical Framework of Flow-Induced Vibrations

3.0 Introduction

As discussed in the previous chapter, it is generally accepted that four distinct flow excitation mechanisms exist in heat exchanger tube arrays, (i) turbulence buffeting, (ii) fluidelastic instability, (iii) Strouhal periodicity, and (iv) acoustic resonance. The first two mechanisms, which have been illustrated in Figure 2.1, will be discussed in detail in the following sections. Acoustic resonance will not be discussed since it is outside the scope of this research. For information on Strouhal periodicity, or vortex shedding, the interested reader can refer to review papers by Fitzpatrick (1985) and Weaver (1993).

3.1 Turbulence Induced Excitation

The turbulence generated by the shell side flow in a tube array will result in random vibrations of the tubes. These are continuous and of small amplitude but can eventually cause long term wear of the tubes at their supports and possibly tube failure. Since the life span of these devices is expected to exceed twenty years, it is desirable to predict the vibration amplitudes of the tubes subjected to this flow excitation so that the length of time for tube failure to occur can be estimated. Formulations for describing tube motion in such a flow field can be developed using the classical linear random vibration theory.

Most research on turbulence buffeting focusses on determining the power spectral density of the fluid forces on a tube array for a variety of flow conditions. A direct measurement of these forces can be obtained from a rigid tube which is mounted on force transducers and is subjected to cross-flow. This method requires force measurements, flow rates and fluid properties to obtain the power spectral density of the flow forces over a frequency range, usually extending up to 100 Hz. An indirect

measurement of the forces can be obtained from the vibration response of a flexible tube equipped with strain gauges, by applying the transfer function to determine the excitation force. This approach is not as attractive because the damping and the correlation length of the fluid forces must be estimated. These quantities are not easy to measure and in many cases a conservative guess must be made.

A number of papers have been published which lay the necessary theoretical groundwork for interpreting random vibration data obtained from experiments. Axisa (1990) and Au-Yang (1999) have developed mathematical expressions from classical random vibration theory to relate the random excitation forces to the rms amplitude response of a tube in cross-flow. Individual studies on turbulence buffeting for single and two-phase flows have been published by Axisa *et al.* (1985,86,88,92), Taylor *et al.* (1988,89,96,99), Pettigrew and Gorman (1973,78) and by Nakamura *et al.* (1982, 91). By comparing various data sets, attempts have been made to develop conservative design guidelines for turbulence buffeting by Taylor *et al.* (96, 99) and De Langre and Villard (1998).

In the case of single-phase flow, it was found that a rather large body of data obtained from various experimental rigs could be reduced to a unique spectrum which gave designers the necessary information for vibration analysis. However, the approach for two-phase flow was found to be more complicated. Researchers failed to reduce the two-phase random vibration data to a consensus using the same scaling factors used in single-phase flow combined with the homogeneous fluid properties. The implication was that more detailed information about two-phase flow modelling was required to develop the appropriate scaling parameters.

3.2 Theory of Random Vibrations

When a fluid flows through a tube array, it generates flow turbulence which causes continuous small amplitude vibration of the tubes. The formulation for determining tube motion in such a scenario can be developed using classical linear random vibration theory, which is applied here to the case of turbulence induced excitation of heat exchanger tubes. The formulation follows the example of Axisa *et al.* (1990) but is simplified to the case of a uniform flow velocity in cross-flow, uniform fluid density, and is limited to the fundamental vibration mode of a tube only.

The random force per unit length of tube, $\mathbf{F}(z,t)$, acting at a location z along the tube is assumed to be stationary and ergodic. The power spectral density of the fluid forces, S_F, may be

determined from the Fourier transform of the cross correlation spectrum,

$$S_F(z_1,z_2,f) = \int_{-\infty}^{+\infty} R_F(z_1,z_2,\tau)e^{-2i\pi f\tau}\,d\tau \ , \tag{3.1}$$

where the units of S_F are $\{N^2/Hz\}$. R_F is the cross-correlation function between locations z_1 and z_2 and is given by,

$$R_F(z_1,z_2,\tau) = \lim_{T\to\infty}\frac{1}{2T}\int_{-T}^{T} \boldsymbol{F}(z_1,t)\cdot \boldsymbol{F}(z_2,t+\tau)dt \ . \tag{3.2}$$

The dimensionless formulation is desired for easier data translation to prototype applications. The excitation forces can be made dimensionless as follows: the locations z_1 and z_2 can be made dimensionless by specifying a range of 0 to 1 for each end of the tube, fluctuating forces per unit tube length are scaled by the dynamic head,

$$F = \frac{1}{2}\rho U^2 D \ . \tag{3.3}$$

Frequency, f, is scaled by the reduced frequency,

$$f_R = \frac{fD}{U} \ . \tag{3.4}$$

When straight tubes are subjected to uniform cross-flow, the forces are not conveyed along the tubes, so that S_F can be reduced to a real function in which the time and space variables are separated,

$$S_F(z_1,z_2,f_R) = \phi_F(f)\ \gamma(z_1,z_2) \ , \tag{3.5}$$

where ϕ_F is the autocorrelation spectrum of the forces per unit tube length which can be restricted to positive frequencies. The coherence function, $\gamma(z_1, z_2)$, characterizes the degree of coherence of the forces along the tube and can be approximated by,

$$\gamma(z_1,z_2) = \exp[-\frac{|z_1-z_2|}{\lambda_c}] \ , \tag{3.6}$$

where λ_c is the non-dimensional correlation length (ie., λ_c=1 corresponds full axial correlation). The non-dimensional form of the autocorrelation spectrum is given by,

$$\tilde{\Phi}_F(f_R) = (\frac{1}{2}\rho U^2 D)^{-2} \frac{U}{D} \Phi_F(f) \ . \tag{3.7}$$

Hence the final form of the forcing power spectrum per unit tube length is given by,

$$S_F(z_1,z_2,f_R) = (\frac{1}{2}\rho U^2 D)^2 \frac{D}{U} \exp(-\frac{|z_1 - z_2|}{\lambda_c}) \ [\tilde{\Phi}(f_R)] \ . \tag{3.8}$$

This form differs slightly from eqn. (16) in Axisa *et al.* (1990) because, in the present formulation, a uniform flow velocity and fluid density profile along the tube length has been assumed. The tube vibration power spectrum per unit tube length, S_y, is found by calculating the autocorrelation spectrum of the forcing power spectrum, S_F, times the square of the system transfer function, $|H(z,f)|^2$ as follows,

$$S_y(z,f) = \int_0^l \int_0^l |H(z,f)|^2 \ S_F(z_1,z_2,f_R) \ dz_1 \ dz_2 \ . \tag{3.9}$$

For a single degree of freedom system, the transfer function can be estimated by,

$$|H(z,f)|^2 = \frac{\sigma^2(z)}{16\pi^4 f_n^4 (m L)^2} * \frac{1}{[1-(f/f_n)^2]^2 + [2\zeta f/f_n]^2} \ , \tag{3.10}$$

where m is the generalized tube mass per unit length which is equal to the tube mass per unit length plus the hydrodynamic mass. The mode shape, $\sigma(z)$, of a cantilevered tube is given by (Blevins, 1984),

$$\sigma(z) = \cosh(\lambda_i z/L) + \cos(\lambda_i z/L) - \kappa_i (\sinh(\lambda_i z/L) + \sin(\lambda_i z/L)) \ , \tag{3.11}$$

where λ_1 = 1.875 and κ_1 = 0.734 for the first mode. Note that at the free end (z = L), $\sigma(L)$ = 4. Combining equation (3.8) and (3.10), equation (3.9) can be expressed as,

$$S_y(z,f) = [\frac{1}{2}\rho V_p^2 D]^2 \, (\frac{D}{V_p}) \, \frac{1}{16\pi^4} \, \frac{[\tilde{\Phi}_F(f_R)] \; \sigma^2(z) J^2}{(m L)^2 f_n^4 \, [(1-(f/f_n)^2)^2 + (2\zeta f/f_n)^2]} \; . \qquad \textbf{(3.12)}$$

where the joint acceptance, J, is non-dimensional and is a measure of the compatibility of the force distribution function to the mode shape of the tube, and is given by,

$$J^2 = (\frac{\pi}{2})^2 \int_0^1 \int_0^1 \sigma(z_1) \; \sigma(z_2) \; \exp[-\frac{|z_1 - z_2|}{\lambda_c}] \; dz_1 dz_2 \; . \qquad \textbf{(3.13)}$$

Note that the term $(\pi/2)^2$ in the equation above arises from the transformation of variables in eqn. (3.12) from radians to the non-dimensional tube length, z. Note also that the joint acceptance, J, is the same as $(L_{cn}/L)^2$ which is found in equation (19) in Axisa *et al.* (1990). The rms amplitude of tube vibration (per unit tube length), $y_{rms}(z)$, can be derived from S_y as follows,

$$y_{rms}^2(z) = \int_0^\infty S_y(z, f_R) \; df \; . \qquad \textbf{(3.14)}$$

If the system damping is light and if the forcing spectrum is broad band and constant over the frequency range of the tube natural frequency, then the following approximation can be made,

$$\int_0^\infty \frac{[\tilde{\Phi}_F(f_R)]}{(m L)^2 f_n^4 \; [(1-(f/f_n)^2)^2 + [2\zeta f/f_n]^2 \,]} \, df = \frac{\pi}{4\zeta (m L)^2 f_n^3} [\tilde{\Phi}_F(f_R)]_n \; , \qquad \textbf{(3.15)}$$

where $[\Phi_F(f_R)]_n$ is the magnitude of the forcing spectrum at the dimensionless tube natural frequency. The preceding equations can be combined to give the mean-square of the response amplitude (per unit length) as a function of spatial position, z,

$$\bar{y}(z)^2 = [\frac{1}{2}\rho V_p^2 D]^2 \, (\frac{f_n D}{V_p}) \, \frac{J^2 \, \sigma^2(z)}{64\pi^3 (m L)^2 \zeta f_n^4} [\tilde{\Phi}_F(f_R)]_n \; . \qquad \textbf{(3.16)}$$

Note that equation (3.16) gives a dimensionless amplitude which is normalized by tube length. To obtain the dimensional form, multiply by the tube length, L. When the correlation length is less than 1% of the tube length, $\lambda_c \leq 0.01$, the joint acceptance, J, can be approximated by,

$$J^2 = a_n \lambda_c \ . \tag{3.17}$$

The value for a_n depends on the tube geometry, and for a cantilevered tube is, $a_n = 0.5$.

Axisa *et al.* (1988) further derived an equivalent dimensionless spectrum as,

$$[\tilde{\Phi}_F]_e = \frac{\lambda_c}{L}[\tilde{\Phi}_F] \ , \tag{3.18}$$

which is the forcing spectrum measured in the laboratory on any given tube length, L, while $[\Phi_F]$ is the local dimensionless spectrum of the flow field. Equation (3.18) is designed to account for the different tube lengths used in different experiments, which in theory will not respond with the same rms amplitude under the same flow field due to the finite correlation length of the flow turbulence. Hence a shorter tube will be subjected to higher unbalanced random forces than a longer tube because the correlation length of the flow is greater as a percentage of the tube length for the shorter tube. Substituting equation (3.18) into (3.16) and introducing a scaling correction factor L_s/L, the final form of the root mean square turbulence response is,

$$\frac{\bar{y}}{D} = \frac{\sqrt{a_n}\,\sigma(s)}{16\pi^{3/2}} \frac{\rho D^2}{m\zeta^{1/2}} [\frac{V_p}{f_n D}]^{3/2} [\frac{L_s}{L}]^{1/2} [\tilde{\Phi}_F(f_R)]_e^{1/2} \ . \tag{3.19}$$

Axisa *et al.* suggested a convenient length scale of L_s = 1.0 m to facilitate comparison with other experimental data sets. Equation (3.19) will be used to compare the single-phase turbulent buffeting data of this study with those of Taylor *et al.* (1999). The two-phase turbulent buffeting data will be compared with other data under the methodology of De Langre and Villard (1998), which is described in more detail in Chapter 10.

3.3 Fluidelastic Instability

Fluid flow through a heat exchanger array will cause motion of the tubes. This motion can alter the flow pattern around the tubes and induce a change in the fluid forces that can lead to greater displacement and so on. Hence unlike turbulence buffeting, where the forces do not require nor depend upon the motion of the tubes, the forces associated with fluidelastic instability exist because of tube

motion. This class of flow-induced vibrations is called self-excited vibrations, where the forces on the tube are path dependent and hence, non-conservative.

In general, instability can be classified as being static or dynamic. Static instability, also known as divergence, occurs when the fluid force is in phase with displacement and it simply overcomes the stiffness of the system so that the structure deflects statically. Dynamic instability exists when there is a phase difference between the tube motion and the resulting fluid force. The component of fluid force which is in phase with the velocity of the tube is called a fluid-damping force, which will result in oscillations at the tube natural frequency. Work is done on the tube by this force and the vibration amplitude will increase until the overall damping is sufficient to dissipate this energy.

The review paper by Price (1995) discusses the known theoretical models of fluidelastic instability for cylinder arrays and compares them with available data obtained in gaseous, liquid and two-phase cross-flows. A short description of a these theoretical models is given below. For a more complete summary of these theoretical models, the interested reader can refer to Price(1995) for a more detailed description or to the primary references given in Table 3.1.

The **Jet switch** model of fluidelastic instability was first developed by Roberts (1966), who observed fluidelastic instability in a single and double row of tubes. The tube motion observed was primarily in the streamwise direction, where the tubes moved out-of-phase with each other. Coinciding with this tube motion, the fluid jets issuing between the tube coalesced in pairs and switched pairing with each fore and aft movement of the tube. Roberts postulated that the fluidelastic forces were caused by a time lag between the cylinder motion and the switching of the jet-pairs. The theoretical model he proposed considered only streamwise motion of a single flexible tube in a downstream row, as illustrated in Figure 3.1. This model did not compare well with experimental data because most of it was obtained in arrays of cylinders, where unstable vibrations occurred most often in the transverse direction.

Table 3.1 Summary of Theoretical Models for Fluidelastic Instability.

Theoretical Model	Instability Mechanism	References
1. Jet Switch	Displacement	Roberts (1962, 66), Y.N. Chen (1980)
2. Potential Flow	Displacement	Dalton & Helfinstine (1971), Chen (1975, 78) Balsa (1977), Dalton (1980), Païdoussis, Mavriplis & Price (1984), Van der Hoogt & van Campen (1984), Païdoussis, Price & Mavriplis (1985).
3. Quasi-Steady	Displacement	Connors (1970, 78), Blevins (1974), Whiston & Thomas (1982)
4. Unsteady	Displacement & Velocity	Tanaka & Takahara (1980, 81), Tanaka, Takahara & Ohta (1982), Chen (1983, 1989), Goyder (1990), Granger & Campitstron (1988), Granger (1991), Granger, Campitstron & Lebret (1993).
5. Semi-analytical	Velocity	Lever & Weaver (1982, 1986a,b), Yetisir & Weaver (1993a,b), Parrondo *et al.* (1993).
6. Quasi-Steady	Velocity	Gross(1975), Blevins (1979), Price & Païdoussis (1982, 83, 84, 1986a,b).
7. Computational Fluid Dynamics	Displacement & Velocity	Marn (1991), Marn and Catton (1991a,b)

The **Potential flow** model of fluidelastic instability assumes that the wake regions behind a cylinder in cross-flow are small enough that inviscid flow can be assumed. The method involves approximating the velocity potential of the flow in series form and determining the unknown coefficients from the known boundary conditions, the most important one being the impermeability of the cylinder surface. Knowing the velocity potential, the Bernoulli equation in its unsteady form is used to determine the unsteady pressure distribution around the cylinders, which leads to the fluid forces. According to Price (1995), the prediction of these models compares poorly with experimental data,

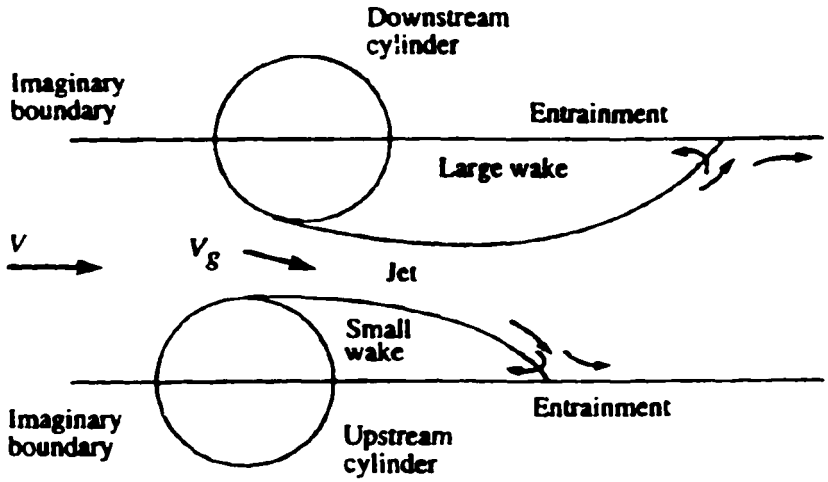

Figure 3.1 Idealized model of jet-flow between two cylinders with opposite displacements in the streamwise direction. Roberts (1962)

and inviscid flow theory is inadequate for stability analyses of cylinder arrays in cross-flow.

A **Quasi-static** model of fluidelastic instability assumes that the dynamic fluid force acting on a vibrating cylinder at any instant of time is the same as the steady force on a statically displaced cylinder. The often used "Connors' formula", represented by equation (3.20), was derived from this type of analysis. Connors (1970) performed experiments on a single row of flexible tubes and determined that the dominant mode shapes during fluidelastic vibration were thin elliptical orbits in both the streamwise and transverse directions. By statically displacing two neighbouring cylinders, he obtained a measure of the fluid forces as a function of tube displacement. Using the measured fluid stiffness coefficients, Connors obtained energy balances in the streamwise and transverse directions, and developed the now famous expression,

$$\frac{V_{pc}}{f_n D} = K\sqrt{\frac{m\,\delta}{\rho D^2}}\,. \qquad (3.20)$$

The so-called Connors constant, K, was found to be 9.9 for the geometry that was tested. This formula has gained wide acceptance for predicting fluidelastic instability for tube arrays, despite being based originally upon the analysis of a single row of tubes. Much effort has gone into determining the value of K for different tube array types.

Blevins (1974) also derived equation (3.20) for a tube row by assuming that the fluidelastic forces were due to relative displacements between a tube and its nearest neighbours. Whiston and Thomas (1982) generalized the analysis by allowing any phase angle between the displacements of neighbouring cylinders. They also extended the analysis to full arrays of cylinders, but it was found to over-predict the critical velocities for a normal triangular array. The agreement was improved when they modified their analysis to included wake effects of upstream tubes. However, according to Price (1995), Whiston and Thomas' theoretical predictions for in-line arrays compared poorly with the body of data.

An **Unsteady** model for fluidelastic instability assumes that a cylinder in an array is subjected to fluidelastic forces caused by its own motion and the motions of its nearest neighbours only. In order to construct the complete force balance for a tube requires the determination of a number of fluid force coefficients which relate the motion (ie., displacement, velocity, and acceleration)of one tube to the forces on itself or its neighbour. Tanaka and Takahara (1980) were the first to measure these force coefficients for a single flexible cylinder in a rigid in-line array and found they varied with reduced velocity (Vp/fD). Chen (1983) pursued this theory further by testing a number of simple cases and demonstrated the existence of two distinct instability mechanisms in cylinder arrays. Negative fluid damping was found to cause instability in a single flexible cylinder in a rigid array, which was revealed by the dominance of the fluid-damping coefficients. Fluid-stiffness coefficients were found to be dominant, even when the damping was positive, in cases of two neighbouring cylinders oscillating in a particular orbit suggested by Connors (1970).

A **Semi-analytical** model for fluidelastic instability is an analytical formulation for determining the stability of a cylinder in cross-flow but requires some empirical data input. Such an analysis was first provided by Lever and Weaver (1982, 1986a,b) for a single flexible cylinder in an otherwise rigid array vibrating in the transverse direction only. This was justified by the experiments of Lever and Weaver (1982) where they found similar critical reduced velocities for a single flexible cylinder vibrating in a rigid array as for a fully flexible array of the same type. The stability analysis was performed by considering a tube situated in a unit cell, shown in Figure 3.2a, whose boundaries were defined by the tube and its nearest neighbours and by the wake regions behind a cylinder. Within the stream-tube, the flow was assumed to be one-dimensional, inviscid and divided into regions of flow

either upstream, downstream or attached to the cylinder in the cell. It was assumed that cylinder motion causes a proportional redistribution of the stream-tube area. Using the unsteady momentum and continuity equations, the unbalanced force on the cylinder is determined by integrating the pressures on either side of the tube surface over the attached region only. A phase lag in the fluid force was introduced to account for the fluid inertia and a resistance term to account for frictional pressure loss. When the predicted stability boundaries are plotted on a graph of $V_{pc}/f\,D$ vs. $m\delta/\rho D^2$, multiple bands of stability regions were encountered at low values of mass-damping parameter, as shown in Figure 3.2b, because the flow-induced damping terms were harmonically dependent upon $1/(V_{pc}/fD)$. In this case, the damping term oscillated between negative and positive values as V_{pc}/fD decreased. Only the first two of these stability bands were accepted as realistic since, for lower bands, the phase lag between cylinder motion and stream-tube area became large. The authors argued that minor flow perturbations due to turbulence would disrupt the pressure variations corresponding to the longer phase-lags. Yetisir and Weaver (1993a,b) advanced the analysis to include the effect of multiple flexible cylinders using the principle of superposition. According to Price (1995) the results of this analysis were in good agreement with the predictions of models by Chen (1983) and Price and Paidousis (1984). Parrondo (1993) also performed a similar analysis for multi-flexible cylinders and achieved comparable results.

A **Quasi-steady** model assumes that the effect of cylinder motion in a cross-flow is to modify the relative velocity vector and the resultant lift and drag forces which are normal and parallel to the relative velocity. It is also assumed that the drag and lift coefficients (C_D, C_L) for the moving cylinder are the same as those measured on a stationary one. Gross (1975) performed the first quasi-steady analysis of a cylinder array in cross-flow and he identified two mechanisms: negative damping and stiffness controlled instability. However, the model considered only negative damping, and an expression for determining the threshold flow velocity was obtained as follows,

$$\frac{V_{pc}}{f_n D} = \frac{m\,\delta}{\rho D^2 (-\partial C_y/\partial \alpha)}, \qquad (3.21)$$

where α is the incidence flow angle (illustrated in Figure 3.3), which increases with transverse cylinder velocity and decreases with absolute flow velocity. This formula predicts that V_{pc} varies linearly with

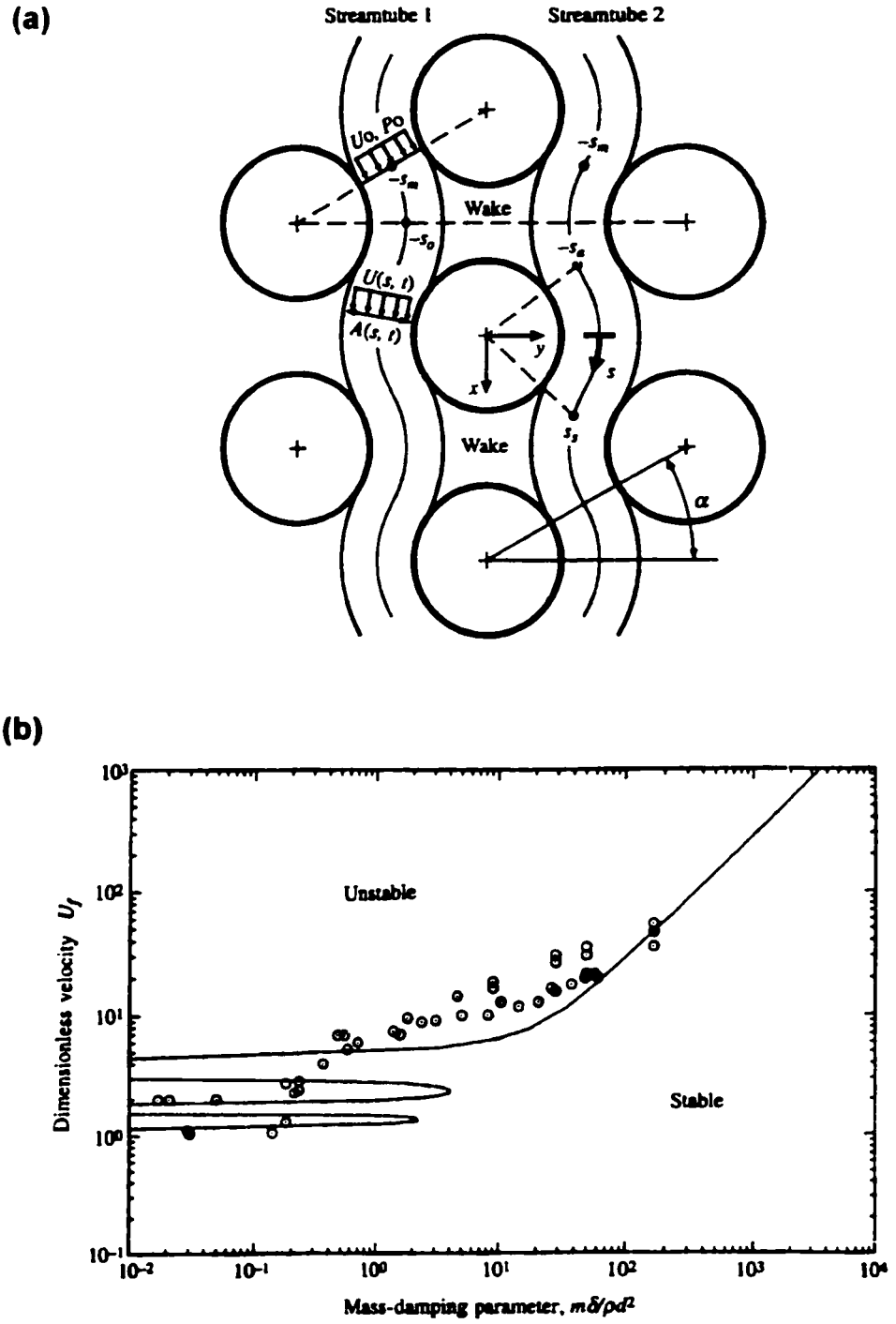

Figure 3.2 (a) Typical Unit cell for semi-analytical analysis of a cylinder in a parallel triangular array. (b) Theoretical stability boundaries obtained for the same array with P/D = 1.375 showing multiple stability regions. Lever and Weaver (1986b).

mass-damping parameter, contrary to most experimental work which shows the exponent to be closer to 0.5.

Price and Païdoussis (1982, 1983) considered a double row of cylinders, and assumed that the fluid force coefficients varied linearly with cylinder displacement and its two immediate neighbours according to,

$$F_y = \frac{1}{2}\rho D L V^2 \left(C_L - \frac{\dot{x}D}{V_p} 2C_L - \frac{\dot{y}D}{V_p} C_D\right), \qquad \textbf{(3.22)}$$

while the in-flow direction force consists of a similar expression. According to Price (1995), the main weakness of their approach was the assumption of a constrained mode, which was employed to decouple a cylinder from the effects of its nearest neighbours. An improved effort was made by Price and Païdoussis (1984, 85, 1986a,b) and Price and Païdoussis and Giannias (1990), where a cell of eight tubes was considered in addition to the effect of time delay between cylinder displacement and fluid force. The authors again used a constrained mode analysis but accounted for the inclination of the wake shed by the transverse motion of an upstream cylinder on the monitored tube. The analysis required determination of the specific modal patterns which would give the minimum V_{pc}, and it was found that this minimum was not constant but varied with $m\delta/\rho D^2$. This was attributed to the change in instability mechanism from damping controlled to stiffness controlled. Similar to Lever and Weaver's findings, they found multiple instability regions at low $m\delta/\rho D^2$, which they also attributed to the phase lag between cylinder motion and fluid force. According to Price (1995), the disadvantage of this analysis, as compared to Lever and Weaver, was the considerable amount of experimental input data that was required, which was less than for the unsteady models, however.

Lately, a few attempts have been made to develop **computational fluid dynamic models** (CFD) for predicting fluidelastic instability in cylinder arrays. One noteworthy example is that of Marn and Catton (1991a), who considered a column of flexible cylinders in a rigid array. Similar to Yetisir and Weaver (1986a), they confined the flow to a two-dimensional unit cell, while the fluid pressure was divided between mean and time varying components, where the latter were assumed to be due solely to tube motion. The force on the cylinder was found by integrating the pressure around the surface. A specific modal pattern of tube motion was assumed in order to develop a stability boundary.

The results obtained showed good agreement for $m\delta/\rho D^2 > 5$, but instability was predicted for the in-flow direction, while cross-flow instability was predicted to occur at a much higher V_p/fD. This does not agree with experiments, which show that instability occurs in the cross-flow direction initially. According to Price (1995), this disagreement is likely due to the cylinder motion and resulting velocity and pressure terms being assumed in-phase with each other. In two later papers, Marn and Catton (1991b,c) extended the analysis to include fully flexible arrays. The results showed that the critical V_p/fD to be proportional to $m\delta/\rho D^2$, rather than to the one-half power or less as experiments showed. However, they found a rather large difference in critical V_p/fD for when the first and last cylinders in the array went unstable, and resorted to choosing a mean value for design purposes. The fact that there is yet no successful solution of the interstitial flow between the cylinders is, according to Price(1995), the reason for the lack of progress in the CFD modelling of fluidelastic instability in cylinder arrays.

Two different mechanisms of fluidelastic instability in cylinder arrays have been brought up in the foregoing discussion. The first mechanism is called stiffness controlled, where the dominant fluid forces are dependent on tube displacement. The second mechanism is called negative damping, where the dominant fluid forces that cause instability is determined primarily from the finite time lag which occurs between cylinder displacement and fluid force. If there is a component of fluid force in phase with cylinder velocity, fluidelastic instability can occur. The following two sections will describe these two forcing mechanisms in more detail.

3.3.1 Displacement Mechanism

The hypothesis of the displacement mechanism model for fluidelastic instability is that the fluid forces are linear and react instantaneously with cylinder displacement. Hence, if a tube in an array is slightly displaced, then the flow pattern changes and the steady fluid force on the tube changes. Since the fluid force on the displaced tube is a function of its position relative to that of the other tubes, a tube in an array will react to the movements of its nearest neighbours. To use this theory, a relationship needs to be developed which relates the fluid force coefficients to the tube displacement. These can be determined theoretically using potential flow theory or they can be measured experimentally.

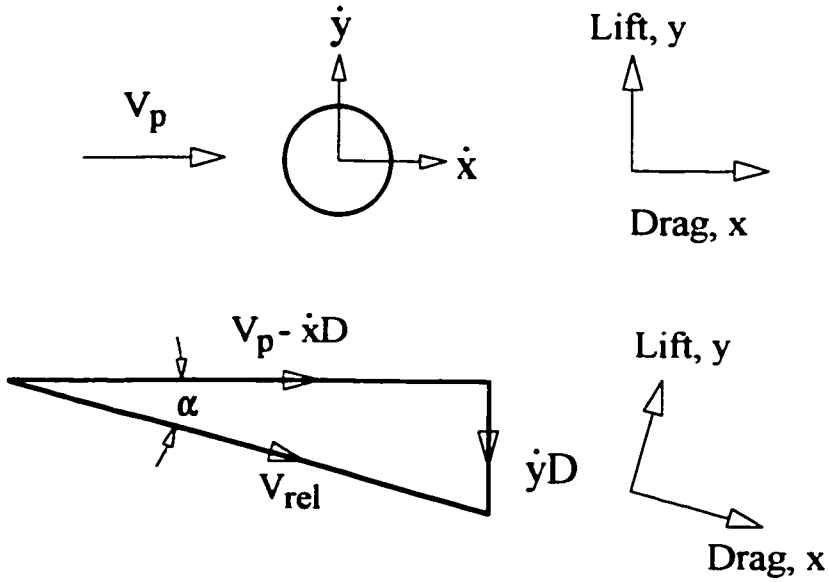

Figure 3.3 Velocity vector diagram for quasi-steady analysis of fluidelastic instability.

A simple analytical approach to the problem of a tube in a row of tubes is developed in Blevins (1990), and the key points are briefly restated here. The equation of motion (force balance) for an assumed one degree of freedom system, as shown in Figure 3.4, is derived in two coordinate directions for tube j,

$$m\ddot{x}_j + 2m\zeta_x\omega_x\dot{x}_j + k_x x_j = \frac{1}{4}\rho U^2[K_{xx}(-x_{j+1} - x_{j-1} + 2x_j) + K_{xy}(y_{j+1} - y_{j-1})] \quad , \tag{3.23}$$

$$m\ddot{y}_j + 2m\zeta_y\omega_y\dot{y}_j + k_y y_j = \frac{1}{4}\rho U^2[K_{yy}(-y_{j+1} - y_{j-1} + 2y_j) + K_{yx}(x_{j+1} - x_{j-1})] \quad , \tag{3.24}$$

where x and y are the tube displacements, K_{xx} and K_{xy} are the constants which relate the x-direction fluid force to the tube displacement in the x and y direction respectively, while K_{yy} and K_{yx} are the constants which relate the y-direction fluid force to the tube displacement in the y and x direction respectively. Hence the fluid force, which is given by the right hand side of the above equations, is assumed to be linearly related to tube relative displacement and symmetrical about the origin. The stability analysis is simplified considerably if certain assumptions are made. If every other tube in a

row is assumed to be out of phase by 180 degrees, and if K_{xx} and K_{yy} are assumed to be negligible, the equations of motion reduce to,

$$m\ddot{x}_j + 2m\zeta_x\omega_x\dot{x}_j + k_x x_j = \frac{1}{2}\rho U^2 K_{xy} y_{j-1} , \tag{3.25}$$

$$m\ddot{y}_{j-1} + 2m\zeta_y\omega_y\dot{y}_{j-1} + k_y y_{j-1} = -\frac{1}{2}\rho U^2 K_{yx} x_j . \tag{3.26}$$

The solutions to these equations are sought such that the oscillations grow or decay exponentially with time, ie.,

$$x_j = \tilde{x}_j e^{\lambda t} , \quad y_{j-1} + \tilde{y}_{j-1} e^{\lambda t} . \tag{3.27}$$

The resulting equations can be put into matrix form, where a solution exists when the determinant is set to zero. The details of the analysis are given in Blevins (1990). If the assumption is made that the damping in the x and y direction are equal, then the solution for critical reduced velocity is,

$$\frac{U_{crit}}{(f_x f_y)^{1/2} D} = \frac{2\sqrt{2}\,\pi}{(K_{xy} K_{yx})^{1/4}} \left(\frac{m}{\rho D^2}\right)^{1/2} \left[\left(1 - \frac{f_x}{f_y}\right)^2 + 4\zeta^2\right]^{1/4} . \tag{3.28}$$

If the further assumption is made that all the tubes have identical natural frequencies in the x and y direction, then the equation for critical velocity reduces to the simple expression that was first derived by Connors (1970),

$$\frac{U_{crit}}{fD} = K\left(\frac{2\pi\zeta m}{\rho D^2}\right)^{1/2} , \tag{3.29}$$

where the constant, K, is given by,

$$K = \frac{2\sqrt{2\pi}}{(K_{xy} K_{yx})^{1/4}} . \tag{3.30}$$

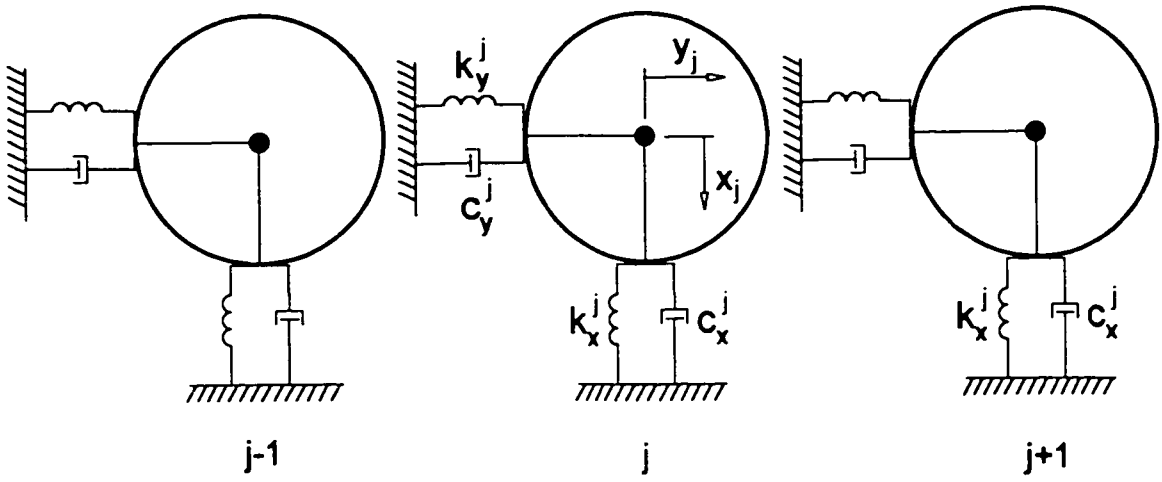

Figure 3.4 Tube row model used for analytical prediction of fluidelastic instability.

One consequence of this model is that a single flexible tube in a rigid array is predicted to be dynamically stable. However, experiments have shown that whether or not a single flexible tube in a rigid array shows instability seems to depend on array geometry, pitch ratio and mass ratio. The experimental evidence is sometimes contradictory, but it seems that the parallel triangular arrays show instability for a single flexible tube while rotated square arrays do not. Experiments have also shown that the exponent on mass damping parameter depends to some degree on array geometry. These discrepancies suggest that other fluid effects need to be identified and incorporated into the displacement model.

3.3.2 Velocity Mechanism

One shortcoming of the displacement mechanism is that it assumes that the fluid force responds instantaneously to a change in tube position. In fact, there is a finite time lag for the fluid force to respond to the change in tube displacement. Some estimates for the time lag between tube motion and fluid force are,

$$\begin{aligned} \tau &= \frac{10D}{V_u} && \textit{Roberts} \text{ (1966)} \\ \tau &= \frac{P}{V_p} && \textit{Lever and Weaver} \text{ (1982)} \\ \tau &= \frac{D}{V_p} && \textit{Price and Paidoussis} \text{ (1986)} \end{aligned} \tag{3.31}$$

Roberts' prediction comes from his experimental observations of jet switching behind a row of tubes. In the latter two predictions, the time delay of displacement induced forces in an array is the same order as the period of vortex shedding.

As the tube vibrates in the flow field, the velocity of the tube relative to the flow adds to fluid damping, where the drag force on a cylinder is given by,

$$F_D = C_D \frac{1}{2} \rho U^2 D \,, \tag{3.32}$$

which can be related to the pressure drop across a row of tubes such that the fluid damping is given by the following components:

$$\begin{aligned} 2\pi\zeta_x &= \frac{C_D}{2} \frac{\rho D^2}{m} \frac{U}{fD} \\ 2\pi\zeta_y &= \frac{C_D}{4} \frac{\rho D^2}{m} \frac{U}{fD} \,. \end{aligned} \tag{3.33}$$

Most often, the development of the equations of motion requires the assumption of a harmonic vibration mode and the selection of a suitable time lag τ for the fluid force to act on the displaced tube. If D/V_p is assumed to be the time lag, then instability is predicted as follows:

$$\frac{U^2}{\omega_j^2 D^2} \sin\frac{\omega_j D}{U} = -\frac{4m\zeta_y}{C_y \rho D^2} \tag{3.34}$$

The sine function implies that multiple ranges of instability exist as long as C_y is negative. C_y is the transverse drag coefficient which must be determined experimentally.

A general linear theory for fluid force on a vibrating tube in a flexible array should include

terms which account for added mass, fluid coupling, time lag effects and tube displacement. The general linear expression by Chen (1983, 87) for fluid forcing is given by,

$$\begin{aligned} F_i = & -\rho D^2 \sum_j (\alpha_{ij}\ddot{x}_j + \beta_{ij}\ddot{y}_j) \\ & - \rho D U \sum_j (\alpha'_{ij}\dot{x}_j + \beta'_{ij}\dot{y}_j) \\ & + \rho U^2 \sum_j (\alpha''_{ij}x_j + \beta''_{ij}y_j) \end{aligned} \qquad (3.35)$$

where α and β are the forcing coefficients for the x and y direction respectively and the zero prime, single prime and double prime indicate that the coefficient applies to acceleration, velocity and displacement of the tube respectively. Now if tube "i" interacts with the two nearest neighbouring tubes, then there are 18 coefficients α, β, α', β', α'', β'' in the expression to be evaluated. Some of these can be determined analytically using potential flow theory but most must be determined experimentally. Price and Païdoussis (1986) have found that the coefficients are strongly dependent upon tube spacing and pattern.

The foregoing review shows that a variety of theories exist for predicting fluidelastic instability, from semi-analytical to semi-empirical. None are entirely satisfactory, but they have served to shed light on the excitation mechanisms involved, which are now reasonably understood for single-phase flows. Design guidelines are presently based upon the abundance of collected experimental data.

3.4 Damping

The mechanism which dissipates vibration energy and causes the amplitude to steadily diminish is called damping. It can take several forms where more than one form may operate at once. Fluid damping is caused by energy transfer from the vibrating structure to the surrounding fluid and may be either viscous or turbulent. Viscous fluid damping is proportional to tube velocity while turbulent fluid damping is proportional to tube velocity squared. Solid or hysteretic damping is caused by the internal friction in a solid as it deforms during vibration.

Components of Damping in Two-Phase Flow

The vibration amplitude of a structure, such as a tube bundle in two-phase flow, is strongly dependent upon the level of total damping which is the summation of several components. If we can assume that the components are independent and additive, then the total damping ratio, ζ_T, is given by,

$$\zeta_T = \zeta_S + \zeta_V + \zeta_{TP}, \qquad (3.36)$$

where the subscripts *S*, *V* and *TP* refer to solid, viscous and two-phase damping components respectively. The solid component includes internal material losses, end support losses and other joint or sealing losses, and it is usually measured with the system vibrating in air. This form of damping is rather easy to measure experimentally if the damping is light and the measurement tools are available. The same applies for viscous damping but it depends upon the circumstances, since the measuring tools must be accessible to the tubes. Fair estimates of viscous damping can also be calculated from theoretical considerations, following the fundamental work of Chen *et al.* (1976). The two-phase damping component, ζ_{TP}, lumps together all of the effects of the two-phase flow. It is important to those interested in predicting the life span of steam generators since it is a large component and has a significant impact on resultant vibration amplitudes and tube fretting wear rates. This component is derived most easily by subtracting the solid and viscous components from the total damping.

At present, there is very little information available on damping in two-phase flow. Carlucci (1980) and Carlucci and Brown (1983) have provided experimental damping measurements related to confined axial two-phase flow. They found that damping is strongly dependent upon void fraction as well as the ratio of hydrodynamic mass to tube mass. Pettigrew *et al.* (1989) studied damping of tube bundles subject to air-water cross-flows and found a similar trend with respect to void fraction as the previous authors. Axisa *et al.* (1984, 1985, 1986 and 1988) measured damping in tube bundles subjected to high void fraction air-water and steam-water cross-flows. They found that damping decreased drastically at void fractions above 85% and that damping in air-water was 50% higher than in steam-water. Pettigrew and Knowles (1992) studied damping of a single cantilevered tube suspended vertically in a cylinder of water, in which air was bubbled to simulate a stationary two-phase environment. They observed an increase in damping with void fraction up to 25%. The effect of surface tension was also tested by adding a surfactant to the water. It was found that damping

increased with surface tension. The authors concluded from these tests that the formulation of design guidelines would not be simple, and would have to wait until further data had been collected at higher void fractions.

Total damping, ζ_T, can be measured by four methods depending upon the circumstances and tools available: the energy dissipation method, the frequency bandwidth method, the magnification factor method and the phase angle method. The first two methods will be discussed since they are the most common and were the methods used in the present study.

3.4.1 Energy Dissipation Method

This method is also referred as the "pluck" method since it is performed by plucking the system and capturing the displacement time history on an oscilloscope. In a viscously damped harmonic oscillator with a single degree-of-freedom, successive amplitudes have a simple logarithmic relation to one another. For lightly damped systems, the damping ratio, ζ, is simply determined by comparing the peak amplitudes and using the relation,

$$2\pi\zeta \approx \delta = \frac{1}{n}\ln\left(\frac{X_o}{X_n}\right), \tag{3.37}$$

where X_o is some initial peak amplitude and X_n is the peak amplitude after n cycles of oscillation (see Figure 3.5). This method is well suited to damping measurements of vibrating tubes in still fluids provided that the non-measured tubes are fixed to prevent energy transfer to and from the measured tube, and only a single mode of vibration is excited. However, this method is usually not suitable for in-flow situations, because in this case, the monitored tube is in continuous motion and there is usually no means of plucking it. This method was used in this work to obtain the structural damping of the monitored tube, measured in still air.

3.4.2 Frequency Bandwidth Method

This method gives a measure of the equivalent viscous damping by measuring the width of the frequency response curve at resonance. The half-power bandwidth of the response Δf, is defined as the width of the frequency response curve at 0.707 times the peak amplitude as shown in Figure 3.6. The

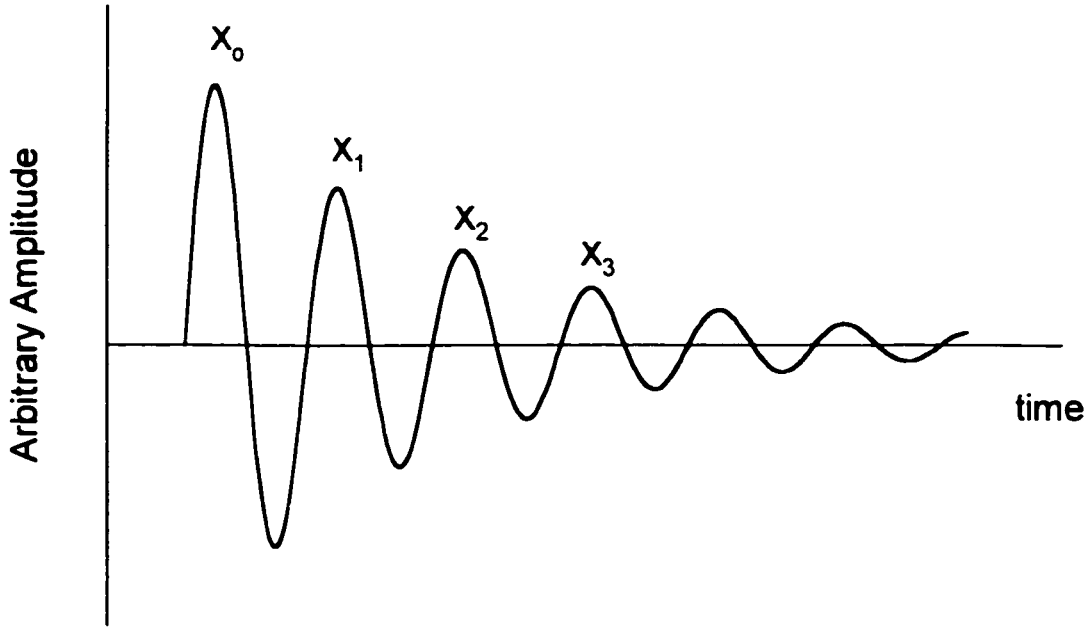

Figure 3.5 Typical amplitude decay trace for a viscously damped harmonic oscillator.

bandwidth at this amplitude is proportional to damping,

$$\zeta = (\frac{\Delta f}{2f_n}) . \qquad (3.38)$$

In this study, the in-flow, two-phase damping data were determined using this method, using a Fortran computer program supplied by AECL. This program fits a frequency response curve to the measured frequency spectra and determines the damping ratio, ζ, as a fitted parameter. This method is often difficult to use in liquid flows because the proximity of the measured tube to neighbouring tubes causes fluid coupling and can produce several natural frequencies which are close together. Analysing such data by this method would give damping values much greater than actual. In this study, the problem of fluid coupling was reduced by securing the neighbouring tubes and measuring the response of a single flexible tube. This is discussed in more detail in Chapter 9.

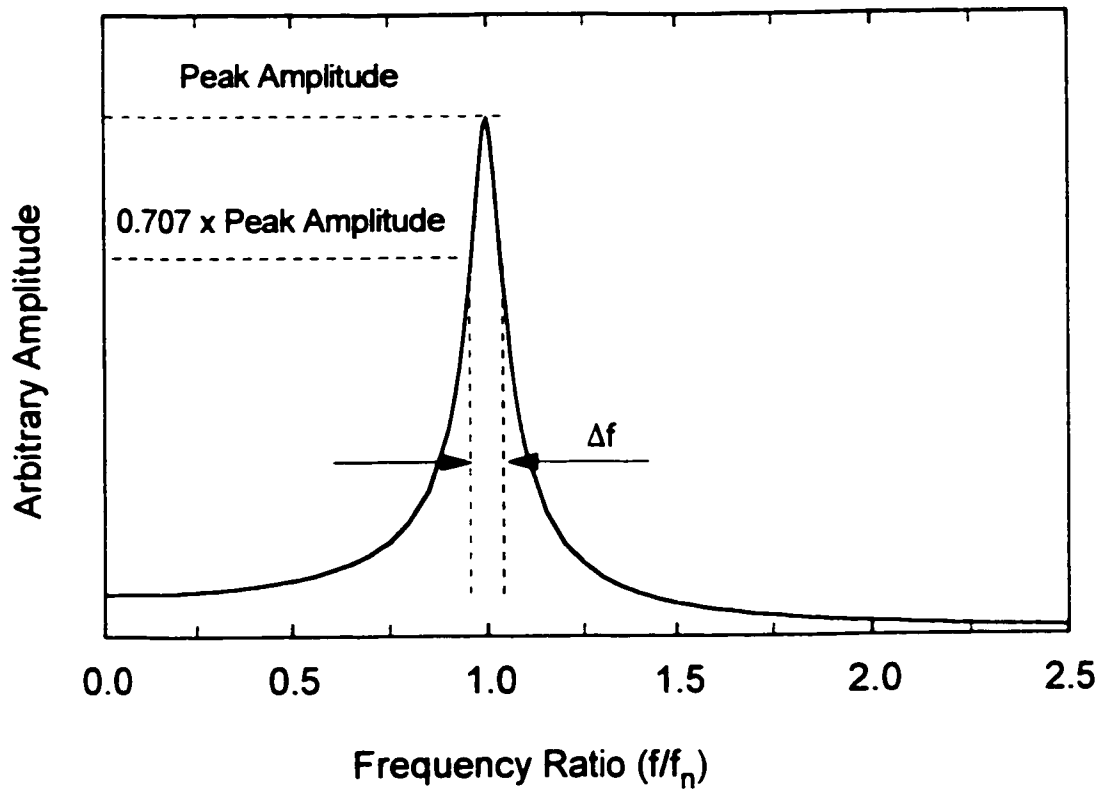

Figure 3.6 Typical amplitude versus frequency response curve for a single degree of freedom oscillator.

An approximate formula which is also applicable to measure system damping ratio is,

$$\zeta = \frac{1}{2\sqrt{(A_1/A_2)^2 - 1}} \left(\frac{\Delta f}{f_n}\right), \qquad \Delta f = f_2 - f_1, \tag{3.39}$$

where A_1 and A_2 are the amplitudes at f_1 and f_2 respectively. This method is most accurate when the frequency ratio is kept small, but for light damping this can create problems experimentally due to the resolution limit of most analysers.

CHAPTER 4

Physical Modelling

A small number of flow-induced vibration problems involve unseparated laminar flows around streamlined bodies and these can be solved satisfactorily using a theoretical treatment. However, the vast majority of flow-induced vibration problems involve unsteady, separated flows around bluff bodies where a purely theoretical treatment is generally not possible. Hence, these problems require experimental treatment, usually performed on a small scale models where the rules of dimensional analysis are employed.

The focal point of this study is the fluid-structure interaction between the vertical upward flow of two-phase steam and water with the tubes in the U-bend region of the nuclear steam generator. In this region, the high velocity steam and water mixture passes through the tubes at roughly right angles to the tube axis (cross-flow). It is known from experience that cross-flow is much more likely to cause serious vibration than parallel flow, which occurs in the lower part of the steam generator. The outermost tubes in this U-bend region are the most susceptible to fluidelastic instability because the tube supports are at their furthest and hence the tubes are the most flexible.

4.1 Dimensional Analysis and Scaling Parameters

It is a fundamental belief that a phenomenon can be studied experimentally with a reduced scale model and the results obtained can be applied to the full scale prototype. This can be done if the all of the parameters governing the phenomenon are dimensionless and scaled exactly. To determine the important scaling parameters, one usually uses the Buckingham Pi theorem. This involves selecting the dimensional variables which are relevant to a given problem, such as flow velocity, V, fluid density, ρ, mass per unit length, m, and vibration frequency, f, and forming dimensionless groups

of these variables such as Reynolds number, Re, reduced velocity, V_r and mass ratio, $m/\rho D^2$, which are fewer in number than the original variables by the number of fundamental dimensions, ie., mass, length and time. Care must be taken not to include too many variables in the analysis because this will make modelling more difficult, while inclusion of too few variable may result in physically incorrect modelling. Some of the most important dimensionless similitude parameters that are used for studying flow induced vibration in heat exchanger tube arrays, specifically turbulence buffeting and fluid-elastic instability are described below.

The geometry of the prototype must be scaled accurately to achieve comparable results. In the case of a heat exchanger, this means that the pitch ratio, P/D, must be scaled and the tube layout pattern must be replicated (ie., parallel triangular, normal triangular, in-line, or rotated square). The slenderness, L/D, need not be scaled accurately from a fluid mechanics perspective so long as a uniform cross flow of fluid occurs in both model and prototype and that end effects are minimized. The slenderness ratio may be important for modelling the structural dynamics such as natural frequency of vibration. However, obtaining a particular natural vibration frequency can be achieved by means independent of the slenderness ratio, such as by mounting a solid tube on external springs so long as distorted mode shapes of vibration can be tolerated.

Reduced velocity, $V_r = V/f_n D$, is used as a velocity scale for periodic phenomena such as the vibration of a tube with natural frequency, f_n, and outer diameter, D, subjected to a cross flow of fluid with velocity, V.

Reynolds number, $Re = \rho VD/\mu$, is the ratio of inertial to viscous forces and is the basic requirement for dynamic similarity in most fluid mechanics experiments. However, distortion of this parameter is rather common since it often cannot be scaled correctly, and usually causes little error in the range from 10^3 to 10^5.

Mass ratio, $m_R = m/\rho D^2$, in the particular case of heat exchanger tube modelling, is the ratio of the tube lineal mass to that of the fluid it displaces. This is important for scaling the amplitude response of the tube.

Damping, ζ, is the measure of energy dissipation and is already dimensionless. This is also important for scaling the amplitude response of the tubes.

Froude number, $Fr = V^2/gL$, is the ratio of inertial to gravitational forces and is important in situations where free surface flows are encountered, and in some two-phase flow problems.
Strouhal number, $St = fD/V_p$, is a time scale for fluid phenomenon such as turbulence and vortex shedding, where pitch flow velocity, V_p, is most often used.

As in most flow induced vibration modelling, it is necessary to scale the fluid mechanics and structural mechanics simultaneously, and in some cases, it is not possible to do so exactly. Hence, one often must settle for a distorted model where the most important parameters are scaled accurately while the lesser important parameters are not. It is desirable that the scaling distortions be conservative, so that any tendency of the structure to exhibit vibration due to flow are not suppressed in the model but rather are amplified. In the process of modelling the structural dynamics of the curved portion of the steam generator tubes, a number of simplifying assumptions were made in order to eliminate the lesser important parameters which would have otherwise made modelling much more difficult. Firstly, it was assumed that the flow was approximately at right angles to the tube axis over most of the tube span, so that the test bundle could be made of horizontal tubes rather than curved tubes. Secondly, it was assumed that the fluid forces associated with fluid-elastic instability were more dependent upon tube pitch ratio and geometry and less dependent upon the exact mode shape of vibration. Hence, the pinned-pinned support configuration of the steam generator tubes was modelled using a cantilevered bank of tubes, whose diameter was scaled to about ½ of the prototype tubes using 0.25" diameter tubes. This permitted close scaling of the tube natural frequency (roughly 40 Hz in the lowest mode) within the confined space of the test section. Thirdly, it is assumed that fluidelastic instability is associated with the transverse direction of vibration, while streamwise vibration is less important. Hence, the determination of the critical velocity of the tube bundle is primarily a function of the transverse natural frequency and is independent of the streamwise natural frequency. This eliminates the need to model the asymmetric stiffness of the curved tubes of the steam generator, where the streamwise frequency is higher. Weaver & Koroyannakis (1983) found that asymmetric stiffness between the streamwise and transverse direction delayed the stability threshold of a tube array up to about 20%, regardless of the magnitude (up to 57% frequency difference) and orientation of the asymmetry. This indicates that a model tube bundle having symmetric frequencies will give

conservatively lower critical flow velocities as compared with that of the curved tubes of the prototype steam generator. More importantly however, is that several other studies have also followed the same approach of using straight tubes with symmetric stiffness, so that the experiments of this study will be comparable to those studies and the effects of fluid modelling may be examined more closely, as discussed below.

4.2 Two-Phase Fluid Modelling

Since the cost of a full scale steam-water experiment is prohibitively expensive, most research in two-phase flow-induced vibration of heat exchanger tubes was done using air-water mixtures (at atmospheric temperature and pressure) as the working fluid. The disadvantage of air-water is that the density ratio at atmospheric pressure is much greater than that of steam water at the operating pressure of 5 MPa. In addition, two component mixtures do not allow for the simulation of vapour generation or bubble collapse that is possible in single component flows. This may be important in flow induced vibration testing because localized pressure fluctuations, which occur around the tubes in a bundle, may cause phase changes which can influence the excitation and damping mechanisms. Arguably, the best approach to modelling the two-phase flow is to use steam-water at the operating pressure in a full scale tube array. However, the heating power required to obtain an 80% void fraction flow through a test section containing a full scale tube array would probably exceed 10 MW. In addition, steam water flow at design conditions would require an operating pressure of roughly 5 MPa so that the flow loop would have to be very robust and hence very expensive. As a consequence, only a few researchers have used steam water in flow-induced vibration testing, including Axisa *et al.* (1985), Nakamura *et al.* (1986, 1991). Table 4.1 summarizes the physical scaling parameters for an actual steam generator, the present study where R-11 was used, and Pettigrew *et al.* (1989a,b) who used air-water and Pettigrew *et al.* (1995) who used R-22. Some quantities are expressed as a range since they vary with flow quality and operating conditions.

It is obvious that the easiest approach to modelling a two-phase flow is to use an air and water mixture, because the experiments can be performed at atmospheric pressure and room temperature. Hence, the flow loop can be built inexpensively since it does not have to withstand any significant

internal pressure. In addition, the flow rates of each fluid can be accurately measured and controlled in separate conduits before mixing them together. For this reason, most researchers have opted forthis approach including: Pettigrew *et al.* (1989a,b), Axisa *et al.* (1984), Nakamura *et al.* (1982), Remy (1982), Heikler & Vincent (1981). At the present time however, researchers have experimented with other fluids. For example, Pettigrew *et al.* (1995) used R-22, Mann and Mayinger (1995) used R-12, Hirota *et al.* (1996) used R-123, and Delenne *et al.* (1997) used a water-R13B1 mixture.

Table 4.1 Summary of Scaling Parameters.

Parameter	Definition	Steam Generator	Air-water (Pettigrew *et al.* (1989b)	R-11 (This Study)	R-22 (Pettigrew *et al.* (1995)
Pitch ratio	P/D	1.3 - 1.5	1.47	1.44	1.5
Mass Ratio	$m/\rho_H D^2$	20 - 40	3 - 240	3 - 51	2 - 13
Reduced velocity	V/fD	13 - 24	2.1 - 6.5	2.3 - 3.0	1.8 - 3.3
Damping (in air)	ζ_a	0.16 - 0.45	0.2	0.1 - 0.16	0.2
Density Ratio	ρ_L/ρ_G	33	830	150	28.3
Quality	x	0.12 - 0.22	0.0 - 0.093	0.0 - 0.1	0.0 - 0.24

The present approach to fluid modelling uses refrigerant R-11 (trichlorofluoromethane) as the working fluid. Single component two-phase flows are generated more easily with R-11 than with steam-water for two reasons: the enthalpy of vaporization of R-11 is about 7.5% that of water, which reduces the power consumption proportionally, and the boiling point of R-11 at atmospheric pressure is 23.6 C, so that the pressure in a two-phase refrigerant flow loop can be kept below 170 kPa above atmospheric (25 psig). A practical steam water flow loop would have to withstand a much higher pressure depending upon the capacity of the cooling system. A comparison of fluid properties is provided in Table 4.2 for steam-water at power plant operating conditions, compared with various modelling fluids such as air-water, R-11 and R-22 at laboratory conditions.

Table 4.2 Typical properties of various fluids used to simulated steam-water.

Quantity	Steam generator conditions	Air-water	R-11	R-22
Temperature, T (°C)	260	22	40	23.3
Pressure, P (kpa)	4700	101	175	1000
liquid density, ρ_L (kg/m^3)	784	998	1440	1197
vapour density, ρ_G (kg/m^3)	23.7	1.2	9.7	42.3
liquid viscosity, μ_L (μPa·s)	103	959	356	139
surface tension, σ (Nm)	0.024	0.073	0.0167	0.0074

4.3 The Homogeneous Equilibrium Model

Fluid parameters in two-phase flow such as density, void fraction and velocity are most easily defined if the Homogeneous Equilibrium Model (HEM) is utilized. This model treats the two-phase flow as finely mixed and homogeneous in density and temperature with no difference in velocity (slip ratio) between the gas and liquid phase. Under this condition, pseudo properties can be defined for the fluid based upon the ratio of the gas phase to the liquid phase. This model has been used a great deal by researchers studying flow-induced vibrations in two-phase flows because it is easy to implement, it is widely recognized and therefore it makes for easier data comparison.

One of the most important two-phase flow parameters is void fraction, α, which is the volumetric fraction of the gas phase in the flow. Researchers most often employ the HEM for calculating void fraction and flow velocity of a two-phase fluid. In two component flows such as air-water, HEM void fraction, α_H, is given by,

$$\alpha_H = [1 + S\frac{\rho_G}{\rho_L}(\frac{1}{x} - 1)]^{-1} , \qquad (4.1)$$

where ρ_G and ρ_L are the gas and liquid phase densities, x is the flow quality and S is the velocity ratio, which is assumed to be unity in the HEM. In the case of a boiling flow, quality is calculated from a thermodynamic energy balance which is described in detail in Section 5.5 of Chapter 5. HEM fluid density is defined as:

$$\rho = \alpha_H \rho_G + (1-\alpha_H)\rho_L , \tag{4.2}$$

where ρ_G and ρ_L are the gas and liquid phase densities respectively. Pitch mass flux, G_p, is defined as the mass flow rate per unit of gap area between the tubes according to,

$$G_p = \frac{\dot{m}}{A}\left(\frac{P}{P-D}\right) , \tag{4.3}$$

where $\dot{m}$ is the mass flow rate, and A is the cross-sectional flow area upstream of the tube bundle. HEM pitch flow velocity is defined as,

$$V_p = \frac{G_p}{\rho} . \tag{4.4}$$

HEM reduced velocity is defined as,

$$V_R = \frac{V_p}{f\,D} , \tag{4.5}$$

where f is vibrating frequency of the flexible tube and D is the characteristic length which in this case is the outer tube diameter.

4.4 Separated Flow Models

There are several types of separated flow models which address the relative velocity between the vapour and liquid phases. The main problem with using the HEM is that it assumes a velocity ratio between the gas and liquid phases of unity. This assumption is not valid in the case of vertical upward flow, because the density ratio between R-11 vapour and liquid at 0.17 MPa is approximately 150, and for steam-water at 10 MPa the density ratio is 33 and for air-water at atmospheric pressure is about 960, so that buoyancy effects are significant. Empirical models exist which can be used in certain situations to estimate the relative velocities of the gas and liquid phase. The simplest of these assumes that slip velocity of the gas phase relative to the liquid phase is equal to the free rise velocity

of a bubble in stagnant liquid. The problem is to determine the bubble velocity, which depends upon a number of factors, such as bubble volume, liquid surface tension, density ratio, and viscosity. However, if one can measure the void fraction of the flow using some method, then one need not resort to a model but can obtain average values of gas and liquid phase velocities. There are several methods commonly used to measure void fraction in a two-phase flow, such as quick-closing valves, gamma densitometry, and electrical capacitance or resistance probes. These are adequately described in Whalley (1987).

When equipment is available to measure void fraction, velocity ratio, S, can be calculated by the following relationship:

$$S = \frac{U_G}{U_L} = \left(\frac{1-\alpha}{\alpha}\right)\left(\frac{x}{1-x}\right)\left(\frac{\rho_L}{\rho_G}\right), \qquad \textbf{(4.6)}$$

where U_G and U_L are the gas phase and liquid phase velocities respectively. Equation 4.6 is a very important relationship which relates three important quantities in two-phase flows: velocity ratio, S, void fraction, α, and quality, x. When one has a measure of the actual void fraction, α, of the flow, then a more accurate measurement of fluid density can be obtained using equation 4.2 with α used in place of the HEM void fraction, α_H.

The calculation of average flow velocity is somewhat complicated by the fact that the two-phases are acknowledged to move at different velocities. One possibility is to define an equivalent flow velocity, V_{eq}, value based upon the addition of the dynamic head of each phase such as,

$$V_{eq} = \sqrt{(\alpha \rho_G U_G^2 + (1-\alpha)\rho_L U_L^2)/\rho}\,. \qquad \textbf{(4.7)}$$

Since special equipment is required to measure void fraction (or velocity ratio), several significant research works in flow-induced vibrations did not report void fraction measurements but instead relied on the homogeneous equilibrium model for calculating the two-phase density and flow velocity.

A more detailed description of the calculations performed for analysing the data obtained from the R-11 flow loop is presented in Section 5.5 of Chapter 5. The issue of velocity ratio in vertical two-phase flow through tube arrays will be discussed in more detail in Chapter 6, where a new model is

presented for predicting this quantity. It will be shown in Chapter 8 how the interpretation of the data for fluid-elastic instability can change significantly when one accounts for velocity ratio of the gas phase in a two-phase flow as opposed to using the simple homogeneous equilibrium model.

CHAPTER 5

Experimental Apparatus and Procedure

5.1 Flow Loop

The author's experimental data was obtained from a specially designed flow loop which is shown in Figure 5.1. This flow loop was designed to produce a uniform two-phase upward flow of R-11 in the test section, while providing accurate control of the flow rate and quality. The initial construction and commissioning of the apparatus is described by Westermann (1986) and Dam (1991). A detailed description of the apparatus was also provided in the present author's earlier work (Feenstra 1993). Several modifications to the flow loop and tube bundles have occurred since those earlier works were published, so a full up-to-date description of the apparatus is provided in this chapter.

A schematic diagram of the loop with labels identifying the important components is shown in Figure 5.2. The following description makes reference to the numbering system of this figure. The test section (#1) is the most important component of the flow loop. It contains the model tube bundle comprised of 10 cantilevered tubes which simulate a heat exchanger tube bundle. The working fluid of the flow loop, trichlorofluoromethane (R-11), is circulated by a variable speed gear pump (#2) located at the lowest point in the loop. The pump has a practical pumping capacity of 1.6 L/s which is equivalent to a single phase mass flux through the test section of G_p = 800 kg/m^{2}s and a pitch velocity of V_p = 0.54 m/s. In two phase experiments, the maximum pitch mass flux of fluid through the test section is about G_p = 550 kg/m^{2}s, which is lower than the single phase case because a portion of the flow must be diverted to the cooling sub-loop for heat removal purposes. A digital tachometer with a resolution of 5 rpm was used for measuring the pump speed. While the pump is designed to operate at a 1750 rpm, experience has shown that it is not possible to exceed 1100 rpm because the current demand of the motor reaches 6.6 amperes, the maximum allowable current for continuous

operation. After passing through the pump, the flow branches off in two directions - the main sub-loop and the cooling sub-loop. The flow rate through each of these sub-loops is measured by orifice plates (#4, #5) and the relative flow rate through each sub-loop is adjusted by the respective control valves in each conduit (#6, #7).

The main sub-loop directs the flow through the main heater (#8) where the R-11 is boiled by electric heating elements. These heaters are presently configured for 19.2 kW, but they have a maximum rated capacity of 48 kW. The heating coils consist of 15 U-bend elements in total; 3 elements produce 4.3 kW each (full power elements) while the remaining 12 elements produce 2.1 kW each (half power elements). Six chromel-constantan thermocouples (type E) are attached to the highest portion of each of the 3 full power heater elements and 3 of the half power elements in order to monitor the sheath temperature. These thermocouples are monitored by the Philips PM8237A thirty channel temperature recorder using an ice point reference, which provides a measurement resolution of .01 mV corresponding to a precision limit of about 0.3° Celsius. This recorder is equipped with an alarm interrupt that responds when the sheath temperature of any heater element exceeds a user determined maximum value. To prevent a heater element from overheating in the event of a boiling crisis, the maximum allowable sheath temperature and the proper alarm response must be programmed into the temperature recorder by the user prior to starting an experiment. The maximum allowable sheath temperature was set to 70°Celsius, which corresponds to a thermocouple voltage of about 4.3 mV. All of the programmable settings for the Philips temperature recorder are summarized on a reference sheet which is provided in appendix E. The list of thermocouples and the temperature they measure is presented in Appendix B.

Above the heater, the two phase R-11 passes through a transition section (#9) before it reaches the test section (#1), where the tube bundle and splitter plates are located. The test section is equipped with a pressure gauge for monitoring system pressure and thermocouples for temperature measurements. Large windows (eight inch square) are fitted in the broad sides of the test section for viewing the two phase flow before and after the tube bundle. A smaller end window facilitates tube vibration measurement using the optical light probe and allows for viewing the fluid-tube interaction at the free end of the tube.

Downstream of (above) the test section, the two phase R-11 passes upwards into the combination tank (#10) where the vapour phase is condensed by mixing with the cooled R-11 from the cooling sub-loop. The cooling sub-loop is equipped with dual water coolers (#11) in which the R-11 flows on the tube side and municipal water flows on the shell side. A cooling water supply of up to 0.78 L/s (12.4 USGPM) was available, but the actual requirements for any given two phase flow experiment rarely exceeded 0.4 L/s (6.4 USGPM). The steady state water supply temperature ranged from a low of 4°C in late winter and early spring, to a high of 17°C in late summer and early fall. It is desirable to use water as cool as possible because, for a given heater power input, the loop can be operated at lower pressure. For safety reasons, the pressure in the flow loop should be kept below of 270 kPa absolute (approx. 25 psi gauge). The windows of the test section are considered to be the weakest component in the system, since excessive deflection of the test section walls might cause them to crack after long term operation. An operating manual is available, Dam (1991), which contains more information on the loop components and the proper use of the two-phase flow loop.

5.2 Test Section and Tube Bundle

The test section, shown schematically in Figure 5.3, is a rectangular flow channel with cross sectional dimensions of 305 mm × 31.8 mm (12" x 1.25"). The tube bundle used in the experiments consisted of 10 cantilevered tubes in a parallel triangular array, which were tuned in air to within ±1% of the mean frequency. This tube bundle is shown in Figure 5.4 along with another bundle. The second bundle in this photograph is a heated tube bundle, where the tubes consist of stainless steel sheathed cartridge heaters. This bundle was used in some experiments but the boiling capability was not utilized. Specifications of the tube bundles are presented in Table 5.1. The tubes in both bundles are roughly ½ scale with respect to the tubes in a nuclear steam generator and have a pitch over diameter ratio of P/D = 1.44, which is a common value for nuclear steam generators and heat exchangers in general. The pitch velocity of the fluid flow is determined by multiplying the upstream velocity by the scaling factor P/(P-D) which is roughly 3 for the arrays used here. In the case of a parallel triangular array, the pitch velocity is not a true measure of fluid velocity in the gaps between the tubes as it is in a normal triangular or normal square array. Rather, it is a convenient definition which gives a close

approximation to the nominal velocity in the tube gap, and it allows for easier comparison with the data of other researchers since it is the standard velocity definition.

5.3 Tube Bundle Instrumentation

The tube vibration response for the unheated bundle was measured with a special optical light probe, which is described in detail in Judd *et al.* (1992) and Feenstra (1993). The essential details of the design are given here for completeness sake and for future reference, especially regarding the technical specifications of the optical parts. An illustration of the light probes used for the unheated bundles and the circuit diagram is provided in Appendix E. The light probe output was processed by a dynamic analyser, which calculated the rms amplitude and frequency spectrum in the frequency range from 0 to 100 Hz. The rms amplitude was averaged over 100 samples.

The light probe described in this section was designed for the unheated tube bundles to allow vibration measurement of tube #5. The tube numbering scheme is shown in Figure 5.5. Strain gauges were not applicable in this case because the glue used for mounting purposes could not withstand the solvent effects of the R11. A schematic diagram of the optical light probe apparatus is shown in Figure 5.5. Inserted into the free end of the instrumented tube is a 5 mm (.197") diameter commercial grade plano-convex lens having a focal length of 3.8 mm, which is sealed in place by glass plug which is 5 mm (.192") in length. Light is transmitted through the lens by a fibre optic cable, 1.5 mm (.059") in diameter which passes through the tube to a light source outside the tube bundle. Light is generated by a 5.0 volt halogen bulb and is focussed into the end of the fibre optic cable by a system of lenses. The light beam projected by the fibre optic cable passes through the end window of the test section (0.5" thick) where it impinges on the light probe. The free end of the instrumented tube must be set very close the glass window to prevent bubbles from passing between the glass end plug and the window which would interfere with proper light transmission. The light probe consists of four diametrically opposed photo-transducers that measure the streamwise and transverse displacement by detecting the change in light intensity between pairs of transducers as the tube vibrates. Details of light probe for heated tube bundle (#4) can be found in the thesis of Gidi (1999).

5.4 General Experimental Procedure

Three series of tests were conducted, designated A, B and C, where each had the specific purpose identified in Table 5.2. Test series A was essentially a repetition of the earlier experiments of Feenstra (1993) which were designed to test for the repeatability of the critical flow velocity data for fluidelastic instability in both single-phase and two-phase flows. This was necessary because three modifications were made to the flow loop since that earlier study: 1st. A flow homogenizer, which was designed to break up the large scale eddies in the approaching flow, was installed in the test section just upstream of the tube bundle. 2nd. A spray nozzle, which was designed to create a spray of the cooled R11 in the combination tank, was installed. This increased the effective surface area for condensing the vapour phase coming from the main sub-loop. This modification allowed flow quality to be determined with greater accuracy since the returning flow was less sub-cooled and hence less of the heater power was used to re-heat the liquid back to the saturation temperature. Previously there was no nozzle and the flow simply dropped into the tank from the end of the 1.25" dia. pipe, which permitted little contact between the liquid and the vapour that it was supposed to condense. 3rd. The cobalt 57 source that had been used earlier with the gamma densitometer was replaced with a Barium 133 source. The new source was significantly stronger than the previous one and the settings on the analyser needed to be altered in order to optimize the measurement of void fraction in the test section (see Appendix D).

Test series B and C were designed primarily for collecting data for void fraction and two-phase damping of a single flexible tube subjected to two-phase flow. Tube #5 was allowed to vibrate while the other 9 tubes were held fixed by a perforated plate that was attached over the free end of the tubes. Tube bundle # 1 was originally used in test series B but was replaced after a irreparable leak developed in the base of the tubes. Tube bundle #3 which was essentially identical except that the tubes were soldered in to the base instead of clamped, was substituted. It had a higher natural frequency and a lower structural damping. Test series C utilized the bundle #4, in which the tubes were made of stainless steel cartridge heaters. These experiments were designed primarily for void fraction measurements while experiments with tube heating were not explored .

Table 5.1 Summary of tube bundle data.

Parameter	Bundle #1	Bundle #3	Bundle #4 (heated)
Tube Diameter, D	6.35 mm	6.35 mm	6.17 mm
Tube Pitch, P	9.16 mm	9.16 mm	9.16 mm
Natural freq., f_a *	38.1 Hz	33.8 mm	39.7 mm
Nat. freq., $f_{R\text{-}11,hq}$ *	32.8 Hz	33.8 Hz	33.6 Hz
Lineal mass, m_t	0.179 kg/m	0.166 kg/m	0.138 kg/m
Stiffness, EI	7.13 Nm^2	7.13 Nm^2	7.65 Nm^2
Tube length, L	0.308 mm	0.308 mm	0.324 mm
Structural damping, ζ_{air} **	0.11%	< 0.05%	≈ 0.22%†
Tube material	Brass (0.049" wall)	Brass (0.049" wall)	Stainless steel
Tube attachment	clamped	soldered	swage lock
Pitch flow area, A_p (m^2)	0.00296 m^2	0.00296 m^2	0.00322 m^2
Effective Diameter, D_e/D	2.48	2.48	2.60

* Measured for Tube #5. ** Measured at an RMS amplitude of 2%Dia.

† Tube structural damping varies with temperature.

Table 5.2 Summary of test series.

	Test Series A	Test Series B	Test Series C
Tube Bundle	1	1, 3	4 (heated)
No. of Flexible Tubes	fully flexible bundle	single flexible tube	single flexible tube
Primary Focus	fluidelastic instability	damping, slip ratio	damping, slip ratio

5.4.1. Procedure for Single Phase Flow Experiments

Initially, experiments were conducted in single-phase liquid flow, because it was important to establish the response of the tube bundle in a realm which is fairly well mapped out by previous research. In this case, it was desired to obtain the vibratory amplitude response of the tube bundle as a function of pitch-flow velocity. Hence, each experiment consisted of a dozen or more trials, where in each trial the vibratory response of the monitored tube was measured for a constant pitch-flow velocity. The flow rate in each trial was set and permitted to run for a few minutes to ensure steady flow conditions. The output of the displacement transducer was input to a Hewlett Packard FFT spectrum analyser, from which amplitude, natural frequency and damping were determined as explained in Section 5.5. The procedure was repeated for increasing flow velocities until tube clashing occurred or was imminent. The experiments were operated at room temperature with no heating of the flow.

5.4.2. Procedure for Two-Phase Flow Experiments.

Experience had shown that the tube response in two-phase flow is a function primarily of two variables for a given fluid type: mass flux and flow quality (or void fraction). Proper determination of the tube amplitude response requires that one parameter be held constant while the other one is varied. In this study, the flow quality was increased in each trial, starting from zero, while the mass flux was maintained constant. By this method, the pump speed, N, was set using the motor speed controller, and the main sub-loop flow rate,Q_1, and cooling sub-loop flow rate, Q_2, were adjusted with the control valves to set the desired mass flux in the test section and sufficient R11 flow in the coolers. Adequate cooling of the flow loop was obtained by setting the water flow rate through the coolers. Flow quality was varied from one trial to the next simply by increasing the heater power. The pressure in the loop was maintained roughly constant by increasing the cooling water flow rate to the coolers at every third or fourth trial. Data acquisition was commenced when steady state conditions had been achieved, as determined by monitoring fluid temperatures at various points around the loop. The RMS tip amplitude of the tube and the frequency spectrum was determined for 100 sample averages, over a frequency range of 0 to 100 Hz on the dynamic analyser.

The procedure just described is the opposite of the procedure employed by other researchers working with two-phase flows (mostly air-water) who held the flow quality (or HEM void fraction) constant while increasing the mass flux until fluidelastic instability was reached. That approach is well suited to experiments in which air and water are used as the working fluid, because the two fluids can be pumped and regulated in separate conduits before mixing them together upstream of the test section. When such control is available over the flow rate of the two phases, it is very simple to obtain the desired HEM void fraction for a given mass flux. However, in the case of single component fluid such as refrigerant R11, where the two-phase flow is produced by boiling, it is much more difficult to maintain a constant void fraction for an experiment in which the mass flux is increased from one trial to the next. The difficulty arises in trying to predetermine the settings of heater power and flow rate to obtain the desired flow quality, because the fluid temperature in the test section, designated T_1, and just upstream of the heater, designated T_2, play a dominant role in the determination of this quantity. Experimentally, it is an iterative process in which (i) the flow rate and heat input must be set, (ii) the fluid must be allowed to circulate long enough for T_1 and T_2 to achieve steady state values, (iii) the void fraction must be calculated using temperatures T_1 and T_2, for comparison with the target value, and (iv) corrections must be made by changing the heater power. Steps (ii), (iii) and (iv) are then repeated until the measured flow quality is reasonably close to the target value. This is a tedious process in which steady state conditions can only be attained by trial and error, which makes data acquisition a time consuming process.

The experimental procedure adopted for this study, in which mass flux was held constant while void fraction was varied, was favoured over the alternate approach adopted by other researchers, mainly because it required fewer variables to adjust when moving from one trial to the next. Since the flow rate was held constant throughout the experiment, much of the uncertainty in this parameter was eliminated.

5.5 Method of Data Analysis

This section itemizes the data that was collected during experiments and describes the method employed for calculating the required parameters. There are slight differences in the data analysis

methods used for each test series (A, B and C) and these are indicated throughout this section. The differences arose to minor modifications made to the flow loop during the study.

Amplitude, Frequency and Damping Determination:

The vibratory response of the monitored tube was measured during steady flow conditions using a Hewlett Packard 35670A FFT spectrum analyser. The streamwise and transverse (drag and lift) directions were analysed on separate channels and response spectra were generated for each, over a frequency range of 0 to 100 Hz with a resolution of 0.25 Hz and averaged over 100 samples. The data pertaining to each frequency spectrum was saved on 3.5" floppy disk for post-processing. The natural frequency of vibration was determined by inspecting the trace on the analyser at the time that the experiments were conducted. It could also be determined later using the software supplied by HP called VIEWDATA.EXE. The rms amplitude was determined using a FORTRAN program called RMS.EXE. (see appendix D) which solves for average rms vibration amplitude according to the relationship,

$$\bar{y}_{rms} = \sqrt{\int_0^{\infty} S_y \, df} \,. \qquad \textbf{(5.1)}$$

However, since the analyser deals with discrete quantities, the integrand in equation (5.1) is replaced with a summation and df is replaced with the frequency resolution, Δf. Care was exercised not to include the very low frequencies (<1 Hz) in the integration to avoid the d.c. offset error of the displacement transducer, which measures absolute displacement. A d.c. signal of zero could be obtained by precise adjustment of the vernier platform, but the steady drag force on the tube during experimental trials would result in a steady offset from the initial setting.

Damping in two-phase flow was determined using the half-power bandwidth method. The frequency spectra data to be saved on floppy disk were first converted to ASCII format using the HP conversion software called SDFTOASC.EXE while invoking the switch /Y:PRD, which instructs the program to set the amplitude units of the output file to that of power spectral density (ie., $Volts^2/Hz$).

Then the program called "ASCTO2D.EXE" was used to generate another set of ASCII files consisting of two data columns, frequency in Hertz and Amplitude in linear units (ie., Volts/$Hz^{0.5}$). These files could be read by the damping program, supplied by AECL, called "2D.EXE" which would calculate the damping ratio. A detailed procedure for performing this vibration measurement analysis is described in Appendix D.

The structural damping component of the tube was determined using the energy dissipation method. The tube bundle was mounted in a heavy vise, and while the other tubes were held from vibrating, the monitored tube was plucked and the decay trace was captured using the data acquisition capability of the computer. The damping value of the decay trace was determined using a FORTRAN program called LOGDEC.EXE which is also described in Appendix D.

Main Sub-Loop Flow Rate:

$$Q_1\,(L/s) \;=\; 0.704\sqrt{H_1 * (1 - \frac{\rho_{RII}}{\rho_{Hg}})} \qquad \textbf{(5.2)}$$

The flow rate through the test section, Q_1, was determined by the orifice plate reading (H_1, in inches of mercury) measured by the U-tube manometer, where ρ_{RII} and ρ_{Hg} are the densities of liquid R11 and mercury respectively. The density ratio (ρ_{RII} / ρ_{Hg}) is roughly 0.109 at 24°C. When the pitch mass flux is below about 200 kg/m^2s, the orifice plate does not give an accurate measurement, because the differential head falls below 0.5 inches of mercury which makes it difficult to read with precision. In this situation, the main sub-loop flow rate is calculated by taking the difference between the total and cooling sub-loop flow rates,

$$Q_1\,(L/s) \;=\; Q_T\,(L/s) \;-\; Q_2\,(L/s), \qquad \textbf{(5.3)}$$

where Q_T is the total flow rate which is described below. Note that the formula used in test series A and B to determine Q_1 is, Q_1 {L/s}= 0.684*$(PT_1)^{0.5}$, where PT_1 is the pressure transducer reading in inches Hg.

Total Flow Rate:

$$Q_T(L/s) = 0.00186 * N(rpm) - 0.139 . \quad (1)$$

Since the pump is a positive displacement type, a linear relationship exists between pump speed, N, and flow rate. This relationship was determined empirically for the pump speed range of $350 < N < 800$ rpm. Note that the formula used in test series A and B to determine the total flow rate, Q_T, is, $Q_T = 0.00182*N$ {rpm} - 0.135.

Cooling Sub-Loop Flow Rate:

$$Q_2(L/s) = 0.296 * \sqrt{H_2 * (1 - \frac{\rho_{RII}}{\rho_{Hg}})} \quad (5.5)$$

The cooling sub-loop flow rate is determined by the differential head (H_2 in inches of mercury) across the orifice plate as measured by a U-tube manometer. Note that the formula used in test series A and B to determine Q_2 is, Q_2 {L/s} $= 0.223*(PT_2)^{0.5}$ where PT_2 is the pressure transducer reading in inches Hg.

Cooling Water Flow Rate:

The cooling water is required to extract heat from the flow upon exiting the test section and to thereby condense the vapour. A minimum flow rate of 0.2 L/s (H_w = 1.8" Hg) is necessary to obtain a spray inside the combination tank. Otherwise the flow just dribbles out of the internal spray nozzle and effective vapour condensation cannot be achieved. Note that the density ratio of water to mercury is about 0.0737.

Fluid Properties Determination

Properties of the fluid upstream of the test section and heater entrance are based upon the temperature at each location. It is assumed that the fluid entering the heater is single phase liquid, and that the two-phase fluid in the test section is in thermal equilibrium (ie., liquid and gas phase are at the

same temperature). Polynomial relationships for all of the R11 properties as a function of temperature are given below. These were derived by a least squares fit of the data from the ASHRAE (1991) tables in the temperature range of 20 to 60 °C. Note that in the following correlations, temperature, T is expressed in °C and EMF represents the voltage reading of the "E" type thermocouples.

Table 5.3 Summary of R-11 property correlations.

Liquid viscosity:	ν_L {μPa} = 563.5 - 6.228T + 0.0262T^2
Gas viscosity:	ν_G {μPa} = 10.16 + 0.0356T
Liquid density:	ρ_L {kg/m^3} = 1533.1 - 2.1962T - 0.003287T^2
Gas density:	ρ_G {kg/m^3} = 2.8291 - 0.062313T + 0.0027383T^2
Liquid enthalpy:	h_L {kJ/kg} = 199.92 + 0.87863T + 0.0003982T^2
Vaporization enthalpy:	h_{LG} {kJ/kg} = 190.5 - 0.34876T - 0.00070376T^2
Saturation pressure:	P_{sat} {MPa} = 0.048611 + 0.00087T + 5.689E-5 T^2
E type thermocouple:	T {deg C} = 0.82277 + 16.014*EMF + 0.10689*EMF^2

Pitch Mass Flux:

$$G_p\,(kg/m^2 s) = \frac{Q_1\,(L/s) * \rho_{L2}\,(kg/m^3)}{A\,(m^2)\ 1000\,(L/m^3)} * \frac{P}{P-D} \quad \textbf{(5.6)}$$

Pitch mass flux, G_p, is the nominal mass flow rate per unit area in the gaps between the tubes and ρ_{L2} is the density of the liquid flow entering the heater section. The upstream flow area is A=0.00967 m^2, the pitch is P= 9.16 mm and tube diameter for tube bundles #1 and 3 is D = 6.35 mm. (D = 6.17 mm for bundle #4).

Enthalpy Rise

$$\Delta h\,(kJ/kg) = \frac{C_L * q\,(kW) * 1000\,(L/m^3)}{\rho_{L2}\,(kg/m^3) * Q_1\,(L/s)} \quad \textbf{(5.7)}$$

The enthalpy rise of the fluid due to heat input of the main heater, Δh, is essentially the ratio of the heating power, q, to the mass flow rate which is liquid density times volumetric flow rate, $\rho_{L2}*Q_1$. The correction factor, C_L, is used to account for the heat lost by convection to the room, which is estimated to be 3% of the electrical heat input, so that $C_L = 0.97$.

Flow Quality:

$$x = \frac{h_{L2} + \Delta h - h_{L1}}{h_{LG1}} . \qquad \textbf{(5.8)}$$

Flow quality is the mass ratio of the gas phase to the total flow approaching the bundle. The experimental uncertainty in this value is high at low quality because the enthalpy rise, Δh, is small compared with the liquid phase densities before and after the heater, h_{L2} and h_{L1} resp. This is described in more detail in the next section on error analysis.

HEM Fluid Density:

$$\rho_H (kg/m^3) = \left(\frac{x}{\rho_{G1}} + \frac{1-x}{\rho_{L1}}\right)^{-1} . \qquad \textbf{(5.9)}$$

HEM fluid density, ρ_H, is a measure of the average density of the two phase flow approaching the tube bundle. It assumes that the phases are finely mixed and travelling together at the same velocity. The subscript "H" indicates that the homogenous equilibrium model is assumed.

HEM Void Fraction:

$$\alpha_H = \left(1 + \frac{\rho_{G1}}{\rho_{L1}}\left(\frac{1}{x} - 1\right)\right)^{-1} . \qquad \textbf{(5.10)}$$

HEM void fraction is the volumetric ratio of the gas phase to the total volume of fluid. This model assumes that the two phases are finely mixed and travel at the same velocity throughout the flow.

HEM Pitch Velocity:

$$V_p = \frac{Q_1(L/s) * \rho_{Ll}(kg/m^3)}{\rho_H(kg/m^3) * A(m^2)\,1000\,(L/m^3)} \frac{P}{P-D} . \qquad (5.11)$$

The HEM pitch velocity, V_p is a measure of the average flow velocity of the two-phase flow as it passes through the tube bundle, where the homogeneous equilibrium model is assumed. It can also be expressed by $V_p = G_p / \rho_H$.

Separated Flow

The preceding quantities such as pitch flow velocity and average fluid density were calculated using the homogeneous equilibrium model. This is an unrealistic assumption for most vertical two-phase flows because the large density difference between the gas and liquid phase leads to a significant velocity ratio between the two phases. In this study, single beam gamma ray attenuation was used to obtain a measurement of the void fraction of the R11 flow in the test section just upstream of the tube bundle. The measurement system consists of a gamma source, lead shielding, a scintillator and the electronics necessary for signal processing These measurements were made by passing the gamma beam through the open region just under upstream of the tube bundle. The theory of this measurement technique is described in more detail in Appendix A. The subscript "RAD" is used to distinguish certain quantities which utilize the radiation attenuation method of void fraction measurement, such as average fluid density, ρ_{RAD}. Other quantities such as gas and liquid phase velocities, U_G, U_L, and equivalent two phase velocity, V_{eq}, were also calculated using the RAD void fraction, α, but these quantities do not utilize the "RAD" subscript.

RAD Void Fraction:

RAD void fraction, α, in the test section is determined from measurements made with the gamma densitometer according to,

$$\alpha = \frac{\ln(N^*/N_L)}{\ln(N_G/N_L)} \qquad where, \quad N^* = N\sqrt{\frac{\rho_{LI}}{\rho_{LC}}}. \tag{5.12}$$

N is the gamma count rate measured during testing, N^* is the corrected count rate during testing (corrected for density change from that at calibration time). N_G and N_L are the reference count rate in the gas and liquid phases respectively which correspond to 100% and 0% void fraction respectively. These gas and liquid reference count rates were obtained just prior to each experiment simply by measuring the gamma count rate in the test section with it empty of liquid or full of liquid respectively. The phase density, ρ_{LC}, is the R-11 liquid density at the time of gamma densitometer calibration, while ρ_{LI} is the liquid density at the time of data acquisition. In all cases, $\rho_{LC} > \rho_{LI}$, since the R-11 was usually at room temperature at the time of calibration while during any test the fluid was above room temperature.

Velocity Ratio:

$$S = \frac{U_G}{U_L} = \left(\frac{1-\alpha}{\alpha}\right)\left(\frac{x}{1-x}\right)\left(\frac{\rho_{LI}}{\rho_{GI}}\right). \tag{5.13}$$

Velocity ratio is the ratio of the gas phase velocity, U_G, to the liquid phase velocity, U_L.

Gas and Liquid Phase Velocities:

$$U_G(m/s) = \frac{x\ G_p(kg/m^2s)}{\alpha\ \rho_{GI}(kg/m^3)} \tag{5.14}$$

$$U_L(m/s) = \frac{(1-x)\ G_p(kg/m^2s)}{(1-\alpha)\ \rho_{LI}(kg/m^3)} \tag{5.15}$$

RAD Fluid Density:

$$\rho_{RAD}\,(kg/m^3) \;=\; \alpha\rho_{GI} + (1-\alpha)\rho_{LI} \qquad \textbf{(5.16)}$$

Equivalent Pitch Flow Velocity:

$$V_{eq} \;=\; \sqrt{(\alpha\,\rho_{GI}\,U_G^2 \;+\; (1-\alpha)\,\rho_{LI}\,U_L^2)/\rho_{RAD}}\;. \qquad \textbf{(5.17)}$$

This formula is a representation of two-phase flow velocity weighted by the dynamic head of each phase. It must be remembered however, that the two phases travel upward through the test section at different velocities. In some instances such as intermittent flow, the flow can be highly unsteady with periods of upward gas surge and liquid back-flow.

Tube Mass per Unit Length:

The mass of the tube per unit length including fluid hydrodynamic mass is determined by,

$$m \;=\; m_t\,(\frac{f_a}{f})^2\,, \qquad \textbf{(5.18)}$$

where (f_a/f) is the ratio of the in-air to in-flow vibration frequency, and m_t is the mass per unit length of the tube by itself. The hydrodynamic mass of the fluid is given by,

$$m_h \;=\; m_t\,[\,(\frac{f_a}{f})^2 \;-\; 1\,] \qquad \textbf{(5.19)}$$

Hydrodynamic Mass Ratio:

The ratio of the hydrodynamic mass in two-phase flow divided by the hydrodynamic mass in liquid R-11 is given by,

$$m_R \;=\; m_h/m_L \;=\; \frac{(f_a/f)^2 - 1}{(f_a/f_L)^2 - 1} \qquad \textbf{(5.20)}$$

Hence, m_R is unity in liquid flow, and is zero in gas flow.

Theoretical Hydrodynamic Mass:

$$m_{h,\,theor.} = \left[\frac{(D_e/D)^2 + 1}{(D_e/D)^2 - 1}\right]\frac{\pi \rho_{RAD} D^2}{4} \qquad \textbf{(5.21)}$$

The theoretical hydrodynamic mass is the lineal mass of fluid displaced by the tube and corrected for confinement of the nearest tubes. The effective diameter ratio, D_e/D, is given in Table 5.1.

Theoretical Hydrodynamic Mass Ratio:

$$m_{R,pred} = \frac{m_{h,pred}}{m_{L,pred}} = \frac{\rho_{HEM}}{\rho_L} \quad or \quad \frac{\rho_{RAD}}{\rho_L} \approx (1 - \alpha_H) \quad or \quad (1 - \alpha) \qquad \textbf{(5.22)}$$

There are two ways to calculate this theoretical mass ratio, depending upon which two phase fluid model is used. Intuitively, the RAD model is a more accurate measure of the average fluid density and therefore should give the most accurate prediction of hydrodynamic mass ratio.

Vibration Damping:

Damping ratio, ζ_T, was determined using special software supplied by AECL called "2D.EXE" which was designed to perform a least square curve fit to the frequency spectra, using the damping ratio as a fitted parameter. (see Appendix D for instructions). This program essentially uses the energy dissipation method (Log-decrement) for damping determination. The in-flow damping values were obtained from the experimental data of Test Series B, in which the tube bundle consisted of a single flexible tube in a rigid array. This was done to minimize the fluid coupling effect of the neighbouring tubes, which causes the frequency to vary due to the variation in added mass. Under such a condition, the assumption of time invariance of the vibratory system is unsatisfied and results in erroneously high damping values.

5.6 Uncertainty Analysis

This section discusses the measurement uncertainty of the experimentally determined variables used in the fluidelastic instability analysis of Chapter 8. The uncertainty in these variables, listed in Table 5.4, were based upon the following measurement uncertainties: The heater power was measured with a 3-phase wattmeter, having a digital display measurement resolution of 0.1 kW. The uncertainty in this measurement is estimated to be ±0.05 kW, which represents ½ the smallest division in the reading. The flow rate of R11 in the main sub-loop (into the test section) was measured either with the motor speed correlation at low mass flux (<200 kg/m^{2}s), or with the orifice plate measurement at higher mass flux. The uncertainty in the pump motor speed is estimated to be ± 5 rpm, which corresponds to a flow rate uncertainty of about ±0.5 L/min. This is the same as the measurement resolution of the present speed indicator but most of the data was acquired using the old speed indicator, which had a resolution of ± 10 rpm. The uncertainty of the orifice plate reading on the U-tube manometer is estimated to be ± 0.1" Hg, which is roughly the lowest resolution, discernable by eye, of the height difference of the mercury column. The E-type thermocouples are measured with a resolution of 0.01 mV, which corresponds to a temperature resolution of 0.16°C. A reasonable measurement uncertainty of this reading is half of the resolution which is ±0.005mV or ±0.08°C.

The uncertainty in quality determination, shown in Figure 5.6, was developed by combining the estimated uncertainties in three primary measurements discussed above, heater power (± 0.05 kW), flow rate (± 0.3 L/min) and thermocouple temperature measurement (± 0.08 °C). Note that the curves in this figure represent the worst case combination of these three errors. Although the relative error seems excessive at low qualities, it must be remembered that the absolute value of the error is small, and of no great consequence to the accuracy of the fluidelastic data, which occurred at qualities at or above 0.01.

A guideline for estimating the uncertainty in void fraction measurements by radiation attenuation provided by Chan and Banerjee (1981), is based upon the error in the counting statistics, e_α, as follows,

$$e_\alpha = (S_n \sqrt{N_\alpha t})^{-1} . \qquad \textbf{(5.23)}$$

For the Barium 133 source, the sensitivity, S_m, was 39%, the count rate in two phase flow, N_α, was between the count rates of liquid, N_L=1260, and gas, N_G=1890, and the counting period, t, was 20s. A conservative estimate of uncertainty using Eq. (5.23) is about ±1.6%. However, during experiments the statistical behaviour of the counts was periodically monitored, and the worst case showed a standard deviation of about ±4% of the mean count, N_α, over 5 samples. This leads to a 95% confidence interval for void fraction of about ±5% of the measurement ($t_{0.95,4}$ = 2.78). This uncertainty is greater than that estimated by equation (5.23), and is likely due to flow unsteadiness.

The uncertainty in the measurement of damping ratio, ζ_T, is difficult to determine because it depends upon the resolution of the frequency spectra compared with the band-width of the frequency peak and the goodness of fit of the least squares regression analysis. However, a practical estimate of this uncertainty was made assuming that the damping was independent of mass flux but dependent upon void fraction. A sample set of damping data was grouped according to void fraction over a range of mass flux conditions, and statistics were performed to determine the mean and standard deviation of these sets of samples. The 95% confidence interval was calculated for each data set and it appeared reasonable that an uncertainty of ±15% be assigned to the measured damping ratio. This relative uncertainty also applies to the log-decrement damping value, δ, since $\delta = 2\pi\zeta$.

An analysis of the uncertainties in the results were performed using the data spreadsheet by implementing the worst combination of the afore-mentioned uncertainties in flow rate, temperature, heater power and RAD void fraction. Sample copies of the spreadsheet program with actual experimental data are provided on the Cd-rom in the back cover of this document. Uncertainty estimates were determined for the following two-phase flow quantities: HEM fluid density, ρ_H, HEM void fraction, α_H, HEM pitch flow velocity, V_p, RAD void fraction, α, and equivalent pitch flow velocity, V_{eq}. Since the uncertainties in these quantities vary with flow quality and mass flux, the analysis was performed on data corresponding to fluidelastic threshold over a wide range of mass flux as shown in Table 5.4. To better illustrate the results of this analysis, the data is plotted in Figure 5.7 (a) and (b) on a typical fluidelastic stability diagram, with horizontal and vertical error bars on the three data points. Note that the following assumptions are made,

$$e(V_p/fD) \approx e(V_p)$$
$$e(m\delta/\rho D^2) \approx \sqrt{e(\delta)^2 + e(\rho)^2} \quad \textbf{(5.24)}$$

Equation (5.24) states that the relative error in dimensionless velocity, $e(V_p/fD)$, is assumed to depend upon velocity alone, while the uncertainty in vibration frequency, f, and tube diameter, D, are assumed negligible in comparison. Likewise, the relative error in mass damping parameter, $e(m\delta/\rho D^2)$, is assumed to depend upon uncertainties in log-decrement damping, δ, and average fluid density, ρ, while the uncertainties in tube mass per unit length, m and tube diameter, D, are assumed negligible in comparison. Figure 5.7 can be compared with similar figures in Chapter 8 where the fluidelastic data of this research is presented. However, it must be noted that the uncertainty bounds presented in Figure 5.7 are based upon measurement uncertainties, and do not account for the effects of unsteadiness in the flow and non-uniformity in the fluid temperature. These effects can be significant for intermittent flow, which is a particular type of two-phase flow regime which is discussed in Chapter 6.

Table 5.4 Calculated Uncertainties in Selected Fluidelastic Instability Data.

Data	Test 01 G_p = 86 kg/m²s	Test 06 G_p = 250 kg/m²s	Test 13 G_p = 478 kg/m²s
Flow Quality	0.0493 ± 25%	0.0188 ± 14%	0.0080 ± 19%
HEM Density, ρ_H	163 ± 18%	382 ± 10%	693 ± 10%
HEM Void Fraction, α_H	0.89 ± 3%	0.74 ± 3%	0.52 ± 8%
HEM Pitch Velocity, V_p	0.53 ± 14%	0.65 ± 8%	0.69 ± 9%
HEM Reduced Velocity, V_{pc}/fD	2.26 ± 14%	2.78 ± 8%	2.95 ± 9%
HEM Mass Damping Parameter, $m\delta/\rho_H D^2$	3.99 ± 23%	2.12 ± 18%	1.07 ± 18%
RAD density, ρ_{RAD}	803 ± 4%	845 ± 3%	988 ± 2%
Equivalent Velocity, V_{eq}	0.13 ± 5%	0.30 ± 6%	0.49 ± 5%
RAD Reduced Velocity, V_{eq}/fD	0.54 ± 5%	1.29 ± 6%	2.08 ± 5%
RAD Mass Damping Parameter, $m\delta/\rho_{RAD}D^2$	0.81 ± 16%	0.96 ± 16%	0.75 ± 16%

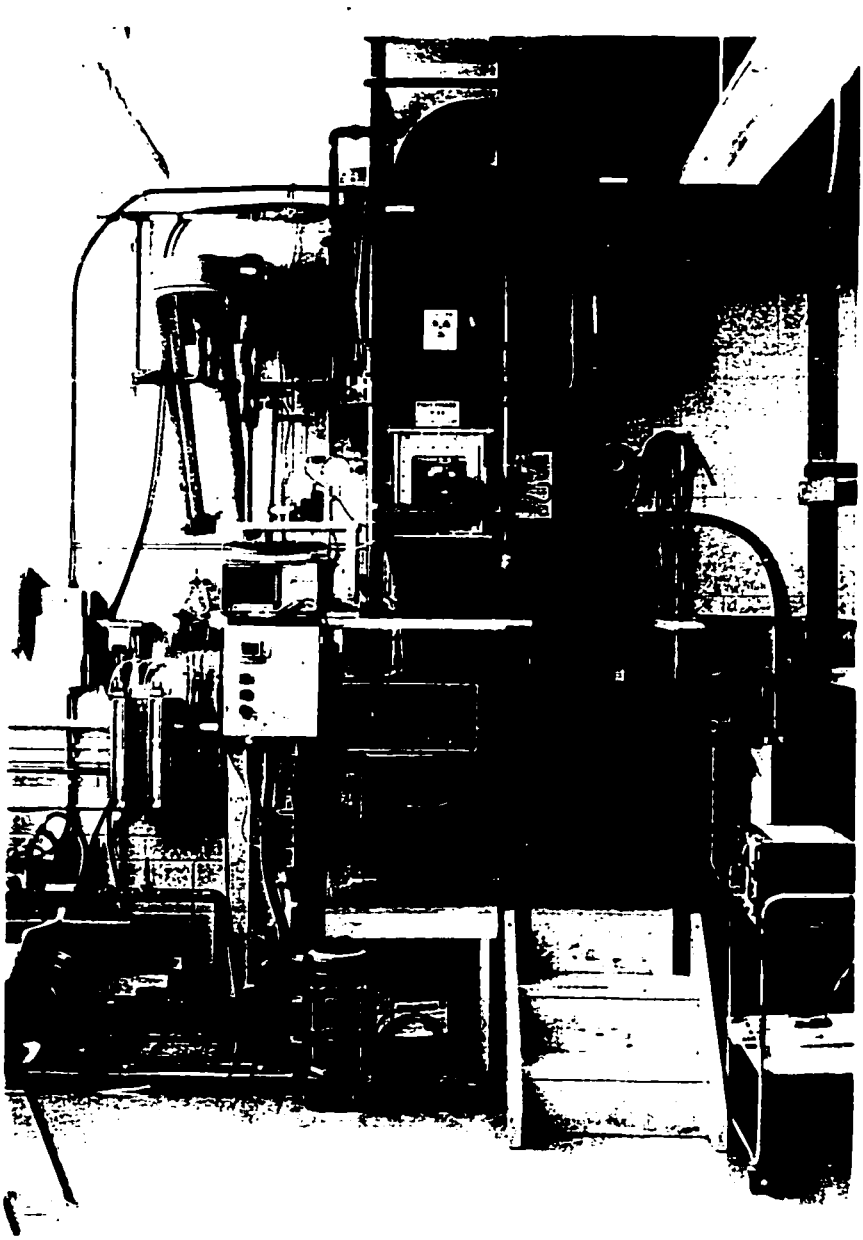

Figure 5.1 Photograph of R-11 flow loop.

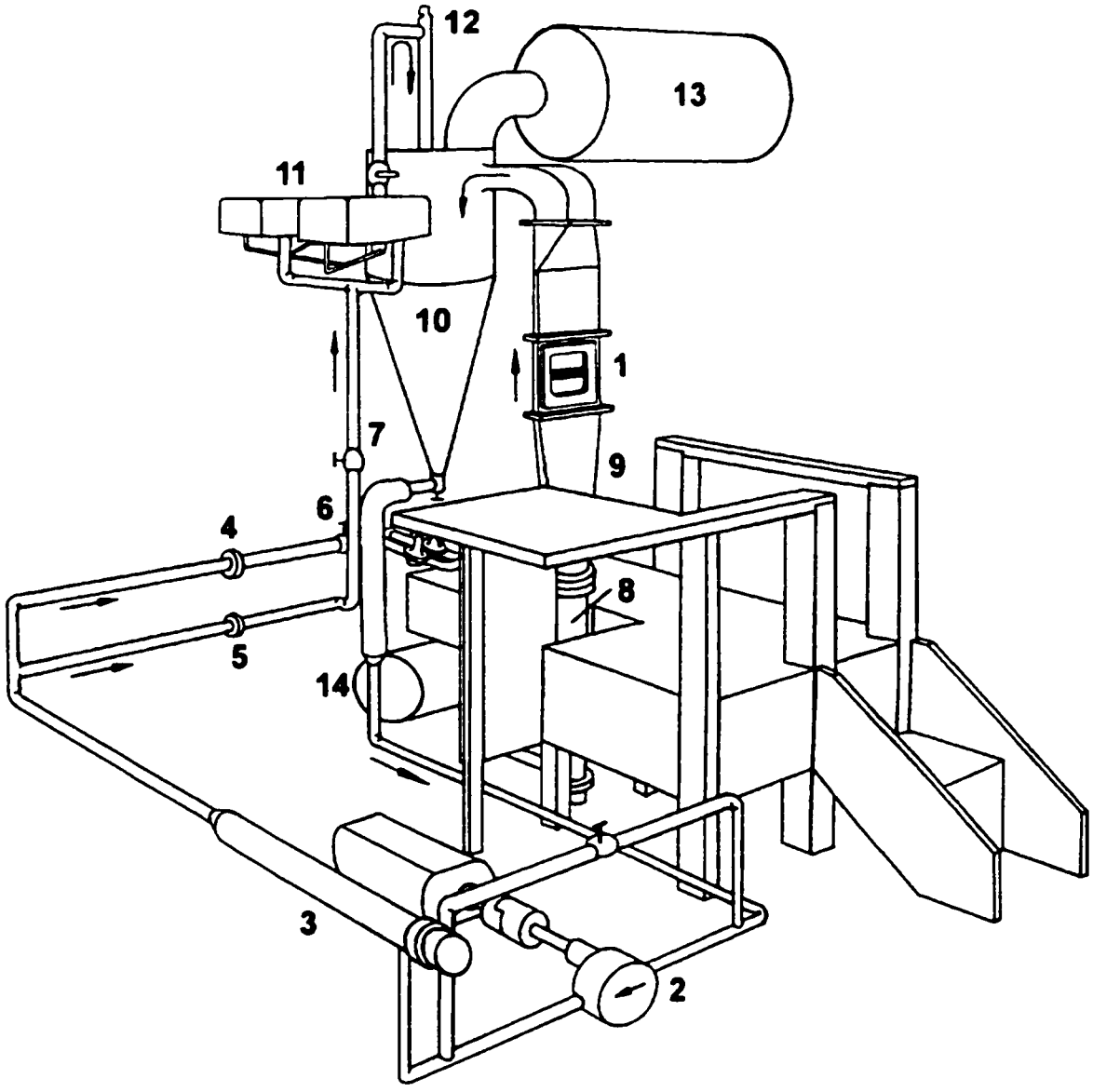

Figure 5.2 Schematic diagram of R-11 flow loop and components. 1-Test section; 2-gear pump; 3-pre-heater (not used); 4, 5- orifice plates for cooling and main sub-loops respectively; 6, 7- control valves for cooling and main sub-loops respectively; 8- main heater section; 9- upstream transition section; 10- combination tank; 11- coolers; 12- pressure relief valve; 13- expansion tank; 14- R-11 storage tank.

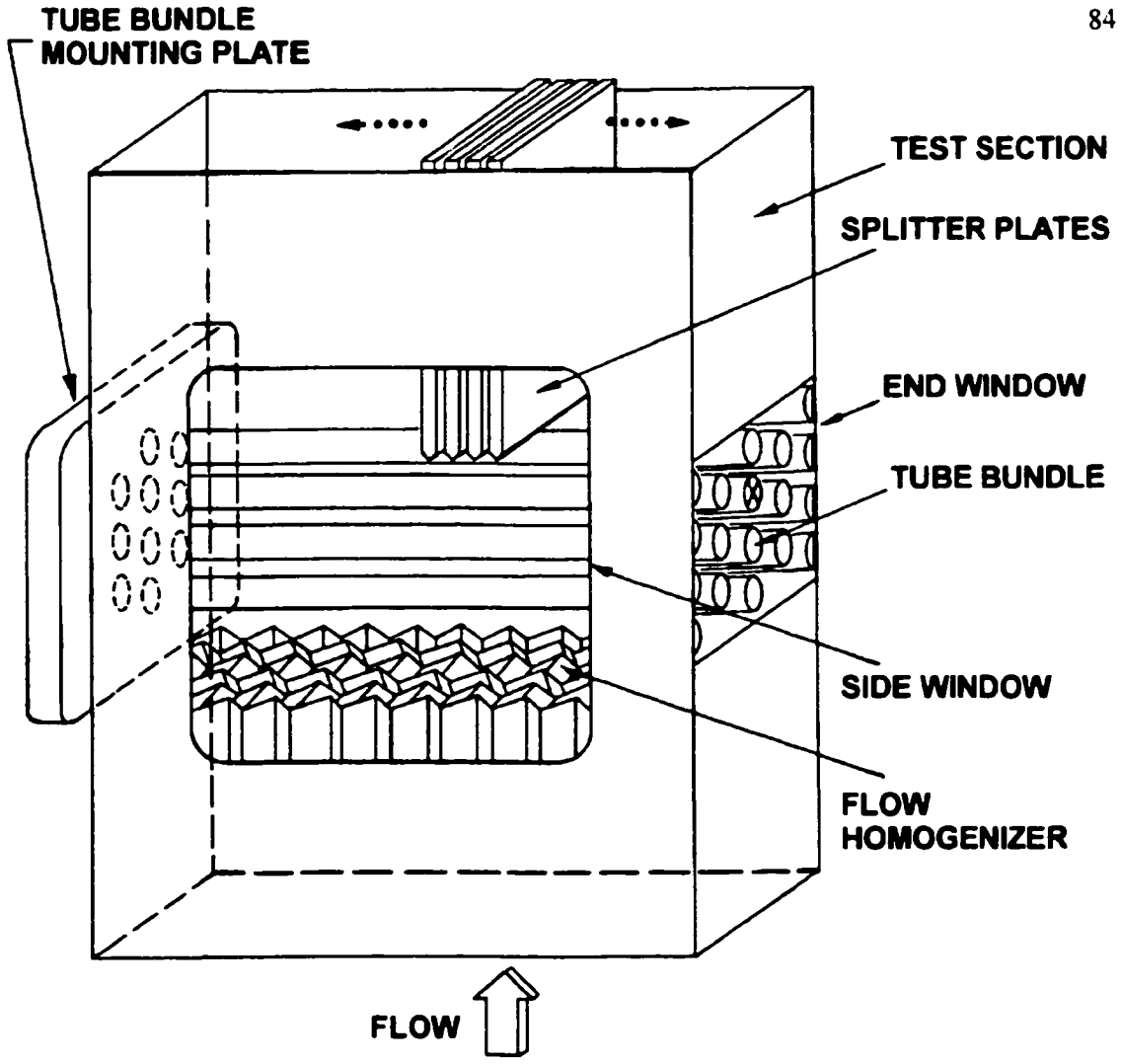

Figure 5.3 Schematic diagram of test section with tube bundle installed.

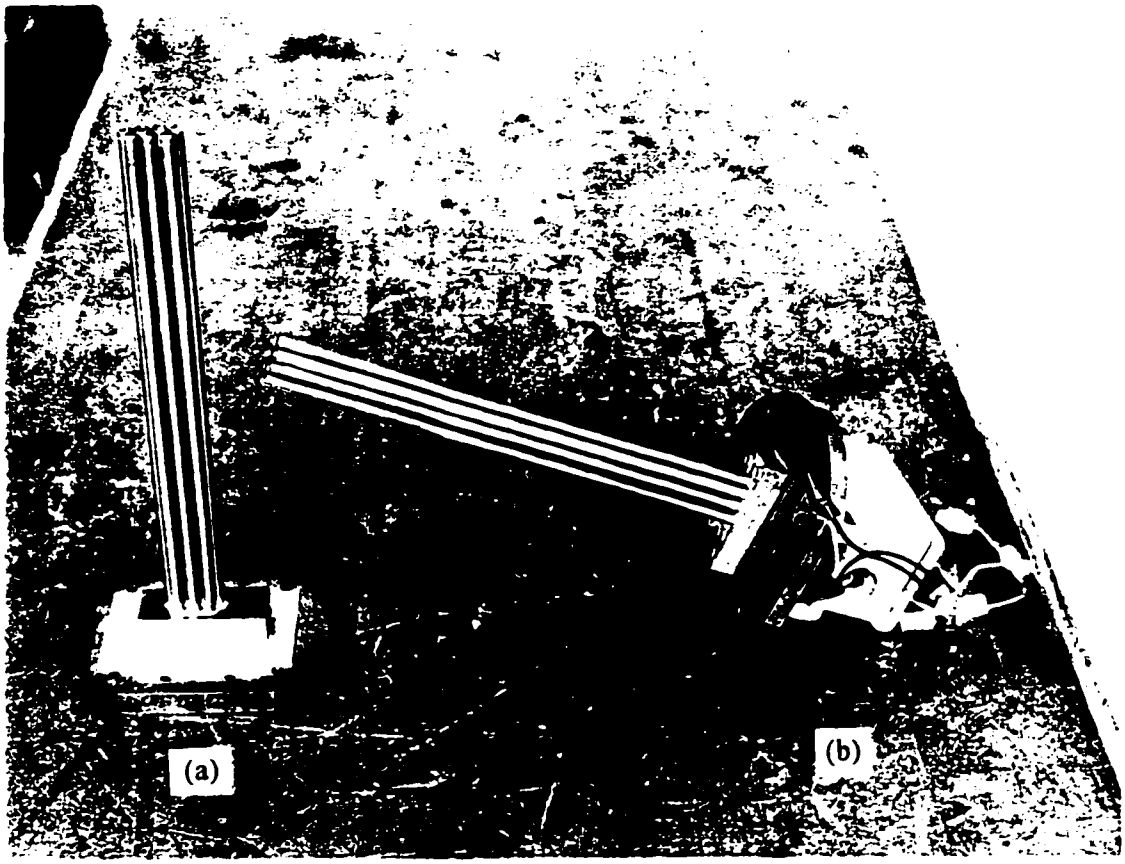

Figure 5.4 Photograph of (a) unheated tube bundle #3 and (b) heated tube bundle #4 (above). (c) Parallel triangular tube pattern of the bundles (below).

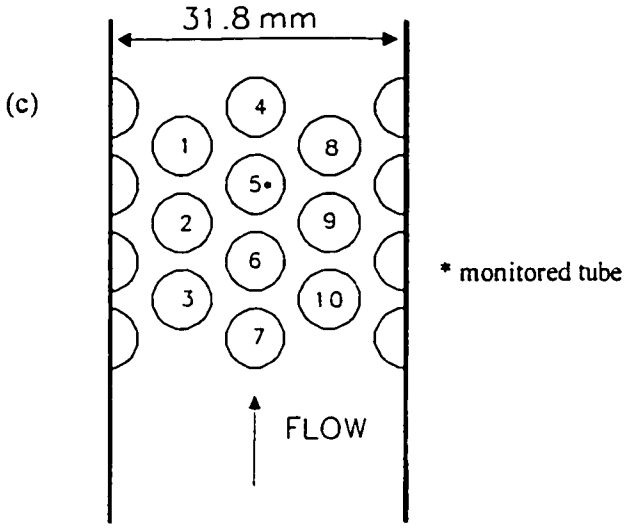

(a)

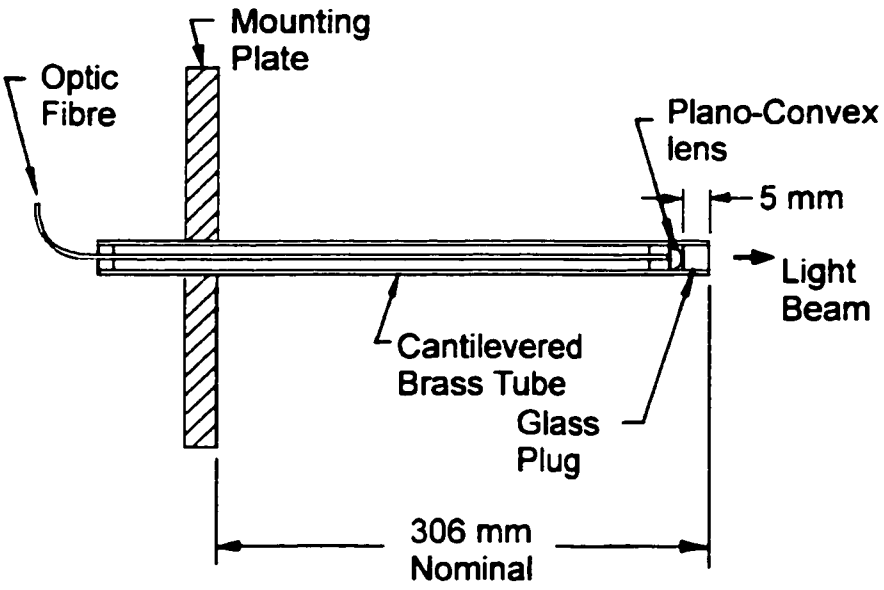

(b)

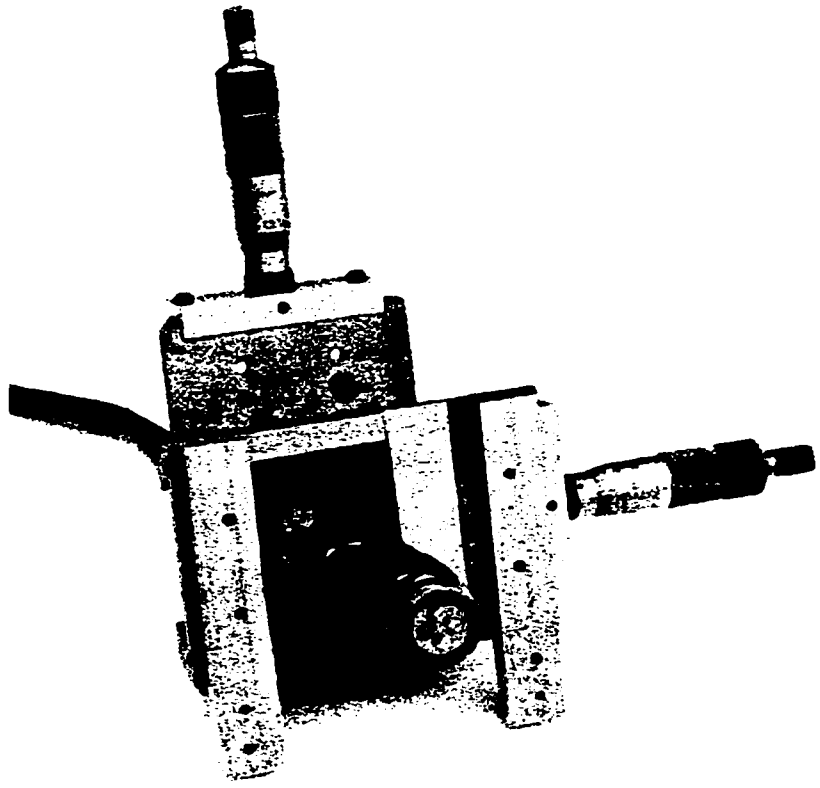

Figure 5.5 Partial instrumentation for tube vibration measurement. (a) tube instrumented with fibre optics, (b) light probe equipped with photo-detector array mounted on an x-y stage.

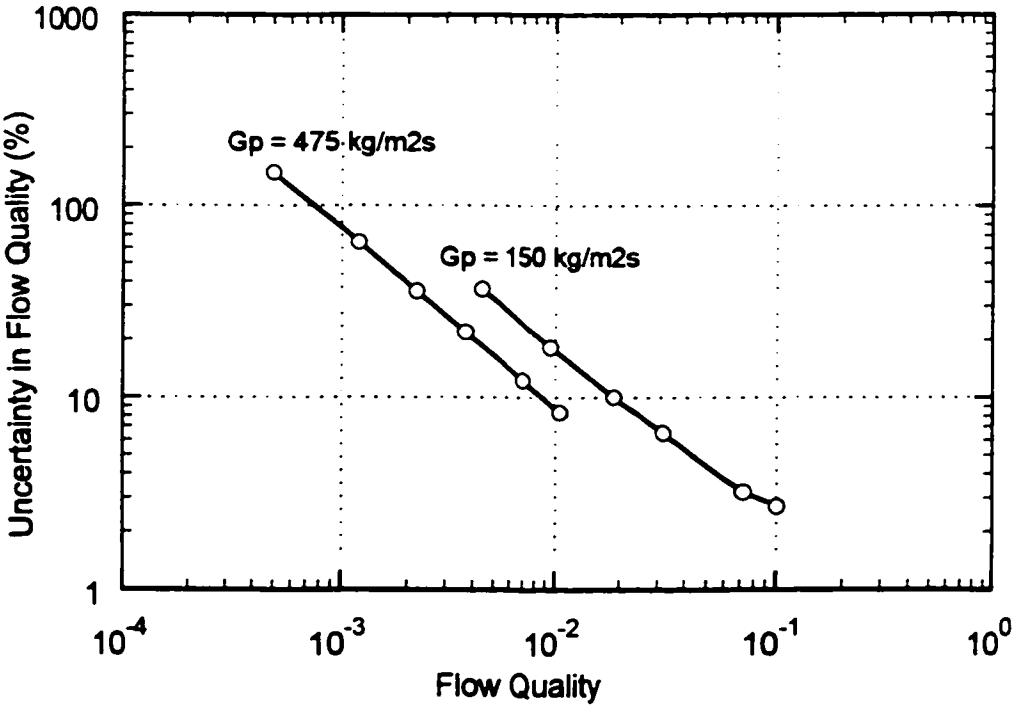

Figure 5.6 Uncertainty in flow quality for R11 data of the present study.

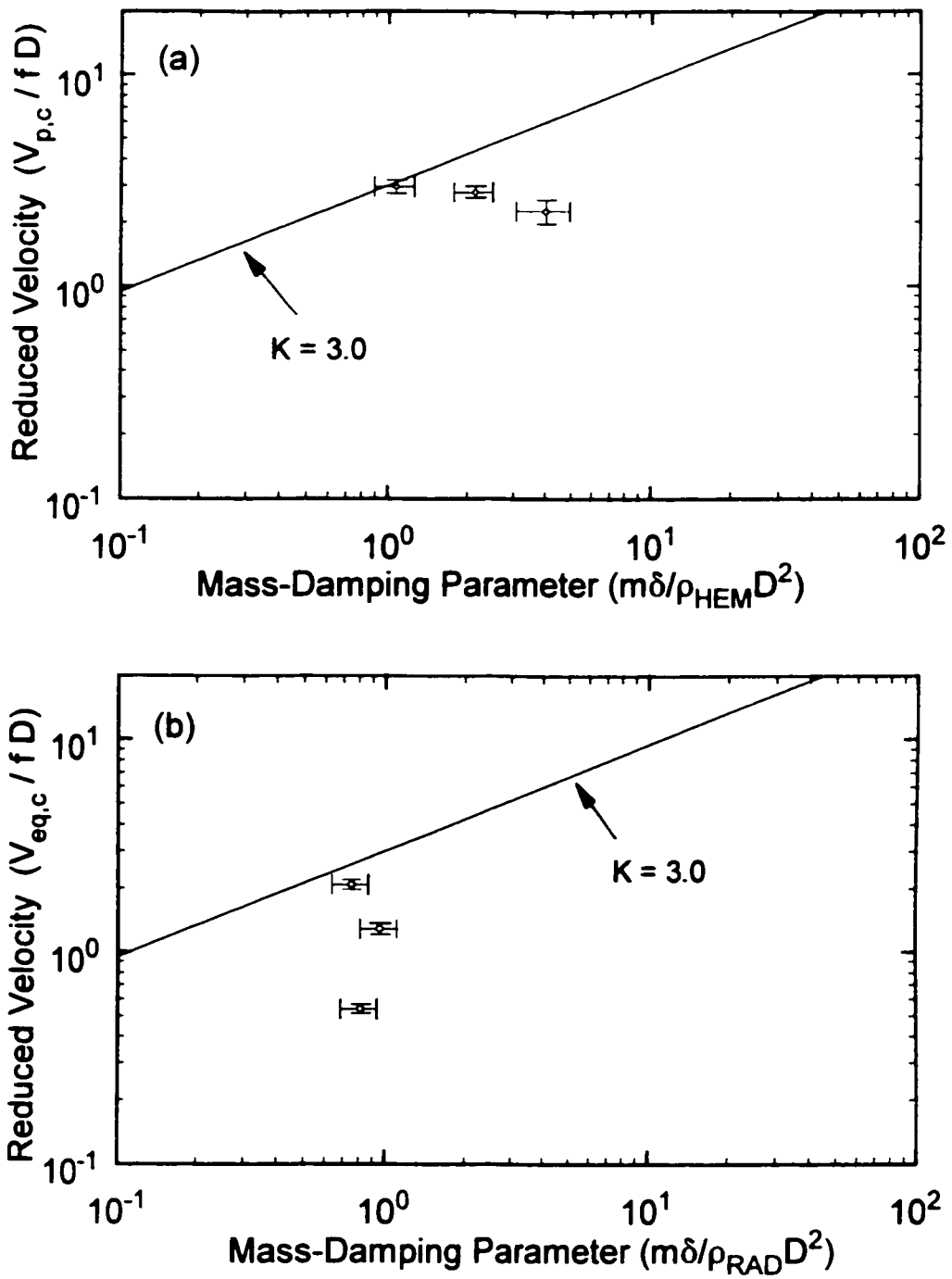

Figure 5.7 Calculated uncertainty in selected fluidelastic instability results for (a) HEM results, (b) RAD results.

CHAPTER 6

Two-Phase Flow Regimes

In gas-liquid two-phase flow, the two-phases can adopt various geometric configurations called flow regimes or flow patterns. It is known that the different flow patterns can have significant effects upon pressure drop and heat transfer rates in boiling channels. Recently, it has been speculated that a flow regime transition can have a profound effect on fluidelastic instability of heat exchanger tubes subjected cross-flow (Pettigrew *et al.*, 1995). It is necessary for designers and researchers to be able to predict the flow regime of a particular two-phase flow application so that design data can be properly interpreted. This chapter presents the most recent knowledge on flow regime in gas-liquid shell-side flows in heat exchanger equipment.

The important physical parameters which affect flow regime are surface tension, which causes liquid to adhere to solid surfaces and which makes bubbles spherical, and gravity, which causes the gas phase to rise through the liquid due to buoyancy. Flow rates and density ratio of the gas and liquid phases also play a role in the formation of a particular flow pattern.

It is generally agreed that three typical flow regimes can occur in vertically upward shell-side flows in tube arrays, namely: bubbly, intermittent and dispersed (or annular) flows. Slug flow, which is often observed in vertical pipe flows, is generally not observed in tube bundle cross-flows. The three photographs in Figure 6.1 illustrate the appearance of these three type of flow patterns in the vertical shell-side flow of a heat exchanger. These flow regimes are described as follows: **Bubbly flow** generally occurs when the gas flow rate is low relative to the liquid flow rate, where the gas phase is distributed as discrete bubbles in a continuous liquid phase. At low void fractions, the bubbles are very small and dispersed, but as the void fraction increases, the bubbles become larger, and may deform and elongate. This type of flow is sometimes described as a pseudo-single-phase flow since the

general behaviour of a bubbly flow (ie., velocity profile, flow steadiness) does not depart significantly from that of a pure liquid flow. **Intermittent flow** occurs when the volumetric gas flow rate is high and comparable to the liquid flow rate. This type of flow appears chaotic and frothy, interspersed with periods of upward vapour surges and downward liquid reversal. **Annular flow** occurs when the volumetric gas flow rate is relatively high compared to the liquid flow rate. The liquid forms a wavy film along the solid surfaces while a continuous gas phase occupies much of the open spaces. Liquid droplets may become entrained in the core if the gas velocity is sufficient to detach them from the liquid film.

Grant (1976) was the first to publish a flow regime map for the shell-side flow from observations in a simulated heat exchanger bundle using a flow mixture of air and water. Three flow regimes were identified: bubbly, intermittent and spray flow. His map is shown in Figure 6.2(a), where the ordinate is expressed in terms of the non-dimensional superficial gas phase velocity, U_{GS}^{*} given by,

$$U_{GS}^{*} = U_{GS}\sqrt{\frac{\rho_G}{d_e g(\rho_L - \rho_G)}}\ , \qquad \textbf{(6.1)}$$

where d_e is defined as an effective diameter which in this case is twice the tube gap (ie., d_e=2(P-D)), and U_{GS} is the superficial gas velocity defined by,

$$U_{GS} = xG_p/\rho_G\ , \qquad U_{LS} = (1-x)G_p/\rho_L\ , \qquad \textbf{(6.2)}$$

where U_{LS} is the superficial liquid velocity. These quantities are interpreted as the velocity the phase would have if it were flowing alone in the pipe, with the other phase absent. The abscissa of Grant's map is in terms of the Martinelli parameter, X, given by,

$$X = \left(\frac{1-x}{x}\right)^{0.9}\left(\frac{\rho_G}{\rho_L}\right)^{0.5}\left(\frac{\mu_L}{\mu_G}\right)^{0.1}\ . \qquad \textbf{(6.3)}$$

The physical meaning of the Martinelli parameter, X, is that it represents the ratio of the frictional pressure gradient of the liquid to the gas phase as follows,

$$X = \sqrt{\frac{(dP/dz)_L}{(dP/dz)_G}} \quad . \tag{6.4}$$

The solid lines in Figure 6.2 are the predicted flow regime transitions of Grant. The symbols which are superimposed on this map correspond to flow conditions at the threshold of fluidelastic instability obtained by various researchers. However, in developing the map, Grant tested only a limited range of flow conditions, which made it inapplicable to many other research works as shown by the various data sets plotted in Figure 6.2(a). Moreover, the flow regime observations made in this study in R-11 flow do not agree well with the map, as shown in Figure 6.2(b). The flow regime of each data point in this figure were determined visually from an experiment which was performed at constant mass flux with stepwise increases in flow quality. A change from bubbly to an intermittent flow was observed for two such experiments, one at low mass flux (G_p=150 kg/m^{2}s), and one at relatively high mass flux (G_p=385 kg/m^{2}s). The dashed line drawn through the data demarcating the two observed flow regimes does not agree with the Grant's prediction.. Note that annular flow is out of reach for the flow loop in its present configuration due to the high heating and (especially) high cooling capacities required to generate such a flow.

Most flow regimes are identified visually, but some researchers have developed methods for making more objective determinations. While these methods are actually calibrated by visual observation, nevertheless they provide a means for identification in cases where visual observation is not possible. Vince and Lahey (1982) used a dual beam X-ray system to make chordal average void fraction measurements, and generated probability density functions (PDF) of the void fraction. The particular signature of the PDF distributions for each flow regime was used as an objective indicator. They were able to discern three flow regimes in vertically upward pipe flow: bubbly, slug and annular flow. Noghrehkar *et al.* (1999) used an electrical resistance probe to measure the void fraction in a shell side flow of air-water in a model tube array. They also generated PDF functions similar to the previous study and were able to identify three flow patterns: bubbly, intermittent and dispersed flow. Their observations did agree somewhat with latest flow regime map produced by Ulbrich & Mewes (1994) which is discussed below. They also found that the void fraction existing inside the bundle was

not necessarily the same as that near the walls, which suggested that the observed flow regimes could differ from the bulk flow in wider test sections.

Since most of the initial two-phase flow regime studies were in support of the oil and gas and power generation industries, most flow regime maps were developed for internal pipe flows, both horizontal and vertical. One notable example is the study of Taitel *et al.* (1980), who developed a pseudo-analytical model for predicting flow regime transition in vertical pipe flows based upon the physical mechanisms associated with each transition. This has been adopted by some researchers for shell-side flows in heat exchangers in order to address the deficiency of the map by Grant (1976).

More recently however, Ulbrich & Mewes (1994) have developed a new flow regime map for vertical upward cross-flow though tube arrays, which was based upon the data of various researchers and their own air-water data. From their extensive analysis, they concluded that 3 significant flow regimes existed in shell side flow, namely bubbly, intermittent and dispersed flow, while classical slug flow was not generally observed. When compared with the observed flow regimes of all the compiled data, Ulbrich & Mewes claimed that the predictions of their map obtained a rate of agreement of 85% with existing data. This was much better than the previous two maps for predicting the flow regime of shell-side flows through tube arrays. The map is shown in Figure 6.3, where the solid lines correspond to Ulbrich & Mewes' predictions while, for comparison purposes, the dotted lines (and the labels in brackets) correspond to that of Taitel *et al.* for R-11 flow. Ulbrich & Mewes used the superfical liquid and gas velocities, U_{LS}, U_{GS}, defined in Equation (6.2), as coordinates for the map, which they argued were the most natural. The present author's flow regime observations are also plotted on this figure and the agreement is fairly plausible given the subjectiveness in the identification method. In Figures 6.4(a) and (b), data of various researchers is superimposed on the map of Ulbrich & Mewes. The data in both figures corresponds to the threshold flow velocities for the onset of fluidelastic instability, and it shows that most of the data sets cross over from the bubbly to the intermittent flow regime. In Figure 6.4(a), the plotted data points corresponds to single component flow of R-11, R-22 and steam-water in a parallel tube array. In Figure 6.4(b), the data points corresponds to two-component flow of air-water for various array types and two different P/D ratios. It will be shown in chapter 8 that the transition from bubbly to intermittent flow regimes coincide with a

significant reduction in critical flow velocity at the threshold of fluidelastic instability, regardless of the differences in fluid type, or array geometry.

This analysis has shown that the Grant flow regime map is not useful for delineating the different flow regimes encountered in this research and that of others. However, the map of Ulbrich & Mewes has shown plausible applicability to the present author's data and therefore will be used as a flow regime indicator for the analyses in the remaining chapters.

A simple flow regime analysis was performed for the Pickering A steam generator based upon information supplied by AECL which can be found in Appendix D. The results of two different analyses are presented in Figure 6.5. In one case, indicated by the solid symbol, it was assumed that the steam-water exited the top of the U-bend region uniformly at a flow quality of 0.125, and a mass flow rate of 67.9 kg/s, or a pitch mass flux of 250 kg/m^{2}s based upon an estimated inner shell diameter of 1.55 m, a pitch ratio of 1.5 and outer tube diameter of 12.7 mm. The phase densities were estimated to be, ρ_G = 20.1 kg/m^3, ρ_L = 800 kg/m^3 base upon an operating pressure of 4.1 MPa (absolute).

In the second case, a simplified non-uniform flow model was assumed for the steam generator, whereby the flow was assumed to exit up through the top of the U-bend region, but only over the hot leg portion, while recirculating (downward) liquid flow was assumed to occur over the cold leg portion. Thus the flow area was halved for the second analysis. Also, the flow quality was treated as a variable and is indicated by the open symbols plotted in Figure 6.5. The superficial gas velocity was a constant because it was fixed according to the steam generation rate of the boiler. The superficial liquid phase velocity varied according to the specified quality at the U-tube exit and it was calculated using a slip ratio model which is introduced in the following chapter. In either case, this analysis suggests that the flow regime for the Pickering "A" boilers is either bubbly or dispersed flows, while the intermittent flow regime seems to be avoided. However, in order to improve the prediction, a more complete thermal-hydraulic analysis of the steam generator is needed to determine a detailed three dimensional flow distribution in the U-bend region. Such an analysis has been performed by Jo and Shin (1999) who showed that the exiting two-phase flow was indeed biassed towards the hot leg, while recirculating flow occurred on the cold leg side as shown in Figure D6 of Appendix D.

NOTE TO USERS

Page(s) not included in the original manuscript are unavailable from the author or university. The manuscript was microfilmed as received.

94

This reproduction is the best copy available.

UMI

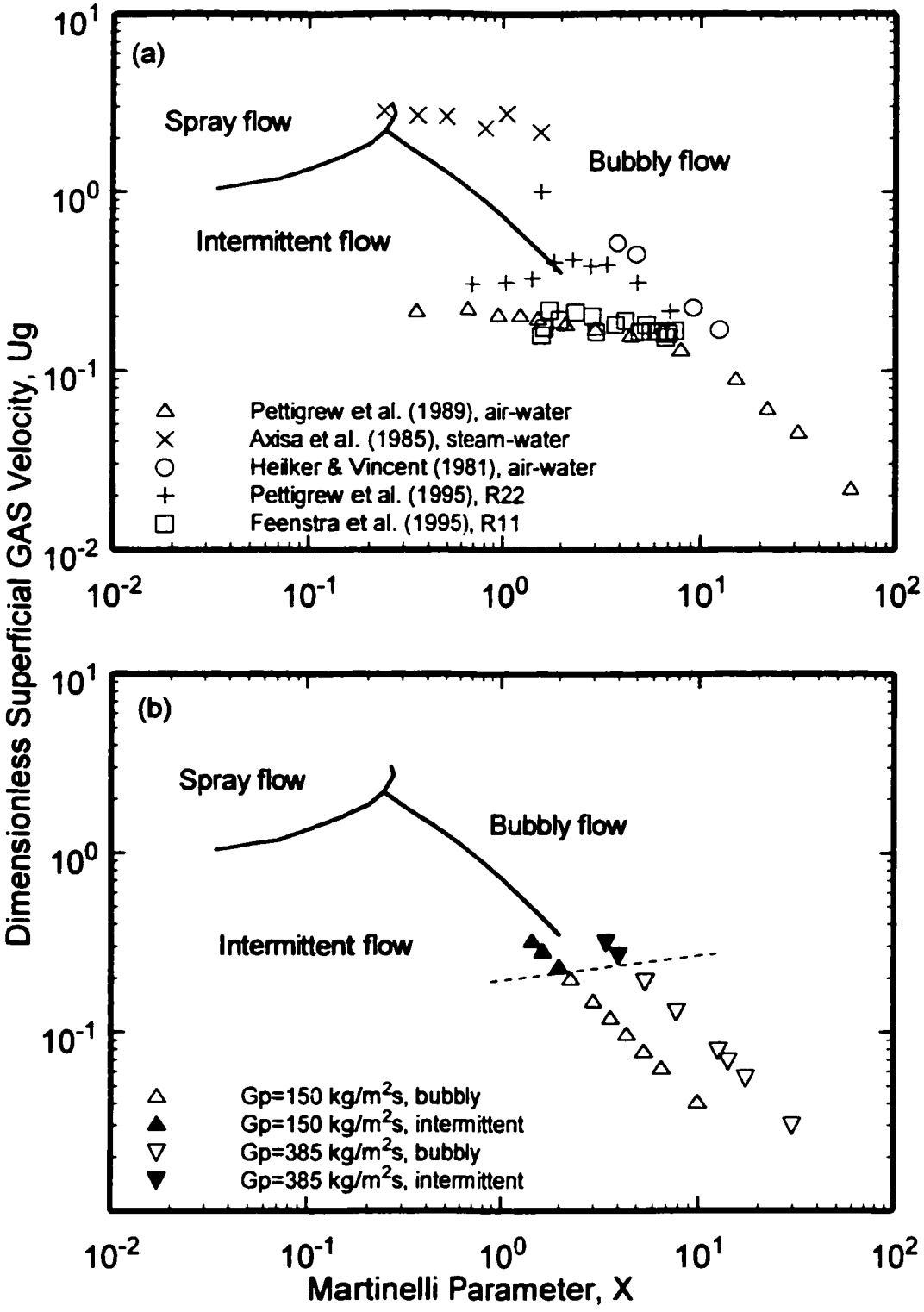

Figure 6.2 Flow regime map developed by Grant (1976) for two-phase vertical cross-flow through an in-line tube array. (a) Superimposed data of threshold flow conditions for fluidelastic instability of various researchers, (b) superimposed flow regime observations of the present author.

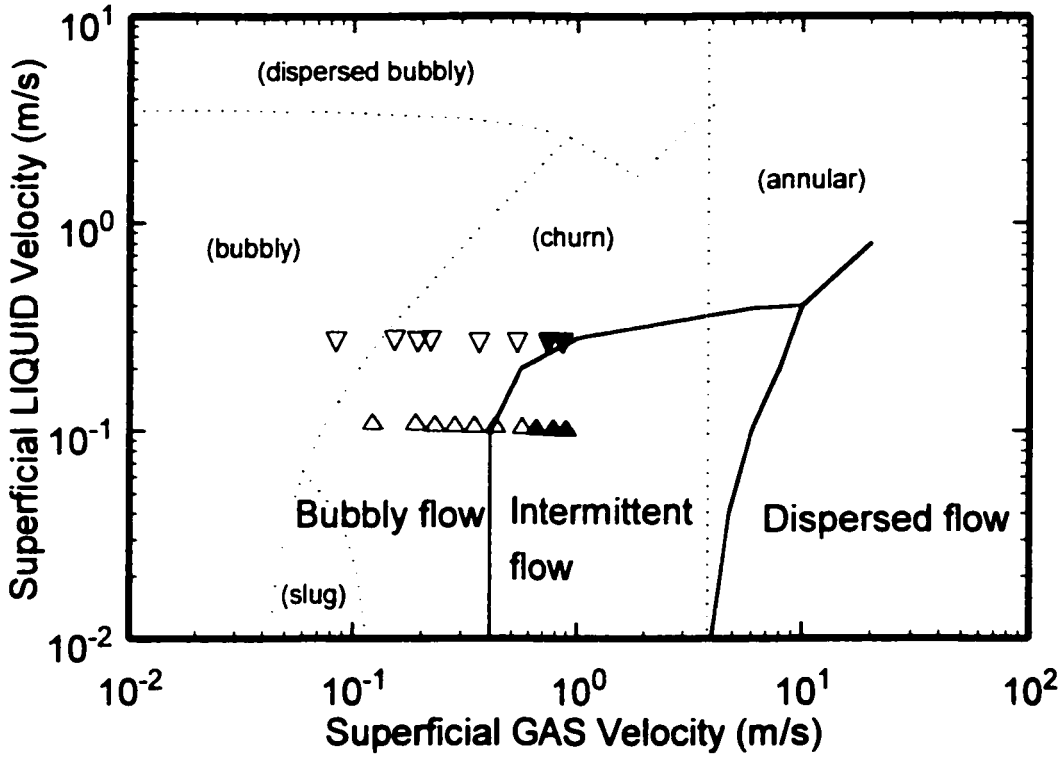

Figure 6.3 Flow regime map developed by Ulbrich and Mewes (1994) for two-phase vertical cross-flow through an in-line tube array. Data points correspond to flow regime observations of the present study for low pitch mass flux, G_p = 150 kg/m^{2}s: △ bubbly flow, ▲ intermittent flow; and for high pitch mass flux, G_p = 385 kg/m^{2}s: ▽ bubbly flow, ▼ intermittent flow. Note that dotted lines correspond to predictions of Taitel *et al.* (1980).

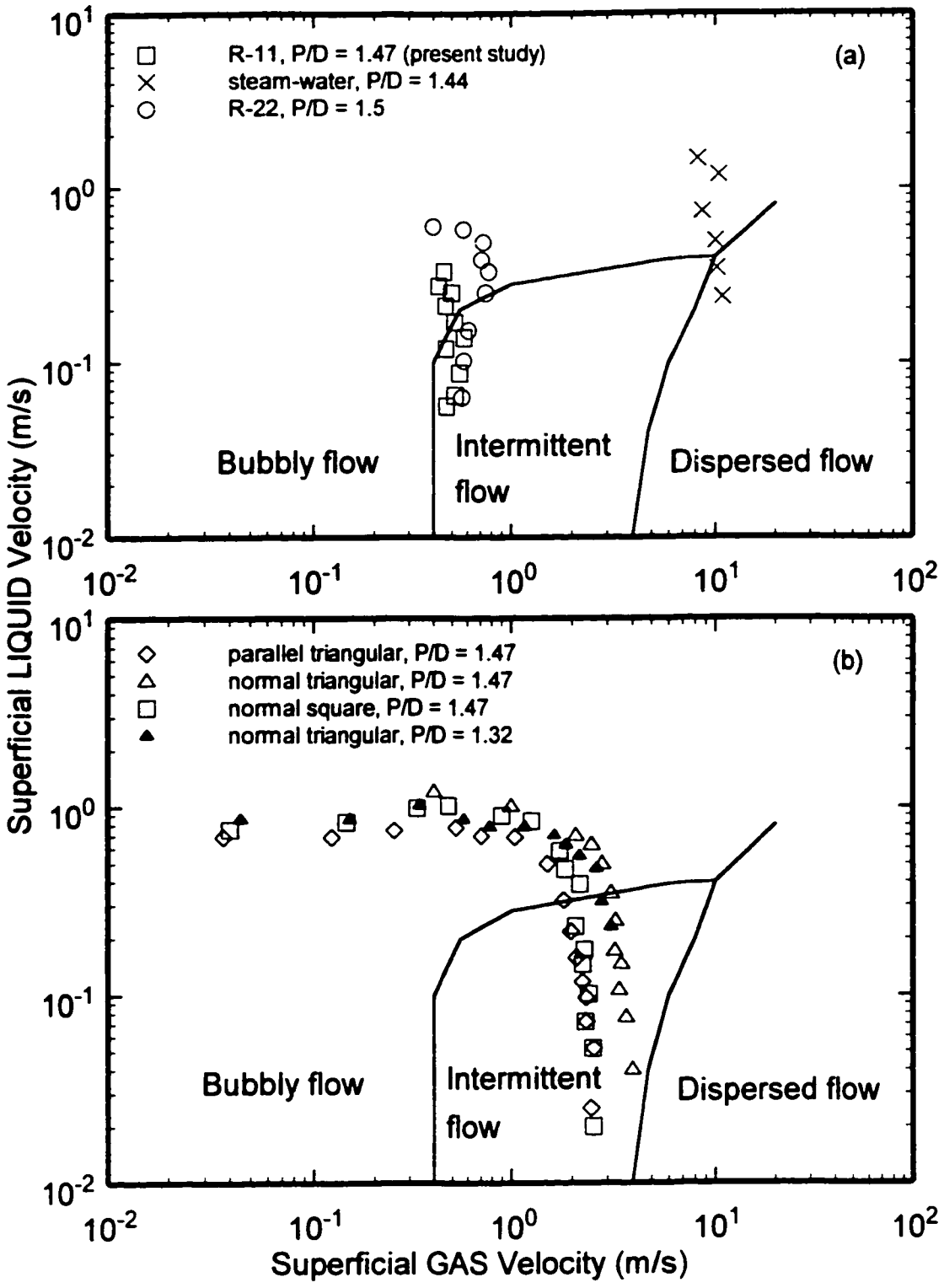

Figure 6.4 Flow regime map developed by Ulbrich and Mewes (1994). (a) Fluidelastic threshold data of, ▫ present study; × Axisa *et al.* (1985); ○ Pettigrew *et al.* (1995). (b) Fluidelastic threshold data of air-water study of Pettigrew *et al.* (1989).

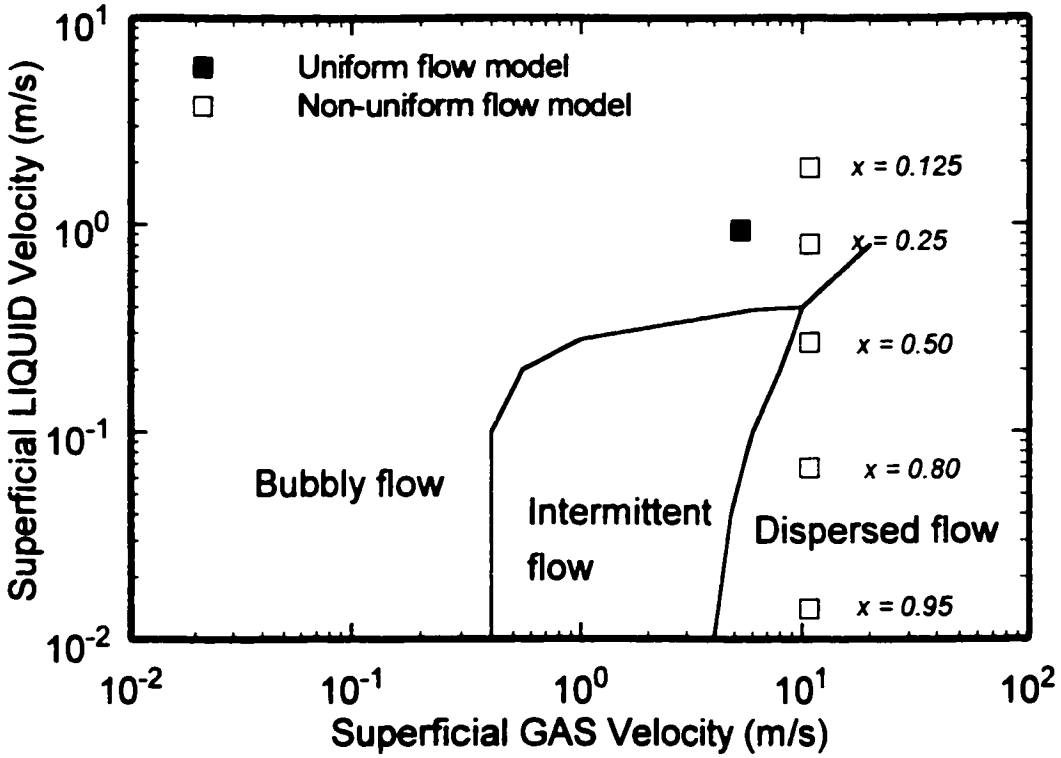

Figure 6.5 Flow regime map developed by Ulbrich & Mewes (1994). Operating data of Pickering A type steam generator of the CANDU nuclear power plant. ■ Uniform flow model, □ non-uniform flow model with flow quality , x, at the U-tube region as a variable.

Chapter 7

Void Fraction Modelling

Introduction

This chapter presents a new model for predicting the void fraction for upward cross-flow through horizontal tube bundles, that was developed from the work of this study. The need for this model arose because several previous researchers who studied fluidelastic instability in two-phase cross-flow did not have the means to measure the void fraction. In those studies, the homogeneous equilibrium model (HEM) was utilized to determine the average fluid density and flow velocity of the two-phase flow. However, the void fraction measurements obtained in this study using the gamma densitometer were significantly different from those predicted by the HEM. Since the fluidelastic instability data obtained from this work was to be compared with previous research works, it was desirable to make the comparison on the basis of both the HEM and upon a more realistic two-phase flow model. The recent availability of void fraction measurement data from this study and from other researchers made it possible to develop this new void fraction model, which could be applied to previous studies of two-phase fluidelastic instability to obtain a better estimate of the actual void fraction.

The new void fraction model agrees well with experimental void fraction measurements obtained in R-11 and in air-water mixtures for a sufficiently wide range of pitch mass flux, quality and P/D ratios. It has also shown improved predictive capability for adiabatic air-water and diabatic R-113 cross-flows than the void fraction models developed by other researchers. The analysis performed also shows plausible applicability of the void fraction model to steam-water data. The new void fraction model will allow researchers and designers to obtain better estimates of void fraction in the shell side flow in applications such as kettle reboilers and the U-bend region of nuclear steam generators than with the customarily used HEM. This will result in better estimates of average fluid density and average velocity of two-phase upward cross-flow through horizontal tube bundles.

7.1 Review of Void Fraction Modelling

Two-phase vapour-liquid flow exists in many shell and tube heat exchangers such as kettle reboilers and steam generators. The flow in these devices depends upon a balance between the driving hydrostatic head and the frictional and accelerational pressure drops. These components of pressure drop need to be known in order to model the thermo-hydraulic performance of these devices because a complex interaction exists between the heat transfer coefficient and the average flow velocity across the tubes. Void fraction is needed in order to calculate the hydrostatic and accelerational pressure drop of the flow, because it determines important flow parameters such as average fluid density and average flow velocity at a particular location in the bundle. Accurately determining the average density and effective flow velocity of two-phase flows is difficult because it depends upon the velocity ratio, S, which is defined as the ratio of gas to liquid phase velocity, $S = U_G/U_L$. These parameters are also needed for flow-induced vibration analyses for predicting fluid forces and the fluidelastic instability threshold of a tube array subjected to two-phase flows.

Several authors such as Palen and Yang (1983), Fair and Klip (1983) and Payvar (1983) have presented circulation boiling models to predict the thermo-hydraulic performance of shell and tube boilers, but the lack of a suitable void fraction model led them to use correlations that were originally developed for internal pipe flows. Others researchers such as Whalley and Butterworth (1983) and Leong and Cornwall (1979) used the HEM to predict void fraction, but this model neglects the effect of velocity ratio altogether. The applicability of these models to shell-side cross-flow in a tube bundle seems difficult to justify.

In recent years, a few articles have been published on the prediction of void fraction in vertical upward flow through tube bundles. Kondo and Nakajima (1980) made indirect void fraction measurements in vertical cross-flow in a bundle but their experiments were performed at very low flow rates ($G_p < 5$ kg/m^{2}s). Schrage *et al.* (1988) made void fraction measurements in an in-line bundle with air-water cross-flow using quick-closing plate valves. They found that void fraction varied with mass flux and was greatly over predicted by the HEM model. Therefore, they developed an empirical void fraction model but did not test it against other data. More recently, Dowlati (1992) and Dowlati

et al. (1990, 1992) measured void fraction using a gamma densitometer in air-water cross-flow experiments in horizontal tube bundles of normal square and normal triangular patterns with pitch-over-diameter (P/D) ratios of 1.3 and 1.75. They found that the HEM significantly over-predicted the void fraction when compared with their gamma densitometer measurements. They developed a model to predict void fraction that was based upon the dimensionless superficial gas velocity, j_G^*, which they argued was an appropriate scaling parameter for vertical upward two-phase flows. Their model agreed well with their own void fraction measurements but was not thoroughly tested due to lack of other appropriate data.

A proper model for predicting void fraction should be applicable to almost any fluid, and preferably should not depend upon a fitting of coefficients specific to only one fluid. Since the literature has recently expanded to include compilations of data in more than one fluid, an attempt was made to develop a model which is physically based and would give predictions to almost any fluid and would not require the fitting of coefficients for different fluids. This chapter presents this new void fraction model for upward two-phase cross-flow in horizontal tube arrays. The functional form of the model is physically based and is given specific form using the present author's measurements in R-11 flow. The model is then used to compute void fraction as a function of quality and mass flux for comparison with other data in the literature.

7.2 Void Fraction Model Development

Assessment of Previous Void Fraction Models: The development of the present void fraction model arose from the need to compare the present author's flow-induced vibration data in R-11 cross-flows to other researcher's data, most of which were obtained with air-water mixtures that were supposed to simulate the steam-water mixture in the U-bend region of a nuclear steam generator. Most of the previous researchers did not employ any means of measuring void fraction, and hence they relied on the HEM to determine average fluid density and flow velocity of the two-phase cross-flow. However, a proper determination of these quantities requires an appropriate, generally applicable two-phase void fraction model to account for the velocity ratio of the phases. Then a better comparison of the various data sets can be made to determine the threshold flow velocities for fluidelastic instability of tube

arrays in cross-flow. Figure 7.1 displays the present author's void fraction measurements in R-11 flow along with various void fraction models for three separate mass flux values. The plotted data points (ie., □, △,○), which were obtained from void fraction measurements using a gamma densitometer, correspond to three different series of experiments, the details of which were explained in chapter 5. The various lines in Figure 7.1 are the predictions of Schrage *et al.* (1988), the void fraction model developed for air-water by Dowlati *et al.* (1992), the well known Drift Flux model and the HEM. The details of the other void fraction models are summarized in Appendix B. The HEM is an inaccurate predictor since it assumes a velocity ratio of unity. Consequently, the HEM represents a logical upper bound, and no data should plot above this curve because this would imply that the liquid phase was flowing faster than the gas phase. Though the void fraction model of Dowlati *et al.* (1992) appears reasonable at low mass flux, it was rejected because it violates this criteria at higher mass flux. The drift flux model was also rejected because it did not accurately agree with the R-11 data. Schrage's model appears to be superior to the others for the R-11 data, but this empirical model was considered inadequate because it compared poorly with air-water data of other researchers. Hence there was a need to develop a physically based model for predicting void fraction in two-phase cross-flows in tube arrays which would be applicable to any fluid and would require input parameters that were easily obtainable.

Theoretical Development of Void Fraction Model: The model development began with the relationship between void fraction, α, and flow quality, x, which is derived from a linear combination of the continuity equation for each phase as follows,

$$\textit{Void Fraction:}\quad \alpha = \left(1 + S\frac{\rho_G}{\rho_L}\left(\frac{1}{x} - 1\right)\right)^{-1} . \tag{7.1}$$

Velocity ratio, S, is the ratio of gas velocity to liquid velocity (U_G / U_L) and is the primary unknown in equation (7.1) since quality, x, and gas and liquid phase densities, ρ_G, ρ_L, are usually easy to determine. It was thought prudent to pursue a model to determine velocity ratio rather than void fraction (as in Schrage's model) or gas velocity (as in the drift flux model) because then equation (7.1) would automatically obey the boundary conditions at 0% and 100% quality.

The problem was to identify the important variables that affected velocity ratio and to form dimensionless groups that were appropriate to the development of the model. It was clear that the buoyancy of the gas phase was the driving force behind the velocity ratio, without which it would be close to unity. Hence, density difference, $\Delta\rho$, and average two-phase density, ρ, are considered to be key parameters. The viscosity of the liquid phase, η_L, was selected since it affects the ability of the gas bubbles to rise through the liquid. Surface tension, σ, was selected since it affects bubble size and shape. Previous experience showed that the gas phase velocity increased as the bubble size increased, owing to increased buoyancy of a larger gas bubble. The gap between the tubes, a, was chosen as the characteristic dimension since this is the space through which the flow must pass. Note that this is contrary to some other models which use tube diameter as the characteristic length dimension. The tube diameter, D, and pitch, P, were thought to play a role in velocity ratio, since they influence the frictional pressure drop through the array. The air-water data of Dowlati (1992) and Noghrehkar (1996) has shown that velocity ratio is generally greater for in-line arrays (ie., normal square) than for staggered arrays (ie., normal triangular). This indicates that the array geometry also affects the velocity ratio in cross-flow, which is likely the result of the different frictional pressure drop, Δp, between these array types. Equation (7.2) expresses the functional dependency of velocity ratio on the previously mentioned variables.

$$S = \frac{U_G}{U_L} = f\,[\Delta\rho,\ \rho,\ V_p,\ \eta_L,\ \sigma,\ g,\ a,\ P,\ D,\ \Delta p]\ . \qquad \textbf{(7.2)}$$

The pitch flow velocity, V_p, is introduced here although it is understood that in two-phase flow it does not have a precise meaning unless some fluid model is assumed. However, it is retained here for clarity of expressing the dimensionless numbers that follow, while in the final form of the model it is eliminated in favour of other more appropriate quantities. Application of the Buckingham pi theorem permitted reducing the number of variables in equation (7.2) into a smaller number of dimensionless groups which is equal to the number of parameters minus the number of fundamental variables: mass, length and time. Thus, using the gap, a, as the basic length scale,

$$S = f\left[\left(\frac{g\,a}{V_p^2}\right)^a, \left(\frac{\rho\,V_p^2\,a}{\sigma}\right)^b, \left(\frac{V_p\,a}{\rho\,\eta_L}\right)^c, \left(\frac{\Delta p}{\rho\,V_p^2}\right)^d, \left(\frac{\Delta\rho}{\rho}\right)^e, \left(\frac{P}{a}\right)^f, \left(\frac{D}{a}\right)^g\right]. \qquad (7.3)$$

The first four dimensionless groups are the Froude, *Fr*, Weber, *We*, Reynolds, *Re*, and Euler, *Eu*, Numbers. The number of variables can be further reduced by combining two or more groups to form a new variable, which is also dimensionless. This also eliminates some of the repetition in the force scale ratios, since for example Reynolds number and Weber number both involve an inertial force scale. The ratio of these two numbers results in the Capillary number,

$$\textit{Capillary No.} = \frac{We}{Re} = \frac{\eta_L V_p}{\sigma} \left(\frac{\textit{viscous force}}{\textit{surface tension force}}\right). \qquad (7.4)$$

Combining Froude number with density ratio results in the Richardson number,

$$\textit{Richardson No.} = \frac{\Delta\rho\,g\,a}{\rho\,V_p^2} \left(\frac{\textit{bouyancy force}}{\textit{inertial force}}\right). \qquad (7.5)$$

The length scale ratios *P/a* and *D/a* can be combined to eliminate *a* to give *P/D*, the so-called pitch ratio, which is commonly used to define tube array geometry. Using these combined forms of the dimensionless groups gives,

$$S = f\left[\left(\frac{\Delta\rho\,g\,a}{\rho\,V_p^2}\right)^a, \left(\frac{\eta_L V_p}{\sigma}\right)^b, \left(\frac{\Delta p}{\rho\,V_p^2}\right)^c, (P/D)^d\right]. \qquad (7.6)$$

Having established possible forms of the relevant dimensionless parameters, the problem became one of determining the precise relationship for velocity ratio and the exponents on the individual dimensionless groups. However, the appropriate representation of parameters such as pitch velocity, V_p, and density, ρ, were not known. Should they represent the individual liquid or gas phase values (ie., ρ_L or ρ_G) or perhaps the average value interpolated with void fraction (ie., $\rho = \alpha\rho_G + (1-\alpha)\rho_L$)? The

appropriate representations were subsequently determined by trial and error, as various forms of equation (7.6) were compared with the void fraction data from the present authors' experiments in R-11 cross-flow.

After testing many correlations, the following form proved to fit the R-11 data well,

$$\textit{Velocity Ratio } (U_G/U_L): \qquad S = 1 + 25.7\,(Ri * Cap)^{0.5}\,(P/D)^{-1} \; . \tag{7.7}$$

In this model, the Richardson number, Ri, has the following form,

$$Ri = \Delta\rho^2\, g\, a / G_p^2 \; . \tag{7.8}$$

Note that this form differs slightly from the more general form given by equation (7.5) in that the pitch velocity, V_p, has been replaced by the pitch mass flux divided by the average fluid density, G_p/ρ. With this substitution, the numerator would have contained a product of average density times phase density difference, $\rho\Delta\rho$, ($\Delta\rho = \rho_L - \rho_G$) but this has been replaced with density difference squared, $\Delta\rho^2$, which gave better agreement with data. This is equivalent to combining Froude number, ga/V_p^2, with the ratio of phase density difference to average density, squared, $(\Delta\rho/\rho)^2$. The capillary number, Cap, in the equation (7.7) has the following form,

$$Cap = \eta_L U_G / \sigma \; . \tag{7.9}$$

The capillary number requires knowledge of the surface tension, σ, and absolute viscosity of the liquid phase, η_L, both of which are readily determined from fluid property tables. To obtain better agreement with the experimental data, the gas phase velocity, U_G, has been used instead of the pitch velocity, V_p, and is determined as follows,

$$U_G = \frac{x\, G_p}{\alpha\, \rho_G} \; . \tag{7.10}$$

Equation (7.10) can be derived from continuity of the gas and liquid phases, assuming both phases are moving in the same direction. The gas phase velocity, U_G, requires a known value of void fraction, α,

that depends upon the velocity ratio. Hence, calculating capillary number is an iterative process whereby the velocity ratio is calculated starting from an assumed value and iterated until the assumed and calculated values agree to within a desired degree of precision, in this case about 0.5%.

Though the Euler number was proposed in the functional relationship given by equation (7.3) and (7.6), it is noticeably absent from the model given by equation (7.7) because, presently, there is insufficient frictional pressure drop data pertaining to the various bundle geometries in various two-phase fluids to determine precisely how it affects the velocity ratio. The frictional pressure drop data obtained by Dowlati (1992) showed unusual trends with respect to array geometry and P/D ratios, which they were unable to explain. Hence it was thought best to exclude Euler number from the proposed model for now until further data could reveal clearer trends.

Before concluding this section, some mention should be made regarding flow regime since it is usually an important factor in any two-phase flow study. Most flow regime analyses have focused on internal pipe flow for vertical and horizontal orientations. There have only been a few studies concerned with shell side cross-flow in tube arrays, notably Grant and Chisholm (1979), Ulbrich and Mewes (1994) and Noghrehkar (1996). Ulbrich and Mewes proposed a new flow regime map, which they claimed had an 85% rate of agreement with existing data. This was much better than any previous map for shell-side flows through tube arrays. Through analysis of their experimental data and those of various other researchers, they found that only 3 significant flow regimes existed in shell side flow, namely bubbly, intermittent and dispersed flow, while classical slug flow was not generally observed. Noghrehkar found that, by using a specially designed electrical resistivity probe, the flow regime inside the bundle is not necessarily the same as that observed from outside the bundle. In the present analysis, it was thought that a flow regime transition from bubbly to intermittent flow might be a factor affecting velocity ratio, and therefore it would require consideration in the model. Most of the void fraction data examined corresponds to the bubbly flow regimes while the remainder corresponds to the intermittent flow regime. It appears that the effect of flow regime on velocity ratio in tube bundles is not significant. However, there are still insufficient flow regime data, especially in intermittent and dispersed flow, to allow one to make any general conclusions regarding its effect on velocity ratio.

7.3 Comparison of Void Fraction Model to R-11 Data

Figure 7.2 demonstrates the comparison of the new void fraction model with the present authors measurements in R-11 cross-flow. This Figure is the same as Fig. 7.1 except that the models of other researchers are omitted, but the HEM is retained because it represents a logical upper bound to the data. Most of the data points correspond to bubbly flow except for a few at the highest levels of quality indicated in Fig. 7.2(c), where the onset of intermittent flow was observed for a few data points. The lack of measurements in the intermittent flow and dispersed flows for the R-11 data makes it impossible to assess any effects of flow regime on velocity ratio.

Clearly, the agreement between the new model and the R-11 void fraction data is very good. Some deviation is noted with certain data points, specifically the "M" series data indicated by the circles, at the lower qualities, which may be attributable to two factors. One factor is that these measurements were obtained prior to the flow-loop overhaul, in which an upstream turbulence generator was installed to provide better upstream flow conditioning and improvements were made to the vapour condenser to minimize subcooling of the liquid during heat removal. The other factor is that an unavoidably large uncertainty exists in the quality measured at low values as discussed in section 5.6 of chapter 5.

7.4 Comparison of Void Fraction Model with Other Data

Figure 7.3 and 7.4 show graphs of void fraction vs. quality for three different pitch mass fluxes for the air-water cross-flow data of Dowlati (1992) for P/D=1.3 and 1.75 respectively, obtained at atmospheric pressure conditions. It is clear that the new model follows the trends of the measured void fraction with respect to quality and pitch mass flux as well as or better than Dowlati's model and much better than the other three models. Of course, since this data was the basis for Dowlait's empirical model, it is expected that their model should fit the data reasonably well. Schrage's model is a clearly a poor fit to the data, which is puzzling because that model was developed under conditions very similar to Dowlati's data of Fig. 7.3. The Drift flux model generally over-predicts the void fraction data of Figs. 7.3 and 7.4 and overall it is inferior to the new void fraction model.

These figures reveal that the data corresponding to the normal triangular array show a higher void fraction than those of the square array. This may be the result of greater pressure drop in the triangular

array geometry, where the flow must follow a more arduous flow path than in the square array. The latter has straight flow lanes between tubes rows. At present, the new model does not account for this difference in behaviour but, as discussed previously, an additional model parameter which accounts for pressure drop, such as the Euler number, could be developed in future as more data becomes available.

It should be noted that Dowlati *et al.* (1992) reported a flow regime of dispersed bubbly and churn-turbulent bubbly flow for all their test conditions. According to Ulbrich and Mewes (1994), only three significant flow regimes exist in two-phase vertical cross-flow through a tube bundle: bubbly, intermittent and dispersed, where the transitions from one to the other generally coincides with increasing void fraction. It appears that Dowlati's data fell into the first category and that the intermittent and dispersed flow regimes were not encountered. Hence, his data does not lend any insight into the effect of flow regime on velocity ratio.

Figure 7.5 presents graphs of void fraction vs. quality for three different pitch mass fluxes for the air-water cross-flow data of Noghrehkar (1996) for P/D=1.47, obtained near atmospheric conditions. The new void fraction model agrees well with this data for the pitch mass flux of 500 kg/m^{2}s shown in Fig. 7.5(b). For the higher and lower mass fluxes, shown in Figs. 5(a) and (c), the fit is still good but the data appears to be more influenced by mass flux than the previous air-water data (ie., Figs. 7.3 and 7.4). It should be noted however, that these void fraction measurements were performed in the open area just downstream of the bundle, so exit effects may be a factor. These void fraction measurements also show a slight tendency for lower velocity ratio (higher void fraction) for the triangular array as opposed to the square array.

Noghrehkar (1996) observed two distinct flow regimes in his experiments, bubbly and intermittent flow, by using a specially designed electrical resistive probe. The transition lines distinguishing the bubbly from intermittent flows are indicated in Figs. 7.5(a), (b) and (c) as vertical lines, dashed for the square arrays and solid for the triangular arrays. An important observation to be made in these figures is that Noghrehkar's data shows an insignificant effect of flow regime on the velocity ratio, at least for the bubbly and intermittent flows, which suggests that the new model need not account for these two flow regimes.

Figure 7.6 shows the comparison of the present model with the cross-flow data of Schrage *et al.* (1988), which was obtained in air-water at atmospheric conditions using quick closing plate valves. The comparison of the present void fraction model with this set of experimental results is not as good as in the previous results, and there appears to be no obvious reason for the discrepancy. However, there is a large difference between the void fraction measurements in Schrage's study and those of Dowlati in Fig. 7.3, for which the present model agrees quite well. The discrepancy between these two researcher's data is puzzling because their experiments were very similar in nature, where the only obvious differences were the void fraction measurement method, the physical size of the test section and tube diameter (see Table 7.1 for a comparison). It is not clear how these differences could cause the void fraction results to differ so much between these to studies. Since Schrage's data shows some peculiar trends especially at high mass fluxes, it seems reasonable not to put too much significance to its lack of fit with the present model.

It should be noted that, initially, the present model was developed to correspond to the available void fraction data, most of which corresponds to adiabatic flow. Experiments in diabatic flow, with boiling or simulated void fraction generation on the tubes, are scarce (Gidi *et al.* 1997, Schrage *et al.* 1988, Hsu 1987, Dowlati *et al.* 1996), and the results are difficult to interpret due to the constantly changing flow quality in the tube bundle. A comparison of the boiling flow data of Dowlait *et al.* (1996) with the void fraction models is shown in Fig. 7.7. These researchers measured the void fraction of a vertical cross-flow of R-113 in a heated, in-line tube array with P/D = 1.3. The array consisted of 5 streamwise rows by 20 transverse rows of tubes with 12.7 mm outer diameter. Boiling of the R-113 occurred on the tube surfaces by means of heated oil which was pumped though all of the tubes. These authors noted that, similar to their adiabatic air-water experiments, mass flux and flow quality had a strong influence on void fraction. The design of their apparatus did not allow visual observation of the flow regime however. The comparison in Fig. 7.7 shows good agreement between the present model and the R-113 data over a wide range of pitch mass flux. In this case both Schrage's model and Dowlati's model agree reasonably well with the data. It is expected that Dowlati's model should fit the data well since the coefficients used in his model were selected from their paper, which was fitted to that data (ie., $C_1 = 10$ and $C_2 = 1$). It should be re-stated however, that a proper,

physically based void fraction model should be applicable to any fluid and preferably should not depend upon a fitting of coefficients that are specific to only one fluid.

In Figure 7.8, the predictions of the present void fraction model and the other models are compared for the case of steam-water cross-flow at conditions tested by Axisa *et al.* (1985) in their flow-induced vibrations experiments. While there were no void fraction measurements obtained in that study, the comparison demonstrates that the void fraction predictions of the new model are plausible because the model plots below the HEM curve and exhibits the expected trend with respect to pitch mass flux.

The present model will allow researchers and designers to obtain better estimates of void fraction in shell side vertical cross-flow in applications such as kettle reboilers and the U-bend region of nuclear steam generators than with the customarily used homogeneous equilibrium model. This will result in better estimates of average fluid density, average flow velocity.

The model does not account for differences in array geometry, even though some results in air-water mixtures show that the velocity ratio is higher (void fraction is lower) in normal square arrays and parallel triangular arrays as opposed to normal triangular arrays. This difference may be due to a greater frictional pressure drop in the latter array type, where the flow path is more arduous. At present, the model does not account for this observed difference in velocity ratio, and predictions are better for flows in square and parallel triangular arrays than for normal triangular arrays. In future, two-phase pressure drop data needs to be obtained to establish clear trends with respect to array geometry, void fraction and fluid type. Then, an additional parameter, such as the Euler number, could be introduced into the model to improve the agreement with the various array types.

Table 7.1 Summary of experimental conditions and tube array data.

Researcher	Array Type†	P/D	Tube Dia. (mm)	Array Size	Fluid(s), Temperature‡	Gas/Liquid Phase Densities, ρ_G/ρ_L (kg/m^3)
Present Study	PT	1.44	6.35	4x7	R-11, 40°C	9.65 / 1440
Dowlati *et al.* (1992a)	NS,NT	1.3	19.05	5x20	Air&Water, 25°C	1.4 / 997
Dowlati *et al.*(1992a)	NS,NT	1.75	12.7	5x20	Air&Water, 25°C	1.4 / 997
Noghrehkar (1996)	NS,NT	1.47	12.7	5x24	Air&Water, 22°C	1.5 / 997
Schrage *et al.* (1988)	NS	1.3	7.94	4x27	Air/Water, 10°C	2.2 / 1000
Dowlati *et al.* (1996)	NS	1.3	12.7	5×20	R-113, 55°C	9.36 / 1489
Axisa *et al.* (1985)	PT	1.44	19	11×11	Steam-water, 260°C	23.7 / 784

† PT = Parallel Triangular, NS = Normal Square (in-line), NT = Normal Triangular.
‡ Fluid temperatures are estimated for the air-water studies, all of which were performed near atmospheric conditions.

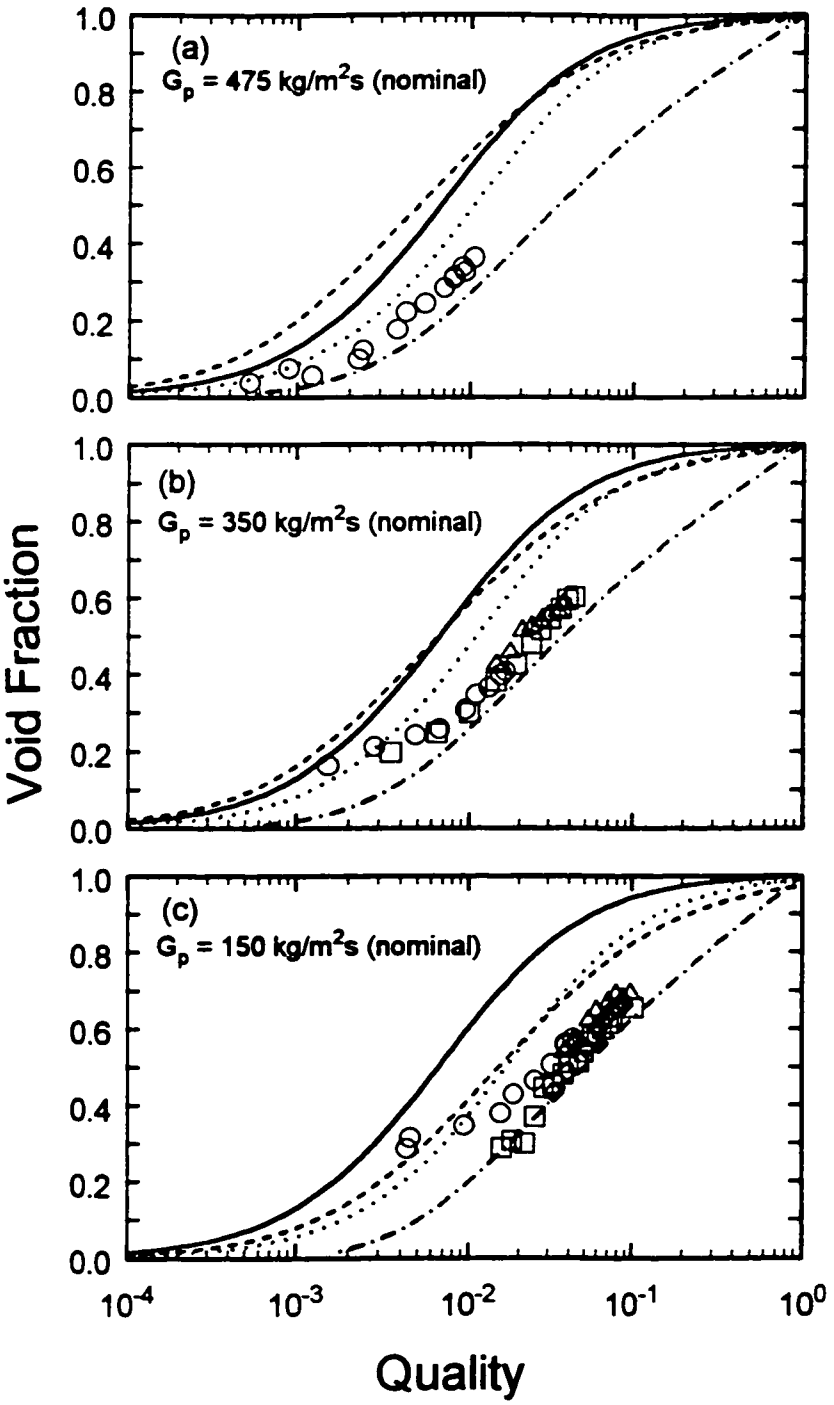

Figure 7.1 Void fraction vs. quality for present authors' R-11 data, P/D = 1.44. Comparison with existing slip models: ——— HEM; - - - - Dowlati *et al.* (1992); · · · · · Drift flux; -·-·-· Schrage *et al.* (1988). Experimental Data: ○ M series; □,◇ B series; △ C series.

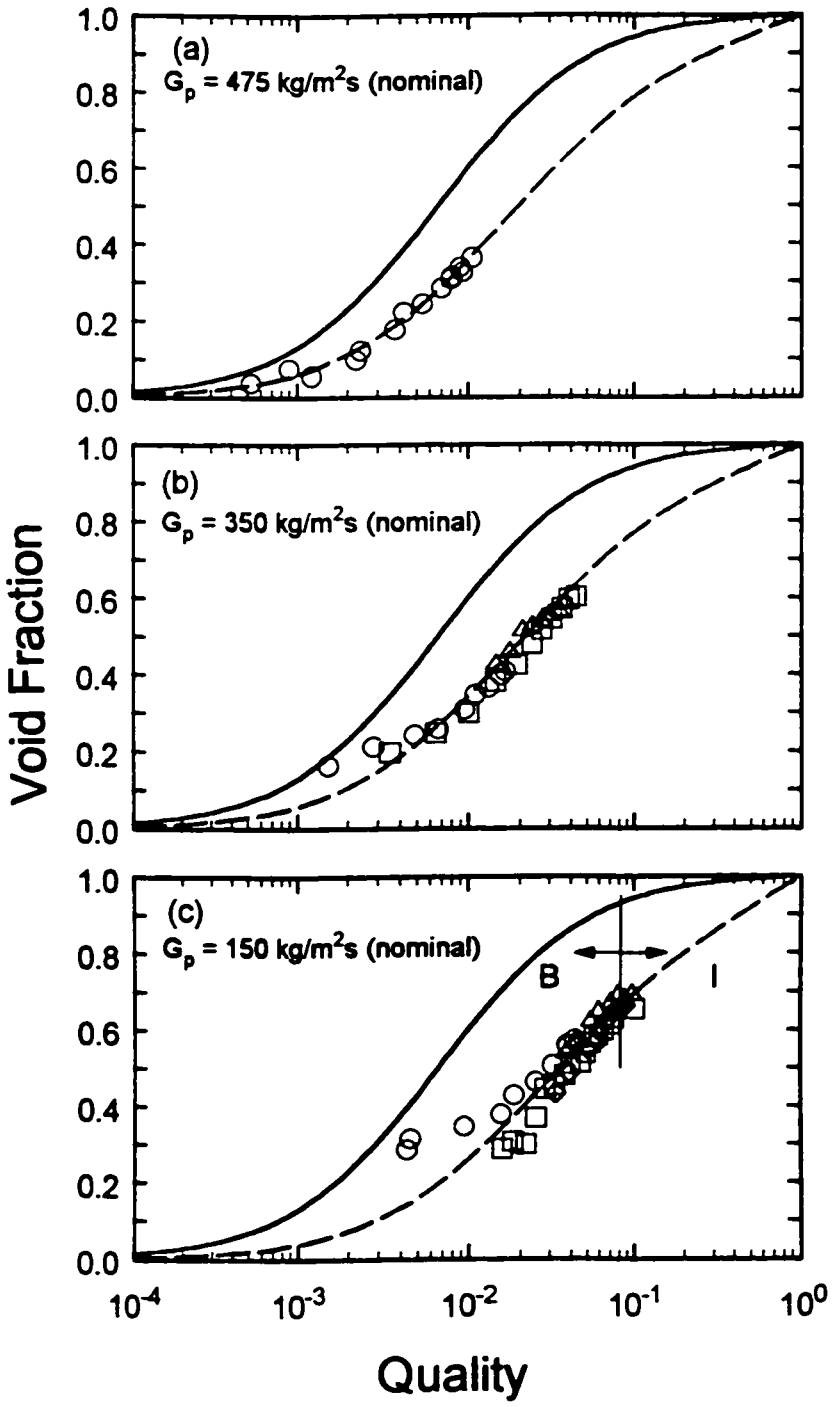

Figure 7.2 Void fraction vs. quality for R-11 data, P/D = 1.44. Comparison with proposed void fraction model. — — — proposed void fraction model; —— HEM. Experimental Data: O M series; □,◇ B series; Δ C series. Vertical line indicates a flow regime transition from Bubbly to Intermittent flow.

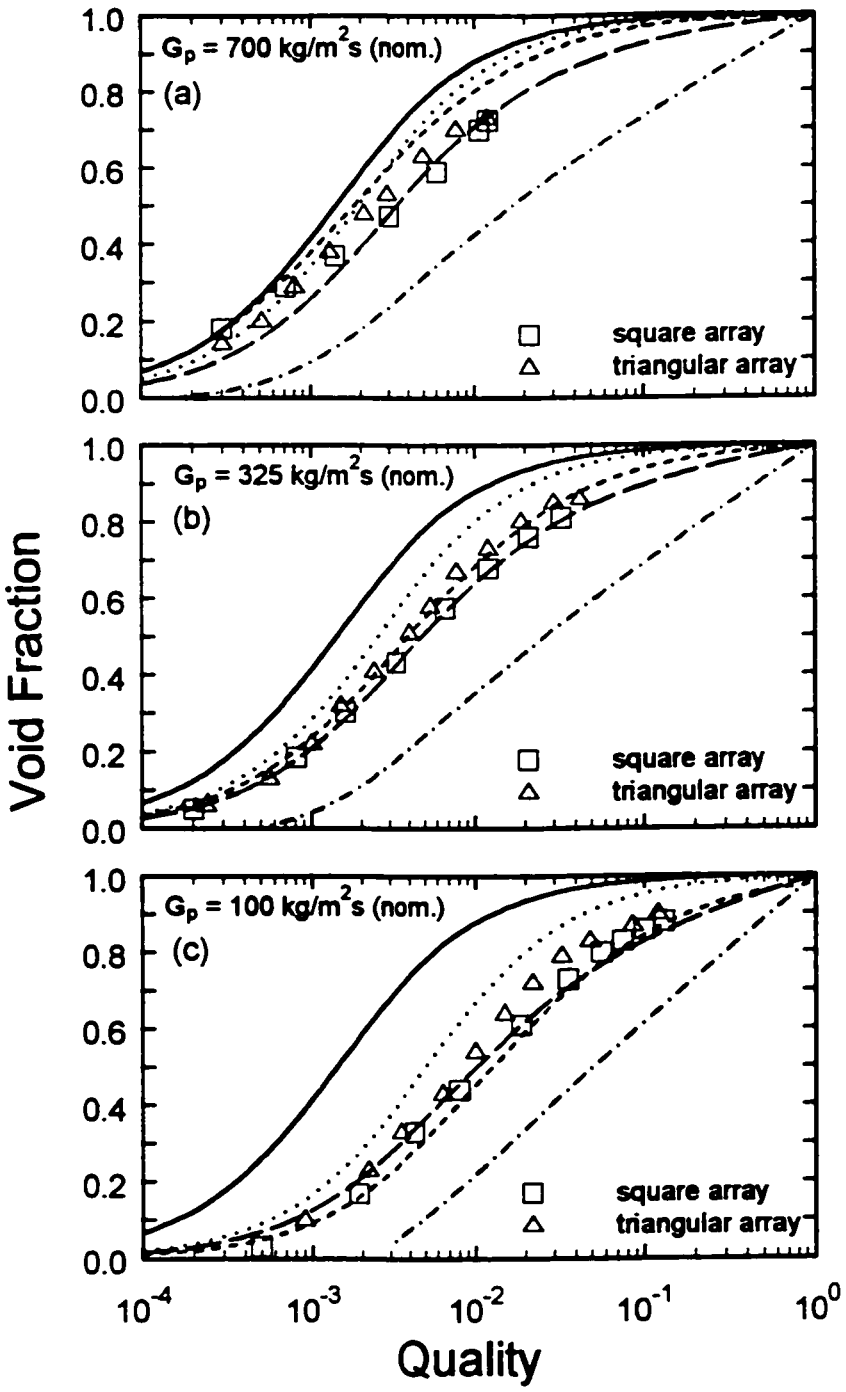

Figure7.3Void fraction vs. quality for air-water data of Dowlati *et al.* (1992), P/D = 1.3. Comparison with void fraction models: ——— HEM; - - - - Dowlati *et al.* (1992); · · · · Drift flux; -·-·-· Schrage *et al.* (1988); — — — proposed void fraction model. Experimental Data: □ square array; Δ triangular array.

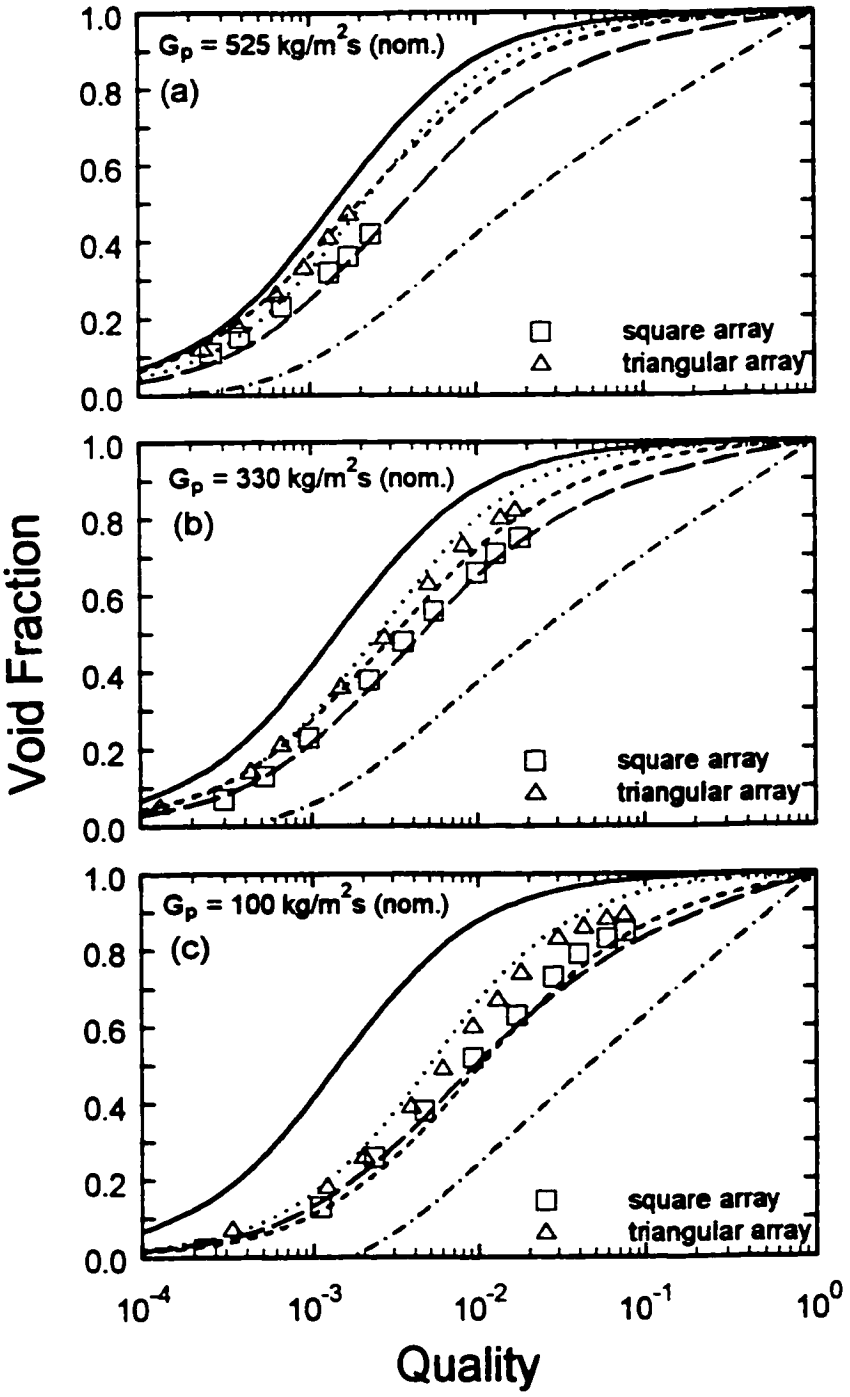

Figure 7.4 Void fraction vs. quality for air-water data of Dowlati *et al.* (1992), P/D = 1.75. Comparison with void fraction models: ——— HEM; - - - - Dowlati *et al.* (1992); · · · · Drift flux, -·-·-· Schrage *et al.* (1988); — — — proposed void fraction model. Experimental Data: □ square array; Δ triangular array.

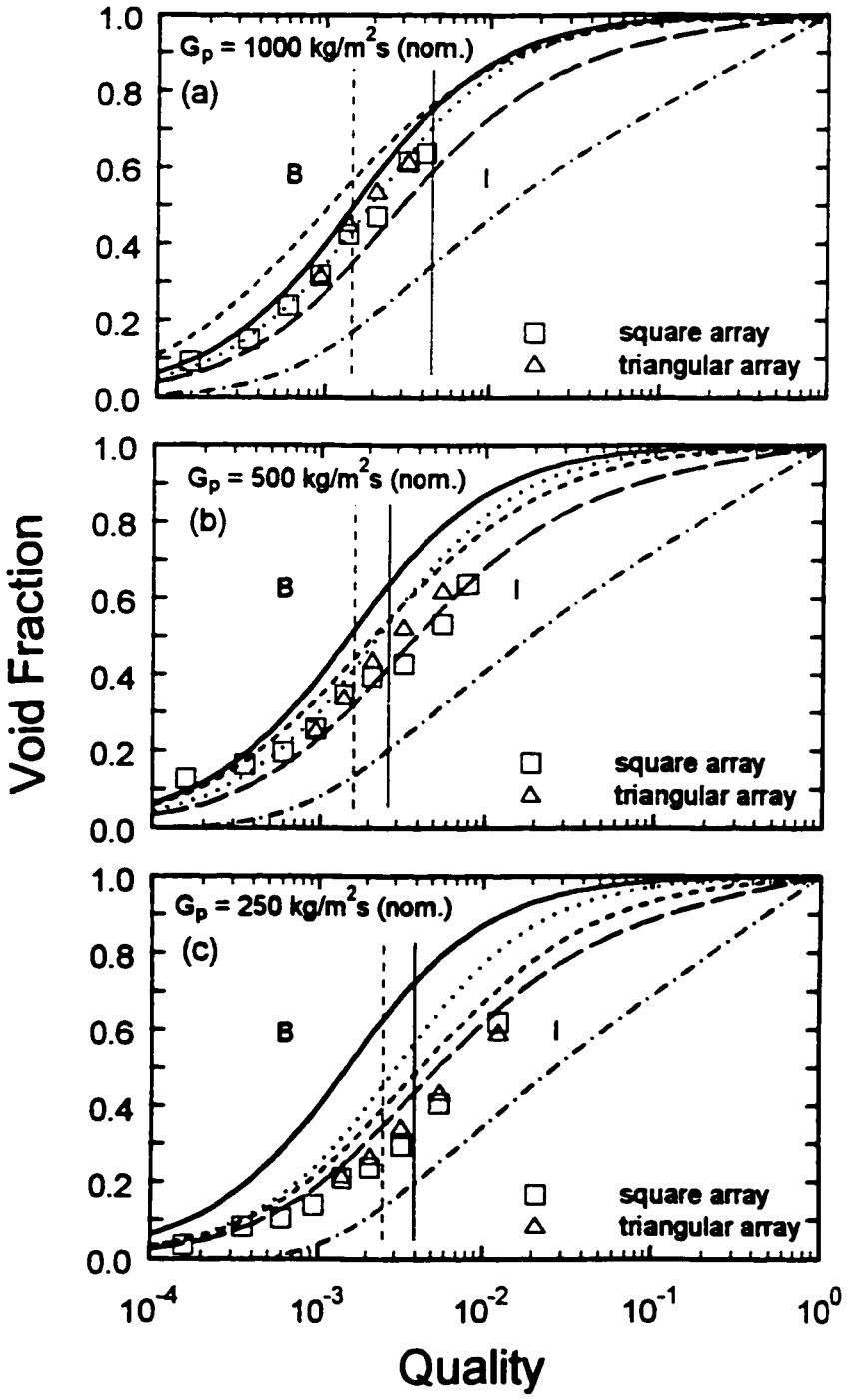

Figure 7.5 Void fraction vs. quality for air-water data of Noghrehkar (1996), P/D = 1.47. Comparison with void fraction models: ——— HEM; - - - - Dowlati *et al.* (1992); · · · · Drift flux; -·-·-· Schrage *et al.* (1988); — — — proposed void fraction model. Experimental Data: □ square array; Δ triangular array. Vertical lines indicate transition from Bubbly to Intermittent flow: solid line for triangular array, dashed line for square array.

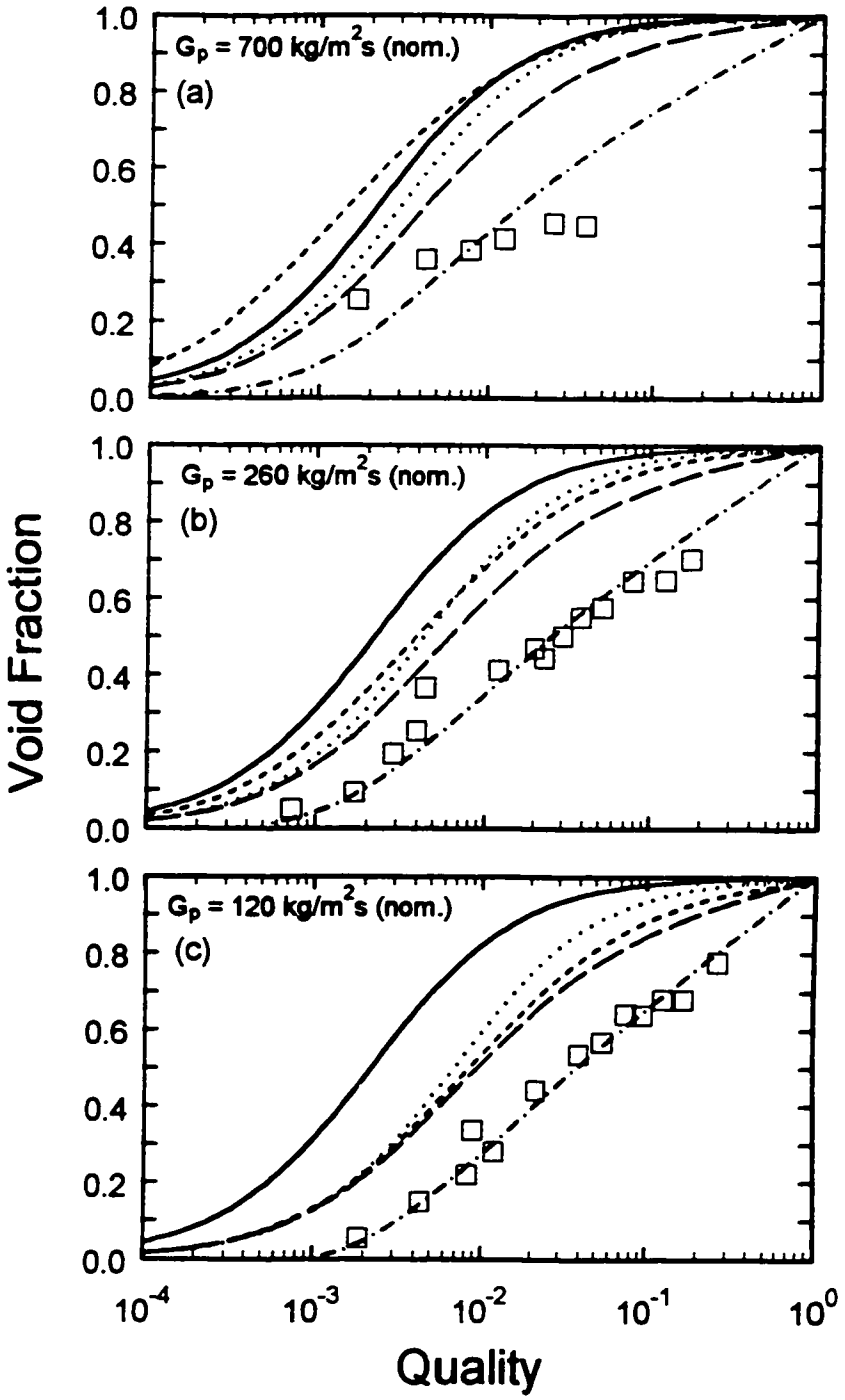

Figure 7.6 Void fraction vs. quality for air-water data of Schrage *et al.* (1988), P/D = 1.3. Comparison with void fraction models: ——— HEM; - - - - Dowlati *et al.* (1992); · · · · Drift flux; -·-·-· Schrage *et al.* (1988); — — — proposed void fraction model.

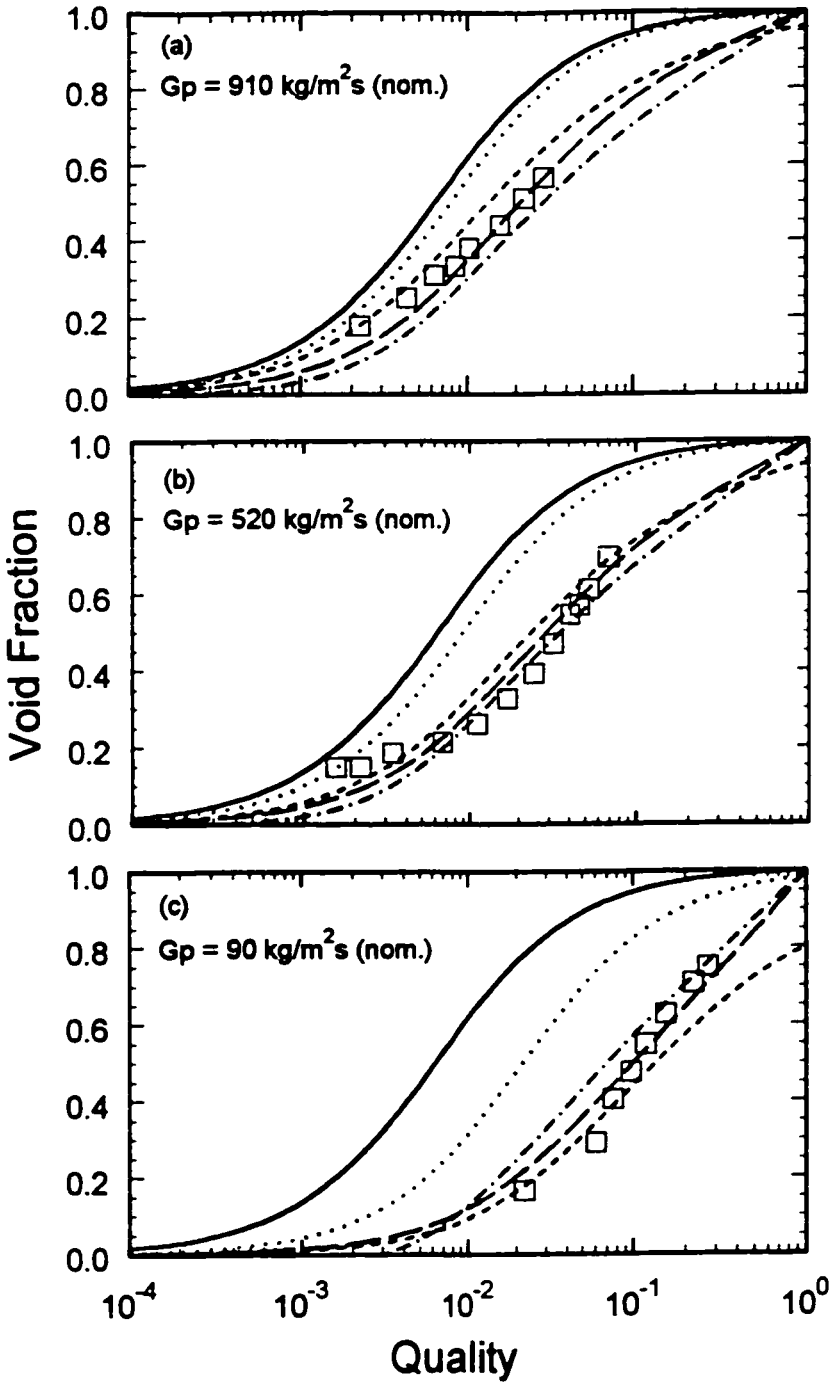

Figure 7.7 Void fraction vs. quality for diabatic R-113 data of Dowlati *et al.* (1996), P/D = 1.3. Comparison with void fraction models: ——— HEM; - - - - Dowlati *et al.* (1996); · · · · Drift flux; -·-·-· Schrage *et al.* (1988); — — — proposed void fraction model.

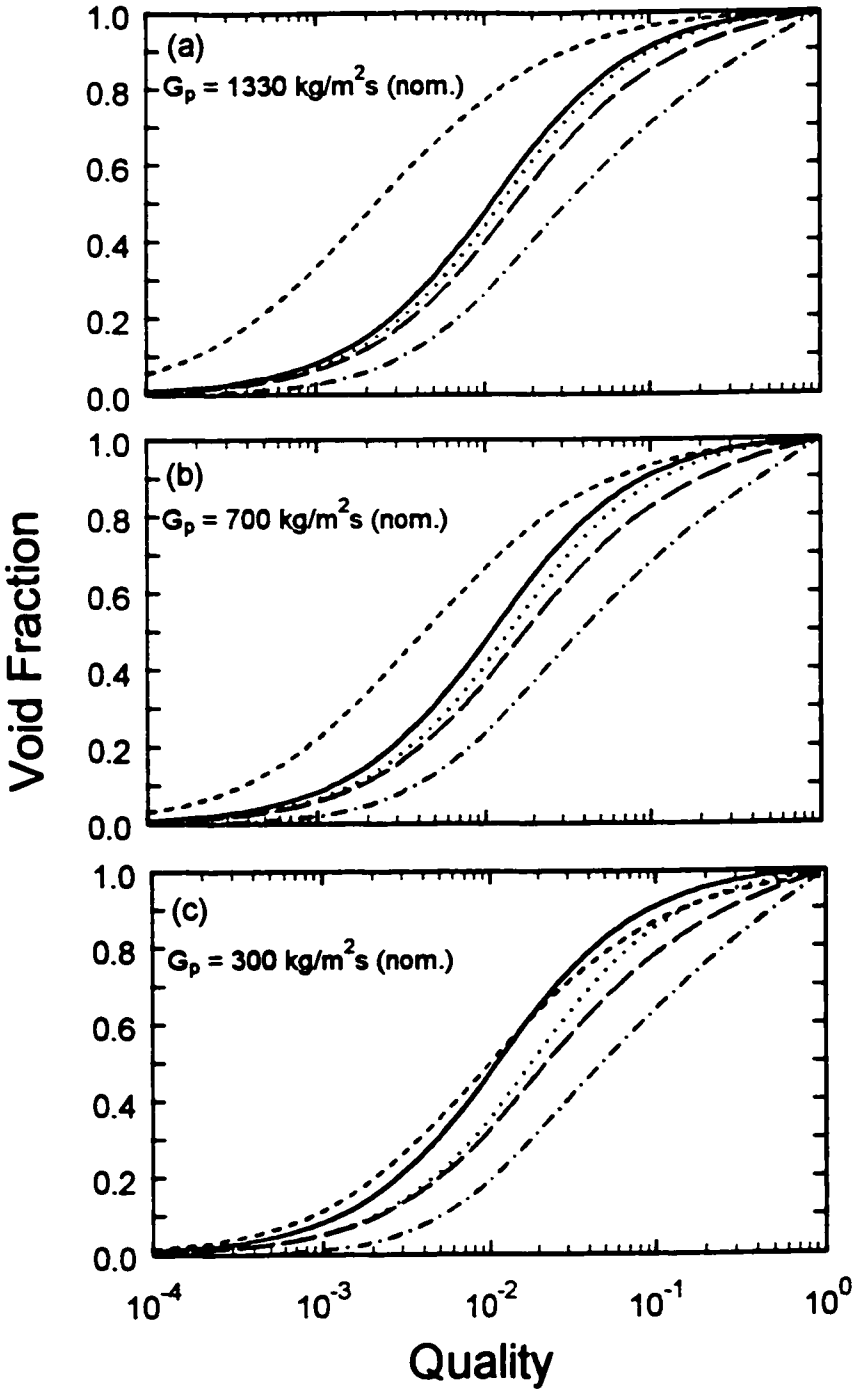

Figure 7.8 Void fraction vs. quality for steam-water at conditions tested by Axisa *et al.* (1985), P/D = 1.44. Comparison with void fraction models: ——— HEM; - - - - - Dowlati *et al.* (1992); · · · · · · Drift flux; -·-·-·- Schrage *et al.* (1988); — — — proposed void fraction model.

CHAPTER 8

Experimental Results for Fluidelastic Instability

Introduction

The experimental results for fluidelastic instability of the model tube array are the focus of this chapter. The main aim of these experiments was to determine the critical flow velocity for the onset of self-excited vibrations for both single-phase (liquid) flow and two-phase (gas-liquid) flow, and to compare the results with those of other researchers who used different modelling fluids. The experimental procedure has already been discussed in section 5.4 of chapter 5. Presented first are the results for single-phase liquid flow, which are compared with data of other researchers. It is important that the amplitude and frequency response in single-phase flow should agree with published results since the knowledge in the single-phase flow regime is relatively sound. This will provide a basis for interpreting the subsequent vibration tests in two-phase flow. Presented next are the experimental results for two-phase flow of varying mass flux and void fraction. A comparison is made between the behaviour of the fully flexible tube bundle and a single flexible tube bundle, which reveals the differing excitation mechanism which operate in single-phase versus two-phase flows. Comparison is also made between data sets which are analysed according to the commonly used Homogeneous Equilibrium Model (HEM), and the void fraction model which was presented in the previous chapter. It will be shown that the use of a more appropriate two-fluid model for determining the average flow velocity and fluid density of the two-phase flow, significantly changes the behaviour of the fluidelastic data. It will be shown that the interpretation of the results for fluidelastic instability in the intermittent flow regime is greatly influenced by the choice of fluid model.

8.1 Fluidelastic Instability in Single-Phase Flow

Fully Flexible Tube Bundle

Figure 8.1(a) shows the amplitude versus pitch flow velocity for the fully flexible bundle (tube #5 was monitored). Below about 0.3 m/s flow velocity, the tube response was very small. In this low range of flow rate, the central frequency peak at 30Hz, shown in Fig. 8.2(a), corresponds approximately to the natural tube frequency measured in still liquid, which was 32.8 Hz. However, other peaks also appear at 23 Hz and 35.5 Hz in the drag direction and 32.6 Hz in the lift direction. The central peak at 30 Hz is rather broad, likely due to coupling between neighbouring tubes which causes the added hydrodynamic mass to vary and thus causes slight shifts in the vibration frequency. More on this is discussed below. At a flow velocity of 0.32 m/s, which is assigned the critical velocity in single-phase flow for the fully flexible bundle, the amplitude response takes an upward slope which roughly follows the solid line overlayed on Fig. 8.1(a). The frequency spectra at this flow, shown in Fig. 8.2(b), reveals two distinct peaks at 29.4 and 31.6 Hz for both the drag and lift directions, where the magnitudes are roughly equal between the drag and lift directions, indicating that the vibration mode was a nearly circular orbit with a beat frequency. The next frequency spectra, Fig. 8.2(c), which corresponds to a post-instability flow velocity of 0.39 m/s, shows that the vibration mode is primarily in the drag direction at 30.5 Hz, but a small peak at 36.1 Hz is also visible. This higher peak shifts slightly upward to 36.4 Hz at increasing flow velocity and it dominates the spectra in Fig. 8.2(d) which corresponds to V_p = 0.45 m/s. In this case the vibration mode is an oval orbit with higher amplitude in the lift direction.

Coupled Natural Frequencies in a Tube Bundle

It was described above that a significant shift in vibration frequency, from about 30 Hz to 36.4 Hz, occurred between the sub-critical flow rates and post-critical flow rates. It appears that a significant reduction in added mass had occurred. It was thought that this reduction in added mass was caused by local vapour flashing of the liquid R-11 on the leeward side of the vibrating tubes, where the local fluid pressure could be slightly below the saturation pressure of the R-11. However the natural frequency of a closely spaced bundle of tubes will vary over a range of values due to the coupling

effect of neighbouring tubes. Using potential flow theory, Chen (1975) has calculated the added mass coefficients for a triangular layout of seven tubes for the case a single flexible tube in a rigid array, α_{ii}, and for a fully flexible array, μ_i. The self-added mass coefficient, α_{11}, for a sample case of a seven tube array with only the central tube flexible were calculated by Chen (1975) and are shown in Figure D1 of Appendix D. It is clear that the self-added mass coefficients are a strong function of gap over radius ratio, G/R, where G is the gap between neighbouring tubes and R is the tube radius. For the case of the seven tube array, there is only one value of α_{11} since it does not vary with the particular mode of vibration of the central tube. The bundle shown in Figure D1 is not exactly the same as the one used in this study but it is close enough to demonstrate the range of expected frequencies for the present bundle. For this study, G/R = 0.89, so that the self-added mass coefficient is $\alpha_{11} = 1.23$. Thus the expected frequency for the single flexible tube bundle in liquid, f_{liq}, is calculated as follows (dropping all subscripts except for α_{11}),

$$f_{liq} = f_{vacuo}\sqrt{\frac{m}{m + \alpha_{11}\pi\rho R^2}}, \qquad \textbf{(8.1)}$$

where m is the mass per unit length of the central tube, and f_{vacuo} can be closely approximated by the frequency obtained in air. It is clear from Figure D1 that as the G/R ratio increases, which approaches a single tube in an infinite liquid, the self-added mass coefficient approaches unity, which means that the added hydrodynamic mass is approaches the mass of fluid displaced by the tube. For bundle #1 of the present study, $f_{air} = 38.1$ Hz, $m = 0.179$ kg/m, $\rho = 1480$ kg/m^3, $R = 0.003175$ m, so that the estimated frequency for a single flexible tube in still liquid is 33.1 Hz. This is about 1% higher than the actual measured value of 32.8 Hz shown in Table 5.1 of Chapter 5.

For the case of a fully flexible bundle of seven tubes in a triangular layout, Chen also provides values of added mass coefficients, μ_i, for the $2i$ modes of vibration, where i is the number of tubes in the bundle, which is shown in Figure D2 of Appendix D. To calculate the 14 coupled frequencies of vibration, equation 8.1 is also used except that α_1 replaced by μ_i. For the present bundle with G/R = 0.89, the values determined from this figure are tabulated below in Table 8.1, along with the predicted frequencies for the present bundle in R-11 liquid at room temperature.

Table 8.1 Theoretical added mass coefficients and vibration frequencies for the fully flexible array in R-11 liquid.

Mode No. (*i*)	μ_i	Coupled Freq. (Hz)	Mode No. (*i*)	μ_i	Coupled Freq. (Hz)
1	2.12	30.6	*9, 10*	0.79	34.7
2, 3	1.95	31.0	*11*	0.68	35.1
4	1.49	32.3	*12, 13*	0.56	35.6
5, 6	1.34	32.8	*14*	0.49	35.9
7, 8	1.01	33.9			

Chen also provides an illustration of the 14 normal modes of vibration of the seven tube bundle, which is reprinted in Figure D3 for the case of P/D = 1.44. Thus, from Table 8.1, the range of coupled mode frequencies predicted by the theory of Chen (1975) is from 30.6 Hz to 35.9 Hz. This may explain to a large extent the frequency shift from about 30 Hz to 36.4 Hz which occurs in the fully flexible bundle when the fluidelastic instability is reached. However, the high frequency mode shapes in Figure D3 show that the central tube oscillates in a purely lift or drag direction, or does not oscillate. This does not match the modal behaviour observed at the fluidelastic threshold and beyond, where an oval orbit of the monitored tube was observed. Thus while much of the frequency shift could be explained by added mass effects, it appears that there must have been some effect of vapour flashing as well.

Vortex Shedding

The results in Fig. 8.1(a) for the fully flexible array demonstrate the lumpy nature of the amplitude response that is characteristic of the vibratory response of fully flexible arrays of tubes subjected to liquid flows. There is, however, the possibility of vortex shedding occurring near the threshold velocity. According to Fig. 2.8(d) in Chapter 2, the Strouhal number, based upon upstream flow velocity for vortex shedding in parallel triangular arrays, is between about 1.9 and 1.3. Using the higher Strouhal number of 1.9, a predicted pitch velocity at the onset of vortex shedding is,

$$V_p = \frac{fD}{S_u}\left(\frac{P-D}{D}\right) = \frac{31.5\,Hz \times 0.00635\,m}{1.9}\,(3.26) = 0.34\,m/s\,, \qquad \textbf{(8.2)}$$

which is just past the critical flow velocity for fluidelastic instability. Using the lower Strouhal number of 1.3, the corresponding pitch flow velocity is 0.50 m/s. Thus, the expected flow velocity range where vortex shedding is expected is between 0.34 and 0.50 m/s. It is possible that the interpretation of the post stable behaviour may be complicated by the simultaneous occurrence of vortex shedding. However, the results discussed below for the single flexible tube array make it clear that the onset of fluidelastic instability is indeed near 0.32 m/s, ie., is unaffected by any vortex shedding which may occur.

Single Flexible Tube in a Rigid Bundle

The amplitude response of tube #5 in the rigid bundle is shown in Fig. 8.1(b) for both the drag and lift directions. The tubes in the bundle were made rigid (except for tube #5) by inserting a thin metal plate over the free ends of the tube in which holes were drilled in the same pattern as the array. This plate had minimal effect on flow obstruction and effectively eliminated the 1st mode of vibration of 9 of the tubes. The hole for tube #5 was drilled oversize to allow it to vibrate. The critical threshold flow velocity, V_{cr}, is very clearly defined in Fig. 8.1(b) at 0.34 m/s which is only about 6% higher than the fully flexible case. Also, the vibration amplitude in the sub-critical flow velocity range is nearly the same for both cases, which indicates that the turbulence buffeting forces which are active in this low flow range do not depend upon motion of the tubes. The close coincidence of V_{cr} for both the flexible and single flexible tube bundle indicates that the velocity mechanism is controlling the fluidelastic instability of the bundle in liquid R-11 flow. Thus, the self-excited forces appear to be influenced most strongly by the mechanism of negative damping rather than the relative displacement with its nearest neighbours, which is characteristic of the displacement mechanism. These concepts were discussed earlier in Section 3.2 in Chapter 3.

A sample set of frequency spectra for the single flexible tube bundle is provided in Fig. 8.3, which were selected from flow velocities which closely correspond with the spectra of the fully flexible array in the previous figure. Inspection of the graphs in Fig. 8.3 shows that in the sub-critical flow range, graphs (a) and (b), the frequency spectra consists of two closely spaced peaks at 31.8 Hz and 32.5 Hz. Recall from above that Chen's (1975) theory predicted a natural frequency for a tube in a

rigid triangular bundle of P/D = 1.44 to be 33.1 Hz in quiescent liquid, which is slightly higher than observed in the actual bundle under cross-flow conditions. Beyond the critical flow, graphs (c) and (d), the spectra consists of a single peak at 31.8 Hz. In each case, the amplitudes were nearly the same in the lift and drag directions, indicating that the vibration orbit was nearly circular. Comparing the spectra of the fully flexible array, Fig. 8.2, with that of the single flexible tube array, Fig. 8.3, reveals that in the sub-critical flow range, the multiple peaks in the fully flexible case are largely absent from the single flexible tube case and indicates that these were not due to structural vibrations of the flow loop. Also, the primary peak is narrower in the single flexible tube case and it occurs at a slightly higher frequency of 31.8 Hz, compared to the frequency of the fully flexible case, 30 Hz. It appears that the effect of de-coupling the monitored tube from its nearest neighbours is to nearly eliminate the fluctuations in the added mass of the flexible tube, which agrees with the predictions of Chen (1975). Beyond the critical flow velocity, the response of the two bundles differed little, except for the frequency peak of the single flexible tube bundle did not shift in frequency, but remained nearly constant at about 31.8 Hz. This indicates that the shift in frequency observed for the fully flexible case, from about 30 Hz to 36.4 Hz, was due to the substantial reduction in added mass due to either to a coupled mode shape of the tubes or to local flashing of vapour on the leeward side of the vibrating tube as discussed earlier. It is generally observed that adjacent tubes move out-of phase with each other in the unstable range. This would produce lower pressures and therefore increase the tendency to cavitation or flashing in fully flexible arrays.

Comparison of Single-Phase Results with Other Data

The results for fluidelastic instability in single-phase were plotted in Fig. 8.4 on a stability diagram and compared with other data. This diagram is expressed in terms of non-dimensional parameters, reduced velocity versus mass damping parameter. Reduced velocity is given by,

$$V_{red} = \frac{V_{p.c}}{f D}, \tag{8.3}$$

where $V_{p.c}$ is the critical pitch flow velocity at the threshold of instability, f is the corresponding

measured vibration frequency at the stability threshold in Hertz and D is the tube outside diameter. The mass damping parameter is given by,

$$mass\text{-}damping\ parameter\ =\ \frac{m\ \delta_a}{\rho\ D^2}\ , \tag{8.4}$$

where m is the tube mass per unit length including fluid added mass, and is given by,

$$m\ =\ m_t(\frac{f_a}{f})^2\ , \tag{8.5}$$

where ρ is the density of the fluid and f_a is the frequency of tube vibration in air (where added mass is assumed zero). δ_a is the logarithmic decrement of the damping in air, which was determined by analysis of the amplitude decay trace of tube #5 after plucking using equation (3.37) in Chapter 3. It should be noted that the in-air damping of the monitored tube was measured with the other tubes held fixed to prevent the vibration energy from transferring to and from the neighbouring tubes through mechanical coupling.

Some researchers have used damping values obtained from measurements in still fluid or in flowing fluid, and these tend to be roughly 10 times the in-air values. However, in-fluid damping is much more difficult to measure, especially in dense fluids such as R-11 or water, where the frequency spectrum consists of multiple, closely spaced peaks, which makes the frequency bandwidth method of damping determination very difficult. However, the net fluid damping component goes to zero as the threshold of stability is reached. Thus, in stability analysis, it is reasonable to use the in-air damping value since it is primarily material damping, the only net energy dissipation mechanism remaining at the stability threshold. The values obtained for tube #5 in the fully flexible bundle subjected to single-phase flow are given as follows: $\delta_a = 2\pi\zeta_a = 0.0069$, $V_{p.c} = 0.32$ m/s, $f = 29.4$ Hz, $f_a = 38.1$ Hz, $D = 0.00635$ m, $m_t = 0.179$ kg/m, $\rho = 1477$ kg/m^3, so that the critical reduced velocity is $V_{red} = 1.71$ and the mass damping parameter is 0.035. When this single data point is plotted on the stability diagram, Fig. 8.4, it agrees well with previous empirical results. The results for the single flexible tube bundle are also plotted on the stability diagram where the differing parameters are as follows: $V_{p.c} = 0.34$ m/s,

f = 31.8 Hz, f_a = 38.1 Hz, so that the critical reduced velocity for the single flexible tube bundle is V_{red} = 1.68 and the mass damping parameter is 0.030. When this data point is plotted on the stability diagram, it coincides closely with that of the fully flexible array as seen in Fig. 8.4.

Conclusions for Fluidelastic Instability in Single-Phase Flow

Single-phase flow-induced vibration experiments were performed on a parallel triangular array of cantilevered tubes with pitch to diameter ratio of 1.44. Two cases were presented; a fully flexible array and a single flexible tube array. Comparison has shown that the critical threshold flow velocity is 0.32 m/s for the fully flexible tube array and about 6% higher for the single flexible tube array. The close coincidence of these two results indicates that the instability is a negative damping type, whereby the self-excited forces are controlled by the velocity of the vibrating tube as opposed to its relative displacement to the neighbouring tubes. The instability threshold parameters (mass damping parameter and reduced velocity) for the fully flexible and single flexible tube cases were plotted in Fig. 8.4 on a stability diagram to compare with the results of others for parallel triangular arrays subjected to mostly single-phase cross-flows. These two points coincided very closely with each other and agreed well with the other researchers' data. This agreement indicates that the present apparatus has provided a sound benchmark in single-phase flow which will enable comparison of the results in two-phase flow.

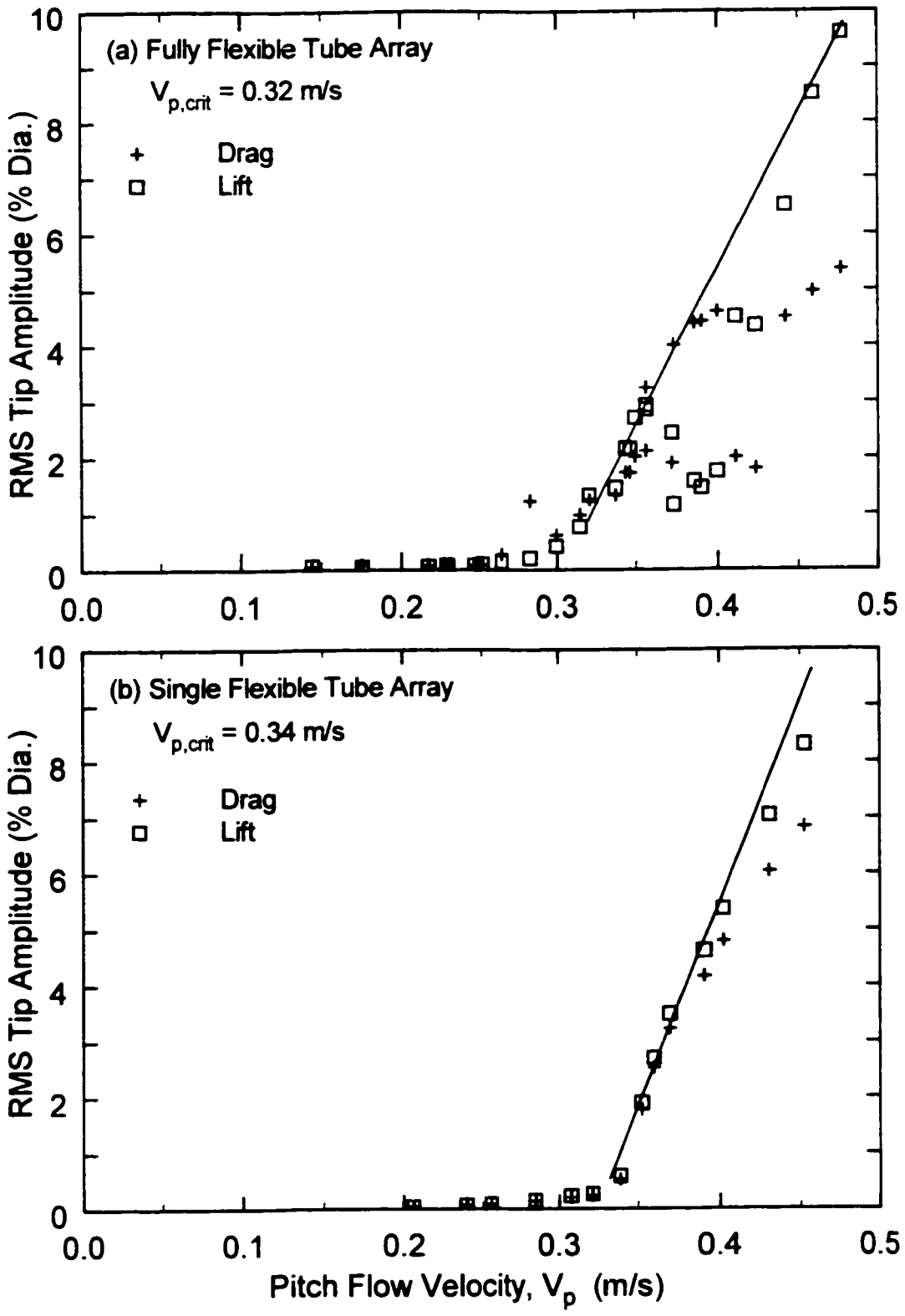

Figure 8.1 Amplitude responses of the tube array subjected to single phase liquid R-11 cross flow. (a) Fully flexible tube bundle, (b) single flexible tube with other tubes held fixed. □ Drag direction, + Lift direction.

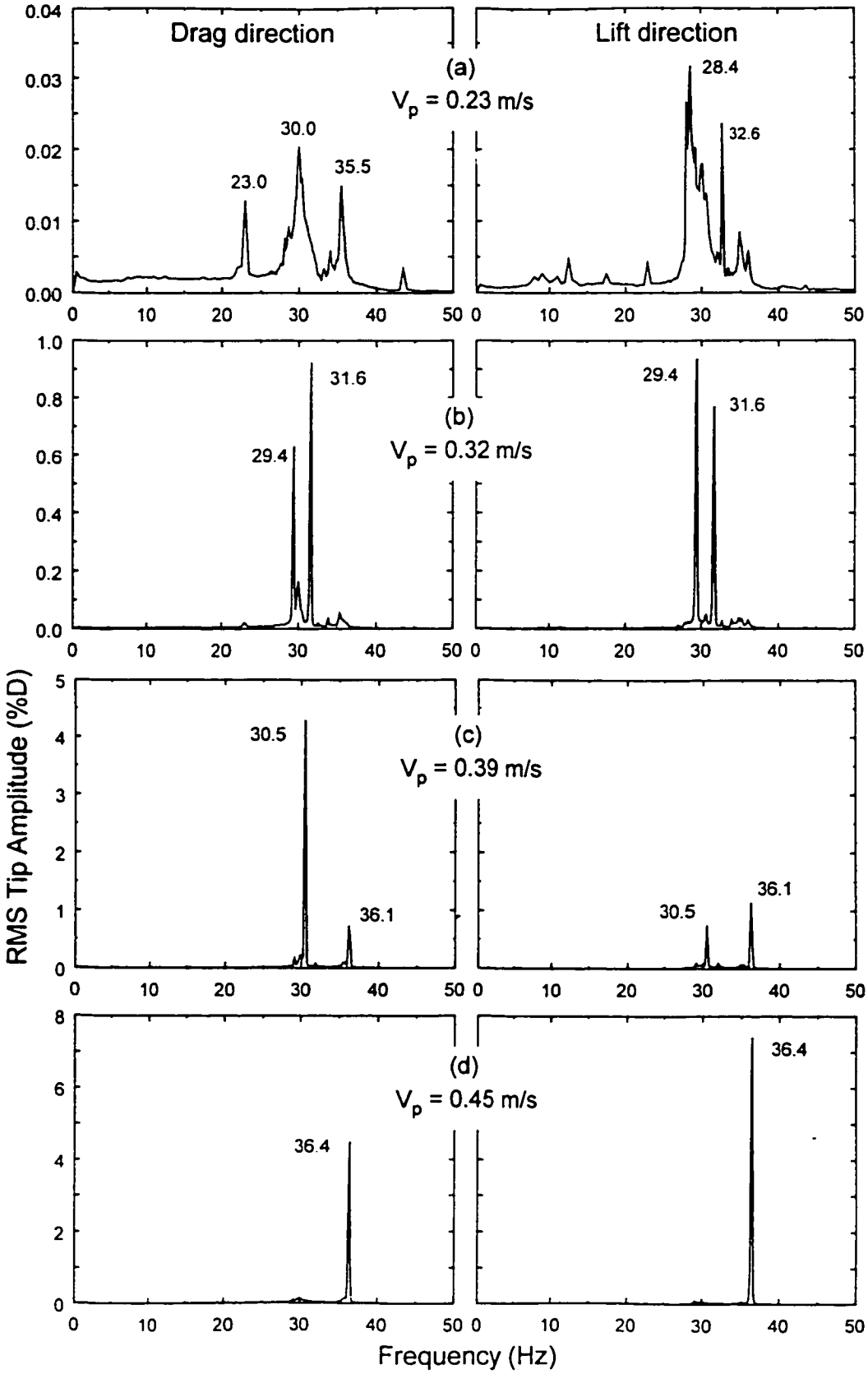

Figure 8.2 Typical frequency spectra for tube #5 in the fully flexible bundle subjected to single phase liquid R-11 cross-flow.

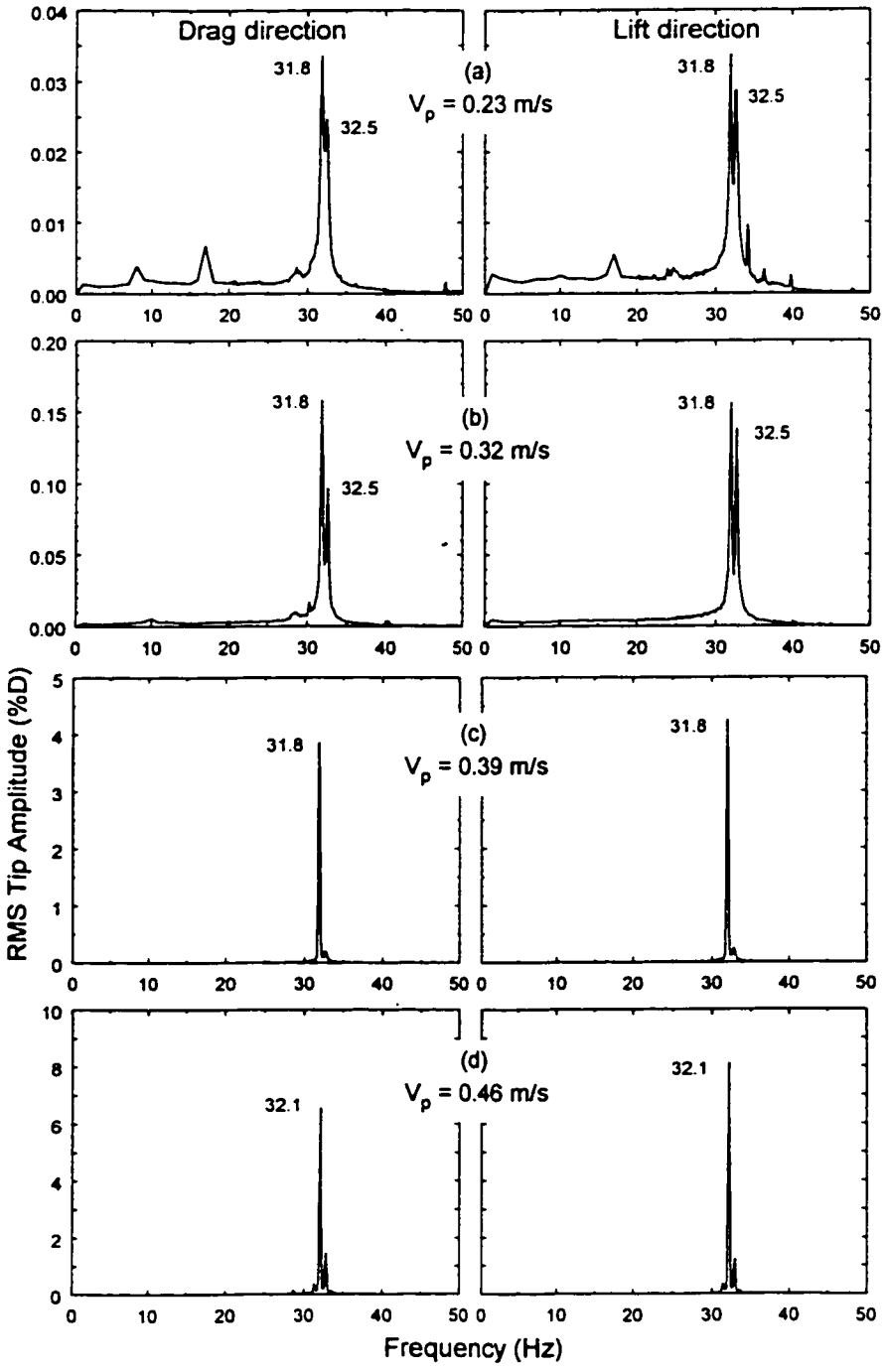

Figure 8.3 Typical frequency spectra for tube #5 in the single flexible tube bundle subjected to single-phase liquid R-11 cross-flow.

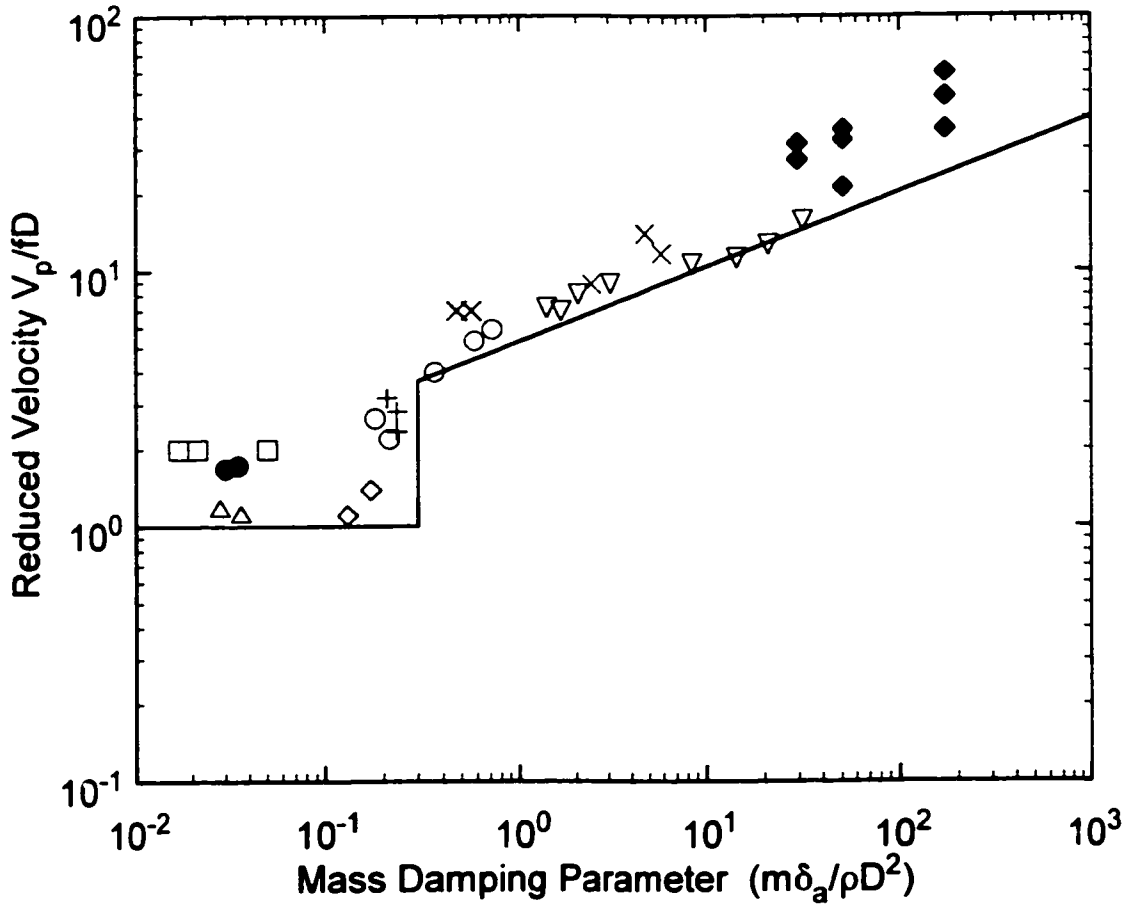

Figure 8.4 Critical flow velocities for fluidelastic instability of parallel triangular tube arrays in cross-flow. ◆ Hartlen (1974 in air, □ Weaver and Yeung (1984) in water, ▵ Weaver and Koroyannakis (1982) in water, ◇ Scott and Weaver (1986) in water, ○ Heilker and Vincent (1981) in air-water, ▽ Weaver and Grover (1978) in air, + Gorman (1976) in water, × Pettigrew et al. (1978) in air-water, ● Present study in liquid R-11. ——— Weaver and Fitzpatrick (1988).

8.2 Fluidelastic Instability in Two-Phase Flow

Introduction

The following sections describe the experimental results for fluidelastic instability in two-phase R-11 flow, where the primary purpose was to determine the threshold velocity for the onset of fluidelastic instability in a two-phase flow of varying void fractions and mass fluxes. The experimental procedure is described in detail in Section 5.4 of Chapter 5. A comparison is made between two methods of data analysis, the traditionally used HEM vs. the newly developed void fraction model which was afforded by the gamma densitometer measurements. A flow regime analysis of the present data and that of others demonstrates that the data points corresponding to bubbly flow showed a significantly different stability behaviour than those corresponding to intermittent flow. Results of the present study are presented for the fully flexible array and for a single-flexible tube array, which reveals that the controlling mechanism of fluidelastic instability in two-phase flow is different than in single-phase flow.

Amplitude Response of Fully Flexible Tube Bundle

Figure 8.5 presents amplitude response curves of the monitored tube (tube #5) in the flexible array which clearly illustrates the phenomenon of fluidelastic instability in two-phase flow. Below the critical flow velocity, which is indicated by the intersection point of the two solid lines, the tube responds to increasing flow by a gradual increase in vibration amplitude. Beyond the threshold velocity however, the vibration amplitude suddenly increases at a much greater slope, especially in the lift direction. In each experiment, the pitch mass flux into the test section was held constant while the void fraction was increased in each trial, so that the flow velocity increased from one trial to the next by virtue of a reduction in the average density of the fluid. In Fig. 8.5, the HEM pitch flow velocity is utilized on the abscissa, which is calculated by $V_p = G_p/\rho_{HEM}$. The same data is re-plotted in Fig. 8.6 except that the effective pitch flow velocity, V_{eq}, is utilized on the abscissa, which is based upon a summation of the dynamic head of the gas and liquid phases according to equation (4.7) in Chapter 4. This calculation was facilitated by the radiation attenuation measurements of void fraction by the gamma densitometer, called RAD void fraction. The fluidelastic threshold in the graphs of Fig. 8.5 are

still clearly defined except that the threshold flow velocities are lower when using RAD analysis as opposed to HEM analysis. For comparison purposes, the various interpretations of two-phase flow velocity are presented in Fig. 8.7 for a particular mass flux level. It can be noted that the HEM velocity is always greater than the equivalent velocity except at 0% and 100% void fraction, where they are equal. This is because the gas velocity is always greater than the liquid phase velocity, a fact which is neglected in HEM analysis.

Comparison of Fluidelastic Instability Results with Data of Other Researchers

The results of the present study for fluidelastic instability are plotted in Fig. 8.8(a) along with data sets of three other researchers who tested parallel triangular arrays using a variety of modelling fluids, and these are: Pettigrew *et al.* (1989b) in air-water, P/D = 1.47; Axisa *et al.* (1985) in steam-water, P/D = 1.44; Pettigrew *et al.* (1995) in R-22, P/D = 1.5. The data, which is also tabulated in Table 8.2, is presented on a graph which features critical reduced velocity versus mass-damping parameter. These are currently believed to be the two most important dimensionless parameters for scaling the phenomenon of fluidelastic instability, while array geometry and pitch ratio are also important. Critical HEM reduced velocity, $V_{r,c}$, is calculated by,

$$V_{r,c} = V_{p,c}/fD \,, \tag{8.6}$$

where the critical HEM pitch velocity, $V_{p,c}$, and the tube vibration frequency, f, are measured at the fluidelastic stability threshold. Mass damping parameter is given by,

$$m\,\delta/\rho_H D^2 \,, \tag{8.7}$$

where m is the mass of the tube per unit length including fluid hydrodynamic mass, δ is the in-flow logarithmic decrement damping value, and ρ_H is the average density of the two-phase flow, which is calculated by equation (4.2). The in-flow damping value, measured at half the mass flux for fluidelastic instability, was used to plot the data of the present study. This was done to be consistent with the analysis methods of Pettigrew *et al.* (1989b). The lower bound Connors' constant, $K = 3.0$, which was determined by Pettigrew *et al.* (1989b) for P/D ratios of between 1.4 and 1.5 in continuous

flow regimes (bubbly), is plotted as a solid line on this figure. The fluidelastic constant, K, follows from the often quoted Connors' relationship,

$$V_{p.c}/fD = K\sqrt{m\delta/\rho_H D^2} \; . \qquad \textbf{(8.8)}$$

Connors' theory predicts that the critical reduced velocity should rise proportionally with mass damping parameter to the one-half power. The data points in Fig. 8.8(a) are distinguished between the different flow regimes encountered, where the open symbols correspond to bubbly flow and the solid symbols represent intermittent flow, except for Axisa *et al.*'s data where the solid symbols represent the dispersed (annular) flow regime. Of particular note in this figure is that the data show a clear change in slope which coincides with the predicted flow regime changes from bubbly to intermittent flow. The air-water data show a levelling off trend in stability while the R-11 and R-22 data show a decrease in stability.

The present data corresponding to the bubbly flow regime shows a slightly lower stability threshold than most of the other data of the bubbly flow type. An appropriate value of Connors' constant which would establish a lower bound on the present author's data is $K = 2.0$. This is lower than the value, K = 3.0, recommended by Pettigrew & Taylor (1994). A possible reason for the difference between the present R-11 results and the air-water data could be due to the effect of using different modelling fluids. R-11 is a single component fluid while air-water is a two-component fluid which cannot simulate any of the local flashing or collapse of vapour on the tube surfaces. This could be a factor affecting the tube forces in the prototype tube bundle which is subjected to steam-water (a single component fluid). It was discussed earlier in Chapter 4 (Section 4.3) that this difference could affect tube damping and fluid excitation mechanisms. However, the steam-water results of Axisa *et al.* (1985) show a higher stability than the air-water results, in which a lower bound Connors' constant for that data is about K = 4.2. Thus the effect of two component vs. single component modelling fluids remains unclear based upon this simple comparison. Another difference between the present results and that of others is the physical scale of the model, where this study uses 6.35 mm (1/4") diameter tubes, the other studies used full scale tube diameters of 12.7 mm (½") or greater. Although it is assumed that using dimensionless numbers for comparing model and prototype behaviour is supposed

to eliminate scale effects, these experiments present a special case due to the presence of bubbles. It is not easily possible to control the size of bubbles in a two-phase flow, so that the ratio of average bubble size to tube diameter will likely be larger in a reduced scale model than in the full scale prototype. When the ratio of bubble diameter to tube diameter increases, this will likely lead to an increase in the correlation length of turbulent buffeting forces and this will result in higher response amplitudes in the sub-critical flow velocity range. This may contribute to the onset of self-excited vibrations at lower velocities and hence lead to a lower stability threshold for such an array.

Fluidelastic Data Comparison using Void Fraction Modelling

The previous analysis was based upon the HEM. This is a simple two-phase fluid model which gained wide acceptance by researchers studying flow-induced vibrations because it was easy to implement. More importantly however was the fact that these researchers did not have access to the measurement tools needed to measure void fraction. To the present author's knowledge, no attempt has yet been made to modify the comparison of the existing fluidelastic instability data using a more accurate two-fluid model for determining the two-phase fluid parameters such as flow velocity and average density. However, since it was established in Chapter 7 that the new void fraction model could accurately predict the void fraction in an upward two-phase flow for a variety of fluids and tube arrays, it is appropriate to recalculate the important parameters of the existing data and make such a modified comparison. In this case, the actual void fraction, α, of the other data is calculated by the void fraction model and the average fluid density was determined according to,

$$\rho = \alpha \rho_G + (1-\alpha) \rho_L \ . \qquad \textbf{(8.9)}$$

This is essentially the same as equation (4.2) except that the HEM void fraction, α_H, is replaced by that predicted by the void fraction model. At present, there is no general consensus as to the proper representation of flow velocity for an upward two-phase flow where the two-phases move at different velocities. However, a logical representation is defined here as an equivalent flow velocity, V_{eq}, which is determined by summing the dynamic head of each phase and weighted by the void fraction,

$$V_{eq} = \sqrt{[\alpha \rho_G U_G^2 + (1-\alpha) \rho_L U_L^2]/\rho} \ . \qquad \textbf{(8.10)}$$

The fluidelastic data of the other researchers mentioned earlier were recalculated using the foregoing void faction model to calculate void fraction, α, and equations (8.9) and (8.10) to calculate average density, ρ, and equivalent pitch flow velocity, V_{eq}, and plotted on a stability diagram as shown in Fig. 8.8(b), along with the data of the present study, in which the RAD void fraction was utilized. Note that for this modified analysis, the tube vibration frequency, f, mass per unit length, m, and damping, δ, remained unchanged from the previous HEM analysis. As done previously, each data set is divided between the various predicted flow regimes, where the open symbols correspond to bubbly flow and the solid symbols correspond to intermittent flow, except for Axisa's data where the solid symbols correspond to dispersed flow. By comparing the lower graph, Fig. 8.8(b), with the upper graph, Fig. 8.8(a), it is clear that the void fraction model has compressed each data set into a smaller range of mass-damping parameter. This is because the variation of average fluid density for each data set was smaller when analysed with the model as opposed to the HEM analysis. The air-water data shows a remarkable change in behaviour between the predicted bubbly and intermittent flow regimes. In bubbly flow, the critical reduced velocity results follow a trend with mass-damping parameter which roughly agrees with Connors' formula (equation 8.8) as indicated by the solid line. However, the data points corresponding to the intermittent flow regime follow an unusual trend, whereby the critical reduced velocities significantly decrease over a small range of mass-damping parameter. This observation runs contrary to Connors' model prediction. Roughly the same observation was observed for the R-22 data, although in this case, some of the data points in the bubbly flow regime also show a decrease in stability with mass-damping parameter. Axisa *et al.*'s steam-water data is rather tightly clustered in both graphs and it is difficult to observe any clear trends in stability behaviour, either with mass damping parameter or flow regime. The R-11 data of the present study shows almost no variation in mass damping parameter, yet it covers a significant range of reduced velocity. This also runs counter to Connors' model prediction.

To extend the comparison, the fluidelastic instability data of the other researchers for other bundle array types, normal triangular, normal square (in-line) and rotated square were also analysed using both HEM and velocity ratio analysis. The purpose of this extended analysis was to show that the flow regime effects observed for the parallel triangular tube array are also observed for other array

geometries and P/D ratios. The air-water results of Pettigrew *et al.* (1989b) for two normal triangular arrays of P/D = 1.47 and 1.32, and a normal square array of P/D = 1.47 are displayed in Fig. 8.9(a) and (b). The upper graph presents their results analysed using the HEM to determine the necessary two-phase fluid parameters, flow velocity and average fluid density. The data which corresponds to bubbly flow (open symbols) follows Connors' theory remarkably well, but those data points which correspond to intermittent flow (solid symbols) clearly deviate from this straight line relationship. In the lower graph the same data is presented using the predictions of the void fraction model for determining void fraction, average fluid density and equivalent flow velocity. In this case, it is clear that the same trends are observed as in the previous graphs, that the bubbly flow data remains in good agreement with the trend established by Connors' theory, but the data corresponding to intermittent flow departs significantly from this prediction. The application of the void fraction model has, in effect, caused the intermittent flow data to take a downward turn, so that the range of mass-damping parameter is greatly reduced while the values of critical reduced velocity have changed from being relatively constant in the upper graph to decreasing significantly over a very small range of mass-damping parameter in the lower graph.

The steam-water data of Axisa *et al.* (1985) and the R-12 data of Mann and Mayinger (1995) are presented in Fig. 8.10, following the same comparison format as in the previous two figures. The data of Axisa *et al.* includes a normal triangular bundle and normal square bundle of P/D = 1.44, but in this case the solid symbols correspond to the dispersed flow regime as predicted by Ulbrich and Mewes' map. The three data points of Mann and Mayinger are for a normal square bundle and correspond to bubbly flow only. In the upper graph, Fig. 8.10(a), the data are analysed using the HEM while in the lower graph, Fig. 8.10(b), the data are analysed using the void fraction model. In this case, all of the data are clustered together and occupy only a small range of mass-damping parameter, making it difficult to discern any trends with respect to that parameter. However, it is clear that no obvious difference exists between the bubbly flow data (open symbols) and the dispersed flow data (filled symbols). In the lower graph, Fig. 8.10(b), the data is only slightly compressed in the horizontal direction, and the modified analysis indicates a slightly lower stability for the dispersed flow regime data vs. the bubbly flow data. The data of Mann and Mayinger in the lower graph has slightly reversed

in trend. In the upper graph the critical reduced velocity increases slightly with mass-damping parameter, while in the lower graph this trend is opposite, showing a slight reduction of critical reduced velocity with mass-damping parameter. However, a drastic decrease in stability is not observed, which is consistent with the bubbly flow data in the previous two figures.

Returning to Figures 8.8(b) and 8.9(b), it was shown that the analysis using the void fraction model caused a deviation in the predicted stability behaviour for the data points in the intermittent flow regime. It is observed that each set of these data points (filled symbols) correspond to nearly the same mass-damping parameter and yet they cover nearly a decade of critical reduced velocity values. In each case, the lowest values correspond to flows with the highest void fraction and lowest mass flux. Such a trend creates a great amount of uncertainty for the designer who wishes to predict the stability limit of a particular heat exchanger design, since it is normally expected that the critical reduced velocity should have a single valued relationship with mass-damping parameter, and should rise with mass-damping parameter in a similar fashion to the prediction of Connors' or Li (1997). The analysis suggests that reduced velocity and mass-damping parameter may be insufficient to properly model flow induced vibration in the intermittent flow regime of two-phase flows, and that there are added complications in this type of two-phase flow which the present analysis neglects. One possible factor is the ratio of bubble size to tube diameter, which could affect the pressure drop of the flow through the array and fluid damping effect. It may also play a role in the correlation length of turbulent forces in the array. The present author has observed that the average bubble size increases with void fraction and decreases slightly with mass flux. At very low void fractions (below 10%) the vapour bubbles are small, have roughly the same velocity and are distributed fairly evenly across the cross-section of the flow conduit. As void fraction rises however, the average bubble size increases and the large bubbles travel upward faster while the smaller bubbles travel slower and often stagnate or become entrained in the periodic liquid down-wash. It was observed with the high speed video camera that, as the void fraction increases to the onset of the intermittent flow regime, the largest of the gas bubbles would elongate and travel upward rapidly. In their wake, the smaller bubbles could often travel as quickly and coalesce with the leading bubble. Under this scenario, the bubbles would continuously coalesce and grow indefinitely. However, turbulence tends to break up the bubbles and at some point a balance

is struck between these two mechanisms, and a certain bubble size and distribution is maintained. When the void fraction increases further to the point where the flow regime becomes intermittent, the flow is not steady and periodic upward surges of high void fraction flow followed by periods of bubble stagnation and large scale liquid down-wash occur. In such a case, defining an average flow velocity for fluidelastic threshold calculations could be inappropriate, because the phenomenon can have a non-linear softening effect as illustrated in Fig. 8.11. This phenomenon, also described as hysteresis, produces a conditionally stable flow velocity range. If the vibration amplitude of the perturbed tube becomes high enough to reach or exceed the unstable path of the amplitude response curve, indicated in Fig. 8.11 as the curved dashed line, this will lower the effective stability threshold of the bundle. Thus, self-excited vibrations may develop at a flow velocity that is lower than $V_{p,c}$. A sudden surge in the flow rate or a random turbulent disturbance may cause such an increase in vibration amplitude. Since the fluidelastic forces are self excited, meaning that they are generated when the flow path is altered by the tube's own motion, the high amplitude vibrations brought on by such a transient event may persist even if the mean flow velocity falls below the critical velocity, $V_{p,c}$, but not into the stable range as shown in Fig. 8.11. Since the intermittent flow regime is characterized by fluctuations in flow velocity, it has a potential for initiating fluidelastic instability at flow rates lower than normally expected for a steady increasing flow rate. The present results show that the stability threshold decreases for lower mass flux levels (corresponding to higher void fractions) which is consistent with the fact that the intermittency is more pronounced at higher void fractions (so long as dispersed flow is not approached).

Note that the data in Figure 8.8(b) has also been plotted in Appendix D, Figure D7 where the in-air damping, ζ_a, was utilized in the determination mass-damping parameter instead of the in-flow measured values. This follows from a hypothesis that the in-air damping values are more appropriate to use for analysing fluidelastic data since it is thought to be the only energy dissipation mechanism at the threshold of instability. This modified analysis has the effect of shifting the data horizontally to the left by roughly one decade. It does not noticeably improve the collapse of the data, but the difference in trend between the bubbly and intermittent flow data is still noticeable. A lower bound value for Connors constant for this modified data analysis is K= 7.0.

8.3 Fully Flexible Bundle vs. Single Flexible Tube Bundle Response in Two-Phase Flow

Typical amplitude response curves for tube #5 are shown in Fig. 8.12 for both the fully flexible array and for the single flexible tube array. The amplitude response is presented in terms of the pitch flow velocity, which was determined according to the HEM for two-phase flow. The upper graph corresponds to a relatively low mass flux while the lower graph corresponds to a relatively high mass flux.

The stability threshold for the fully flexible array is fairly well defined in both the upper and lower graphs, but for the single flexible tube case the fluidelastic threshold is absent at conditions for which it occurred in the fully flexible array. Fluidelastic instability might have been obtained in the single flexible tube bundle experiments at a higher flow velocity, but this would have required increasing the heater power to raise the void fraction. This was not possible because, for the results shown in Fig. 8.12, the pressure in the loop reached maximum and the tests could not be taken further. That the stability threshold is delayed or effectively eliminated for the single flexible tube bundle case suggests that the mechanism of fluidelastic instability in two-phase flow is dominated by a fluid-stiffness mechanism, where the fluidelastic forces are controlled by the relative motion of neighbouring tubes. This is different than the case for single-phase liquid flow, where the dominant mechanism was found to be negative damping, because detuning the tubes had little effect upon the critical velocity. Interestingly, Lever and Weaver (1986b) found for this array type, that the stability threshold in air cross-flow was the same for both the fully flexible and single flexible tube bundle. Thus it appears that the presence of two-phase flow appreciably influences the mechanism of self-excitation for a single flexible tube in a rigid bundle. From a practical point of view, this suggests that for heat exchangers subjected to two-phase flows, de-tuning of the tubes should have a beneficial effect in increasing the stability of a tube array from self-excited vibrations. Figure 8.12 also reveals that, for flow rates below the fluidelastic threshold (in the turbulence buffeting region) the vibration amplitudes are about the same for the fully flexible and single flexible tube array. This demonstrates the suitability of using the single flexible tube array for the determination of turbulence buffeting forces and fluid damping.

The frequency spectra for the fully flexible array for a relatively low mass flux, G_p = 150 kg/m^{2}s, are shown in Fig. 8.13 (a) to (d) which correspond to selected data points in Fig. 8.12(a). Two

peaks are observed at flow rates below the fluidelastic threshold. The higher peak at 37 Hz is the dominant frequency at the critical flow velocity and beyond, which is surprisingly similar to the frequency behaviour in single-phase liquid flow. The two peak spectra makes it unsuitable to determine damping by the half-power bandwidth method from the response of the fully flexible bundle. In comparison, graphs (e) to (h) in Fig. 8.13 are for the single flexible tube bundle, where the vibration response more nearly resembles the classical response of a single degree of freedom oscillator subjected to broad band random excitation.

Figure 8.14 shows the frequency spectra for the flexible and single flexible tube bundles for a relatively high mass flux, G_p = 350 kg/m^{2}s, and correspond to selected data points in Fig. 8.12(b). Similar to the previous set of frequency spectra, the two peak behaviour of vibration is evident for the fully flexible bundle at sub-critical flows, where the higher peak at 37 Hz becomes dominant at the fluidelastic threshold and beyond. The frequency spectra of the single flexible tube bundle, shown in graphs (e) to (h), closely resemble the classical, single degree-of-freedom system response which facilitates damping measurements by the half-power bandwidth method.

8.4 Conclusions for Fluidelastic Instability in Two-Phase Flow

Experimental results for fluidelastic instability have been presented for a parallel triangular tube bundle, with P/D = 1.44, subjected to two-phase R-11 cross-flow. The results were obtained by subjecting the bundle to a constant mass flux while gradually incrementing the void fraction in each trial until high amplitude, self-excited vibrations were observed. Two configurations of the tube bundle were tested: all 10 tubes flexible (fully flexible bundle), and one tube flexible and the other tubes held fixed (single flexible tube bundle). For the fully flexible bundle, fluidelastic instability was encountered over the full range of mass flux tested, from about 80 to 500 kg/m^{2}s. For comparison with data of other researchers, the present data were non-dimensionalized in terms of critical reduced velocity and mass-damping parameter and plotted on a stability diagram. The data was subdivided into the different flow regimes that were predicted to occur according to the predictive map of Ulbrich and Mewes (1994).

Two different versions of the stability diagram were presented, in which the average flow

velocity and fluid density were calculated using two different fluid models: the most commonly used homogeneous equilibrium model (HEM) and the void fraction model which was presented in Chapter 7. In the HEM analysis, the present data showed a lower stability threshold than the air-water and R-22 data of Pettigrew *et al.* (1989b, 95). Also, there appeared to be a difference in stability behaviour between the bubbly flow data and the intermittent flow data, where the latter deviated from Connors' theory towards lower stability than predicted. In the modified analysis, the data was compressed into a narrower range of mass-damping parameter than in the HEM analysis, because the void fraction model predicted lower void fractions than the HEM and thus the range of average fluid density covered by each of the experimental data sets was smaller. Most of the bubbly flow data still followed the trend of Connors' theory in both analyses approximately. However, the intermittent flow data showed a significantly different trend in the velocity ratio analysis, whereby a significant drop in critical reduced velocities was observed over very small range of mass-damping parameter.

The single flexible tube bundle did not exhibit fluidelastic instability over any of the two-phase flow conditions to which it was subjected. This was surprising since, in single-phase liquid flow, the critical flow velocity was nearly the same for both the fully flexible and single flexible tube bundle. This result suggested that the mechanism for fluidelastic instability in two-phase flow is dominated by a fluid-stiffness mechanism, where the fluidelastic forces are controlled by the relative motion of neighbouring tubes. From a practical point of view, this suggests that de-tuning of the tubes should have a beneficial effect in increasing the stability of a tube array from self-excited vibrations. This is different than the case in single-phase liquid flow, where the dominant mechanism was found to be fluid-damping. The frequency spectra of the single flexible tube bundle revealed a single vibration peak at the natural frequency which closely resembled the classical response of a single degree-of-freedom oscillator subjected to a random excitation. In comparison, the vibration spectra of the fully flexible bundle revealed two peaks at sub-critical flows, which made it difficult to determine the damping of the system. Hence, damping measurements were obtained from experiments with a single flexible tube in a rigid array, which is the subject matter of the next chapter.

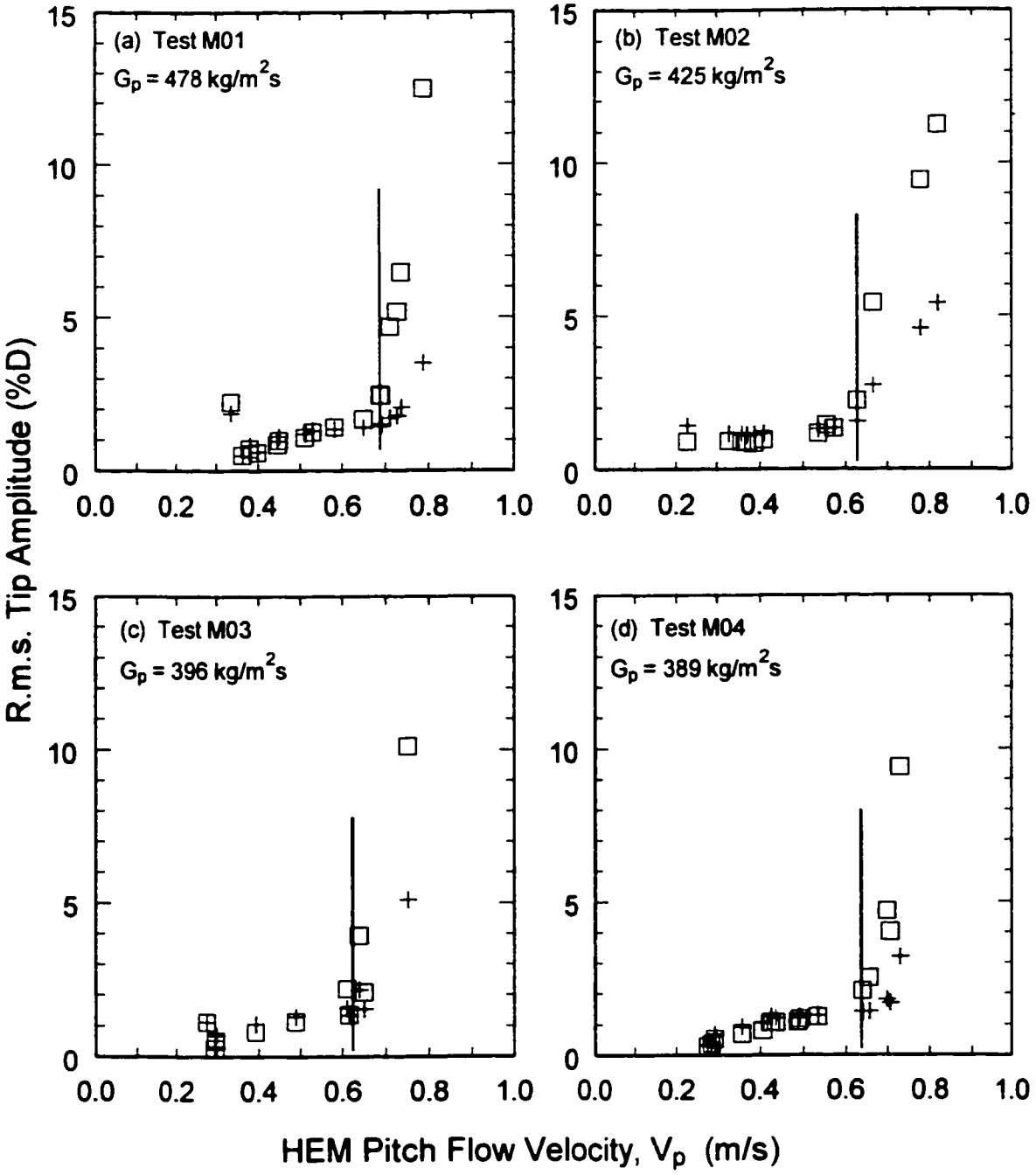

Figure 8.5 (a-d) Amplitude response of the tube array subjected to two-phase R-11 cross-flows of various mass fluxes. + Drag direction, □ Lift direction. Abscissa in terms of V_p, as determined by the HEM. The vertical line represents the conditions selected as corresponding to the fluidelastic threshold.

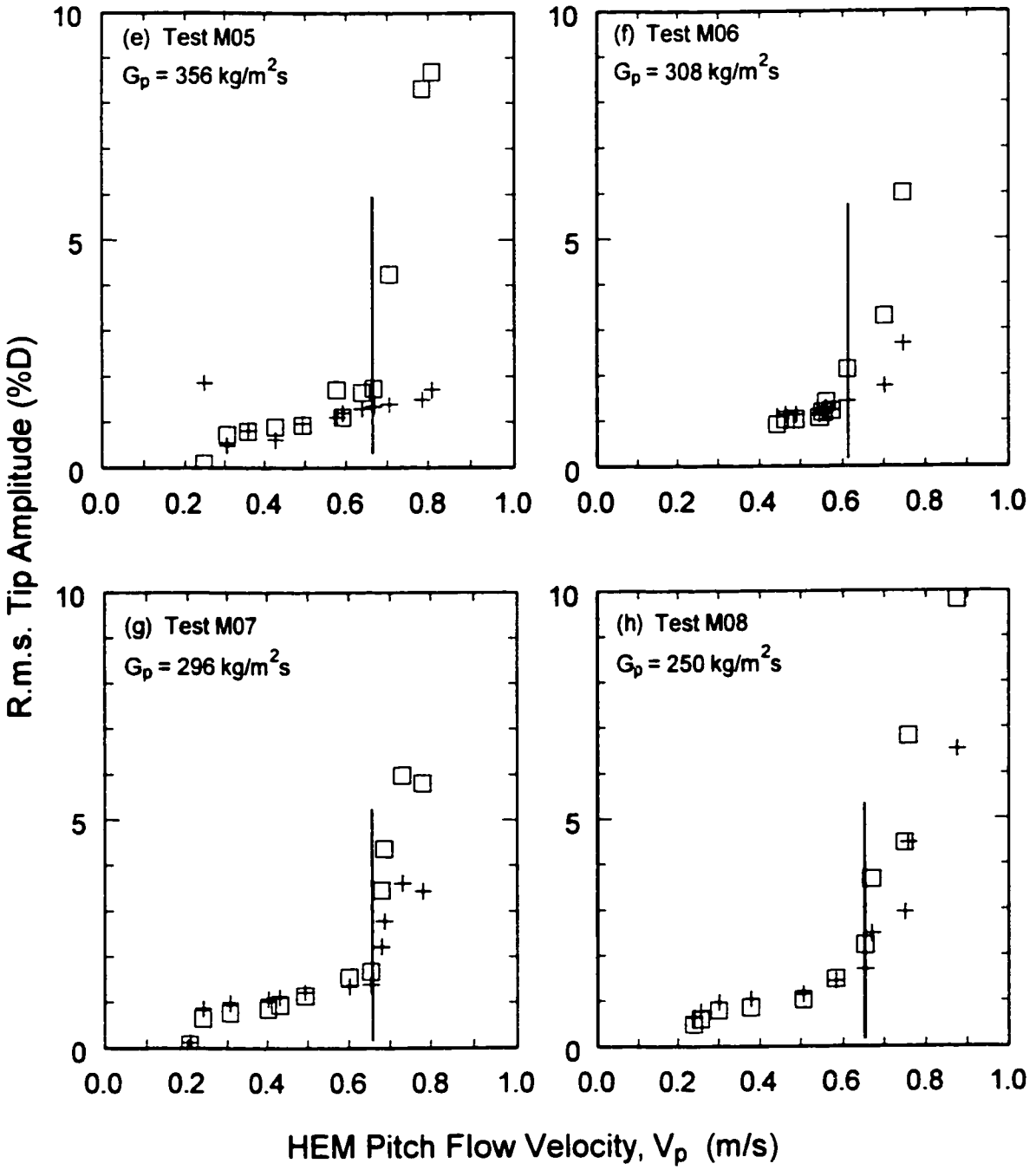

Figure 8.5 (e-h) Amplitude response of the tube array subjected to two-phase R-11 cross-flows of various mass fluxes. + Drag direction, □ Lift direction. Abscissa in terms of V_p, as determined by the HEM. The vertical line represents the conditions selected as corresponding to the fluidelastic threshold.

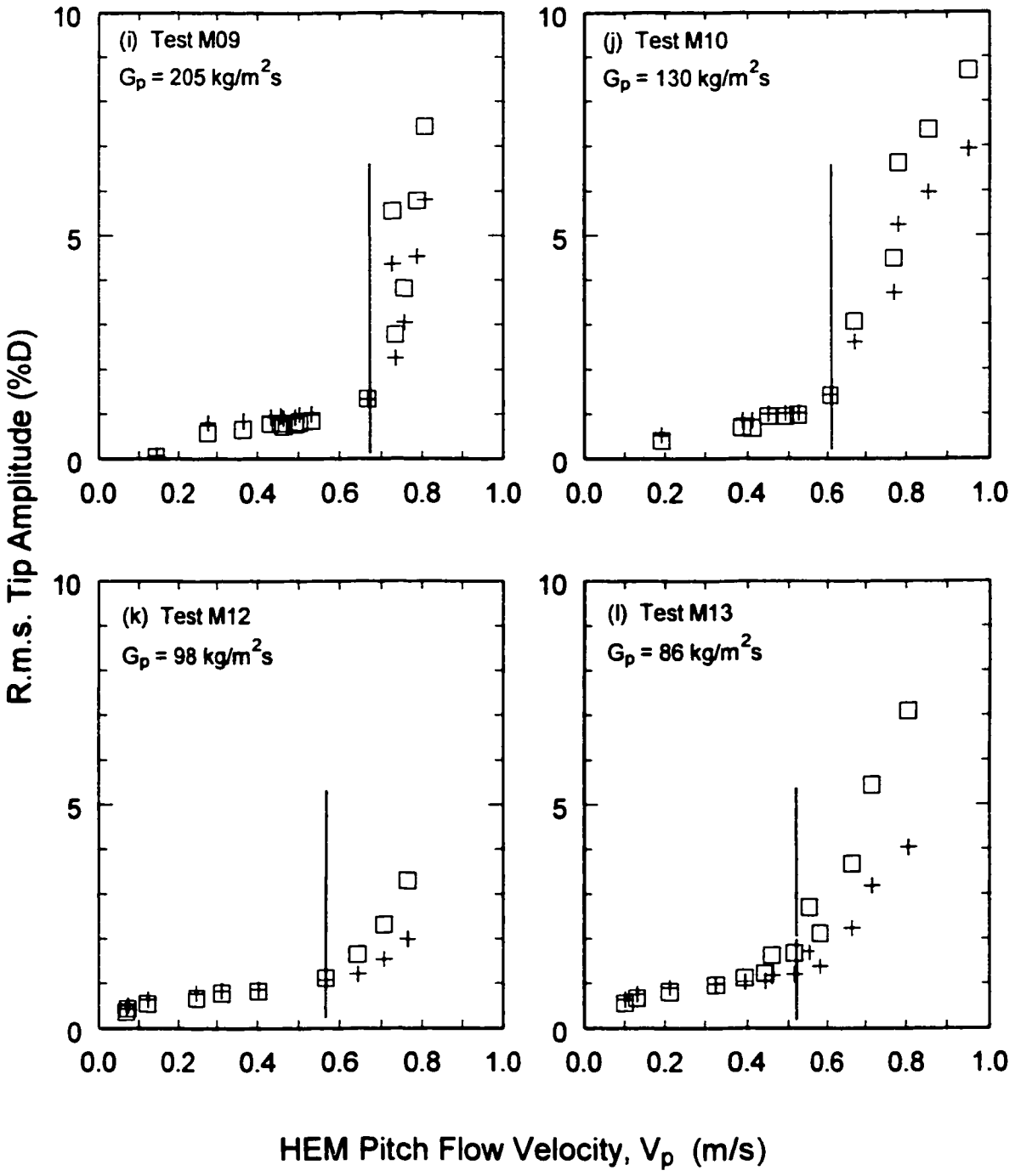

Figure 8.5 (i - l) Amplitude response of the tube array subjected to two-phase R-11 cross-flows of various mass fluxes. + Drag direction, □ Lift direction. Abscissa in terms of V_p, as determined by the HEM. The vertical line represents the conditions selected as corresponding to the fluidelastic threshold.

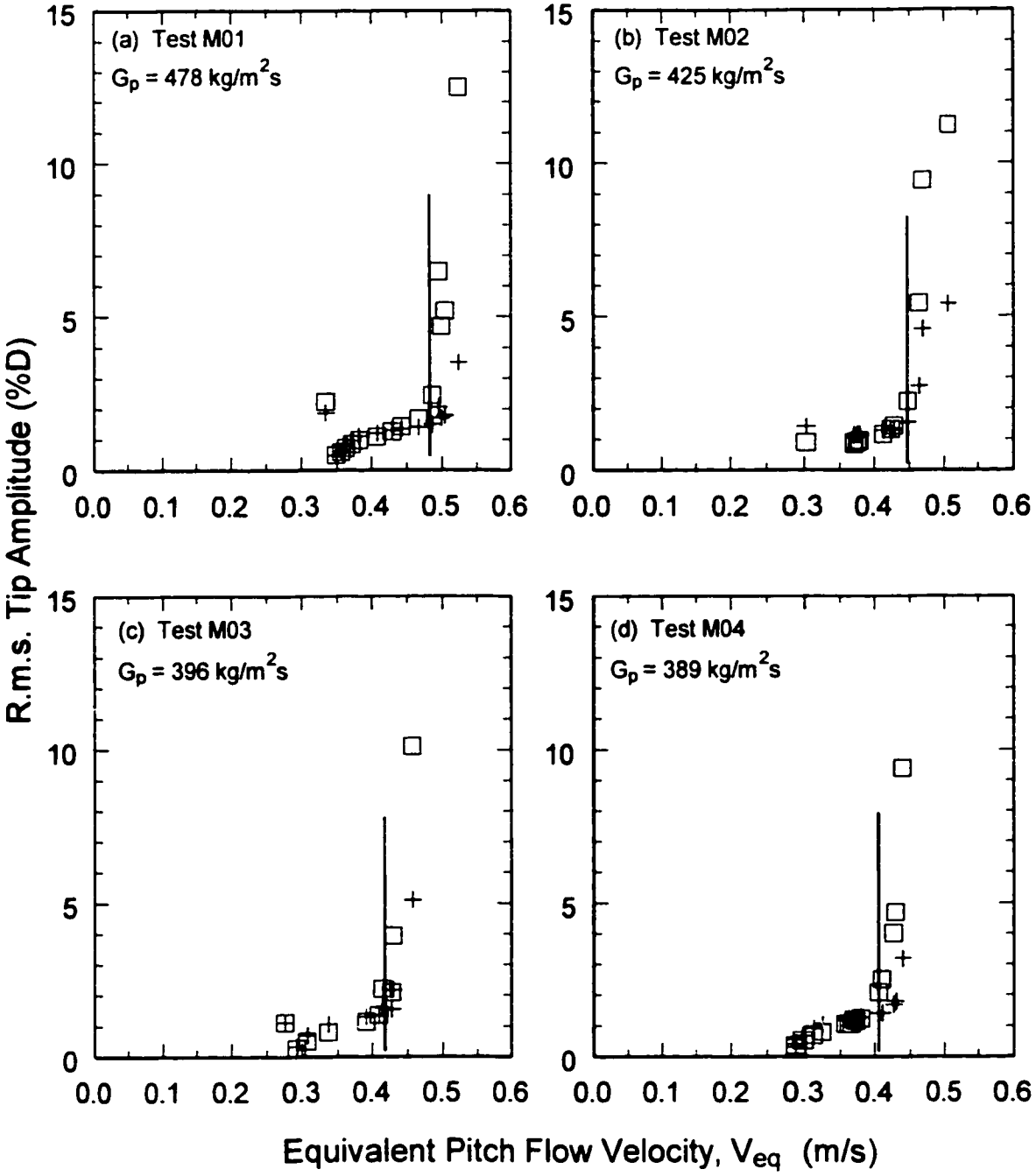

Figure 8.6 (a - d) Amplitude response of the tube array subjected to two-phase R-11 cross-flows of various mass fluxes. + Drag direction, □ Lift direction. Abscissa in terms of V_{eq}, as determined from the RAD method of void fraction measurement. The vertical line represents the conditions selected as corresponding to the fluidelastic threshold.

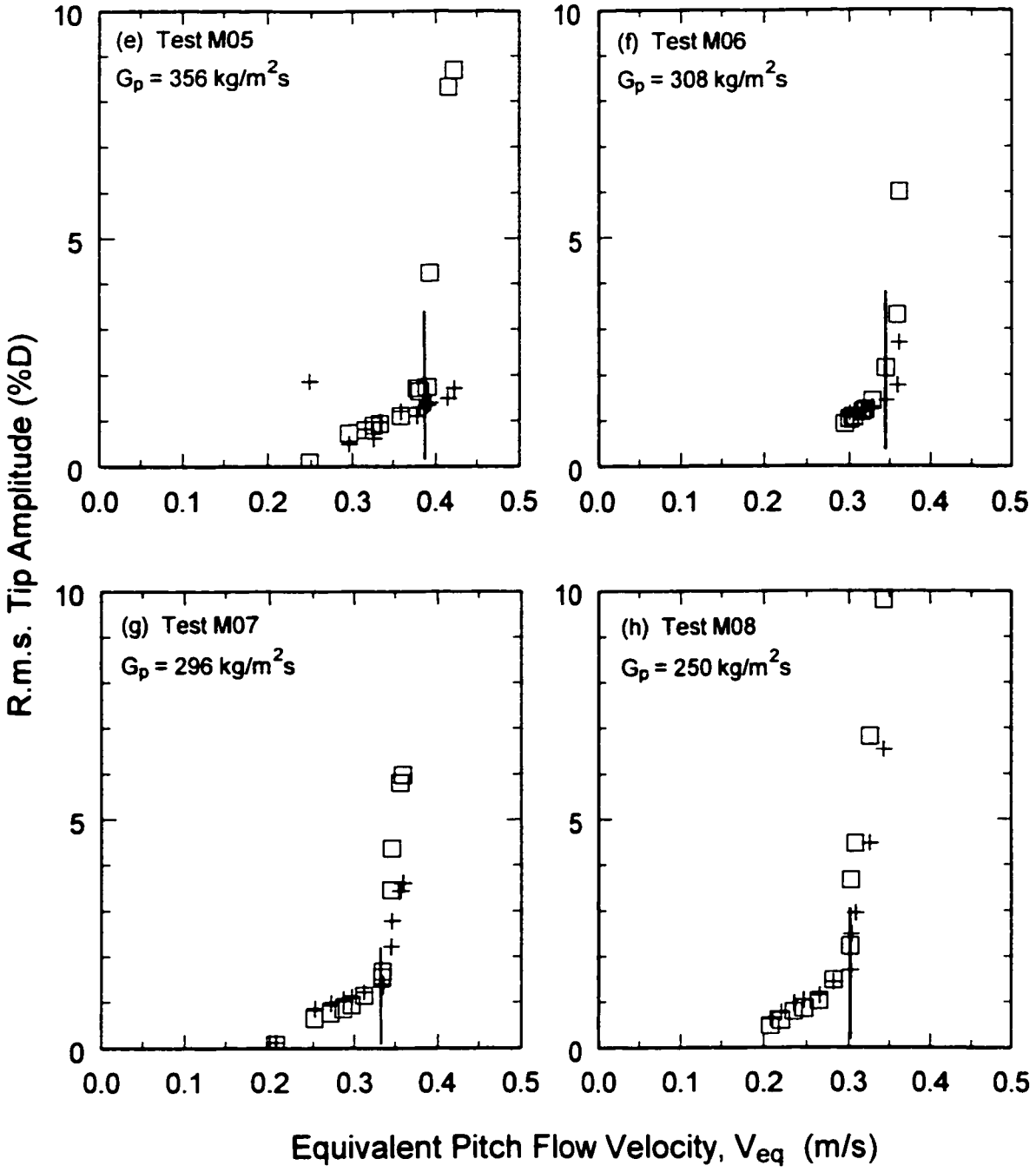

Figure 8.6 (e - h) Amplitude response of the tube array subjected to two-phase R-11 cross-flows of various mass fluxes. + Drag direction, □ Lift direction. Abscissa in terms of V_{eq}, as determined from the RAD method of void fraction measurement. The vertical line represents the conditions selected as corresponding to the fluidelastic threshold.

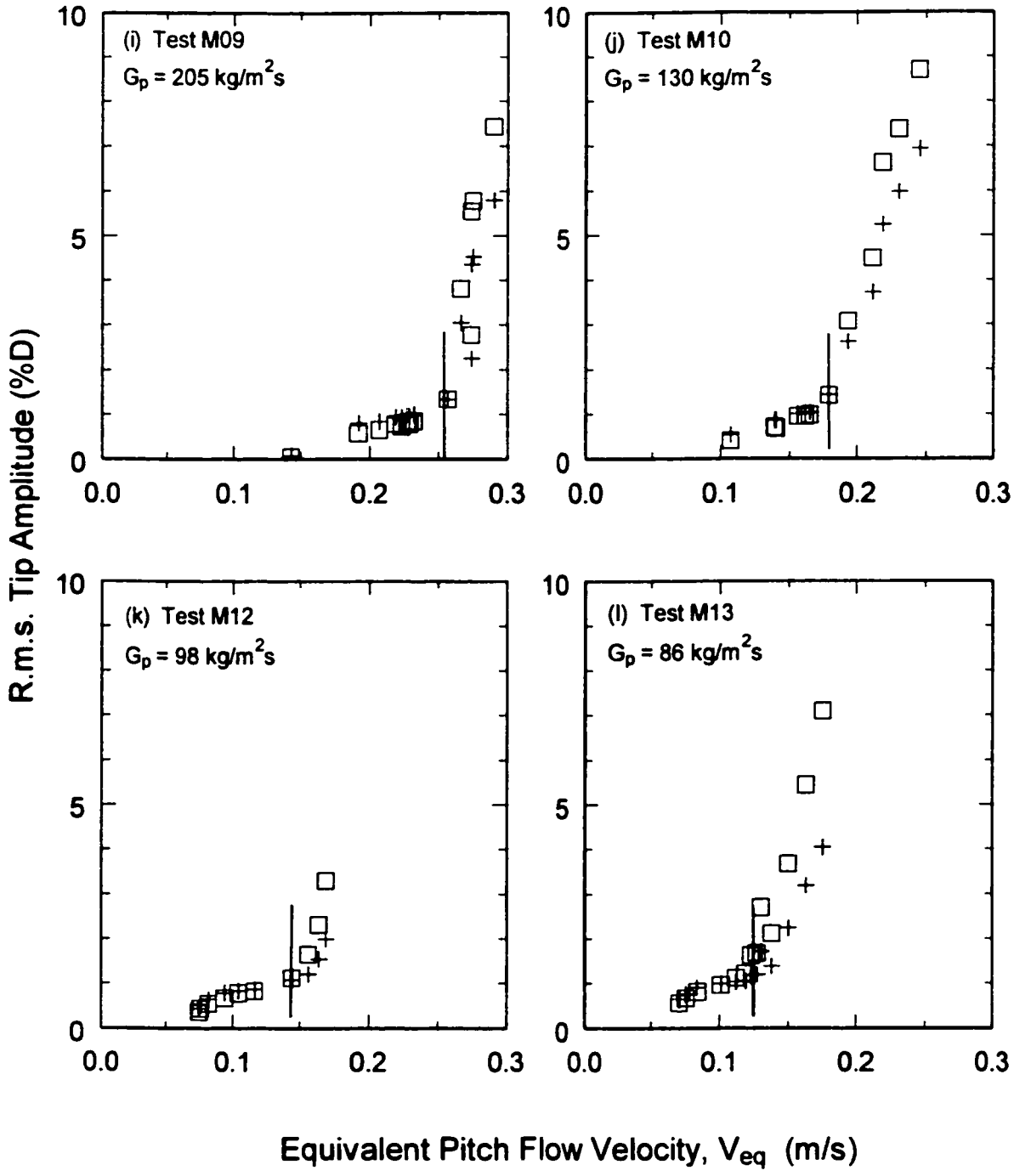

Figure 8.6 (i - l) Amplitude response of the tube array subjected to two-phase R-11 cross-flows of various mass fluxes. + Drag direction, □ Lift direction. Abscissa in terms of V_{eq}, as determined from the RAD method of void fraction measurement. The vertical line represents the conditions selected as corresponding to the fluidelastic threshold.

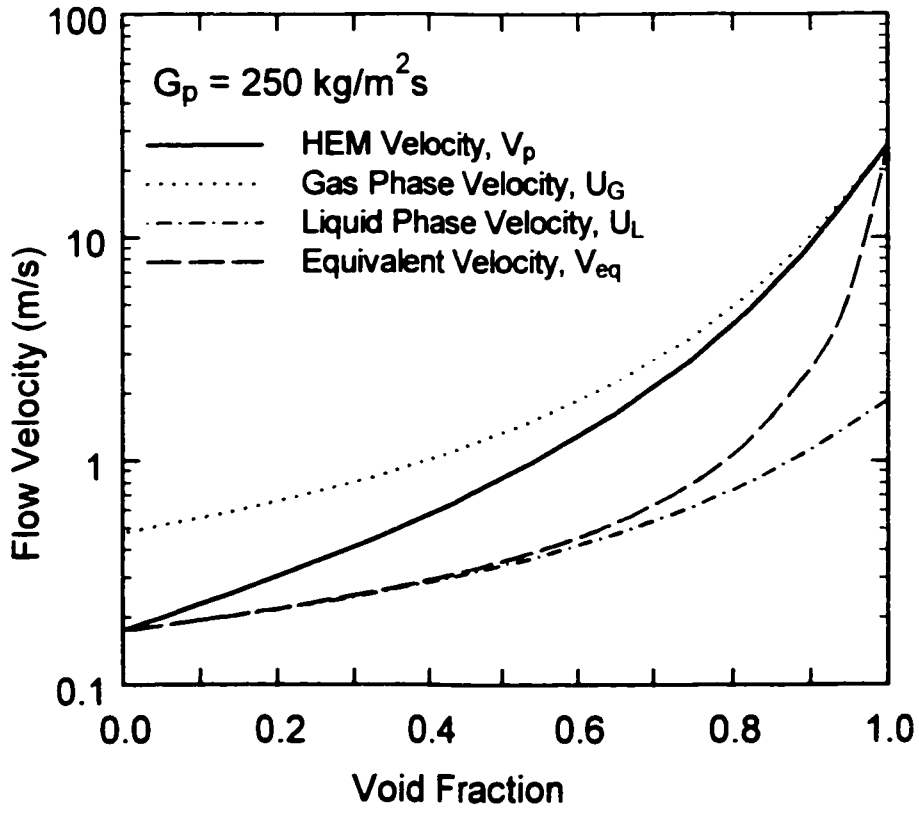

Figure 8.7 Comparison of flow velocity calculation methods for two-phase flow.

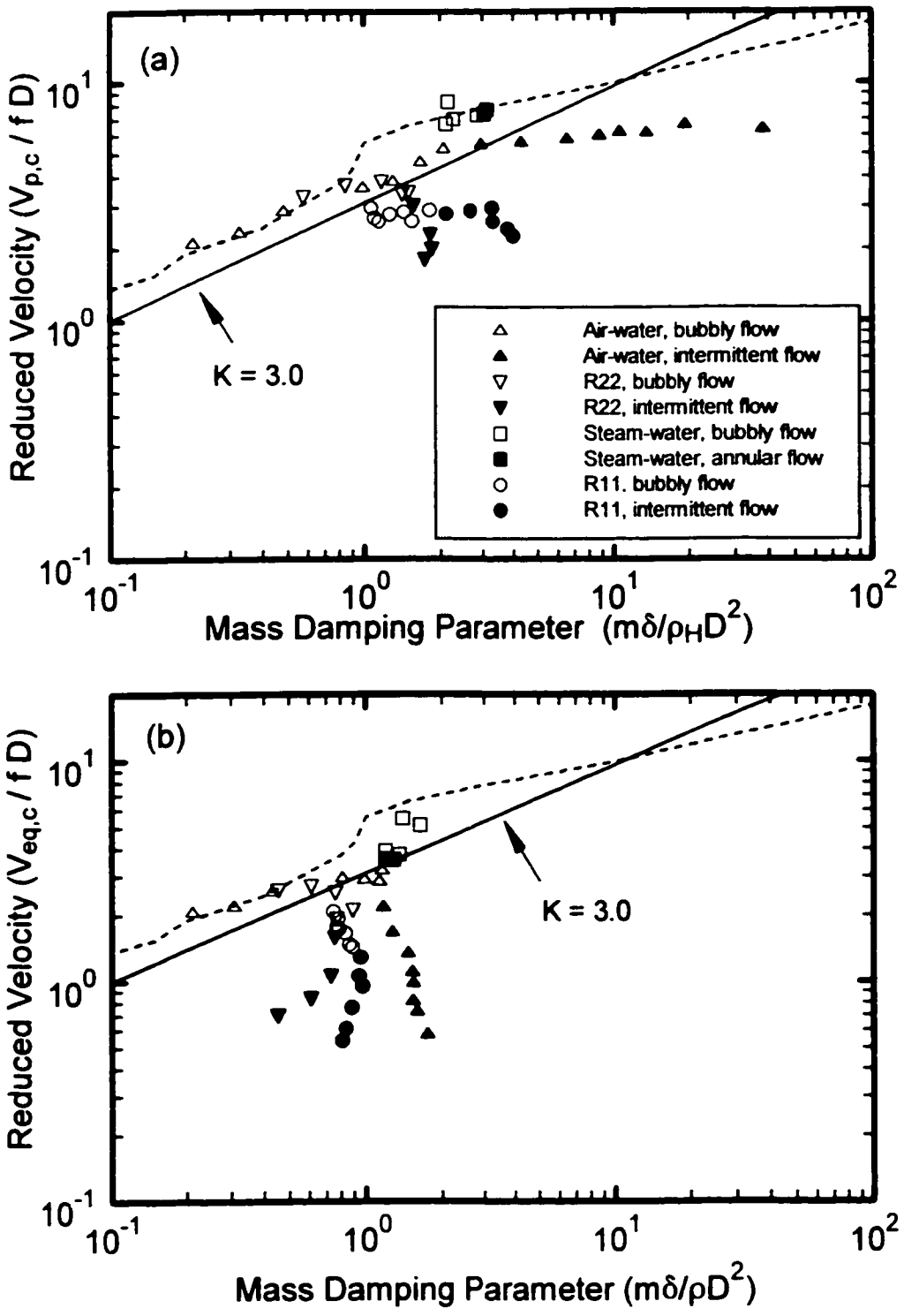

Figure 8.8 Critical flow velocities for fluidelastic instability of parallel triangular tube arrays in two-phase cross-flow. Data analysis by: (a) HEM model, (b) void fraction model. ○● Present study in R-11, △▲ Pettigrew *et al.* (1989b) in air-water, ▽▼ Pettigrew *et al.* (1995) in R-22, □■ Axisa *et al.* (1985) in steam-water, ——— Connors' theory, ------ analytical prediction of Li & Weaver (1997).

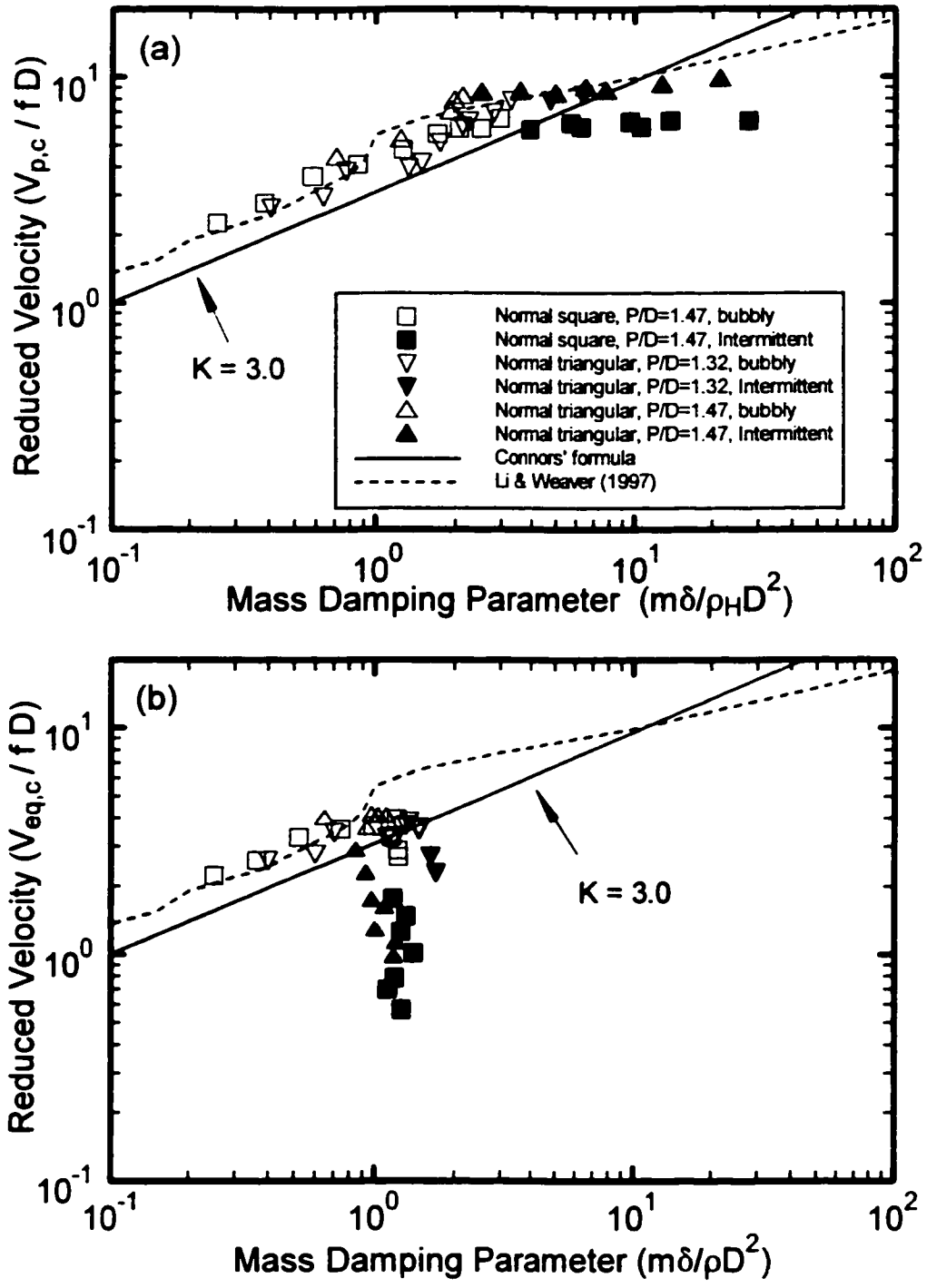

Figure 8.9 Critical flow velocities for fluidelastic instability for the data of Pettigrew *et al.* (1989b) for various tube arrays subjected to two-phase air-water cross-flow. Data analysis by: (a) HEM model, (b) Void Fraction model. ▫▪ normal square array, P/D = 1.47, ▽▾ normal triangular array, P/D = 1.32, △▴ normal triangular array, P/D = 1.47. ——— Connors' theory, ----pred. of Li & Weaver (1997).

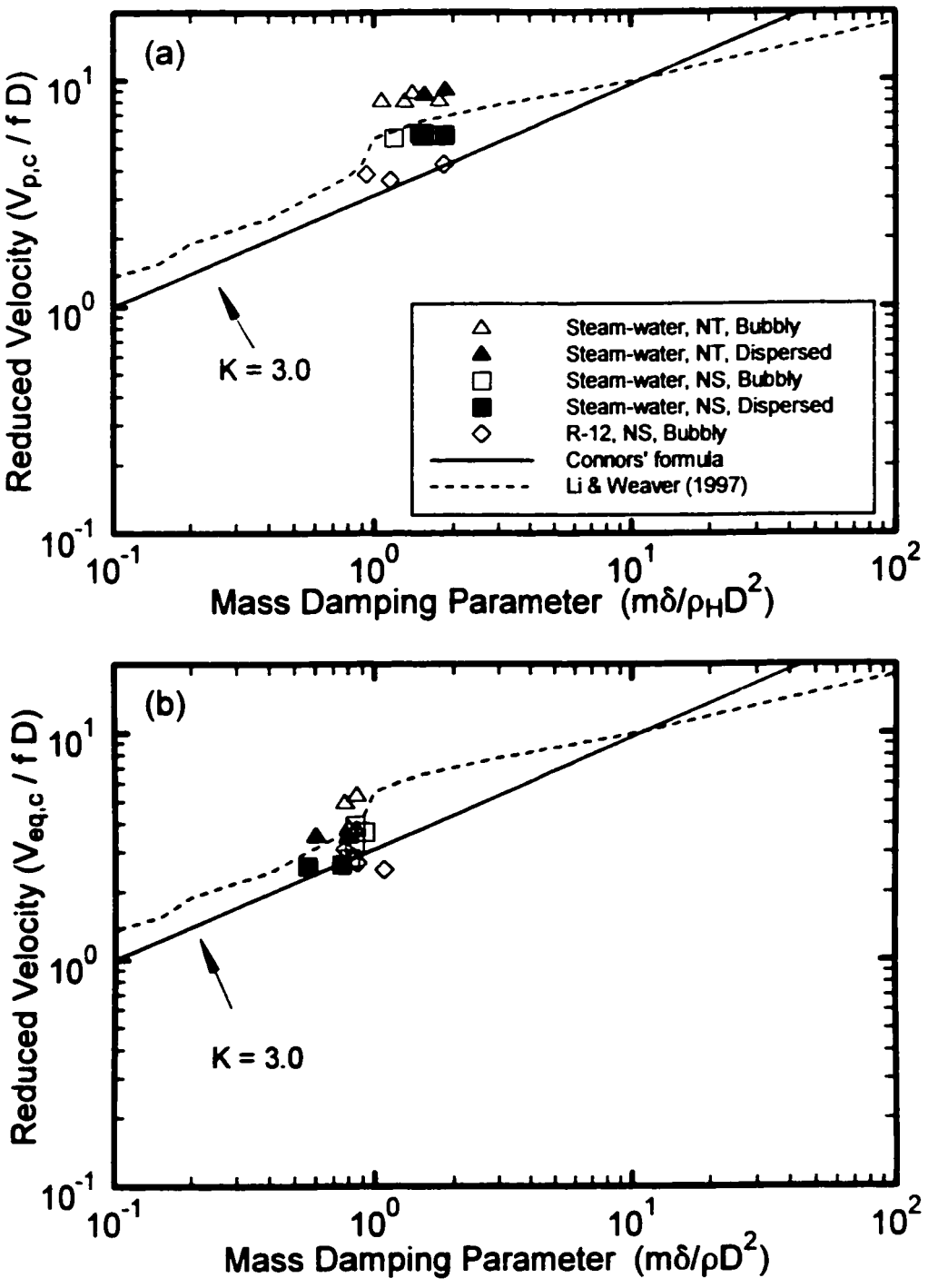

Figure 8.10 Critical flow velocities for fluidelastic instability for the data of other researchers for various tube arrays subjected to two-phase cross-flow. Data analysis by: (a) HEM model, (b) Void Fraction model. △▲, □■ Axisa *et al.* (1985) in steam-water; ◇ Mann and Mayinger (1995) in R-12. ——— Connors' theory, ----- analytical prediction of Li & Weaver (1997).

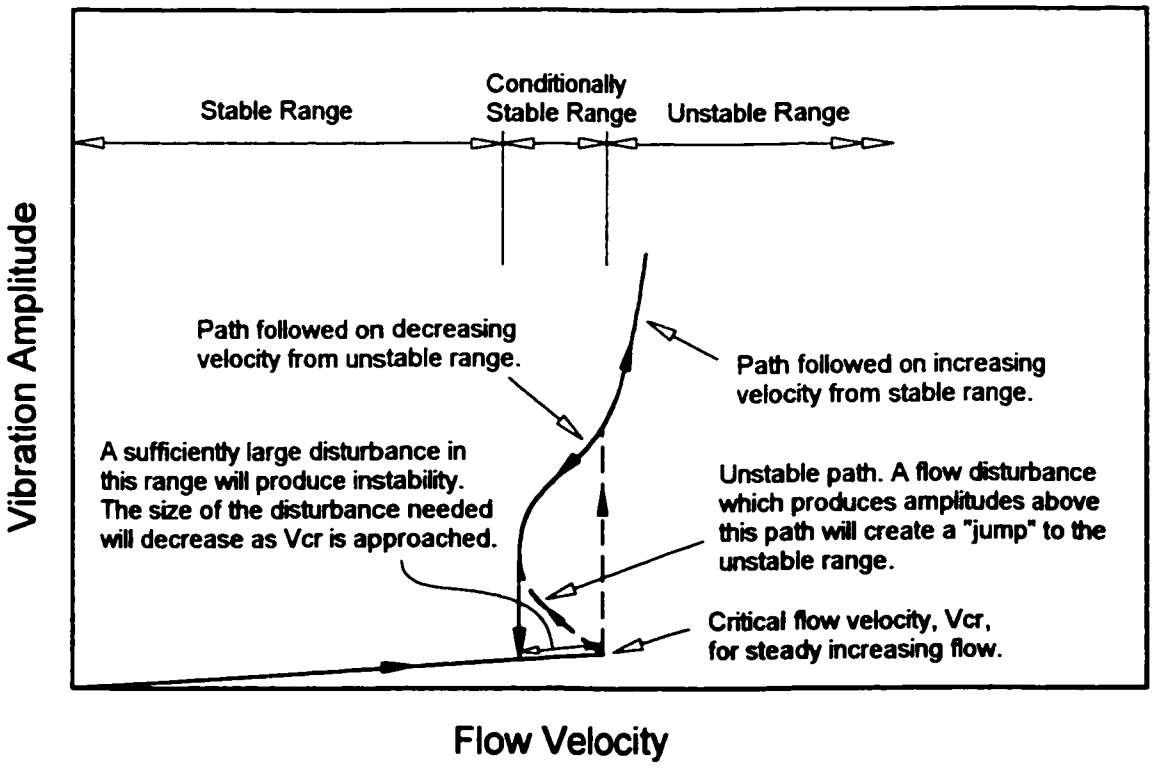

Figure 8.11 Illustration of the non-linear softening effect near the fluidelastic stability threshold of a tube bundle.

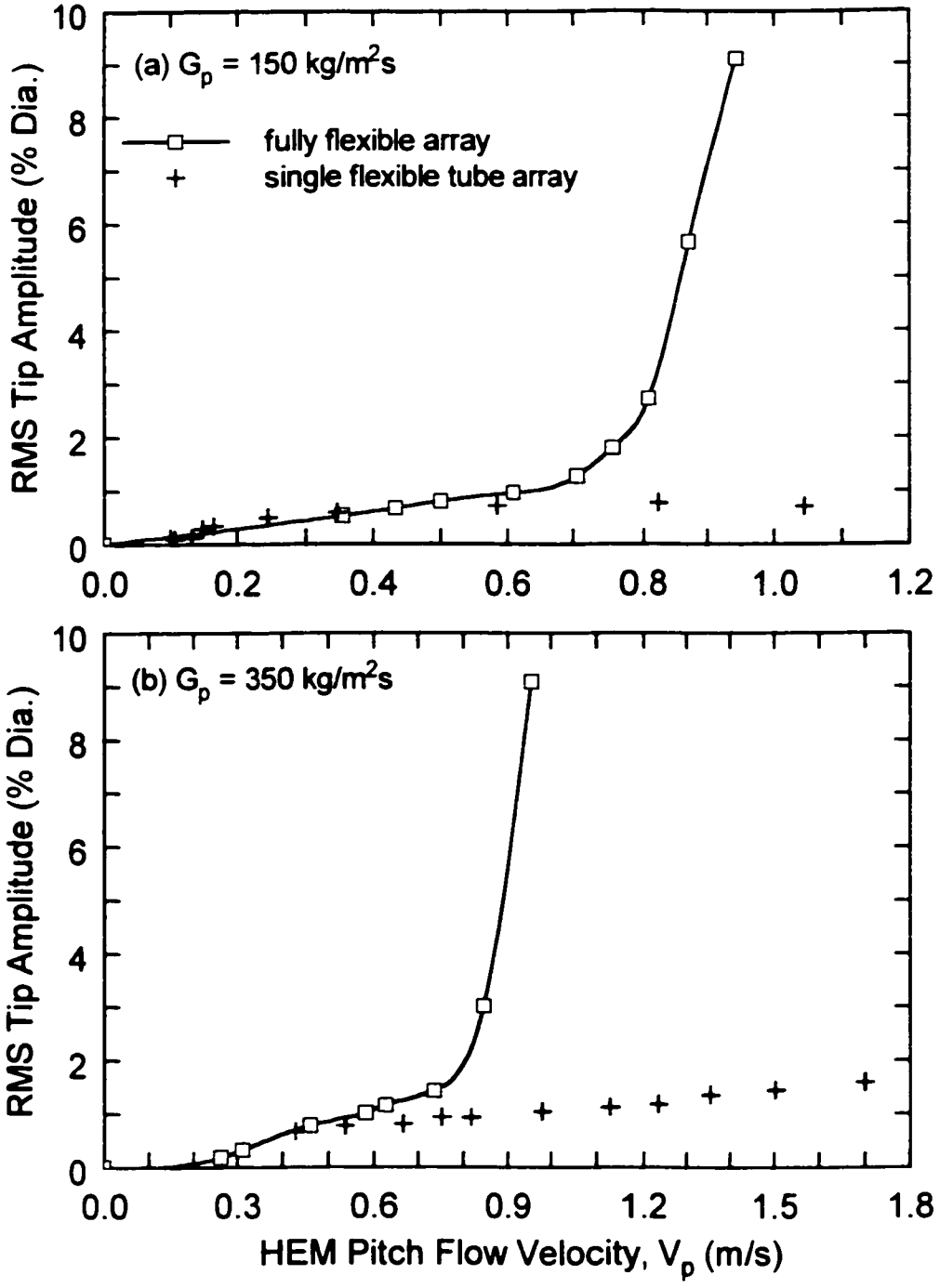

Figure 8.12 Comparison of amplitude response of the fully flexible tube bundle vs. the single flexible tube bundle subjected to two-phase cross-flow for, (a) relatively low mass flux of 150 kg/m^{2}s and (b) relatively high mass flux of 350 kg/m^{2}s.

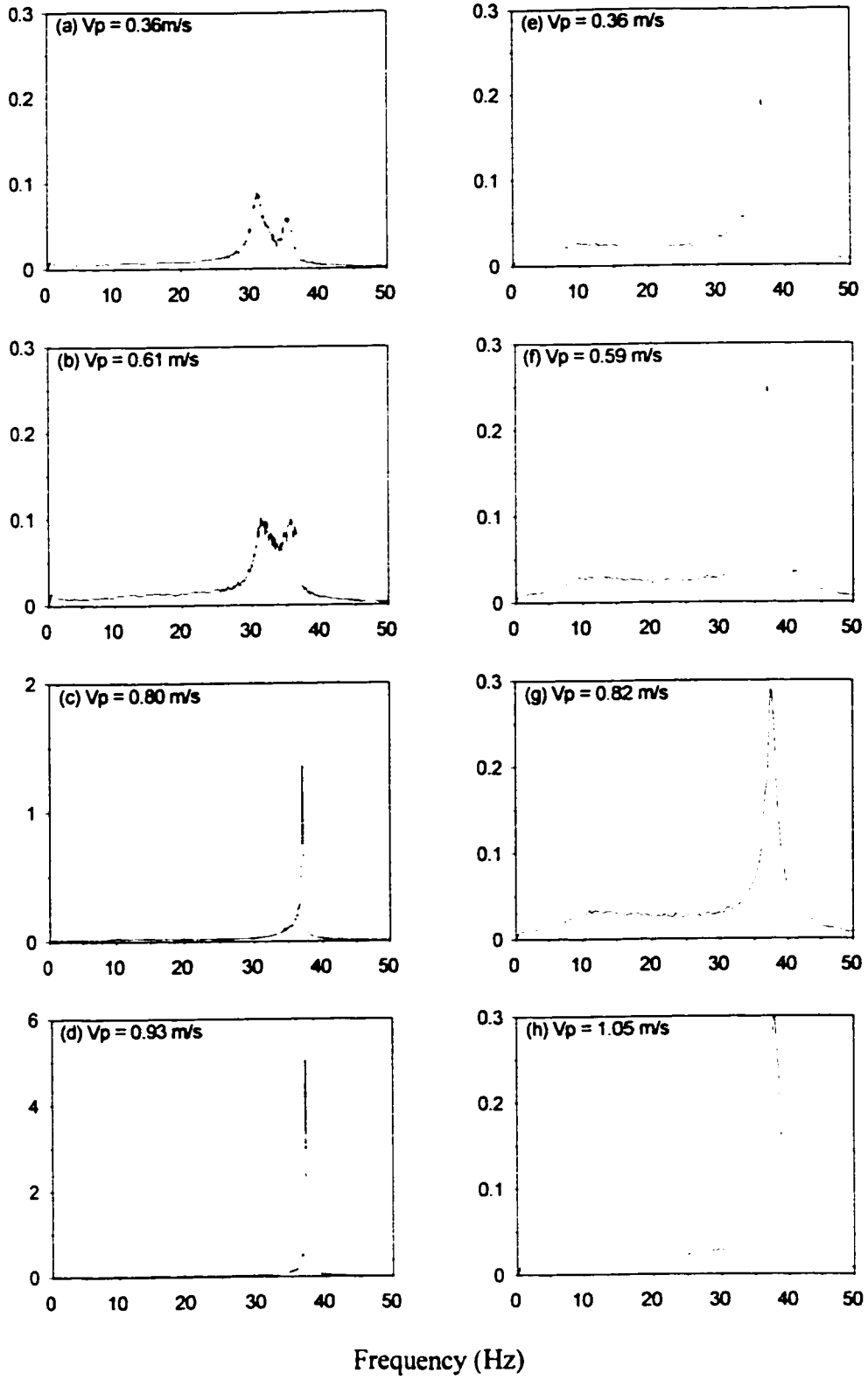

Figure 8.13 Frequency spectra of the monitored tube in the lift direction for a relatively low pitch mass flux of 150 kg/m^{2}s. Graphs (a) to (d) correspond to the fully flexible tube bundle, graphs (e) to (h) correspond to the single flexible tube bundle.

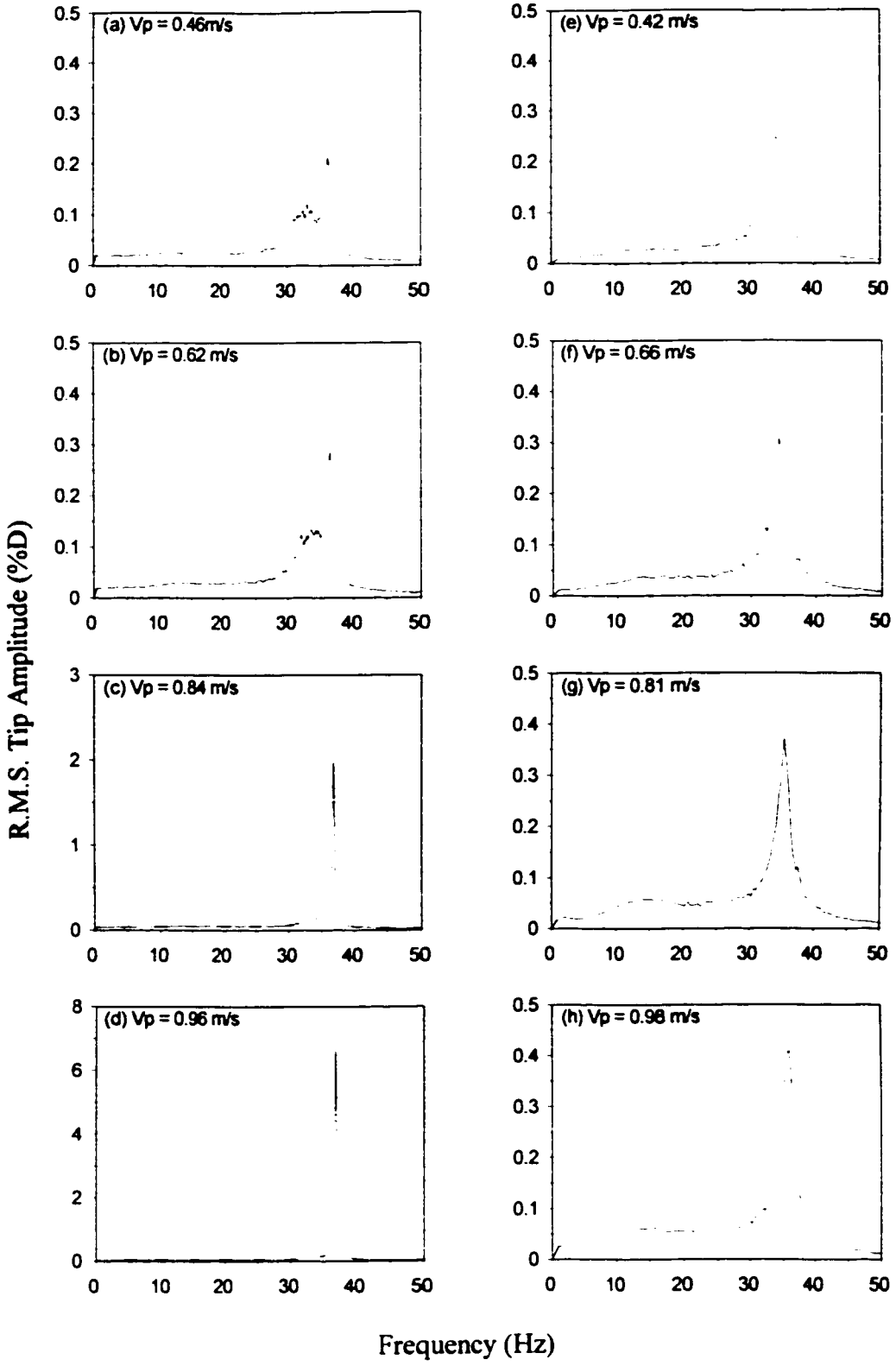

Figure 8.14 Frequency spectra of the monitored tube in the lift direction for a relatively low pitch mass flux of 350 kg/m^{2}s. Graphs (a) to (d) correspond to the fully flexible tube bundle, graphs (e) to (h) correspond to the single flexible tube bundle.

Table 8.2 Summary of Fluidelastic Instability Data for Parallel Triangular Arrays.

Test No.	G_p (kg/m²)	x	ϕ (%)	α (%)	f (Hz)	ζ (%)	m (kg/m)	HEM MODEL $m\delta/\rho_H D^2$	HEM MODEL $V_{p.c}/fD$	VF MODEL $m\delta/\rho D^2$	VF MODEL $V_{eq.c}/fD$
Present Study, R-11, 40°C, P/D =1.44, Dia = 0.00635m, f_a = 38.8 Hz, ζ_a = 0.11%.											
M01	478	0.0080	52.0	31.3	36.8	2.50	0.190	1.07	2.95	0.749	2.078
M02	425	0.0086	53.5	34.3	37.0	2.52	0.188	1.10	2.67	0.782	1.921
M03	396	0.0088	55.2	33.3	37.0	2.53	0.188	1.14	2.60	0.771	1.760
M04	389	0.0101	58.5	32.8	36.8	2.57	0.190	1.27	2.78	0.786	1.730
M05	356	0.0118	63.2	36.2	37.0	2.63	0.188	1.44	2.84	0.837	1.658
M06	308	0.0132	65.5	37.7	37.0	2.66	0.188	1.55	2.60	0.867	1.472
M07	296	0.0162	70.1	38.0	37.0	2.71	0.188	1.82	2.89	0.887	1.431
M08	250	0.0188	73.9	41.6	37.0	2.76	0.188	2.12	2.78	0.957	1.285
M09	205	0.0256	79.1	42.4	37.0	2.77	0.188	2.63	2.88	0.975	1.094
M10	176	0.0311	83.1	41.4	37.0	2.82	0.188	3.28	2.95	0.973	0.948
M11	130	0.0392	85.7	44.7	37.0	2.41	0.188	3.30	2.59	0.882	0.761
M12	98	0.0458	88.6	46.2	37.0	2.24	0.188	3.79	2.41	0.838	0.611
M13	86	0.0493	89.3	45.2	37.0	2.22	0.188	3.99	2.26	0.810	0.537
Pettigrew *et al.* (1989b), air-water, 22°C, P/D = 1.47, Dia = 0.013m, f_a = 33 Hz, ζ_a = 0.2%.											
R-1	688	6.33e-5	5	2.9	26.7	1.1	0.50	0.22	2.09	0.211	2.05
R-2	688	2.12e-4	15	9.0	26.8	1.5	0.50	0.33	2.32	0.307	2.18
R-3	750	4.01e-4	25	15.8	27.0	2.0	0.49	0.49	2.85	0.434	2.54
R-4	775	8.02e-4	40	26.7	27.7	3.4	0.47	0.99	3.58	0.811	2.94
R-5	700	0.0012	50	33.8	28.3	3.9	0.45	1.30	3.80	0.987	2.88
R-6	689	0.0018	60	42.2	28.9	4.2	0.43	1.66	4.58	1.162	3.17
R-7	500	0.0036	75	54.1	29.5	3.4	0.41	2.08	5.20	1.126	2.84
R-9	320	0.0068	85	61.9	30.0	3.0	0.4	2.95	5.43	1.167	2.16
R-11	220	0.0107	90	65.9	30.2	3.0	0.39	4.35	5.54	1.267	1.66
R-13	160	0.0157	93	68.5	30.2	3.2	0.39	6.60	5.73	1.463	1.33
R-15	120	0.0224	95	70.6	30.4	3.1	0.39	8.77	5.94	1.518	1.09
R-17	100	0.0281	96	71.9	30.5	3.0	0.39	10.5	6.13	1.531	0.98
R-19	75	0.0375	97	72.7	30.4	2.9	0.39	13.5	6.09	1.525	0.81
R-21	55	0.0557	98	74.6	30.4	2.8	0.39	19.1	6.57	1.583	0.73
R-23	28	0.1060	99	76.0	30.5	2.9	0.39	37.3	6.31	1.736	0.57
Axisa *et al.* (1985), steam-water, 210°C, P/D = 1.44, Dia = 0.019m, f_a = 74 Hz, ζ_a = 0.2%.											
A	1334	0.059	84.7	77.4	69.0	3.4	0.559	2.27	7.00	1.644	5.11
B	1111	0.090	89.7	82.8	69.8	2.3	0.546	2.15	8.27	1.406	5.48
C	709	0.117	92.1	84.4	70.0	1.8	0.540	2.11	6.67	1.197	3.90
D	518	0.186	95.3	88.3	72.1	1.6	0.532	2.85	7.28	1.364	3.76
E	392	0.250	96.7	90.2	71.0	1.3	0.529	3.04	7.39	1.293	3.57
F	306	0.340	97.8	92.2	71.8	1.0	0.526	3.13	7.68	1.204	3.60
Pettigrew *et al.* (1995), R-22, 23.3°C, P/D = 1.5, Dia = 0.0127m, f_a = 28.5 Hz, ζ_a = 0.15%.											
A	732	0.023	40	22.6	23.9	2.79	0.394	0.58	3.28	0.457	2.59
B	713	0.034	50	29.6	24.6	3.61	0.374	0.85	3.67	0.613	2.69
C	611	0.050	60	36.2	25.0	4.31	0.354	1.18	3.80	0.762	2.52
D	491	0.061	65	38.6	25.3	5.02	0.344	1.50	3.41	0.893	2.10
E	428	0.076	70	41.9	25.8	4.25	0.334	1.42	3.36	0.773	1.92
F	330	0.095	75	44.2	26.0	4.13	0.324	1.57	3.01	0.758	1.58
G	208	0.123	80	44.6	26.3	4.09	0.314	1.83	2.27	0.732	1.05
H	146	0.166	85	47.2	26.9	3.37	0.304	1.85	1.98	0.610	0.83
I	99	0.240	90	51.5	27.5	2.39	0.294	1.73	1.79	0.454	0.70

CHAPTER 9

Damping In Two-Phase Flow

Introduction

This chapter presents damping measurements obtained in this study from the tube bundle in two-phase cross-flows. The results are compared with similar results of other researchers who used a variety of modelling fluids. These results show that the two-phase damping follows a similar trend with respect to HEM void fraction as that of others results, and when normalized by liquid mass ratio and a confinement function, the damping results agree well with other researchers' values.

9.1 Background

There are several noteworthy studies on damping in two-phase flows, such as those of Carlucci (1980) and Carlucci and Brown (1983), who studied axial vibrations and damping for a single tube confined in an annulus and subjected to vertical two-phase flow. They found that damping in two-phase flow was considerably higher than in single-phase flow of either liquid or gas, and it reached a maximum at about 30% to 60% void fraction. Hara and Kohgo (1980) studied the effect of void fraction, confinement and bubble size on damping. Pettigrew and Knowles (1992) performed experiments similar to those of Carlucci (1980) except they also investigated the effect of tube frequency and surface tension. They found the former had a weak effect while the latter had a strong effect, at least for the limited 0% to 25% void fraction range which they covered. Pettigrew *et al.* (1989a) measured damping in tube arrays as part of a program at AECL to study tube bundle vibration in two-phase cross-flow. This experimental program produced extensive two-phase air-water damping data for a variety of tube bundle geometries and

pitch ratios. Axisa *et al.* (1985, 88) have also provided tube bundle damping results in steam-water and air-water flows, mostly at high void fractions.

In this chapter, damping and hydrodynamic mass measurements have been obtained in two-phase R-11 cross-flow using a single flexible tube in a rigid array. One of the primary goals of this research was to compare the damping values obtained in R-11 with those of other researchers who have obtained such data for similar tube arrays using a variety of other fluids. The most comprehensive set of damping data was obtained by Pettigrew *et al.* (1989a) in air-water, over a wide range of void fractions and for four standard tube patterns. Pettigrew *et al.* (1995) obtained damping data in R-22 for a parallel triangular tube array, over a homogeneous void fraction range between 40% and 90%. In both of these studies, the damping data was obtained with a single flexible tube in an array of rigid tubes in order to minimize the hydrodynamic coupling of the surrounding tubes. They found that the hydrodynamic coupling in fully flexible arrays caused the frequency response peaks to broaden, and consequently produced unrealistically high damping values by the half-power bandwidth method. Axisa *et al.* (1985) reported damping data in steam-water at 1.9 MPa for a parallel triangular array, but their study was limited to higher homogeneous void fractions between 85% and 98%. Their data was obtained in a fully flexible array using the half power bandwidth method, so it might be expected that their values would be higher than the comparable data obtained with a single flexible tube in a rigid array. However, at the high void fractions studied by these researchers, the effect of hydrodynamic coupling is small, so that the half power bandwidth method of damping determination could yield results similar to those for the single flexible tube in a rigid array. The fluidelastic stability threshold data over the range of void fraction obtained in the present study are compared with two-phase data from the literature.

9.2 Hydrodynamic Mass Measurements

Hydrodynamic mass is the fluid added mass (or virtual mass) which appears to vibrate with the tube. Hydrodynamic mass ratio, m_R, is the added fluid mass divided by the added mass of the liquid phase, and is determined according to,

$$m_R = \frac{(f_a/f)^2 - 1}{(f_a/f_L)^2 - 1}, \qquad (9.1)$$

where f, f_a and f_L are the tube vibration frequencies in two-phase flow, in air and in liquid respectively. Added mass reduces the natural frequency of a structure when it is moved from a "light" fluid such as air to a "heavy" liquid, such as water. This information is important to designers who wish to better estimate the natural frequencies of the tubes in their heat exchangers. Although the modal frequencies (in air) can be estimated at the design stage and later tested upon construction, it may not be possible to test the frequency under service conditions, where the fluid added mass can cause a significant reduction in modal frequencies. The formulae for determining the experimental and theoretical hydrodynamic mass ratio are defined in the section 5.5 of chapter 5. The measurements were obtained from tube #5 in the single flexible tube array. Figure 9.1 illustrates the hydrodynamic mass ratio as a function of HEM void fraction and RAD void fraction. In these graphs, the data points correspond to measured hydrodynamic mass ratio for various mass fluxes, calculated according to eqn.'s (5.19) and (5.20). The solid line in Figure 9.1 represents the predicted hydrodynamic mass ratio according to eqn. (5.22). Tube bundle #1 was used, which had 1st mode natural frequencies of 31.8 Hz in liquid R-11 and 38.1 Hz in air (which is close to that in vapour R-11) In this case, the measurements were calculated from an average of the lift and drag natural frequency, which often differed by less than 2%. The data in the upper graph, Figure 9.1(a), shows generally a higher hydrodynamic mass ratio than predicted using the HEM void fraction. This is expected since it was earlier demonstrated that the HEM generally over-predicts the relative amount of vapour phase in the flow and thus it is expected to predict a lower added mass. However, in the lower graph, the data shows a lower hydrodynamic mass ratio than predicted using the RAD void fraction. This is not expected however because the RAD void fraction is a better measure of the actual void fraction in the flow than the HEM. It appears as if the tube vibrates in a "lighter" fluid than indicated by the RAD void fraction. If the void fraction were calculated based upon the added mass measurements, it would predict a value in between the HEM and RAD void fraction values: lower than the HEM but higher than the measured RAD value. If a correction

factor, C, were applied to the theoretical prediction of hydrodynamic mass ratio as follows,

$$m_{R,theor} = C(1-\alpha) \quad or \quad C_H(1-\alpha_H), \tag{9.2}$$

then the values which would bring the data into best fit agreement with prediction are $C = 0.52$ or $C_H = 1.44$ for the RAD predictions and HEM respectively. Interestingly, under HEM analysis, the data in Figure 9.1(a) shows some dependency upon mass flux, where high mass flux leads to lower added mass. Under the RAD analysis however, the data shows negligible dependency of mass flux upon added mass.

9.3 Two-Phase Damping Measurements and Analysis

The damping measurements in two-phase flows reported in the previous chapter were obtained from tube #5 in the single flexible tube array. For these measurements, tube bundle #3 was used because bundle #1 had developed an irreparable leak. To be consistent with the method of Pettigrew *et al.* (1989b, 95) for reducing the fluidelastic data, special care was taken to obtain damping values at half the critical mass flux, in order to avoid conditions at which significant fluidelastic forces were present. The data points from the present study shown in Fig.9.2 illustrate that a nearly linear relationship that exists for the R-11 data between the HEM void fraction and pitch mass flux for conditions at the stability threshold. The data of Pettigrew *et al.* (1989b, 95) are plotted as well to illustrate that a similar behaviour was observed in air-water and in R-22 for a mass flux less than about 650 kg/m^{2}s. The dotted line in the graph represents the conditions at half the mass flux for instability for the present study, which was used in subsequent experiments as a target for obtaining the required conditions for damping measurements. This line extends only over a limited range of HEM void fraction from about 54% to 89%. Conditions above 89% HEM void fraction are out of range because it is not practical to operate the flow loop at a pitch mass flux less that about 50 kg/m^{2}s. Below 54% HEM void fraction is out of range because the required threshold flow velocity requires a pitch mass flux in excess of 500 kg/m^{2}s, which is the present maximum capacity of the flow loop in two-phase flow.

The damping data for this study are presented in Fig. 9.3(a) as a function of HEM void

fraction, obtained from a least-square regression fit to the frequency spectra of tube #5, which was averaged over 600 seconds of data and a frequency resolution of 0.125 Hz. It is clear that the measured damping is consistently lower in the lift direction, which is also the direction that the tube becomes fluidelastically unstable in two-phase flow.

In Fig. 9.3(b), the average damping data of the present study (average of the lift and drag direction) are compared with damping data of Pettigrew *et al.* (1989a, 95) in air-water and R-22 and Axisa *et al.* (1985) in steam-water. This figure illustrates that the measured damping ratios, ζ, of the present study are roughly the same as the air-water and steam-water data above 70% homogeneous void fraction, but somewhat lower at void fractions below 70%. Table 9.1 contains the essential damping data for the present study as well as for the other studies used for comparison in this paper.

In Fig. 9.3(c), the average two-phase damping data of the present study are compared with those of the other studies. The two-phase component of tube damping is found when the structural and viscous components are subtracted from the measured damping (ie., $\zeta_{TP} = \zeta - \zeta_s - \zeta_v$). The structural component, ζ_v, for all of the other cases studied in this paper was 0.2% or less so that it represents a nearly negligible component of the overall damping. The viscous component, ζ_s, of damping varies inversely with void fraction, and it can been seen in Table 9.1 that this component becomes negligible above 80% void fraction.

The normalized two-phase component of damping ratio, $(\zeta_{TP})_D$, is plotted in Fig. 9.3(d) along with the other data. Though it is not yet known which parameters are valid for normalizing the two-phase damping data for different fluids, this work follows one method of Pettigrew *et al.* (1994) as follows,

$$(\zeta_{TP})_D = \zeta_{TP}\left[\frac{m}{\rho_L D^2}\right]\left[\frac{(1-(D/D_e)^2)^2}{1+(D/D_e)^3}\right], \qquad (9.3)$$

where ζ_{TP} is the two-phase damping component and the other terms are the liquid mass ratio, and the inverse confinement function. Interestingly, the comparison reveals that the present normalized damping data agree reasonably well with the air-water and R-22 results of Pettigrew *et al.* (1989a,

95). The explanation for the relative upward shift in magnitude between the R-11 data and the air-water data from (c) to (d) in this figure can be found by examining the terms used to normalize the data. In both the R-11 and air-water results, the confinement functions were roughly equal at 1.55 and 1.52 respectively, because this function is fixed by the array type and the pitch-to-diameter (P/D) ratio, which were about the same for all of the comparison data. However, the inverse liquid mass ratio is significantly lower for the R-11 data than for the air-water and R-22 data, which caused the upward shift in the magnitude of the R-11 data when it was normalized using eqn. (9.3). Interestingly, the damping data of the present study achieved satisfactory agreement with the air-water and R-22 data without any correction for surface tension effects. However, initial experiments by Pettigrew and Knowles (1992) in air-water showed a roughly linear correlation between damping and surface tension of the liquid phase for lower tube frequencies (ie., 28 Hz and lower). This observation suggested an additional surface tension term in equation (9.3) such as,

$$\textit{Surface Tension Term} = \left[\frac{\sigma_{H_2O,\,20^\circ C}}{\sigma_T}\right] . \qquad \textbf{(9.4)}$$

However, if this surface tension term were included as a normalizing parameter, then the R-11 damping results in Fig. 9.3(d) would increase by a factor of about 4 (verified easily by comparing the surface tension data in Table 4.1 in Chapter 4) which would set them far apart from the other data. This suggests that the effect of surface tension is not as strong as first believed, but there are a number of issues which must be resolved before a reliable design factor can be devised to account for it. Firstly, it is well known that a small amount of contaminant in the liquid can significantly decrease the surface tension from the published value, so that a reliable measurement method of the actual liquid surface tension is required. Secondly, the initial work by Pettigrew and Knowles (1992) did not extend beyond 25% void fraction, and their results for tube frequencies of 28Hz tended towards a decreasing dependence on surface tension as the void fraction was increased from 5% to 15% to 25%. Hence the effect of surface tension is excluded from this analysis until more comprehensive data become available.

The effect of varying mass flux on the measured damping for the single flexible tube in the

rigid array is illustrated in Fig. 9.4. Each graph in this figure corresponds to a roughly constant void fraction. It appears, for HEM void fractions below about 80%, that increasing mass flux leads to a slight increase in the damping effect of the two-phase flow. It is not known why this trend should exist, but it must be noted that the effect of velocity ratio is greater at low mass flux, and therefore the difference between the actual void fraction and the HEM predicted value will be greater. Hence, the slightly lower damping value in the lower range of mass flux may arise because the actual void fraction decreases as the mass flux decreases. The flow regime diagram of Ulbrich and Mewes (1994) is shown in Figure 9.5, where the data corresponding to the damping measurements is plotted. This figure indicates that the damping measurements were made in the bubbly flow regime. Therefore, any damping effect of intermittent flow is not likely to be exhibited in the damping measurements of this chapter.

9.4 Conclusions for Hydrodynamic Mass and Damping

This chapter presents damping and hydrodynamic mass measurements that have been obtained in two-phase R-11 cross-flow using a single flexible tube in a rigid array. Special care has been taken to obtain these measurements at pitch mass fluxes which correspond to roughly half the value at the fluidelastic instability threshold.

Damping measurements have been obtained from the single flexible tube array, showing that the tube damping in two-phase cross-flow peaks at about 75% to 80% HEM void fraction, and decreases at lower and especially higher void fraction. This is in reasonable quantitative agreement with air-water and R-22 data. Comparison has revealed that, while the measured two-phase damping values in R-11 are slightly lower than comparable air-water data, the normalized two-phase component of damping is actually a bit higher than in air-water, owing to the large difference in liquid mass ratio (a normalizing parameter) between these two sets of data. However, it must be noted that the present normalizing parameters are still in the developmental stages, since the effects of liquid surface tension or flow regime have not been adequately determined.

9.5 Method of Damping Data Analysis

Two-Phase Damping Component:

Following the recommendations of Pettigrew and Taylor (1994), the two-phase fluid component of tube damping is determined by subtracting the structural and viscous components from the measured (total) damping,

$$\zeta_{TP} = \zeta - (\zeta_s + \zeta_v) \ . \tag{9.5}$$

The structural component ζ_s, can be determined by applying the logarithmic decrement analysis to the decay trace of the tube vibrating in air.

Viscous Damping Component:

The viscous damping coefficient in two-phase mixtures is taken to be analogous to viscous damping as discussed in Pettigrew *et al.* (1986),

$$\zeta_v = \frac{\pi}{\sqrt{8}}\left(\frac{\rho_{HEM} D^2}{m}\right)\left(\frac{2\nu_{TP}}{\pi f D^2}\right)^{0.5} \frac{[1+(D/D_e)^3]}{[1-(D/D_e)^2]^2} \ . \tag{9.6}$$

The equivalent two-phase viscosity, ν_{TP}, follows the method of McAdams *et al.* (1942),

$$\nu_{TP} = \frac{\nu_L}{1 + \phi\left(\frac{\nu_L}{\nu_G} - 1\right)} \ . \tag{9.7}$$

The confinement term, (D/D_e), for a parallel triangular tube array follows the work of Rogers *et al.* (1984), and is given by,

$$\frac{D}{D_e} = \left[\left(0.96 + 0.50\,\frac{P}{D}\right)\frac{P}{D}\right]^{-1} \ , \tag{9.8}$$

where D_e is an equivalent diameter of the surrounding tubes.

Normalized Two-Phase Damping

Following the proposed design guideline of Pettigrew and Taylor (1994), the normalized two-phase damping, $(\zeta_{TP})_D$, is given by,

$$(\zeta_{TP})_D = \zeta_{TP}[\frac{m}{\rho_L D^2}][\frac{(1-(D/D_e)^2)^2}{1+(D/D_e)^3}] , \qquad \textbf{(9.9)}$$

where the normalizing parameters are the liquid mass ratio and the inverse confinement function.

Table 9.1 Summary of damping data analysis for parallel triangular arrays subjected to two-phase cross-flows.

Test No.	ϕ (%)	f (Hz)	ρ (kg/m^3)	m (kg/m)	ν_{TP} (μN/m)	ζ	Damping Ratio (%) ζ_s	ζ_v	ζ_{TP}	$(\zeta_{TP})_D$
Present Study: Refrigerant 11, 36°C, P/D = 1.44, D = 0.00635 m, D_e/D = 2.42. $\nu_L = 2.57*10^{-7}$ m^2/s, $\nu_G = 1.32*10^{-6}$ m^2/s, ρ_L = 1450 kg/m^3.										
A	52	35.7	699	.203	0.44	2.91	0.11	0.33	2.47	5.6
B	58	35.8	607	.202	0.48	2.44	0.11	0.30	2.03	4.7
C	62	35.4	556	.208	0.51	2.82	0.11	0.29	2.42	5.4
D	64	36.1	531	.199	0.53	2.68	0.11	0.27	2.29	5.2
E	71	35.7	427	.204	0.60	2.91	0.11	0.24	2.56	5.7
F	76	35.5	355	.207	0.66	3.15	0.11	0.21	2.83	6.3
G	80	35.1	295	.211	0.72	3.11	0.11	0.18	2.82	6.2
H	88	36.7	183	.192	0.88	2.49	0.11	0.13	2.25	4.8
Pettigrew *et al.* (1989a): Air-water, 22°C, P/D = 1.47, D = 0.013 m, D_e/D = 2.48. $\nu_L = 1.0*10^{-6}$ m^2/s, $\nu_G = 1.47*10^{-5}$ m^2/s, ρ_L = 998 kg/m^3.										
R-2	15	26.8	850	0.50	1.2	1.5	0.2	0.93	0.4	0.8
R-3	25	27.0	750	0.49	1.3	2.0	0.2	0.87	0.9	1.7
R-4	40	27.7	600	0.47	1.6	3.4	0.2	0.76	2.4	4.4
R-5	50	28.3	501	0.45	1.9	3.9	0.2	0.68	3.0	5.3
R-6	60	28.9	401	0.43	2.3	4.2	0.2	0.59	3.4	5.7
R-7	75	29.5	251	0.41	3.3	3.4	0.2	0.44	2.8	4.5
R-9	85	30.0	151	0.40	4.8	3.0	0.2	0.32	2.5	3.9
R-11	90	30.2	101	0.39	6.3	3.0	0.2	0.24	2.6	4.0
R-15	95	30.4	51	0.39	8.8	3.1	0.2	0.14	2.8	4.3
R-19	97	30.4	31	0.39	11.0	2.9	0.2	0.10	2.6	4.0
R-23	99	30.5	11	0.39	13.0	2.9	0.2	0.04	2.7	4.1
Axisa *et al.* (1985): Steam-water, 210°C, P/D = 1.44, D = 0.0191 m, D_e/D = 2.42. $\nu_L = 1.5*10^{-7}$ m^2/s, $\nu_G = 1.66*10^{-6}$ m^2/s, ρ_L = 852 kg/m^3.										
A	84.7	69.0	145	0.56	0.59	3.4	0.2	0.07	3.1	3.6
B	89.7	69.8	101	0.55	0.74	2.3	0.2	0.05	2.0	2.3
C	92.1	70.0	80	0.54	0.85	1.8	0.2	0.05	1.6	1.8
D	95.3	72.0	51	0.53	1.0	1.6	0.2	0.03	1.4	1.6
E	96.7	71.0	39	0.53	1.2	1.3	0.2	0.03	1.1	1.2
F	97.8	71.8	29	0.53	1.3	1.0	0.2	0.02	0.8	0.9
Pettigrew *et al.* (1995): Refrigerant 22, 23.3°C, P/D = 1.5, D = 0.0127 m, D_e/D = 2.57. $\nu_L = 1.36*10^{-7}$ m^2/s, $\nu_G = 3.02*10^{-7}$ m^2/s, ρ_L = 1197 kg/m^3.										
A	40	23.9	737	0.39	3.31	2.8	0.2	0.26	2.3	3.2
B	50	24.6	621	0.37	3.73	3.6	0.2	0.24	3.2	4.1
C	60	25.0	505	0.35	4.34	4.3	0.2	0.21	3.9	4.8
D	65	25.3	448	0.34	4.76	5.0	0.2	0.20	4.6	5.5
E	70	25.8	390	0.33	5.31	4.3	0.2	0.18	3.9	4.5
F	75	26.0	332	0.32	6.06	4.1	0.2	0.16	3.8	4.3
G	80	26.3	274	0.31	7.11	4.1	0.2	0.14	3.8	4.1
H	85	26.9	216	0.30	8.73	3.4	0.2	0.11	3.1	3.2
I	90	27.5	158	0.29	11.5	2.4	0.2	0.09	2.1	2.2

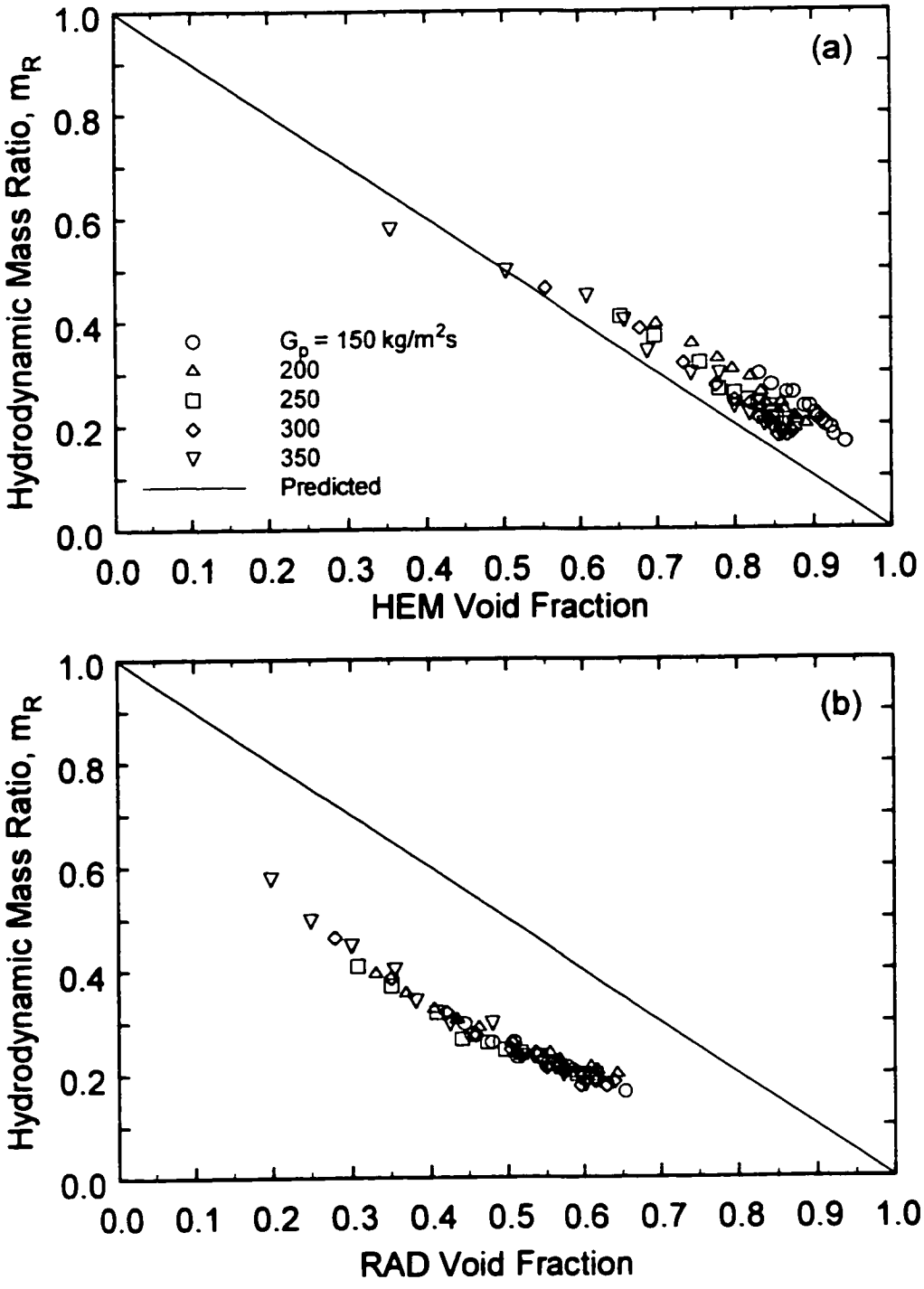

Figure 9.1 Measured data for hydrodynamic mass ratio, m_R, for the single flexible tube bundle subjected to two-phase R-11 cross-flow. Comparison of measurement and theory using, (a) HEM void fraction and, (b) RAD void fraction.

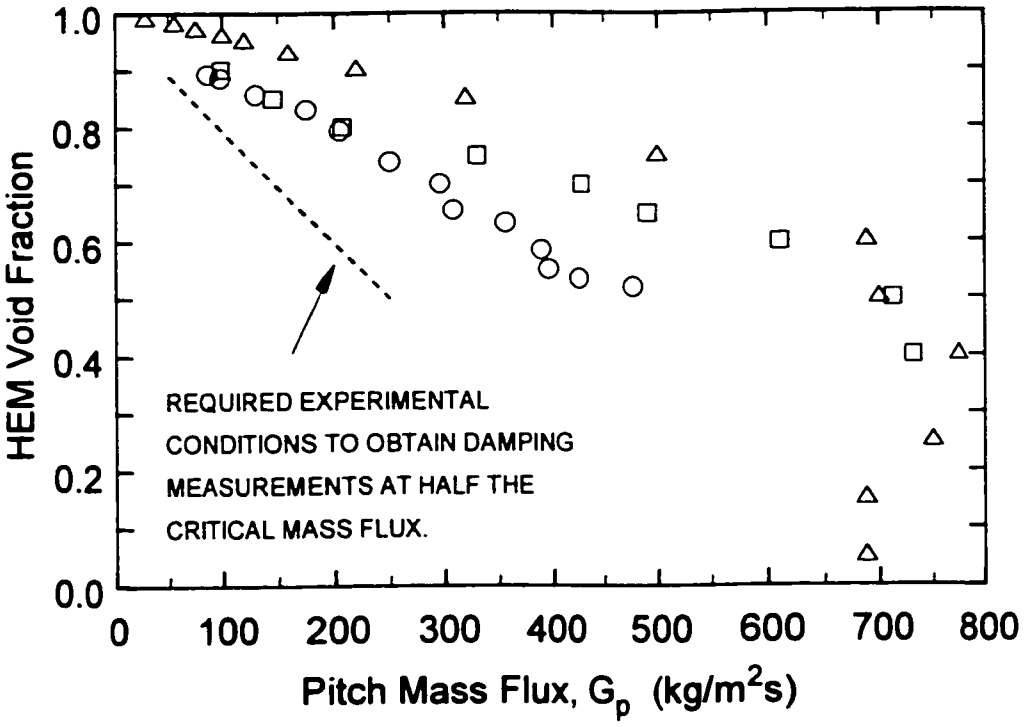

Figure 9.2 Summary of conditions corresponding to the fluidelastic stability threshold for fully flexible, parallel triangular arrays subjected to two-phase cross-flow. o Present study in R-11, ▵ Pettigrew *et al.* (1989b) in air-water, □ Pettigrew *et al.* (1995) in R-22.

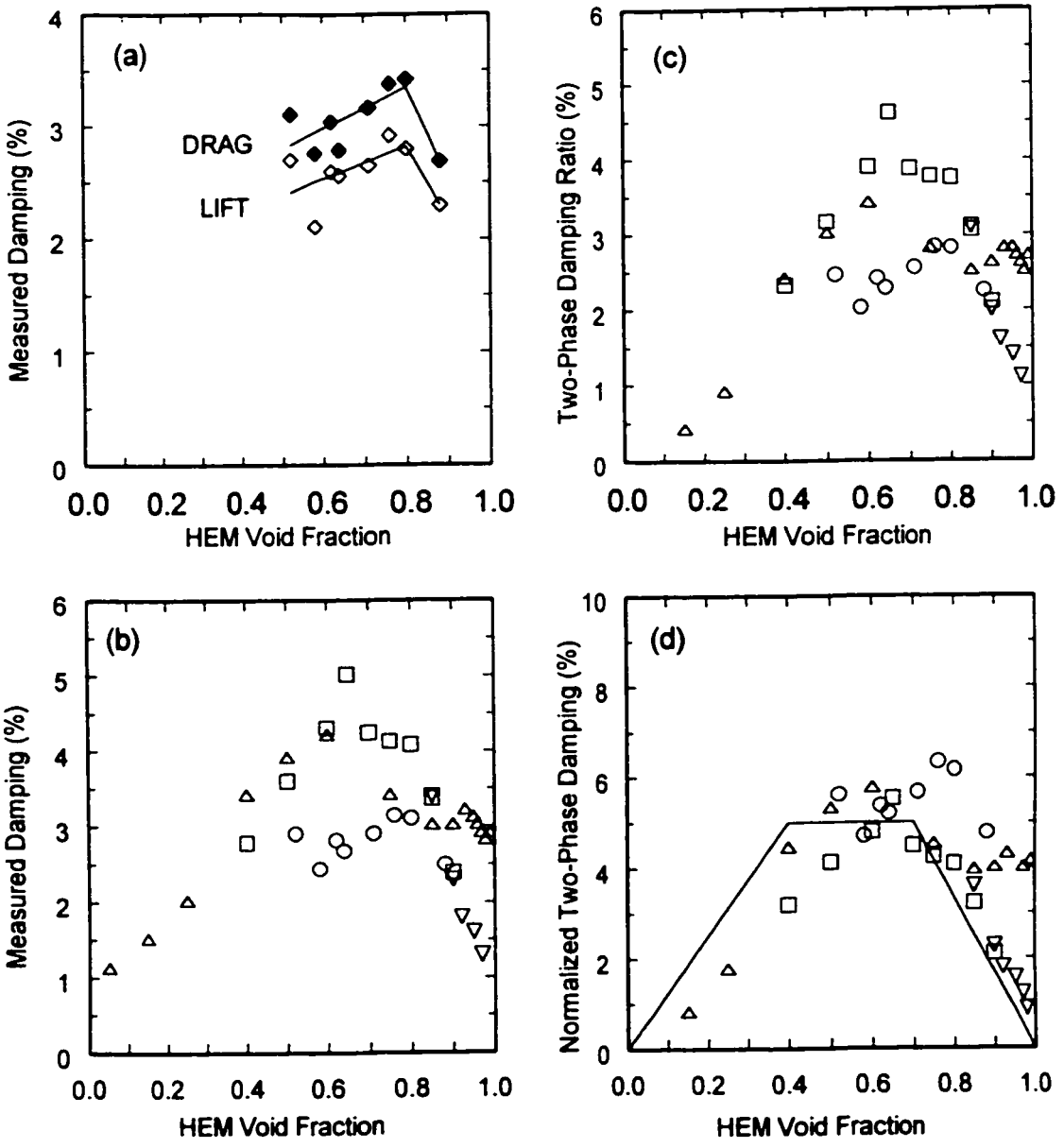

Figure 9.3 Summary of damping measurements for a single flexible tube in parallel triangular arrays, subjected to two-phase cross-flow. (a) Present study in R-11, ◇ lift direction, ◆ drag direction. (b) Measured damping comparison, (c) two-phase damping comparison, (d) normalized two-phase damping comparison. ○ Present study in R-11, △ Pettigrew *et al.* (1989b) in air-water, □ Pettigrew *et al.* (1995) in R-22.

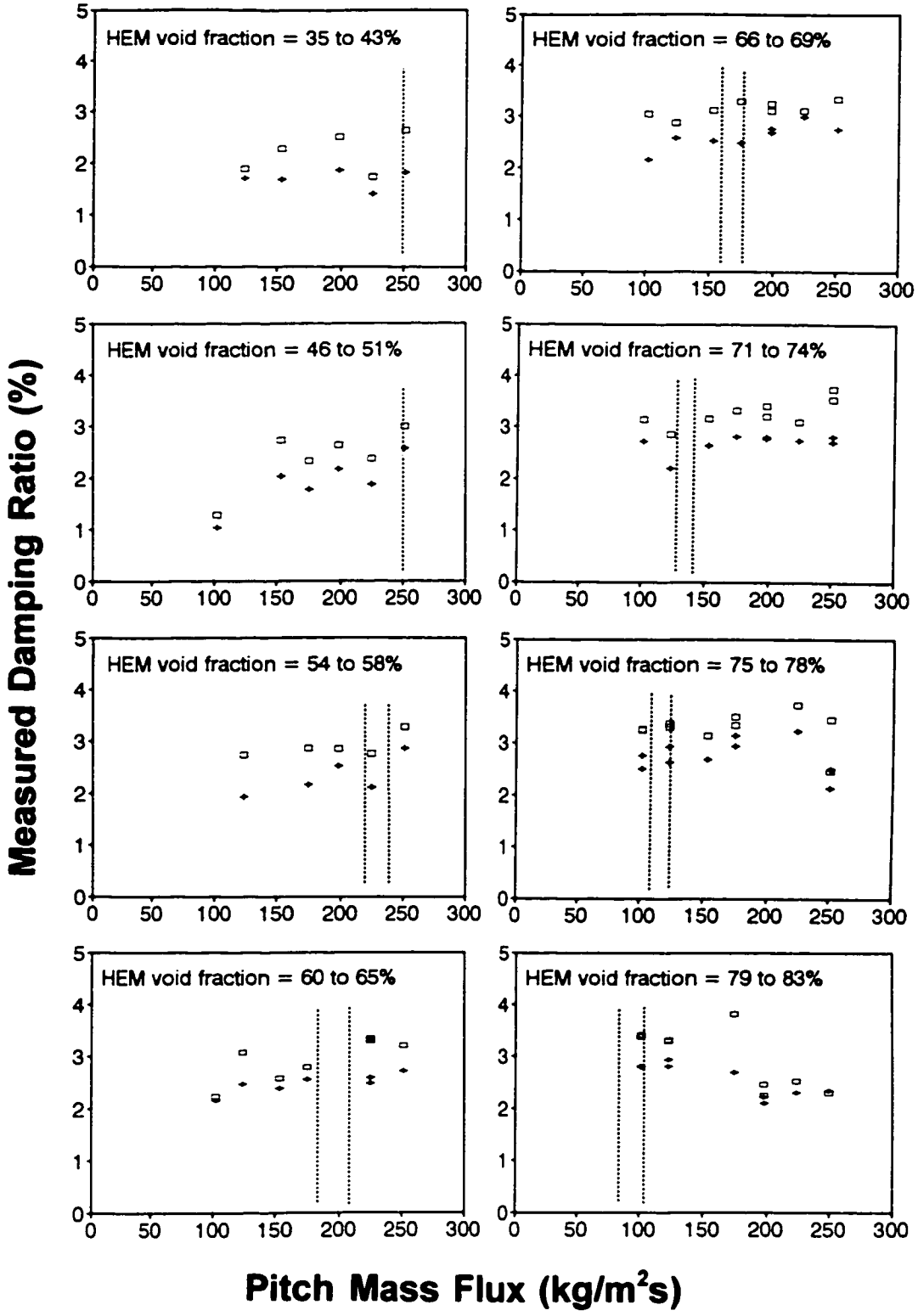

Figure 9.4 Measured damping in two-phase R-11 cross-flow as a function of pitch mass flux and for roughly constant HEM void fraction. Data obtained from the semi-rigid bundle. Dashed lines correspond to half the critical mass flux of the fully flexible array. + lift, □ drag.

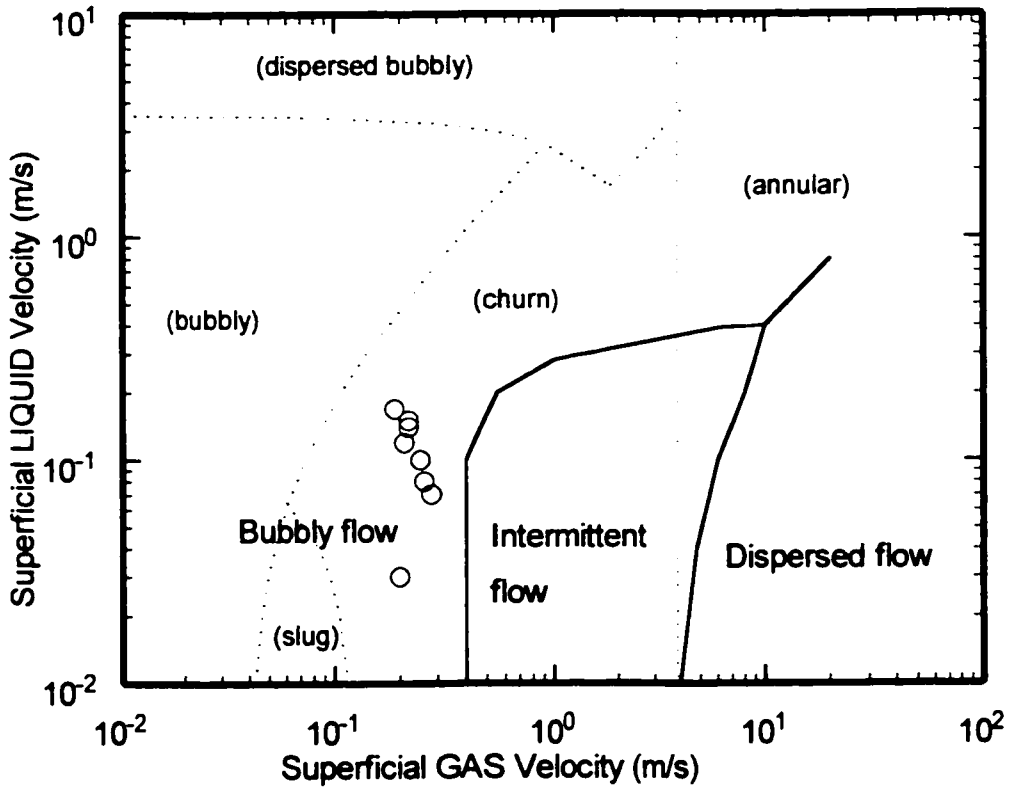

Figure 9.5 Flow regime map for vertical upward flow of two-phase R-11. Flow regime boundaries developed by: —— Ulbrich and Mewes (1994), ····· Taitel *et al.* (1980). ○ Conditions corresponding to damping measurements.

CHAPTER 10

Turbulence Buffeting Data

This chapter presents the measurements of turbulence induced vibration of the tube bundle in single and two-phase cross-flow. The primary purpose of this analysis is to determine the forcing amplitude in non-dimensional form due to random turbulence buffeting of the flow. An upper bound on these forces is desired, which will provide designers with a means of predicting the likely maximum vibration amplitude for this tube array. There are two main approaches to determining these forces: the direct approach, were the rigid tube is mounted on force transducer and the fluid forcing is measured directly, and the indirect approach, were the response of a flexible tube is monitored and the forces are determined from a spectral analysis of the frequency response function. The results of this chapter follow the latter approach.

The results corresponding to single-phase flow are normalized according to the method of Axisa *et al.* (1990), which has been demonstrated to be a satisfactory means of collapsing the data for comparison with the results of others. The results obtained in two-phase flow are analysed using the method of de Langre & Villard (1998), who have had success in collapsing the two-phase data of a number of researchers who used a wide variety of fluids. They accomplished this by comparing various non-dimensional parameters, which were physically relevant, for normalizing the forcing spectral density data and choosing the set which worked best. This was necessary since the dimensionless parameters which worked quite well for the data in single-phase flow were found to be inadequate for collapsing the two-phase flow data.

The data analysis method for random excitation of a tube was outlined in Chapter 3, so only a brief summary is provided in this chapter. The HEM is used to analyse the data since this was the fluid model used by all the other researchers. Application of the new void fraction model is not pursued here because the other researchers data is not detailed enough to perform the required calculations.

10.1 Summary of Results for Single-Phase Flow

The data analysed in this section were obtained from the single flexible tube array as opposed to the fully flexible array. This was done because the vibration amplitudes below the critical velocity were found to be about the same for both cases, except that in the single flexible tube case the frequency spectra was more like the classical response of a single degree of freedom oscillator, which made it easier to determine the vibration frequency and damping ratio.

The equation for the r.m.s. tube deflection was derived previously in chapter 3, and is given by,

$$\frac{\bar{y}_{rms}}{D} = \frac{\sqrt{a_n}\,\sigma(L)}{16\pi^{3/2}} \frac{\rho D^2}{m\zeta^{1/2}} \left[\frac{V_p}{f_n D}\right]^{3/2} \left[\frac{L_s}{L}\right]^{1/2} \left[\tilde{\Phi}_F(f_R)\right]_e^{1/2} , \qquad \textbf{(10.1)}$$

where $\bar{y}_{rms}$ is the rms tip deflection averaged over many cycles, a_n is the modal factor ($a_n = 0.5$ for a cantilevered tube), $\sigma(L)$ is the mode shape factor ($\sigma(L) = 2$ for a cantilevered tube), ρ is the average fluid density, ζ is the damping ratio measured in-flow, D is the tube diameter, m is the mass per unit length including hydrodynamic mass, V_p is the pitch flow velocity, f_n is the in-flow natural frequency, L_s is a length scale ($L_s = 1.0$ m), L is the tube length, and $[\tilde{\Phi}_F(f_R)]_e$ is the equivalent dimensionless forcing spectrum (E.D.F.S) which is the unknown quantity to be determined from this analysis. Note that equation (10.1) is valid for any boundary condition such as fixed-pinned or pinned-pinned etc. The reduced frequency, f_R, is given by,

$$f_R = fD/V_p . \qquad \textbf{(10.2)}$$

The results for a single experiment are tabulated in Table 10.1 for drag and lift directions, and are compared with other data in Figure 10.1. The other data points in the figure were obtained by Taylor *et al.* (1996) and Pettigrew and Gorman (1978) for interior tubes (ie., far from the inlet or exit of the bundle), while the upper bound guidelines were provided by Oengoren and Ziada (1995) and Taylor and Pettigrew (1999). The data of the present study appears to plot higher than the extensive data points of Taylor *et al.* (1996), but they are mostly within the upper bound determined by Taylor and Pettigrew (1999). Note that there is a significant amount of vertical scatter between the various data

for reduced frequencies above 0.4. This is not likely due to uncertainties in f_R since vibration frequency, f, tube diameter, D, and pitch flow velocity, V_p, are all relatively easy to determine with little uncertainty. The quantities which have the highest uncertainty are the damping, ζ, and the correlation length, λ_c. The latter does not appear in equation (10.1) because, in the present formulation, it has not been separated from $[\tilde{\Phi}_F(f_R)]_e$. Recall that Axisa *et al.* (1990) suggested that instead of trying to determine the spectrum of local forces, $[\tilde{\Phi}_F]$, one can determine an equivalent spectrum,$[\tilde{\Phi}_F]_e$, provided that the tube length, L, be given, ie.,

$$[\tilde{\Phi}_F]_e = \frac{\lambda_c}{L}[\tilde{\Phi}_F] \; . \tag{10.3}$$

The local forcing spectrum, $[\tilde{\Phi}_F]$, is difficult to measure because in most cases the forcing data is obtained from a tube of finite length, and the correlation length, λ_c, is not known and therefore the individual contributions of the two parameters towards the vibration response cannot be determined. The justification for invoking equation (10.3) is that the effect of λ_c on the vibration amplitude should be inversely proportional to tube length, L, as long as λ_c remains small relative to the shortest tube length that is generally tested.

10.2 Summary of Results for Two-Phase Flow

The formulation presented in the previous section for reducing the single-phase data has proven to be very unsatisfactory for reducing two-phase flow data. Several attempts have been made to reduce the two-phase turbulence buffeting data into dimensionless form for comparison and design purposes by researchers such as Axisa *et al.* (1990), Axisa and Villard (1992), Papp and Chen (1994) and Taylor *et al.* (1989, 1992, 1996). The latest and most satisfactory formulation is provided by de Langre and Villard (1998). In developing their formulation, these authors drew from a database that included most of the available experimental data, which included direct and indirect force measurements. Different mixtures such as air-water, steam-water, and various types of refrigerants were included in the database. Their primary objective was to define an upper bound on the magnitude of the buffeting forces which would serve as a practical tool for designers who wished to estimate the

continuous tube vibration levels of a heat exchanger tube bundle. By exploring various scaling parameters, they found that neither viscosity nor surface tension were acceptable for defining a dimensionless spectrum. In addition, the particular flow regime and the nature of the gas and liquid phases did not appear to play a role in the analysis. However, scaling factors based upon gravity forces and void length provided a reasonable collapse of the data. A brief description of the data reduction procedure is summarized below.

The most common method to derive the experimental values of the Dimensionless Reference Equivalent Spectrum (D.R.E.S.), $\Phi^0_E(f)$, is to monitor the vibration of a flexible tube under two-phase cross-flow. Provided that the modal behaviour is simple and no strong coupling exists between modes, a value is obtained at the modal frequency $f = f_n$ according to,

$$\Phi^0_E(f_n) = (\frac{L}{L_0})(\frac{D_0}{D})\frac{64\,\pi^3 f_n^3 m_n^2 \zeta}{\varphi_n^2(s)\,a_n}\,y_n^2\,, \qquad \textbf{(10.4)}$$

where all of the parameters above were defined in section 10.1. A dimensionless form of eqn. (10.4) is desired to facilitate the comparison of results from one configuration to another. Two scaling parameters are needed, a time scale to define the reduced frequency, $f_R = f/f_o$, and a force scale, p_o. Thus a dimensionless reference equivalent spectrum is defined as follows,

$$\bar{\Phi}^0_E(f_R) = \frac{f_o}{(p_o D)^2}\,\Phi^0_E(f)\,. \qquad \textbf{(10.5)}$$

The reduced frequency is defined by,

$$f_r = \frac{f}{f_o} = \frac{f D_w}{V_p}\,, \qquad \textbf{(10.6)}$$

which means that the time scale is $f_o = V_p/D_w$. The length scale, D_w, is defined as,

$$D_w = 0.1\,D/\sqrt{1-\alpha_H}\,. \qquad \textbf{(10.7)}$$

The force scale factor of the fluid forcing is defined as,

$$p_o = \rho_L g D_w . \quad \textbf{(10.8)}$$

The results of this analysis are provided in Table 10.2 and are plotted in Figure 10.2 for comparison with other data. Only the lift direction data is plotted since there was no significant difference between the lift and drag amplitudes in two-phase flow. The present data all lies well below the upper bound proposed by de Langre and Villard (1998), which seems to support to their method of data reduction. It is clear that the present results compare well with the other researchers data, but it lies slightly higher than average (vertically). This indicates that the tubes experienced higher than average turbulence excitation response compared with the other data. This may be the result of the relatively high ratio of average vapour bubble diameter to tube diameter, since relatively small diameter tubes were used in this study as compared with most other studies. This was discussed in Chapter 8 as a possible reason for the relatively low fluidelastic results of this study as compared to other fluidelastic data where larger tubes were used. The results of this chapter seem to support this hypothesis.

Table 10.1 Summary of Turbulence Excitation Data of the Present Study for Single-Phase Liquid R-11 Cross-Flow

Test No.	V_p (m/s)	m (kg/m)	f (Hz)	y_{rms} drag (%D)	y_{rms} lift (%D)	f_R (-)	E.D.F.S drag (-)	E.D.F.S. lift (-)
01	0.206	0.244	32.6	0.04	0.02	1.00	6.7e-5	1.7e-5
02	0.239	0.257	31.8	0.07	0.03	0.84	1.3e-4	2.5e-5
03	0.256	0.246	32.5	0.08	0.04	0.81	1.4e-4	3.5e-5
04	0.285	0.244	32.6	0.14	0.07	0.73	3.1e-4	7.7e-5
05	0.307	0.244	32.6	0.20	0.12	0.67	5.0e-4	1.8e-4
06	0.321	0.257	31.8	0.24	0.16	0.63	6.5e-4	2.9e-4

Exp. B09, ρ_L = 1478 kg/m^3, ζ = 0.02, P/D =1.44, Dia = 0.00635 m, L = 0.308 m, f_a = 38.8 Hz.
E.D.F.S. = Equivalent Dimesionless Forcing Spectrum

Table 10.2 Summary of Turbulence Excitation Data of the Present Study for Two-Phase R-11 Cross-Flow (lift direction only)

Test No.	x (-)	α_H (-)	$V_{p,H}$ (m/s)	ρ_H (kg/m³)	f (Hz)	ζ (-)	m (kg/m)	y_{rms} (%D)	f_R (-)	D.R.E.S. (-)
B01,06	0.0323	0.85	0.65	229	36.0	0.020	0.200	0.94	0.091	2.48
B01,17	0.1013	0.94	1.54	95	36.9	0.013	0.191	1.25	0.062	1.53
B02,01	0.0137	0.70	0.45	443	35.1	0.022	0.211	0.79	0.091	3.71
B02,12	0.0554	0.89	1.19	165	36.6	0.014	0.194	1.16	0.059	2.81
B03,01	0.0114	0.65	0.48	508	35.0	0.026	0.212	0.72	0.078	4.78
B03,12	0.0513	0.88	1.31	186	36.5	0.013	0.195	1.16	0.050	3.39
B04,04	0.0136	0.68	0.63	470	35.2	0.025	0.210	0.78	0.063	6.38
B04,14	0.0491	0.87	1.55	190	36.4	0.012	0.196	1.28	0.042	4.76
B05,02	0.0065	0.50	0.48	722	34.3	0.024	0.221	0.78	0.064	9.03
B05,12	0.0433	0.86	1.63	211	36.6	0.012	0.194	1.66	0.038	9.91

P/D =1.44, Dia = 0.00635 m, L = 0.308 m, f_a = 38.8 Hz.

D.R.E.S. = Dimensionless Reference Equivalent Spectrum

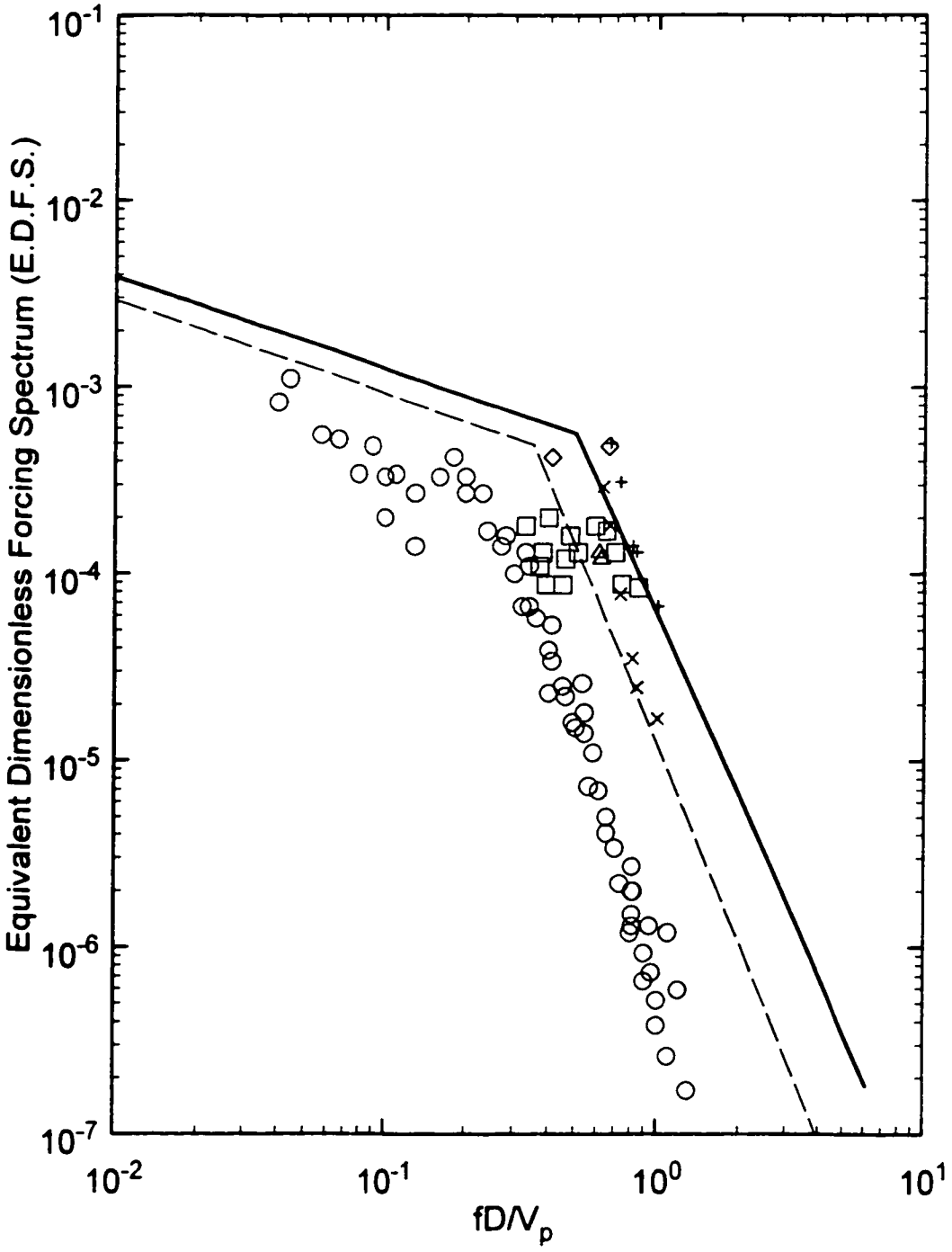

Figure 10.1 Summary of results for turbulence excitation in single-phase flows. Present results for, + drag, × lift directions. ○ Taylor *et al.* (1996), □ Pettigrew and Gorman (1978), △ Wolgemuth (1994), ◇ Pettigrew and Gorman (1978), steam-water. ——— Taylor and Pettigrew (1999). – – – – Oengören and Ziada (1992), P/D = 1.5.

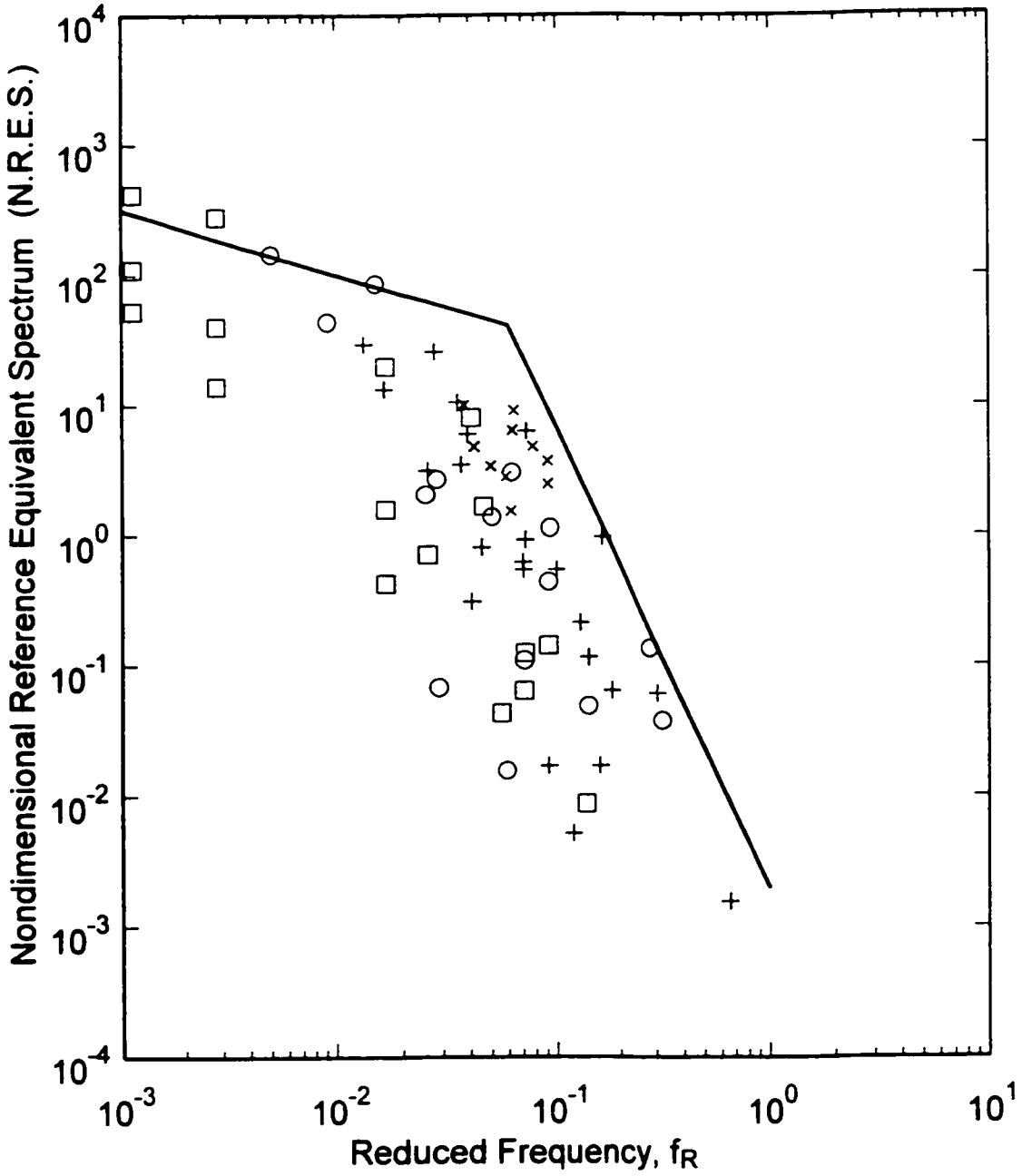

Figure 10.2 Summary of results for turbulence excitation in two-phase flows. × Present results for lift direction only. Other data points and proposed upper bound were drawn from deLangre and Villard (1998), ○ air-water data, □ steam-water data, + Freon data, ——— proposed upper bound.

Chapter 11
Conclusions and Recommendations

The problem of flow-induced vibration in nuclear steam generators is a serious concern in terms of cost and safety. Consequently, a significant amount of research has been conducted to study the fluid-structure interaction between tube arrays subjected to two-phase cross-flows. However, proper modelling of two-phase flow, as it relates to flow induced vibration, is still rather underdeveloped.

The purpose of this research was to contribute new insights to the phenomenon of flow-induced vibration in the U-bend region of nuclear steam generators. The main objective was to re-evaluate the analysis tools for fluidelastic instability in two-phase flows by using more accurate estimates of average fluid density and critical flow velocity of two-phase flows than with the traditionally used homogeneous equilibrium model (HEM). The original contributions of this work include: the development of a new model for predicting void fraction in shell side flows for various fluids, comparison of new fluidelastic data of this research with those of others using the newly developed void fraction model, new measurements of the damping effect on tube vibration in two-phase flows, and the analysis of turbulence buffeting forces from an analysis of the amplitude response of the bundle. A summary of these findings of the thesis are given in more detail below:

1. A physically based model has been developed to predict the void fraction for vertical upward cross-flow through horizontal tube bundles. It was demonstrated that it agreed well with experimental void fraction measurements in refrigerant 11 and air-water mixtures for a sufficiently wide range of pitch mass flux, quality and P/D ratios. It has also shown better predictive capability for these fluids than the void fraction models developed by other researchers. The analysis performed also showed that the

void fraction model agreed with surface boiling cross-flow data of refrigerant 113 and showed plausible applicability to steam-water cross-flow conditions. The results show that the neglect of slip in the HEM may lead to significant errors in the determination of void fraction as well as average flow velocity and fluid density. The present model will allow researchers and designers to obtain better estimates of void fraction in shell side vertical cross-flow in applications such as kettle re-boilers and the U-bend region of nuclear steam generators than with the customarily used homogeneous equilibrium model. This will result in better estimates of average fluid density, and average flow velocity.

2. The experimental results showed that the R-11 data showed slightly lower stability threshold than the air-water and steam water data for data in the bubbly flow regime. An appropriate value of Connors' constant which would establish a lower bound on the present author's data is $K = 2.0$. This is lower than the value recommended by Pettigrew & Taylor (1994) which is $K = 3.0$. The reason for the difference between these two data sets could be due to the effect of using different modelling fluids. R-11 is a single component fluid while air-water is a two-component fluid which cannot simulate any of the local flashing or collapse of vapour on the tube surfaces. This could be a factor affecting the tube forces in the prototype tube bundle which is subjected to steam-water (a single component fluid). This difference could affect tube damping and fluid excitation mechanisms. However, the steam-water results of Axisa *et al.* (1985) show a higher stability than the air-water results, in which a lower bound Connors' constant for that data is about K = 4.2. However, Axisa's data was not affected by intermittent flows since the flow regime analysis indicated that all their data points for fluidelastic instability corresponded to the either the bubbly or dispersed flow regime. Thus the effect of two component vs. single component modelling fluids remains unclear based upon this simple comparison. Another difference between the present results and that of others is the physical scale of the model, where this study uses 6.35 mm (1/4") diameter tubes, the other studies used full scale tube diameters of 12.7 mm (½") or greater. Although it is assumed that using non-dimensional parameters for comparing model and prototype behaviour is supposed to eliminate scale effects, these experiments present a special case due to the presence of bubbles. It is not possible to adjust the size of bubbles in

a two-phase flow, so that the ratio of average bubble size to tube diameter will likely be larger in a reduced scale model than in the full scale prototype. When the ratio of bubble diameter to tube diameter increases, this will likely lead to an increase in the correlation length of turbulent buffeting forces and this will result in higher response amplitudes in the sub-critical flow velocity. This may contribute to the onset of self-excited vibrations at lower velocities and hence lead to a lower stability threshold for such an array.

3. Measurements of the damping effect of two-phase flows were obtained in the present study from the single flexible tube array, and are presented and compared with previous data using an existing analysis technique. Damping measurements showed that the tube damping peaks at about 75% to 80% HEM void fraction, and decreases at lower and especially higher void fraction. This is in reasonable quantitative agreement with air-water and R-22 data. Comparison with other researcher's data has revealed that, while the measured two-phase damping values in R-11 are slightly lower than comparable air-water data, the normalized two-phase component of damping is actually a bit higher than in air-water, owing to the large difference in liquid mass ratio (a normalizing parameter) between these two sets of data.

4. The latest flow regime map, developed by other researchers for predicting the two-phase flow regimes in the shell-side cross-flows in tube bundles, was applied to the present fluidelastic results. This analysis showed that the sudden change in stability behavior which appeared in various data sets were directly related to a predicted change in flow regime from bubbly to intermittent flow.

5. The turbulence buffeting response of the tubes was measured and from this the non-dimensional spectrum of turbulent forces was determined and compared with existing data as a function of reduced frequency, f/V_pD. In single phase flow, the data of the present study appears to plot higher than the extensive data points of Taylor *et al.* (1996), but they are mostly within the upper bound determined by Taylor and Pettigrew (1999). There was a significant amount of vertical scatter between the various data sets for reduced frequencies above 0.4. This was not likely due to uncertainties in f_R since

vibration frequency, f, tube diameter, D, and pitch flow velocity, V_p, were all relatively easy to determine with little uncertainty. The quantities which had the highest uncertainty were damping, ζ, and correlation length, λ_c. In two-phase flow, the present data for dimensionless forcing were determined using the data reduction procedure of deLangre and Villard (1998), whose method seemed to satisfactorily reduce all of the existing two-phase data of various researchers. All of the present results plotted well below the upper bound proposed by deLangre and Villard, which seemed to lend support to their method of data reduction. The present results compared well with the other researchers data, but they plotted slightly higher than average, indicating that forces felt by the tubes in this study were higher than average. This was thought to be a scale effect since the tube diameter in this study was about one-half that used in most other studies, and thus a relatively high bubble diameter to tube diameter is to be expected. This was also discussed in the fluidelastic analysis as a possible reason for the relatively low fluidelastic threshold observed in the present bundle as compared to other comparable data where larger tubes were used. The results of that chapter seemed to support this hypothesis.

Future Recommendations

There are two main recommendations for future work that would address some of the questions raised in this analysis. There are also a few other recommendations that are specific to the apparatus. The following subheadings discuss each of the future recommendations.

Investigation of the Intermittent Flow Regime

The analysis of the fluidelastic instability data showed that a change in flow regime from bubbly flow to intermittent flow has a very detrimental effect on the stability of the tube bundle. When analysed on the traditional stability diagram featuring critical reduced velocity, V_{pc}/fD, versus mass-damping parameter, $m\delta/\rho D^2$, the data in the bubbly flow regime showed roughly the expected trend, but the data in the intermittent flow regime did not. The latter data showed a steady decrease in V_{pc}/fD, over a small range of $m\delta/\rho D^2$, in which the decrease in stability seemed to correspond to an increase

in void fraction. This suggested that the two main scaling parameters, reduced velocity and mass-damping parameter may be insufficient to predict fluidelastic instability in the intermittent flow regime, and that added complications arise in this flow regime which all of the existing analyses neglect. The most likely reason for this loss of stability in the intermittent flow regime is due to the unsteadiness of the flow, in which the flow velocity undergoes a cyclic pattern of surges and lulls, which are not accounted for in the determination of average flow velocity, V_p or V_{eq}. The flow surges may be large enough to initiate the self-excited vibrations, making it appear that the level of stability has decreased to a lower value of V_{pc}/fD. This intermittent flow behaviour is not typical of some of the data of previous researchers which corresponded to single or two-phase flows in the bubbly flow regime, where the flow was much more steady and the stability behaviour roughly obeyed Connors' trend. It would be beneficial to a designer to be able to determine tube stability in the case of intermittent flow. This would require either the inclusion of additional non-dimensional parameters to properly scale the two-phase flow, or perhaps a model for determining an equivalent flow velocity that effectively includes the intermittency of the flow.

Investigation of Average Bubble Size

Another possible factor affecting the comparison of fluidelastic instability data may be the difficulty of modelling the proper ratio of average bubble size to tube diameter. It was mentioned earlier that performing an experiment on a reduced scale presents a problem when dealing with two-phase flows because the size of the vapour bubbles or liquid slugs cannot be controlled and therefore they cannot be scaled up or down with the tube diameter. Even at full scale modelling, distorted bubble scaling could result from the using a different fluid to model the actual steam-water in the steam generator, or average bubble size could vary with operating pressure and surface tension. Average bubble size could also affect the pressure drop of the flow through the array and fluid damping effect. It would certainly influence the magnitude and frequency of turbulent forces experienced by the tubes as they are impacted by alternate vapour bubbles and liquid slugs. Average bubble size may also play a role in the correlation length of turbulent forces. To the author's knowledge, no attempt has yet been made to determine average void size as functions of void fraction, operating pressure or fluid type, and

to correlate this with tube response or tube impact force. Information in this area would resolve some questions regarding the suitability of using air-water or refrigerants to model the steam-water flow in a steam generator.

Investigation of Exit Effects

There remains some doubt regarding the modelling of the flow conditions and void fraction of the U-bend region of nuclear steam generators. The actual void fraction in this region is expected to be high, at least 85%, so that the occurrence of intermittent flow can also be expected. In addition, it is the present author's opinion that there must exist a clearly defined liquid/vapour interface in the open region just above the top of the U-tube bundle. The P/D ratio of the bundle is about 1.5, which means that the solidity ratio in the tube bundle is about 40%, while the flow though the tube gaps is one-half the total flow area. Therefore, the cross-sectional flow area in these devices must increase nearly two-fold just beyond the top of the tube bundle, and this is likely where much of the vapour-liquid separation would occur. In this open region just above the top of the U-tube bundle, the average flow velocity would certainly decrease and some portion of the liquid phase which was carried up by the momentum of the gas phase would subsequently fall back down into the tube region. This liquid "down-wash" would then impede the up-flow of the steam-water mixture, causing local jetting of the flow through the tubes and ejecting the excess liquid into the open area again. On the other hand, large-scale re-circulation could also be occurring, whereby the upward two-phase flow would be biased towards the hot-leg side of the boiler. In this case, steam would eject from the top of the bundle, while the remaining liquid phase would simply flow en-mass around the outer tube spans (in parallel flow), and then down along the cold leg of the U-bend region. The present author believes that this is a likely hypothesis because a flow condition similar to this was observed in the present apparatus under certain conditions, with large-scale re-circulation in the test section occurring, especially at low mass fluxes. The paper by Jo and Shin (1998) showed the predicted flow field in a steam generator model using the ATHOS3 thermo-hydraulic code. This code predicted a local recirculating flow field in the U-bend region which was Under such a scenario, the outer-most tubes in the bundle of the steam generator would see the effect of this cyclic flow surges and liquid down-wash the most, which is important to

recognize because this region is the most susceptible to fluidelastic instability due to the long spans. The present apparatus does not accurately model these hypothesized flow conditions, because the tubes in the U-bend region of the actual steam generator are high up near the vapour-liquid interface, while in present apparatus, the tube bundle is located roughly in the middle of the vertical flow column, far below the rough division of the liquid-vapour interface. It is the author's opinion that the experimental approach could be modified to more accurately reflect the actual conditions in the steam generator. This would require that the flow loop be modified to allow better control over the flow rate, so that the vapour-liquid interface could be maintained at a specified position with respect to the tube bundle.

Interaction of Two-Phase Flow with Bundle Geometry

It was demonstrated in this work that the stability of the tube bundle was significantly reduced at the onset of the intermittent flow regime. It would be of practical use to investigate the role of tube pattern and P/D ratio on flow regime, as certain array types may show greater resistance to the destabilizing effects of this flow regime. It may be possible, for example, that the square and parallel triangular arrays may exhibit different stability behaviour than the rotated square and normal square geometry, since the flow in the former array types passes between tubes and could leave stagnant zones in the tube wakes, while the latter array types follows a more torturous path and leaves fewer stagnant zones. It may be possible that the stagnant zones may harbor a disproportionate amount of gas or liquid phase which could be released in bursts, and thereby help to initiate the onset of intermittent flow regime or exacerbate its effects. Resolving this question would lend insight into the designers choice of array pattern in the U-bend of steam generators to minimize the detrimental effects of intermittent flows.

References

[1] Transactions of the 6th International Conference of Structural Mechanics in Reactor Technology, Paris, 1981.

[2] Naudascher E. & Rockwell D. (eds.) Proceedings IUTAM-IAHR Symposium on Practical experiences with Flow Induced Vibrations, Springer-Verlag, Berlin 1980.

[3] King R. (ed.) Proceedings of the 1st International Conference on Flow Induced Vibrations, Brownes-on-Windermere, England, May 12-14, 1987.

[4] Paidoussis M.P. *et al.* (eds.) 1984 ASME Symposium of Flow-Induced Vibrations. ASME Winter Annual Meeting, New Orleans.

ASHRAE Handbook, 1991 Fundamentals, SI Edition, American Society of Heating, Refrigeration, and Air-Conditioning Engineers, Atlanta, Georgia, pp. 17.1-17.3.

Au-Yang M.K., 1999, "Joint and Cross Acceptances for Cross-Flow-Induced Vibration, Part I - Theoretical and Finite Formulations, Part II - Charts and Applications", *Flow-Induced Vibration*, PVP-Vol. 63, Boston, pp. 19-33.

Austermann R & Popp K, 1995, "Stability Behaviour of a Single Flexible Cylinder in Rigid Tube Arrays of Different Geometry Subjected to Cross-Flow", *Journal of Fluids and Structures*, Vol. 9, pp. 303-322.

Axisa F., Villard B., Gibert R.J., Hetsroni G. & Sundheimer P., 1984, "Vibration of Tube Bundles Subjected to Air-Water and Steam-Water Cross Flow: Preliminary Results in Fluidelastic Instability", In Proceedings *ASME Symposium on Flow-Induced Vibration*, Vol. 2: Vibration of Arrays of Cylinders in Cross-flow, (eds. M.P. Pāidoussis, M.K. Au-Yang & S.S. Chen), pp. 269-284, New York: ASME.

Axisa F., Boheas M.A., & Villard B., 1985, "Vibration of Tube Bundles Subjected to Steam Water Cross Flow: A Comparative Study of Square and Triangular Arrays", Paper B1/2, *8th Int. Conference on S.M.R.T.*, Brussels.

Axisa F., Villard B. & Sundheimer P., 1986, "Flow Induced Vibration of Steam Generator Tubes", *Electric Power Research Institute Report*, EPRI-NP4559, May 1986.

Axisa F., Antunnes J. & Villard B., 1988a, "Overview of Numerical Methods for Predicting Flow-Induced Vibrations", *Journal of Pressure Vessel Technology*, Vol. 110, pp. 6-14.

Axisa F., Wullschleger M., Villard B. & Taylor C.E., 1988b, "Two Phase Cross Flow Damping", *ASME Publication, PVP-Vol. 133*, Damping-1988, presented at the ASME-PVP Conference, Pittsburg Pa., June 1988.

Axisa F., Antunnes J. &, Villard B., 1990, "Random Excitation of Heat Exchanger Tubes by Cross-Flows", *Journal of Fluids and Structures*, Vol. 4, pp. 321-341.

Axisa F. & Villard B., 1992, "Random Excitation of Heat Exchanger Tubes by Two Phase Cross Flows", *1992 International Symposium on Flow-Induced Vibration and Noise*, Vol. 1, pp. 119-139.

Blevins R.D., 1974, "Fluidelastic Whirling of a Tube Row", *ASME Journal of Pressure Vessel Technology*, Vol. 96, pp. 263-267.

Blevins R.D., Gilbert R.J. & Villard B., 1981, "Experiments on Vibration of Heat Exchanger Tube Arrays in Cross Flow", Paper B6/9 in [1].

Blevins R.D., 1984, "A Rational Algorithm for Predicting Vibration-Induced Damage to Tube and Shell Heat Exchangers (eds M.P. Paidoussis, J.M. Chenoweth & M.D. Bernstein), pp. 87-101. New York: ASME.

Blevins R.D., 1990, "Flow-Induced Vibration", Van Nostrand Reinhold, New York..

Carlucci L.N., 1980, "Damping and Hydrodynamic Mass of a Cylinder in Simulated Two-Phase Flow", *Journal of Mechanical Design*, Vol. 102, pp. 597-602.

Carlucci L.N. & Brown J.D., 1983, "Experimental Studies of Damping and Hydrodynamic Mass of a Cylinder in Confined Two-Phase Flow", *Journal of Vibration, Acoustics, Stress and Reliability in Design*, Vol. 105, pp. 83-89.

Chan A.M.C., & Banerjee S., 1981, "Design Aspects of Gamma Densitometers for Void Fraction Measurements in Small Scale Two-Phase Flows", *Nuclear Instruments and Methods*, Vol. 190, pp. 135-148.

Chen S.S., 1975, "Vibration of Nuclear Fuel Bundles", *Nuclear Engineering and Design*, Vol. 35, pp. 399-422.

Chen S.S., Wambsganss M.W. & Jendrzyczyk J.A., 1976, "Added Mass and Damping of a Vibrating Rod in Confined Viscous Fluids", *ASME Journal of Applied Mechanics*, Vol 43, pp. 325-329.

Chen S.S. & Jendrzejczyk J.A., 1981, "Experiments on Fluid Elastic Instability in Tube Banks Subjected to Liquid Cross Flow", *Journal of Sound and Vibration*, Vol. 78(3), pp. 355-381.

Chen S.S., 1983, "Instability Mechanisms and Stability Criteria of a Group of Circular Cylinders Subjected to Cross-Flow, Part I: Theory", "Part II: Numerical Results and Discussions". *ASME Journal of Vibration, Acoustics, Stress and Reliability in Design*. Vol. 105, pp. 51-58 and 235-260

Chen S.S., 1984, "Guidelines for the Instability Flow Velocity of Tube Arrays in Cross-Flow", *Journal of Sound and Vibration*, Vol. 93(3), pp. 439-455.

Chen S.S., 1987, "Flow-Induced Vibration of Circular Cylindrical Structures", Hemisphere Publishing Corp., Washington, D.C.

Chen S.S., 1989, "Some Issues Concerning Fluid-Elastic Instability of a Group of Circular Cylinders in Cross-Flow", *ASME Jounal of Pressure Vessel Technology*, Vol. 111, pp. 507-518.

Chen Y.N., 1980, "Jet Swing as a Governing Factor for Fluid-Elastic Instability of Tube Bundles", In *Century 2 Pressure Vessel and Piping Conference*, San Francisco, Paper 80-C2/PVP-103. New York, ASME.

Connors H.J. Jr., 1970, "Fluidelastic Vibration of Tube Arrays Excited by Cross Flow", Flow-Induced Vibration in Heat Exchangers, edited by D.D. Reiff, ASME, New York, 1979.

Dam R., 1991, "Two Phase Flow-Induced Vibrations for Tube Banks in Cross Flow: Creating an Experimental Facility", Master's Thesis, Department of Mechanical Engineering, McMaster University, Hamilton, Ontario, Canada.

De Langre E. & Villard B., 1998, "An Upper Bound on Random Buffeting Forces Caused by Two-Phase Flows Across Tubes", *Journal of Fluids and Structures*, Vol. 12, pp. 1005-1023.

Delenne B., Gay N., Campistron R., & Banner D., 1997, "Experimental Determination of Motion-Dependent Fluid Forces in Two-Phase Water-Freon Cross Flow", In *Proceedings of the ASME Int. Symposium on Fluid-Structure Interaction: Aeroelasticity, Flow-Induced Vibration and Noise*, AD-Vol. 53-2, (eds. M.P. Païdoussis *et al.*), Vol. II, pp. 349-356.

Dowlati R., Kawaji M.D., Chisholm D., & Chan A.M.C., 1992, "Void Fraction Prediction in Two-Phase Flow Across a Tube Bundle", *AIChE J.*, Vol. 38, No. 4, pp. 619-622.

Dowlati R., 1992, "Hydrodynamics of Two-Phase Cross-Flow and Boiling Heat Transfer in Horizontal Tube Bundles", Ph.D. Thesis, Univ. of Toronto, Dept.of Chemical Engineering and Applied Chemistry, Toronto, Canada.

Dowlati R., Kawaji M., & Chan A.M.C., 1996, "Two-Phase Crossflow and Boiling Heat Transfer in Horizontal Tube Bundles," *ASME Jounal of Heat Transfer.*, Vol. 118, pp. 124-131.

Fair J.R. & Klip A., 1983, "Thermal Design of Horizontal Reboilers", *Chem. Eng. Prog.*, Vol. 79, No. 8, pp. 86-96.

Feenstra P.A., 1993, "Two-Phase Flow-Induced Vibration in Heat Exchanger Tube Arrays: An Experimental Investigation", Master's Thesis, Department of Mechanical Engineering, McMaster University, Hamilton, Canada.

Feenstra, P.A., Judd, R.L. & Weaver, D.S., 1995, "Fluidelastic Instability in a Tube Array Subjected to Two-Phase R-11 Cross-Flow", *Journal of Fluids and Structures*, Vol. 9, pp. 747-771.

Feenstra, P.A., Weaver D.S. & Judd R.L., 1996, "Instability of Parallel Triangular Arrays Subjected to Two-Phase Cross-Flow", Canadian Society of Mechanical Engineers, Annual Conference, May 1996, McMaster University, Hamilton Canada.

Feenstra, P.A., Weaver D.S. & Judd R.L., 2000, "An Improved Void Fraction Model for Two-Phase Cross-Flow Through Horizontal Tube Arrays", *Int. Journal of Multiphase Flow*. (To be published).

Fitzpatrick J.A., 1985, "The Prediction of Flow-Induced Noise in Heat Exchanger Tube Arrays", *Journal of Sound and Vibration*, Vol. 99, pp. 425-435.

Frick T.M., Sobeck T.E. & Reavis J.R., 1984, "Overview on the Development and Implementation of Methodologies to Compute Vibration and Wear of Steam Generator Tubes", In reference [4], Vol. 3, pp. 149-161.

Gidi A., Weaver D.S., & Judd R.L., 1997, "Two-Phase Flow-Induced Vibrations of Tube Bundles with Surface Boiling", *Proceedings of the ASME Int. Symposium on Fluid-Structure Interaction: Aeroelasticity, Flow-Induced Vibration and Noise*, Vol. AD Vol. 53-2, M.P. Païdoussis *et al.* (Eds.), pp. 381-389, Dallas, U.S.A., New York: ASME.

Gidi A., 1999, "Two-Phase Flow-Induced Vibrations Tube Bundles with Surface Boiling", PhD Thesis, Department of Mechanical Engineering, McMaster University, Hamilton, Canada.

Grant I.D.R. & Murray I., 1972, "Pressure drop on the shell-side of a segmentally baffled shell-and-tube heat exchanger with vertical two-phase flow", *Report NEL-560*, National Engineering Lab.

Grant I.D.R., 1976, "Pressure Drop on the Shell-Side of Shell and Tube Heat Exchangers in Single and Two-Phase Flows", HTFS Design Report No. 16 (revised).

Grant I.D.R., & Chisholm D., 1979, "Two-Phase Flow on the Shell Side of a Segmentally Baffled Shell-and Tube Heat Exchanger", *ASME Journal of Heat Transfer*, Vol. 101, pp. 38-42.

Gross H.G., 1975, "Untersuchung Aerodynamischer Schwingungs-Mechanismen und Deren Berucksichtigung bei der Auslegung von Rohrbundelwarmetauschern", PhD Thesis, Technical University of Hannover.

Hara F, & Kohgo O., 1982, "Added Mass and Damping of a Vibrating Rod in a Two-Phase Air-Water Mixed Fluid", *ASME Publication PVP*, Vol. 63, Orlando, Florida, pp. 1-8.

Heilker W.J. & Vincent R.Q., 1981, "Vibration in Nuclear Heat Exchangers Due to Liquid and Two Phase Flow", *ASME Journal of Engineering for Power*, Vol. 103, pp. 358-365.

Hirota K., Nakamura T., Mureithi N.W., Kasahara J., Kusakabe T. & Takamatsu H., 1996, "Dynamics of an In-Line Tube Array in Steam-Water Cross-Flow. Part III: Fluidelastic Instability Tests and Comparison with Theory", *Proceedings ASME PVP Conference* , Montreal, Vol. 328, pp.123-134.

Hsu J.T., 1987, "A Parametric study of Boiling Heat Transfer in Horizontal Tube Bundles", Ph.D. Thesis, Univ. of Wisconsin, Milwaukee.

Jo J.C., & Shin W.K., 1999, "Fluidelastic Instability Analysis of Operating Nuclear Steam Generator U-Tubes", *Nuclear Engineering and Design*, Vol. 193, pp. 55-71.

Judd R.L., Dam R. & Weaver D.S., 1992, "A Photo-Optical Technique for Measuring Flow-Induced Vibrations in Cantilevered Tube Bundles", *Experimental Thermal and Fluid Science*, Vol. 5, pp. 747-754.

Kawamura K., Yasou A. & Inada F.,1997, "Turbulence Induced Tube Vibration in a Parallel Steam-Water Two-Phase Flow", *Proceedings of the ASME Int. Symposium on Fluid-Structure Interaction: Aeroelasticity, Flow-Induced Vibration and Noise*, AD Vol. 53-2, (eds. M.P. Païdoussis *et al.*), Vol. II, pp.83-91.

Kim B. S., Pettigrew M. J. & Tromp J. H., 1988, "Vibration Damping of Heat Exchanger Tubes in Liquids: Effect of Support Parameters", *Journal of Fluids and Structures* Vol. 2, pp. 593-614.

Kondo M. & Nakajima K.I., 1980, "Experimental Investigation of Air-Water Two-Phase Upflow Across Horizontal Tube Bundles", *Bull. JSME*, Vol. 23, No. 177, pp. 385-393.

Leong L.S. & Cornwell, K., 1979, "Heat Transfer Coefficients in a Reboiler Tube Bundle", *The Chemical Engineer*, No. 343, pp. 219-221.

Lever J. H. & Weaver D. S., 1986a, "On the Stablity Behaviour of Heat Exchanger Tube Bundles. Part 1-Modified Theoretical Model", *Journal of Sound and Vibration* Vol. 107, pp.375-410.

Lever J.H. & Weaver D.S., 1982, "A Theoretical Model for Fluid-Elastic Instability in Heat Exchanger Tube Bundles", *Journal of Pressure Vessel Technology*, Vol. 104, pp. 147-158.

Lever J. H. & Weaver D. S., 1986, "On the Stability Behaviour of Heat Exchanger Tube Bundles. Part 2-Numerical Results and Comparison with Experiments", *Journal of Sound and Vibration* Vol. 107, pp. 393-410.

Li M. & Weaver D.S., 1997, "A Fluidelastic Instability Model with an Extension to Full Flexible Multi-Span Tube Arrays", In: *Proc. ASME PVP Conf.*, Dallas, Vol. II, Flow-Induced Vibration and Noise.

Mann W. & Mayinger F., 1995, "Flow-Induced Vibration of Tube Bundles Subjected to Single and Two-Phase Cross-Flow", *Proc. 2nd Int. Conference on Multiphase Flow*, Vol. 4, Kyoto, Japan.

Marn J. & Catton I., 1991a, "Flow-Induced Vibration in Cylindrical Bundles: Two-Dimensional Analysis into Normal Modes.", In *Numerical Modelling of Basic Heat Transfer Phenomena in Nuclear Systems* (eds. F.B. Cheung & L.E. Hochreiter), HTD-Vol. 165, pp. 9-14. New York: ASME.

Marn J. & Catton I., 1991b, "Flow-Induced Vibration in Cylindrical Structures using Vorticity Transport Equation", In *Multidisciplinary Applications for Computational Fluid Dynamics* (ed. O. Baysal), FED-Vol. 129, pp. 75-82. New York: ASME.

Marn J. & Catton I., 1991c, "Stability of Finite Cylindrical Array Subjected to Single Phase Cross-Flow", In *Fluid Transients and Fluid-Structure Interactions* (eds F.J. Moody & D.C. Wiggert), PVP-Vol. 224/FED-Vol. 126, pp. 1-3, New York, ASME.

McAdams W.H., 1942, "Vapourization Inside Horizontal Tubes-II-Benzene-Oil Mixtures", *Transactions ASME*, Vol. 64, pp. 193.

Nakamura T., Kanazawa H., & Sakata K., 1982, "An Experimental Study on Exciting Force by Two-Phase Flow", *Flow-Induced Vibration of Circular Cylindrical Structures*, PVP-Vol. 63, pp. 19-29.

Nakamura T., Yamagucci N., Fujita K., Sakata K. & Saito I., 1986a, "Study of Flow-Induced Vibration of a Tube Array by a Two-Phase Flow, 1st Report: Large Amplitude Vibration by Air-Water Flow", *Transactions of JSME*, Vol. 52, No. 473.

Nakamura T., Fujita K., Kawanishi K. & Saito I., 1986b, "A Study on the Flow-Induced Vibration of a Tube Array by a Two-Phase Flow, 2nd Report: Large Amplitude Vibration by Steam-Water Flow", *Transactions of JSME*, Vol. 52, No. 473.

Nakamura T. & Fujita K., 1988, "Large Amplitude Vibration of a Tube Bundle by Two Phase Flow", *Journal of Wind Engineering*, Vol. 37, pp. 599-608.

Nakamura T., Fujita K., Kawanishi K., Yamagucci N. & Tsuge A., 1991a, "Study on the Vibrational Characteristics of a Tube Array caused by Two Phase Flow, Part 1 - Random Vibration", *ASME Publication PVP* , Vol. 206, pp. 19-24.

Nakamura T., Fujita K., Kawanishi K., Yamaguchi N. & Tsuge A., 1991b, "Study on the Vibrational Characteristics of a Tube Array caused by Two Phase Flow", Part 2 - Fluidelastic Vibration, *ASME Publication PVP*, Vol. 206, pp. 25-30.

Noghrehkar, G., 1996, "Investigation of Local Two-Phase Parameters in Cross Flow-Induced Vibration of Tubes in Tube Bundles", PhD Thesis, Department of Chemical Engineering and Applied Chemistry, University of Toronto, Toronto, Canada.

Noghrehkar G.R., Kawaji M., Chan A.M.C., 1999, "Investigation of Two-Phase Flow Regimes in Tube Bundles under Cross-Flow Conditions" *Int. Journal of Multiphase Flow*, Vol 25, pp.857-874.

Oengören A. & Ziada S., 1995, "Vortex Shedding, Acoustic Resonance and Turbulent Buffeting in Normal Triangular Tube Arrays", Proceedings of the 6th Int. Conf. on Flow-Induced Vibration, (ed. P.W. Bearman), London, U.K., pp. 295-313.

Païdoussis M.P., 1982, "A Review of Flow Induced Vibrations in Reactors and Reactor Components", *Nuclear Engineering and Design*, Vol. 74, pp. 31-60.

Païdoussis M.P. & Price S.J., 1988, "The Mechanisms Underlying Flow-Induced Instabilities of Cylinder Arrays in Cross Flow", *Journal of Fluid Mechanics*, Vol. 187, pp. 45-59.

Païdoussis M.P., Price S.J., Nakamura T., Mark B., & Mureithi N., 1989, "Flow-Induced Vibrations and Instabilities in a Rotated-Square Cylinder Array in Cross-Flow", *Journal of Fluids and Structures*, Vol. 3, pp. 229-254.

Palen J.W. & Yang C.C., 1983, "Circulation Boiling Model for Analysis of Kettle and Internal Reboiler Performance", *Heat Exchangers for Two-Phase Applications*, Eds. J.B. Kitto and J.M Robertson, HTD-Vol. 27, ASME, New York, pp. 55-61.

Papp L. & Chen S.S., 1994, "Turbulence Induced Vibration of Tube Arrays in Two-Phase Cross-Flow", *ASME Journal of Pressure Vessel Technology*, Vol. 116, pp. 312-316.

Parrando J.L., Equsquiza E. & Santolaria C., 1993, "Extension of Lever and Weaver's Unsteady Analytical Model to the Fluidelastic Instability of Arrays of Flexible Cylinders", *Journal of Wind Engineering and Industrial Aerodynamics*, Vol. 49, pp. 177-186.

Payvar P., 1983, "Analysis of Performance of Full Bundle Submerged Boilers", *Two-Phase Heat Exchanger Symposium*, HTD-Vol. 44, ASME, NewYork, pp. 11-18.

Pettigrew M.J. & Gorman D.J., 1973, "Experimental Studies on Flow-Induced Vibration to Support Steam Generator Design, Part III: Vibration of Small Tube Bundles in Liquid and Two Phase Cross Flow", Report 5804, Atomic Energy of Canada Limited.

Pettigrew M.J. & Gorman D.J., 1978, "Vibration of Heat Exchanger Tube Bundles in Liquid and Two-Phase Cross Flow", *Proceedings B.E.N.S.International Conference on Vibration in Nuclear Plant*, Keswick U.K., Paper 2.3.

Pettigrew M.J., Sylvestre Y. & Campagna A.O., 1978, "Vibration Analysis of Heat Exchanger and Steam Generator Designs", *Nuclear Engineering and Design*, Vol. 48, pp. 97-115.

Pettigrew M.J. & Campagna A.O., 1980, "Heat Exchanger Tube Vibration: Comparison between Operating Experiences and Vibration Analysis", Paper in [2].

Pettigrew M.J., Goyder H.G.D., Qiao Z.L. & Axisa F., 1986, "Damping of Multispan Heat Exchanger Tubes-Part I: In Gases, Part II: In Liquids", *Symposium on Special Topics of Structural Vibration*, ASME Pressure Vessel and Piping Conference, Chicago, Vol. 104, pp. 81-88, 89-98.

Pettigrew M.J., Taylor C.E. & Kim B.S., 1989a, "Vibration of Tube Bundles in Two-Phase Cross Flow. Part 1 - Hydrodynamic Mass and Damping", *Journal of Pressure Vessel Tech.*, Vol. 111, pp. 466-477.

Pettigrew M.J., Tromp J.H., Taylor C.E. & Kim S., 1989b, "Vibration of Tube Bundles in Two-Phase Cross-Flow: Part 2 - Fluid-Elastic Instability", *ASME J. of Pressure Vessel Tech.*, Vol. 111, pp. 478-487.

Pettigrew M.J. & Taylor C.E., 1991, "Fluid-Elastic Instability of Heat Exchanger Tube Bundles: Review and Design Recommendations", *ASME Journal of Pressure Vessel Technology*, Vol. 113, pp. 242-256.

Pettigrew M.J. & Taylor C.E., 1992, "Two Phase Flow Induced Vibration: An Overview", *Journal of Pressure Vessel Technology*, Vol. 116, pp. 233-253.

Pettigrew M.J. & Knowles G.D., 1992, "Some Aspects of Heat Exchanger Tube Damping in Two-Phase Mixtures", *1992 International Symposium on Flow Induced Vibration and Noise*, Vol. 1, pp. 141-160.

Pettigrew M.J. & Taylor C.E., 1994, "Two-Phase Flow-Induced Vibration: An Overview", Survey paper, ASME Journal of Pressure Vessel Technology,. Vol. 116, pp. 233-253.

Pettigrew M.J., Taylor C.E. & Yasou A., 1994, "Vibration Damping of Heat Exchanger Tube Bundles in Two-Phase Flow", *Welding Research Council Bulletin*, No. 389, New York, pp. 1-41.

Pettigrew, M.J., Taylor C.E., Jong J.H., & Currie I.G., 1995, "Vibration of a Tube Bundle in Two-Phase Freon Cross-Flow", *ASME J. of Pressure Vessel Tech*nology, Vol. 117, pp.321-329.

Price S. J. & Païdoussis M. P., 1982, "A Theoretical Investigation of the Parameters Affecting the Fluidelastic Instability of a Double Row of Cylinders Subject To Cross-Flow. In *Proceedings 3rd International Conference on Vibrations in Nuclear Plant*, pp. 107-119, Keswick, U.K.

Price S. J. & Païdoussis M. P., 1983, "Fluidelastic Instability of a Double Row of Circular Cylinders Subject to Cross-Flow, *ASME Journal of Vibration, Acoustics, Stress and Reliability in Design*, Vol. 95, pp. 59-66.

Price S. J. & Païdoussis, M.P., 1984, "An Improved Mathematical Model for the Stability of Cylinder Rows Subject to Cross-Flow, *Journal of Sound and Vibration*, Vol. 97, pp. 615-640.

Price S. J. & Païdoussis M.P., 1985 "Fluidelastic Instability of a Full Array of Flexible Cylinders Subected to Cross-Flow, In *Fluid-Structure Interaction and Aerodynamic Damping* (eds E. H. Dowell & M. K. Au-Yang), pp. 171-192. New York: ASME.

Price S. J. & Païdoussis, M.P., 1986a, "A Constrained-Mode Analysis of the Fluidelastic Instability of a Double Row of Circular Cylinders Subject to Cross-Flow: A Theoretical Investigation of System Parameters, *Journal of Sound and Vibration*, Vol. 105, pp. 121-142.

Price S. J. & Païdoussis, M.P., 1986b, "A Single Flexible Cylinder Analysis for the Fluidelastic Instability of an Array of Flexible Cylinders in Cross-Flow, *ASME Journal of Fluids Engineering*, Vol. 108, pp. 193-199.

Price S.J., Päidoussis M.P., MacDonald R. & Mark B., 1987, "The Flow-Induced Vibration of a Single Flexible Cylinder in a Rotated Square Array of Rigid Cylinders with Pitch over Diameter Ratio of 2.12", *Journal of Fluids and Structures*, Vol. 1, pp. 359-378.

Price S.J. & Païdoussis M.P. 1987, "The Flow-Induced Vibration of a Single Flexible Cylinder in an In-Line Array of Rigid Cylinders", *Journal of Fluids and Structures*, Vol. 3, pp. 61-82.

Price S.J. & Païdoussis M.P. & Giannias N., 1990, "A Generalised Constrained-Mode Analysis for Cylinder Arrays in Cross-Flow", *Journal of Fluids and Structures*, Vol. 4, pp. 171-202.

Price S.J. & Kuran S., 1991, "Fluidelastic Stability of a Rotated Square Array with Multiple Flexible Cylinders Subjected to Cross-Flow", *Journal of Fluids and Structures*, Vol. 5, pp. 551-572.

Price S.J., 1995, "A Review of Theoretical Models for Fluidelastic Instability of Cylinder Arrays in Cross-Flow", *Journal of Fluids and Structures*, Vol. 9, pp. 463-518.

Remy R.M., 1982, "Flow Induced Vibration of Tube Bundles in Two Phase Cross Flow", Paper 1.9, *Proceedings of the 3rd International Conference of Vibrations in Nuclear Plants*, Keswick UK, Vol. 1, pp. 135-160.

Roberts B.W., 1962, "Low Frequency Self-Excited Vibration in a Row of Circular Cylinders Mounted in an Air Stream", PhD Thesis, Univ. of Cambridge, U.K.

Roberts B.W., 1966, "Low Frequency Aeroelastic Vibrations in a Cascade of Circular Cylinders", *I.Mech. E. Mechanical Engineering Science Monograph*, No. 4.

Rogers R.G., Taylor C.E. & Pettigrew M.J., 1984, "Fluid Effects on Mulit-Span Heat Exchanger Tube Vibration", *Proceedings of the ASME-PVP Conference*, San Antonio, Texas.

Romberg O. & Popp K.,1997, "Random Excitation by Fluid Forces Acting on a Single Flexible Tube in bundles Subjected to Cross-Flow", In *Proceedings of the ASME Int. Symposium on Fluid-Structure Interaction: Aeroelasticity, Flow-Induced Vibration and Noise*, AD Vol. 53-2, (eds.M.P. Païdoussis *et al.*) Dallas, pp. 173-181.

Schrage D.S., Hsu J.T., & Jensen M.K., 1988, "Two-Phase Pressure Drop in Vertical Cross Flow Across a Horizontal Tube Bundle," *AIChE J.*, Vol. 34, No. 1, pp. 107-115.

Schroeder K. & Gelbe H., 1999, "New Design Recommendations for Fluidelastic Instability in Heat Exchanger Tube Bundles", *Journal of Fluids and Structures*, Vol. 13, pp. 361-379.

Taitel Y., Bornea D., & Dukler A.E., 1980, "Modelling Flow Pattern Transitions For Steady, Upward Gas-Liquid Flow in Vertical Tubes. *AIChE J.* 26:345-354.

Tanaka H. & Takahara S. 1980, "Unsteady Fluid Dynamic Forces on a Tube Bundle and Its Dynamic Effect on Vibration", *In Flow-Induced Vibration of Power Plant Components*, (ed. M.K. Au-Yang), PVP-Vol. 41, pp. 77-92. New York: ASME.

Taylor C.E., Pettigrew M.J., Axisa F., & Villard B., 1988, "Experimental Determination of Single and Two-Phase Cross Flow-Induced Forces on Tube Rows", *ASME Journal of Pressure Vessel Technology*, Vol. 110, pp. 22-28.

Taylor C.E., 1992, "Random Excitation Forces in Tube Arrays Subjected to Two-Phase Cross-Flow", In *Proceedings ASME Int. Symposium on Flow-Induced Vibration and Noise; Vol. 1*, (ed. M.P. Päidoussis), HTD-Vol. 230/NE-Vol. 9, Anaheim U.S.A. New York: ASME.

Taylor C.E., Pettigrew M.J., & Currie I.G., 1996, "Random Excitation Forces in Tube Bundles Subjected to Two-Phase Cross-Flow", *ASME Journal of Pressure Vessel Technology*, Vol. 118, pp. 265-277.

Taylor C.E. & Pettigrew M.J., 1999, "Random Excitation in Heat Exchanger Tube Bundles", In *ASME PVP-Vol. 389, Flow-Induced Vibration*, Boston.

Ulbrich, R., & Mewes D., 1994, "Vertical, Upward Gas-Liquid Two-Phase Flow Across a Tube Bundle", *Int. Journal of Multiphase Flow*, Vol. 20(2), pp. 249-272.

Vince M.A. & Lahey R.T. Jr., 1982, "On the Development of an Objective Flow Regime Indicator", *Int. Journal of Multiphase Flow*, Vol. 8(2), pp. 93-124.

Weaver D.S. & Lever J., 1977, "Tube Frequency Effects on Cross Flow-Induced Vibrations in Tube Arrays", Paper IV.4, *5th Biennial Symposium on Turbulence*, Department of Chemical Engineering, University of Missouri-Rolla, Oct.1977.

Weaver D.S. & Grover L.K., 1978, "Cross-Flow Induced Vibrations in a Tube Bank-Turbulent Buffeting and Fluidelastic Instability", *Journal of Sound and Vibration*, Vol. 59, pp. 277-294.

Weaver D.S. & Koroyannakis D., 1982, "The Cross-Flow Response of a Tube Array in Water - A Comparison With the Same Array in Air", *Journal of Pressure Vessel Technology*, Vol. 104, pp. 139-146.

Weaver D.S. & Yeung H.C., 1983, "Approach Flow Direction Effects on the Cross-Flow Induced Vibrations of a Square Array of Tubes", *Journal of Sound and Vibration*, Vol 87(3), pp. 469-482.

Weaver D.S. & Koroyannakis D., 1983, "Flow-Induced Vibrations of Heat Exchanger U-Tubes: A Simulation to Study the Effects of Asymmetric Stiffness", *Journal of Vibration, Acoustics, Stress, and Reliability in Design*, Vol. 105, pp. 67-75.

Weaver D.S. & Yeung H.C., 1984, "The Effect of Tube Mass on the Flow Induced Response of Various Tube Arrays in Water, *Journal of Sound and Vibration*, Vol. 93, pp. 409-425.

Weaver, D.S. & Fitzpatrick J.A,, 1988, "A Review of Cross-Flow Induced Vibrations in Heat Exchanger Tube Arrays", *Journal of Fluids and Structures*, Vol. 2, pp.73-93.

Weaver D.S., 1992, "An Introduction to Flow-Induced Vibrations", Course Notes for Graduate Course No. ME-723, "Flow-Induced Vibrations", Dept. of Mechanical Eng., McMaster University, Hamilton Canada.

Weaver D.S., 1993, "Vortex Shedding and Acoustic Resonance in Heat Exchanger Tube Arrays", In *Technology for the '90s. Part III: Fluid-Structure Interaction*, Edited by M.K. Au Yang, pp. 775-810, New York, ASME.

Westermann G.D., 1981, "The Design and Construction of a Flow Loop for the Study of Two-Phase Cross Flow-Induced Vibrations of Heat Exchanger Tubes", Master's Thesis, McMaster University, Hamilton, Canada.

Whalley P.B. & Butterworth D., 1983, "A Simple Method for Calculating the Recirculating Flow in Vertical Thermosyphon and Kettle Reboilers", *Heat Exchangers for Two-Phase Applications*, HTD-Vol. 27, ASME, New York, pp. 47-53.

Whalley P.B., 1987, "Boiling Condensation and Gas-Liquid Flow", Oxford University Press, N.Y.

Whiston G.S. & Thomas G.D., 1982, "Whirling Instabilities in Heat Exchanger Tube Arrays", *Journal of Sound and Vibration*, Vol. 81, pp. 1-31.

Wolgemuth G.A., 1994, (personal communication with authors of Taylor & Pettigrew, 1999)

Yetisir M. & Weaver D.S., 1993a, "An Unsteady Theory for Fluidelastic Instability in an Array of Flexible Tubes in Cross-Flow. Part I: Theory", *Journal of Fluids and Structures*, Vol. 7, pp. 751-766.

Yetisir M. & Weaver D.S., 1993b, "An Unsteady Theory for Fluidelastic Instability in an Array of Flexible Tubes in Cross-Flow. Part II: Results and Comparison with Theory", *Journal of Fluids and Structures*, Vol. 7, pp. 767-782.

Yeung H.C. & Weaver D.S., 1983, "The Effect of Approach Flow Direction on the Flow-Induced Vibrations of a Triangular Tube Array", *Journal of Vibration, Acoustics, Stress, and Reliability in Design*, Vol. 105, pp. 76-82.

Zuber N., & Findlay J.A., 1965, "Average Volumetric Concentration in Two-Phase Flow Systems," *ASME Journal of Heat Transfer.*, Vol. 87, pp. 453-468.

APPENDIX A

VOID FRACTION MEASUREMENT by RADIATION ATTENUATION

Introduction

Void fraction is probably the most important parameter which characterizes any gas-liquid two phase flow, so that a wide variety of techniques have been proposed to measure this quantity. Radiation absorption is the most attractive method at present because it is non intrusive and relatively reliable.

Gamma ray attenuation was used in this research to measure the void fraction of the two-phase R-11 flow in the test section. The system, as shown schematically in Figure A1, consisted of a gamma source, metal shielding, a scintillator and the electronics necessary for signal processing. The following section summarizes the theory of radiation absorption as applied to two-phase, gas-liquid void fraction measurement.

Radiation Attenuation Methods:

Void fraction measurement by radiation attenuation is one of the most popular techniques, because it is reliable and non-intrusive. In most applications, this technique is used to make a global measurement of void fraction for a steady state process or a slow transient. However, if high intensity neutron or x-ray beams are used, then void fraction can also be measured in a fast transient process, and with additional equipment and special measuring techniques, local void fraction measurements can also be made. Banerjee and Lahey (1981) and Hewitt (1978) provide excellent reviews on the subject as well as an extensive list of researchers who have experimented with various attenuation devices. Chan and Banerjee (1981) provide an excellent design guideline for small scale gamma densitometers

specifically for void fraction measurement.

The gamma densitometer, shown schematically in Figure A1, is completely external to the flow system, so that it can be installed wherever enough space exists to collimate the radiation beam and pass it through the walls of the test section.

Theory of Radiation Attenuation:

The basic principle of the gamma ray attenuation method is that the intensity of the gamma beam will decrease exponentially when it passes through any medium. The attenuated flux is given by,

$$N = N_0 \exp(-\mu x) \tag{A1}$$

where, N= intensity of flux after passing through the medium

N_0= reference value of emitted flux

μ= absorption coefficient through the medium

x= distance travelled through the medium

The absorption coefficient is linearly related to the density of the substance by,

$$\mu = \eta \rho \tag{A2}$$

where η is constant. The intensity of a gamma beam for various conditions is then given by,

$$N_L = N_0 \exp(-\eta \rho_L x) \quad ;\textit{channel full of liquid} \tag{A3}$$

$$N_G = N_0 \exp(-\eta \rho_G x) \quad ;\textit{channel full of gas} \tag{A4}$$

$$N = N_0 \exp(-\eta \rho x) \quad ;\textit{channel full of two phase flow} \tag{A5}$$

The two phase density is related to the gas and liquid density by,

$$\rho = \alpha \rho_G + (1 - \alpha) \rho_L \tag{A6}$$

combining (A3) to (A6) we get,

$$\alpha = \frac{\ln N - \ln N_L}{\ln N_G - \ln N_L} \qquad \text{(A7)}$$

where N is the number of counts registered by the detector in two phase flow while N_G and N_L are the reference counts registered for the gas and liquid condition respectively. Equation (A7) imposes several restrictions. First, the source should be well collimated to ensure that the photons move in parallel paths, because equation (A1) formally defined attenuation in one coordinate direction only. This requirement was satisfied in this study, because the source and scintillator were separated by approximately 50 cm and collimator plates were placed in between to absorb any stray radiation. The maximum deviation angle of the photons from the perpendicular path in these experiments was about eleven degrees. This deviation angle could have been reduced by increasing the separation distance between the source and scintillator, but the consequence would have been a reduced photon flux received by the scintillator due to the reduced view factor. Hence, a lower signal to noise ratio would result. The second restriction of equation (A7) is that the photons are assumed to be mono-energetic. This condition is approximated in practice by admitting only the desired photons using a single channel analyzer, which counts only those photons with energies that fall within the prescribed range. This range was set on the gamma densitometer after calibration using a multi-channel analyzer, which was used to discern the various energies detected by the scintillator. One final restriction imposed by equation (A7) is that the fluid in the test section must be homogeneous. For most applications involving two phase flow, this requirement cannot be satisfied. However, the theory still holds in the case of separated flow if the interface between the two phases is perpendicular to the photon flux. In these experiments where the two phase flow was vertically upward, the condition of homogeneity is well satisfied at low void fraction flow where the bubbles are generally small and well mixed.

Despite being the most popular method of void fraction measurement, one must be aware that radiation absorption has a number of disadvantages:

1. Bulky and heavy metal shielding is required for human safety. However, if enough space exists in an application to accommodate the shielding, then this is not a major problem.

2. Since the absorption process is exponential, the average signal detected does not represent the average void fraction in the case of slug flow, where the void changes periodically from near zero to unity, corresponding to the passage of a liquid slug followed by a vapour slug respectively. This problem was studied by Harms and Forrest (1971) who developed a correlation factor for determining void based upon an idealized slug flow model. LeVert and Helminski (1973) proposed a way of reducing the errors by using two gamma ray beams having widely different energies. The ratio of the time averaged intensities from the two beams gave a result for the mean void fraction in the time varying flow.

3. A fundamental inaccuracy exists in measuring void fractions using a statistical analysis of the photon fluctuations received by the scintillator. This error reduces with longer counting periods and stronger sources. Chan and Banerjee (1981) provide a guideline for estimating the uncertainty in the void fraction, $\epsilon(\alpha)$, measurement based upon the error in counting statistics as follows,

$$\epsilon(\alpha) = 1/(Sn\sqrt{N_\alpha t}) \; . \qquad \textbf{(A8)}$$

For the present Barium 133 source the sensitivity, Sn, is given by,

$$Sn = \frac{N_G - N_L}{(N_G + N_L)/2} \; . \qquad \textbf{(A9)}$$

Since the count rate in two phase flow, N_α, was between the count rates of liquid, N_L = 1260, and gas, N_G = 1890, and the counting period, t, was 20s, the sensitivity was about 40%. A conservative estimate of uncertainty using equation (A9) is about ±1.6%. However, during experiments the statistical behaviour of the counts was periodically monitored, and the worst case showed a standard deviation of about ±4% of the mean count, N_ϵ, over 5 samples. Using a "t" test with a 95% confidence interval, a value of $t_{0.95,4} = 2.78$ is calculated, so that the uncertainty in void fraction measurement is about ±5% . This uncertainty is greater than that given by equation (A9), and is likely due to flow unsteadiness

Gamma Ray Attenuation:

Table A1 gives the commercially available gamma sources which are useful for void fraction measurements. Gamma rays are an attractive source for void fraction measurements because different energies can be selected depending upon the strength needed to penetrate metal walls. This of course must be balanced against the required fluid sensitivity, which decreases as the source strength increases. For good measurement resolution, the sensitivity should be greater than approximately 25%, but values as low as 10% are common. In these experiments, a sensitivity of 40% was achieved due to the low absorption of the glass walls. A Barium 133 source was used which had a half life of 5.8 years. This was sufficiently long to ensure that the photon flux would remain constant throughout an experiment.

Calibration of Gamma Densitometer (Single Channel Analyzer)

This section explains the proper use of the gamma densitometer for measuring the void fraction in the test section. Presently, the gamma densitometer consists of the following items shown in Figure A1. The settings on the electronics which were found to give the highest sensitivity and zero energy peak shift are:

Coarse gain = 160 Fine gain = 1.0 NON INV Bipolar

E = 1.5 ΔE = 1.0 Discriminator = 3.0 V Scintillator excitation = 600 V

In addition, the front head of the scintillator needs to be grounded to eliminate the noise which is picked up from the pump motor. This noise adds about 2000 counts/sec to the count rate. Grounding is most easily accomplished using a thin aluminium strip that is pressed against the head and connected to the ground screw at the back of the scintillator using a wire with alligator clips.

Once the gamma densitometer has been set up properly as outlined above, it needs to be calibrated. This is performed by measuring the count rate for 0% void and 100% void in stagnant (or flowing fluid). When measuring the count rate for 100% void fraction, the test section should be dry, so that walls of the test section should be allowed to dry out if the liquid had just been drained. The calibration count can be of any duration, but it is best form to normalize the count by dividing by the

number of seconds to obtain the count rate in counts/second. It is also useful to measure the standard deviation of the calibration counts, which can only be done properly if consistency is maintained. For example, if during the experiment, it is decided to use a counting duration of 120 seconds, then the calibration counts should be of the same duration, and at least 5 counts should be obtained in order to determine the standard deviation of the samples (in percent).

Other Non-Intrusive Methods of Void Fraction Measurements

X-ray systems are sometimes used instead of gamma rays because higher source intensities can be obtained, which is necessary for fast transient measurements where the counting period must be very short. One serious drawback to using x-rays however, is that the beam intensity is not stable and will naturally fluctuate, which necessitates the need for an additional reference detector and makes the signal analysis complicated. Low penetration through metal walls and other high density materials is another drawback which sometimes renders x-rays as inapplicable to many applications.

Fast Neutron scattering and absorption methods are attractive for steam-water void fraction determination because the neutron beam is strongly absorbed and scattered by hydrogenous fluids yet is less affected by metal walls than either gamma or x-ray beams. In addition, there exists a unique relationship between the energy and direction of a neutron scattered by a proton. This method has been used mostly for global measurements of void fraction but special techniques have been devised and tested by Hussein (1983) to use neutron scattering for crude local void measurements.

This technique requires only a single exposure of short duration, which allows for fast transient measurements. The shielding requirement is much reduced compared with gamma rays, and the beam is less affected by the metal walls. The main disadvantage of this method is that it requires access to a reactor port to obtain a collimated fast/epithermal neutron beam. Thermal or "slow" neutrons are useless because they are subject to multiple scatterings in water and lose memory of the details of their passage, which makes it impossible to interpret the scattering data.

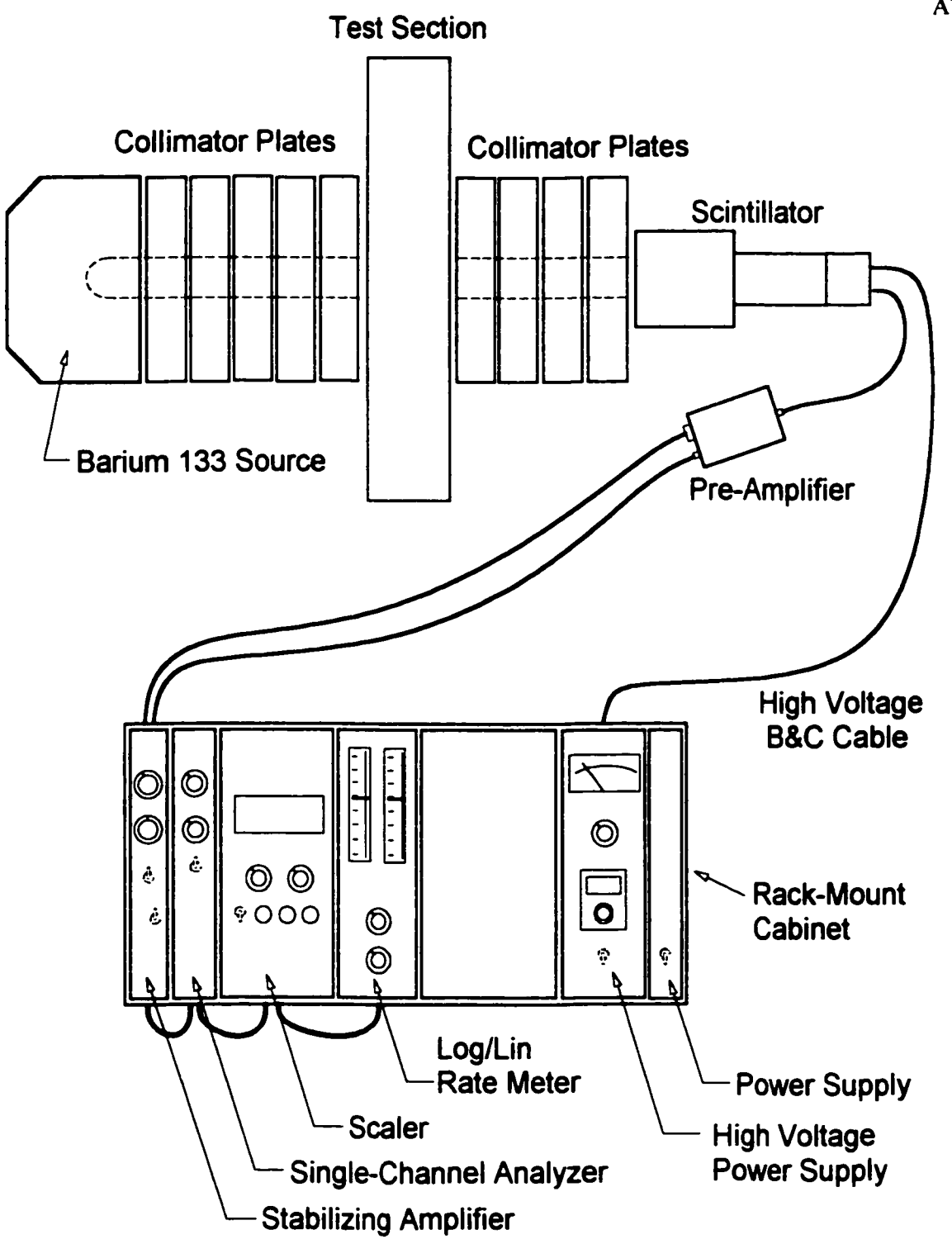

Figure A1 Schematic diagram of gamma densitometer equipment.

Table A1 Some commercially available gamma sources.

Isotope energy	Half-life	Principle photon (keV)	Emission (%)
Americium-241	433 y	11.9 - 22.3 59.5	40 approx 35.3
Barium-133	10.8 y	30-36 8081 276.0 303.0 356.0 384.0	123 approx. 36.2 7.2 18.7 61.5 8.9
Cadmium-109	453 d	22.1 - 26.0 88.0	102.3 3.6
Cesium-137	30.1 y	32.0 - 38.0 662.0	8.0 85.1
Cobalt-57	270.5 d	6.4 - 7.0 14.4 122.0 136.5	55 approx. 9.4 85.2 11.1
Cobalt-60	5.27 y	1173.0 1333.0	99.86 99.98
Curium-244	17.8 y	12.1 - 23.0	8 approx.
Gadolinium-153	241.5 y	41.3 - 47.3 69.7 97.4 103.2	110 approx. 2.6 30 20
Iodine-129	1.57×10^7 y	30 - 35 40.0	69 approx 7.5
Lead-210	22.3 y	9.42 - 16.4 46.5	21 approx. 4 approx.
Manganese-54	312.5 d	835.0	100
Plutonium-238	87.75 y	11.6 - 21.7	13 approx.
Tellurium-123m	119.7 d	27.4 - 31.1	50 approx.
Thulium-170	128 d	50.0 - 59.7 84.3	5 approx. 3.4

APPENDIX A REFERENCES

Banerjee S. & R.T. Lahey, 1981, "Advances in Two Phase Flow Instrumentation", *Adv. Nucl. Sci. Tech.*, Vol. 13, 227-414.

Chan A.M.C., S. Banerjee, 1981, "Design Aspects of Gamma Densitometer for Void Fraction Measurements in Small Scale Two Phase Flows", *Nuclear Instruments and Methods*, Vol. 190, 135-148.

Harms A.A., C.F. Forest, 1971, "Effects in Radiation Diagnosis of Fluctuating Voids", *Nucl. Sci. & Eng.*, Vol. 46, 408-413.

Hewitt G.F., I. King, P.C. Lovegrove, 1961, "Holdup and Pressure Drop Measurements in the Two Phase Annular Flow of Air-Water Mixtures", AERE-R3764.

Hussein E.M.A., 1983, "Fast Neutron Scattering Method for Local Void Fraction Distribution Measurement in Two Phase Flow", PhD Thesis, McMaster University, Dep't of Eng. Phys. Hamilton, Canada.

LeVert, F.E. & E. Helminski, 1973, "Dual-Energy Method for Measuring Void Fractions in Flowing Media", *Nuclear Technology*, Vol. 19 (1), pp. 58-60.

Appendix B

Empirical Void Fraction Models of Other Researchers

The following empirical models were developed by other researchers for predicting the actual void fraction in two-phase upward flow. The first model was developed simply for in-tube flows while the latter two were developed for the shell-side flows in the heat exchanger tube arrays. During the course of this research, it was found that none of these models agreed with the void fraction measurements made using the gamma densitometer. This fact initiated the search for the newly developed void fraction model, which is presented in Chapter 7.

Drift Flux Model

One of the earliest void fraction models was developed by Zuber and Findlay (1965), who proposed a weighted mean velocity of the gas phase, $\bar{U}_G$, given by Eq. (B1),

$$\bar{U}_G = C_o (j_G + j_L) + V_B , \qquad \textbf{(B1)}$$

where $(j_G + j_L)$ is the mixture mean velocity and V_B is the drift velocity which can be interpreted as the rise velocity of bubbles in stagnant liquid. The distribution parameter, C_o, was suggested to be 1.13 by Zuber and Findlay but other researchers have adjusted this constant to better fit their data. For example, Dowlati *et al.* (1992) used 1.035, while Delenne *et al.* (1997) used 0.9 which best fit their data for flow across tube bundles. In the present work, C_o=1 was chosen for comparison with the other models for all the data comparisons so that the boundary condition at x=1 would be satisfied. Following the method of Delenne *et al.*, the drift velocity, V_B, was determined from Eq. (B2),

$$V_B = 1.53 (\sigma g (\rho_L - \rho_G)/\rho_L^2)^{1/4} , \qquad \textbf{(B2)}$$

which gives 0.16 m/s for R-11, while for air-water at atmospheric conditions gives 0.25 m/s which agrees with experimental measurements of Whalley (1987). For the R-113 data of Dowlati *et al.* (1996) (shown in Figure 7.7 of Chapter 7), the drift velocity was calculated to be $V_B = 0.147$ m/s. The void fraction, ϵ, can be determined as follows.

$$\epsilon = \frac{x G_p}{\rho_G \bar{U}_G} . \qquad \textbf{(B3)}$$

Void Fraction Model of Schrage *et al.* (1988)

These authors performed experiments with two-phase flows in a normal square tube bundle subjected to air-water upward cross-flow in which the void fraction was measured with a quick closing plate valves positioned on either end of the bundle. Their measurements revealed that the void fraction was greatly over-predicted by the homogeneous equilibrium model, and was strongly affected by mass flux. A correlation to predict void fraction was developed as below,

$$\epsilon = \epsilon_H (1 + 0.123\, Fr^{-0.191} \ln(x)) . \qquad \textbf{(B4)}$$

Froude number, Fr, was determined by,

$$Fr = G_p / (\rho_L \sqrt{g D}) . \qquad \textbf{(B5)}$$

The homogeneous void fraction, ϵ_H, was determined by,

$$\epsilon_H = (1 + \frac{\rho_G}{\rho_L}(\frac{1}{x} - 1))^{-1} . \qquad \textbf{(B6)}$$

Void Fraction Model of Dowlati *et al.* (1992)

This model was based upon extensive experimental work in vertical air-water void fraction measurements in normal square and normal triangular bundles of pitch over diameter ratios of 1.3 and 1.75 each. Gamma densitometry was used to measure the void fraction in the array, where an average

value was obtained from four measurement locations. Their experiments revealed that the homogeneous equilibrium model was insufficient to predict void fraction because it did not account for velocity ratio and the effects of mass flux. It was observed that velocity ratio tended to decrease with mass flux. Since buoyancy was the driving force of the velocity ratio and the mass flux effect was caused by a balance of buoyancy and inertial forces, they used the dimensionless gas velocity, j_G^*, as a controlling parameter,

$$j_G^* = \frac{x G_p}{\sqrt{g D \rho_G (\rho_L - \rho_G)}} . \qquad \textbf{(B7)}$$

Subsequently, they found that their void fraction data correlated well using Eq. (B8) below,

$$\epsilon = 1 - (1 + C_1 j_G^* + C_2 j_G^{*2})^{-0.5} . \qquad \textbf{(B8)}$$

Initially they selected constants C_1=35 and C_2=1 respectively as a best fit for square arrays and suggested using C_2=30 when j_G^*>0.2 (Dowlati *et al.* 1990). However, in the subsequent paper, (Dowlati *et al.* 1992), they set constants C_1=30 and C_2=50 to give the best overall fit for the square and triangular tube arrays in air-water flow, and these values were used to plot their void fraction model in Figs. 1, 3-6. For R-113 flow, Dowlati *et al.* (1996) found that C_1=10 and C_2=1 provided the best fit, and these values were used to plot their void fraction model in Fig. 7.7 of Chapter 7.

Appendix C

Selected Experimental Data Tables

Test Series A - Experiments A25, A27 for the fully flexible array using tube bundle #3.

Test Series B - Experiments B02, B03 and B05 for the single flexible array using tube bundle #1.

Test Series C - Experiments C12, C13 and C14 for the single flexible array using tube bundle #4.

Data Sheet for Two-Phase Flow-Induced Vibration — Fully flexible bundle #3

Exp A25 Apr 23/96 — Gamma Densitometer Calibration

Light Probe Calibration — SCA

217 V/inch STRM — 65080 -LIQ- — rho_L = 1484 kg/m3

216 V/inch TRNS — 84640 -GAS- — * Fluidelasbc threshold

Trial #	1	2	3	4	5	6	7	8	9*	10	11	12	13	14
Q1 (in)														
Q2 (in)	3.7	3.8	3.8	3.8	3.8	3.8	3.8	3.8	3.8	3.8	3.8	3.8	3.8	3.8
T1d (mV)	1.67	1.81	1.9	1.97	1.99	2.01	2.03	2.04	2.05	2.06	2.07	2.07	2.1	2.11
T1u (mV)	1.66	1.79	1.9	1.99	2.05	2.07	2.09	2.11	2.11	2.12	2.13	2.13	2.15	2.16
T2 (mV)	1.38	1.46	1.51	1.58	1.64	1.66	1.69	1.73	1.75	1.78	1.8	1.81	1.85	1.9
Power (kW)	2.65	3.25	3.6	4.2	4.6	5.1	5.3	5.65	5.75	5.95	6.1	6.3	6.65	6.9
N (rpm)	535	535	535	535	535	535	535	535	535	535	535	535	535	535
SCA Count	65900	66200	67100	69000	71400	73400	74500	75300	76350	76740	77500	77800	78400	79000
P1 (psi)	5.5	6	6.5	6.6	6.7	6.8	6.9	7	7.1	7.2	7.2	7.3	7.5	7.6
T4 (mV)	0.85	0.87	0.86	0.84	0.84	0.8	0.82	0.82	0.82	0.82	0.85	0.82	0.82	0.83
T5 (mV)	0.51	0.5	0.49	0.49	0.47	0.46	0.46	0.45	0.46	0.46	0.46	0.45	0.45	0.45
Qw (inHg)	0.3	0.3	0.4	0.5	0.5	0.8	0.8	0.8	0.8	0.8	0.8	1	1	1
Calculated Data														
Q (L/s)	0.839	0.839	0.839	0.839	0.839	0.839	0.839	0.839	0.839	0.839	0.839	0.839	0.839	0.839
Q1 (L/s)	0.410	0.404	0.404	0.404	0.404	0.404	0.404	0.404	0.404	0.404	0.404	0.404	0.404	0.404
Q2 (L/s)	0.429	0.435	0.435	0.435	0.435	0.435	0.435	0.435	0.435	0.435	0.435	0.435	0.435	0.435
T1d (C)	27.9	30.2	31.6	32.8	33.1	33.4	33.8	33.9	34.1	34.3	34.4	34.4	34.9	35.1
T1u (C)	27.7	29.8	31.6	33.1	34.1	34.4	34.8	35.1	35.1	35.3	35.4	35.4	35.7	35.9
T1_corrected (C)	27.8	30.1	31.6	32.9	33.4	33.7	34.1	34.3	34.4	34.6	34.7	34.7	35.2	35.3
T2 (C)	23.1	24.4	25.2	26.4	27.4	27.7	28.2	28.8	29.2	29.7	30.0	30.2	30.8	31.6
Fluid Properties														
rhoL1 (kg/m3)	1469	1464	1460	1457	1456	1455	1454	1454	1454	1453	1453	1453	1452	1451
rhoG1 (kg/m3)	6.68	7.18	7.54	7.84	7.97	8.05	8.13	8.18	8.21	8.25	8.29	8.29	8.41	8.45
hf1 (kJ/kg)	225	227	228	229	230	230	230	230	231	231	231	231	231	231
hfg1 (kJ/kg)	180.3	179.4	178.8	178.3	178.1	177.9	177.8	177.7	177.7	177.6	177.5	177.5	177.4	177.3
rhoL2 (kg/m3)	1481	1477	1476	1473	1471	1470	1469	1467	1466	1465	1464	1464	1462	1460
hf2 (kJ/kg)	220	222	222	223	224	225	225	226	226	226	227	227	227	228
Gp (kg/m2s)	204	201	201	200	200	200	200	200	200	199	199	199	199	199
dh (kJ/kg)	4.27	5.33	5.92	6.92	7.59	8.41	8.75	9.33	9.50	9.83	10.08	10.41	11.00	11.41
quality	0.00029	0.00144	0.00091	0.00598	0.01204	0.01669	0.0194	0.02492	0.02693	0.03048	0.03273	0.03542	0.03982	0.04553
Homogeneous Flow														
rhoH (kg/m3)	1381.9	1132.2	1243.3	692.3	456.6	363.6	326.7	269.0	253.2	229.3	216.8	202.6	185.2	165.4
HEM Void	0.06	0.23	0.15	0.53	0.69	0.75	0.78	0.82	0.83	0.85	0.86	0.87	0.88	0.89
HEM Vp (m/s)	0.147	0.176	0.160	0.266	0.434	0.545	0.606	0.735	0.781	0.863	0.912	0.976	1.067	1.194
Separated Flow														
Corr. Factor	0.995	0.993	0.992	0.991	0.991	0.990	0.990	0.990	0.990	0.990	0.989	0.989	0.989	0.989
RAD Void	0.03	0.04	0.09	0.19	0.33	0.44	0.50	0.54	0.59	0.61	0.65	0.67	0.70	0.73
Velocity ratio	2.14	7.03	1.81	4.62	4.56	3.96	3.61	3.92	3.38	3.51	3.18	3.23	3.13	3.09
U_G (m/s)	0.31	1.00	0.27	0.78	0.92	0.95	0.96	1.13	1.11	1.20	1.21	1.26	1.35	1.48
U_L (m/s)	0.14	0.14	0.15	0.17	0.20	0.24	0.27	0.29	0.33	0.34	0.36	0.40	0.43	0.48
rho (kg/m3)	1427	1405	1332	1175	981	823	738	678	598	569	513	491	447	404
V_EQ (m/s)	0.14	0.14	0.15	0.17	0.21	0.25	0.28	0.30	0.34	0.36	0.40	0.42	0.46	0.51
Superficial Gas and Liquid Phase Velocities														
U_GS	0.009	0.040	0.024	0.153	0.303	0.415	0.477	0.606	0.655	0.736	0.786	0.851	0.943	1.071
U_LS	0.139	0.137	0.137	0.137	0.136	0.135	0.135	0.134	0.134	0.133	0.133	0.132	0.132	0.131
RMS Amplitude (% dia.)														
Srms (%)	0.03	0.04	0.14	0.49	0.87	1	1.02	1.09	1.15	1.37	1.66	2.25	4.29	5.95
Trms (%)	0.01	0.02	0.12	0.37	0.64	0.84	0.97	1.25	1.64	2.61	4.75	6.76	10.87	14.1
Frequency Hz														
Strm 1	31.75	31.5	31.75	33.75	33.75	36.5	37.75	37.75	38	38.5	38.5	38.5	38.5	38.5
Trms 1	31.25	31.25	31.5	33	32.75	36	38	38.25	38.25	38.5	38.5	38.5	38.5	38.5

Data Sheet for Two-Phase Flow-Induced Vibration — Fully flexible tube bundle # 3

Exp A27 Apr 25/96 — Gamma Densitometer Calibration

Light Probe Calibration — SCA

232 V/inch STRM — 66026 -LIQ- — rho_L = 1483 kg/m3

226 V/inch TRNS — 66093 -GAS-

* Fluidelastic Threshold

Trial #	1	2	3	4	5	6	7	8	9	10	11	12	13*	14	16
Q1 (in)															
Q2 (in)	4	4	4	4	4	4	4	4	4	4	4	4	4	4	4
T1d (mV)	2.03	2.05	2.09	2.12	2.16	2.1	2.13	2.17	2.17	2.17	2.13	2.13	2.15	2.18	2.22
T1u (mV)	2	2.05	2.1	2.15	2.21	2.15	2.17	2.21	2.21	2.22	2.17	2.18	2.2	2.23	2.02
T2 (mV)	1.74	1.77	1.8	1.85	1.91	1.81	1.85	1.93	1.92	1.94	1.84	1.85	1.9	1.95	2.02
Power (kW)	3.55	3.75	4.05	4.2	4.55	5.05	5.5	6.1	6.3	6.45	5.7	5.85	6.1	6.7	7.35
N (rpm)	640	640	640	640	640	640	640	640	640	640	640	640	640	640	640
SCA Count	66700	66960	68500	69950	73000	72840	74000	76100	76250	76800	74400	74800	75700	77300	78500
P1 (psi)	7.6	7.9	8	8.1	8.5	8	8	8.5	8.5	8.5	8	8	8.2	8.5	9
T4 (mV)	1.16	1.15	1.17	1.17	1.2	0.99	0.99	1	0.96	0.95	0.92	0.92	0.95	0.93	0.95
T5 (mV)	0.65	0.63	0.61	0.59	0.57	0.53	0.52	0.56	0.49	0.48	0.48	0.49	0.49	0.49	0.48
Qw (inHg)	0.25	0.25	0.25	0.25	0.25	0.5	0.5	0.5	0.6	0.6	0.6	0.6	0.6	0.8	0.8
Calculated Data															
Q (L/s)	1.030	1.030	1.030	1.030	1.030	1.030	1.030	1.030	1.030	1.030	1.030	1.030	1.030	1.030	1.030
Q1 (L/s)	0.584	0.584	0.584	0.584	0.584	0.584	0.584	0.584	0.584	0.584	0.584	0.584	0.584	0.584	0.584
Q2 (L/s)	0.446	0.446	0.446	0.446	0.446	0.446	0.446	0.446	0.446	0.446	0.446	0.446	0.446	0.446	0.446
T1d (C)	33.8	34.1	34.8	35.3	35.9	34.9	35.4	36.1	36.1	36.1	35.4	35.4	35.7	36.2	36.9
T1u (C)	33.3	34.1	34.9	35.7	36.7	35.7	36.1	36.7	36.7	36.9	36.1	36.2	36.6	37.1	33.6
T1_corrected (C	33.6	34.1	34.8	35.4	36.2	35.2	35.6	36.3	36.3	36.3	35.6	35.7	36.0	36.5	36.9
T2 (C)	29.0	29.5	30.0	30.6	31.8	30.2	30.8	32.1	32.0	32.3	30.7	30.8	31.6	32.5	33.6
Fluid Properties															
rhoL1 (kg/m3)	1456	1454	1453	1451	1449	1452	1451	1449	1449	1449	1451	1451	1450	1449	1450
rhoG1 (kg/m3)	8.02	8.14	8.32	8.47	8.66	8.41	8.52	8.69	8.69	8.70	8.52	8.53	8.62	8.75	8.61
hf1 (kJ/kg)	230	230	231	232	232	231	232	232	232	232	232	232	232	233	232
hfg1 (kJ/kg)	178.0	177.8	177.5	177.3	177.0	177.4	177.2	176.9	176.9	176.9	177.2	177.2	177.0	176.8	177.1
rhoL2 (kg/m3)	1467	1465	1464	1462	1460	1464	1462	1459	1460	1459	1463	1462	1460	1458	1456
hf2 (kJ/kg)	226	226	227	227	228	227	227	229	228	229	227	227	228	229	230
Gp (kg/m2s)	288	288	288	288	287	288	288	287	287	287	288	288	287	287	286
dh (kJ/kg)	4.05	4.28	4.63	4.81	5.22	5.78	6.30	6.99	7.22	7.40	6.53	6.70	6.99	7.68	8.42
quality	-0.0007	0.00072	0.00158	0.00374	0.0072	0.00706	0.01106	0.01834	0.01879	0.0212	0.01152	0.01308	0.01723	0.02284	0.0356
Homogeneous Flow															
rhoH (kg/m3)	1657.4	1290.0	1140.4	886.7	659.3	656.1	505.0	358.8	352.2	321.4	491.8	451.7	373.5	304.3	208.3
HEM Void	-0.14	0.11	0.22	0.39	0.55	0.55	0.66	0.76	0.76	0.78	0.66	0.69	0.75	0.79	0.86
HEM Vp (m/s)	0.173	0.222	0.251	0.322	0.432	0.435	0.565	0.794	0.809	0.887	0.580	0.632	0.764	0.936	1.369
Separated Flow															
Corr. Factor	0.991	0.990	0.990	0.989	0.989	0.989	0.989	0.989	0.989	0.988	0.989	0.989	0.989	0.988	0.989
RAD Void	0.00	0.02	0.10	0.18	0.35	0.34	0.40	0.51	0.52	0.55	0.43	0.45	0.49	0.58	0.64
Velocity ratio	-40.13	7.49	2.38	2.85	2.25	2.34	2.80	2.95	2.93	2.95	2.67	2.79	3.03	2.86	3.55
U_G (m/s)	-7.98	1.51	0.53	0.69	0.68	0.70	0.92	1.18	1.19	1.27	0.91	0.99	1.16	1.30	1.86
U_L (m/s)	0.20	0.20	0.22	0.24	0.30	0.30	0.33	0.40	0.41	0.43	0.34	0.35	0.38	0.46	0.52
rho (kg/m3)	1451	1430	1303	1185	945	956	867	709	698	657	836	808	738	620	532
V_EQ (m/s)	0.20	0.20	0.22	0.24	0.30	0.30	0.33	0.41	0.42	0.44	0.35	0.38	0.39	0.47	0.55
Superficial Gas and Liquid Phase Velocities															
U_GS	-0.024	0.025	0.055	0.127	0.239	0.242	0.373	0.605	0.621	0.699	0.389	0.441	0.574	0.749	1.184
U_LS	0.196	0.196	0.196	0.197	0.197	0.197	0.196	0.194	0.194	0.194	0.196	0.196	0.196	0.193	0.190
RMS Amplitude (% dia.)															
Srms (%)	0.05	0.08	0.24	0.46	0.96	1	1.06	1.22	1.31	2.11	1.11	1.13	1.22	2.92	7.04
Trms (%)	0.03	0.04	0.19	0.35	0.73	0.75	0.92	1.77	2.72	5.9	1.07	1.16	1.77	9.33	15.3
Frequency Hz															
Strm 1	31.75	31.5	31.75	33.75	33.75	36.5	37.75	37.75	38	38.5	38.5	38.5	38.5	38.5	38.75
Trms 1	31.25	31.25	31.5	33	32.75	36	38	38.25	38.25	38.5	38.5	38.5	38.5	38.5	38.75
Heat Rejection Calculations															
T4 (C)	19.5	19.3	19.7	19.7	20.2	16.6	16.6	16.8	16.1	16.0	15.5	15.5	16.0	15.6	
T5 (C)	10.9	10.6	10.2	9.9	9.6	8.9	8.7	9.4	8.2	8.1	8.1	8.2	8.2	8.2	
Mw (kg/s)	0.105	0.105	0.105	0.105	0.105	0.148	0.148	0.148	0.148	0.163	0.163	0.163	0.163	0.163	0.188
Cp (kJ/kg K)	4.189	4.189	4.189	4.189	4.189	4.189	4.189	4.189	4.189	4.189	4.189	4.189	4.189	4.189	
Qwater (kW)	3.77	3.84	4.14	4.29	4.66	4.81	4.91	4.60	5.38	5.38	5.04	4.92	5.27	5.82	
Qroom (kW)	-0.22	-0.09	-0.09	-0.09	-0.11	0.24	0.59	1.50	0.92	1.07	0.66	0.93	0.83	0.88	
Qroom (%)	-6.2	-2.5	-2.2	-2.0	-2.3	4.8	10.7	24.6	14.6	16.3	11.6	15.9	13.7	13.2	

Data Sheet for Two-Phase Flow-Induced Vibration — Single Flexible Tube (#5) in a Rigid Tube Array

Exp B02 June 06/96 Gamma Densitometer Calibration

Light Probe Calibration		SCA		MCA			
32.3	V/inch STRM	26078	-LIQ-	27861	rho_L =	1444	kg/m3
43.3	V/inch TRNS	37795	-GAS-	42866			

Trial #	1	2	3	4	5	6	7	8	9	10	11	12
Q1 (in)												
Q2 (in)	1	1	1	1	1	1	1	1	1	1	1	1
T1d (mV)	2.17	2.19	2.2	2.23	2.25	2.28	2.31	2.34	2.38	2.4	2.45	2.51
T2 (mV)	1.94	1.97	2	2.04	2.08	2.13	2.15	2.21	2.24	2.28	2.32	2.39
Power (kW)	3.7	4	4.2	4.4	4.65	4.8	5.05	5.4	5.7	6.1	6.4	7.05
N (rpm)	420	420	420	420	420	420	420	420	420	420	420	420
SCA Count	29441	29873	30264	30621	30944	31461	31528	32067	32236	32756	32876	33224
MCA Count	31740	32351	32596	32729	33759	34301	34336	34741	34988	35548	35724	36245
P1 (psi)	8.5	8.5	8.7	8.9	9.4	9.6	10	10.4	10.7	11.2	11.5	12.6
T4 (mV)	1.11	1.12	1.13	1.13	1.15	1.12	1.13	1.12	1.11	1.07	1.07	1.09
T6 (mV)	0.84	0.84	0.84	0.84	0.84	0.83	0.84	0.83	0.82	0.82	0.82	0.82
Qw (inHg)	0.55	0.55	0.55	0.55	0.55	0.7	0.7	0.95	0.95	1.5	1.5	1.5
Calculated Data												
Q (L/s)	0.629	0.629	0.629	0.629	0.629	0.629	0.629	0.629	0.629	0.629	0.629	0.629
Q1 (L/s)	0.406	0.406	0.406	0.406	0.406	0.406	0.406	0.406	0.406	0.406	0.406	0.406
Q2 (L/s)	0.223	0.223	0.223	0.223	0.223	0.223	0.223	0.223	0.223	0.223	0.223	0.223
T1d (C)	36.1	36.4	36.6	37.1	37.4	37.9	38.4	38.9	39.5	39.9	40.7	41.7
T1_corrected (C)	36.3	36.7	36.8	37.3	37.7	38.2	38.6	39.1	39.8	40.1	41.0	42.0
T2 (C)	32.3	32.8	33.3	33.9	34.6	35.4	35.7	36.7	37.2	37.9	38.6	39.7
Fluid Properties												
rhoL1 (kg/m3)	1449	1448	1448	1447	1446	1445	1443	1442	1440	1440	1438	1435
rhoG1 (kg/m3)	8.71	8.80	8.84	8.97	9.06	9.19	9.33	9.46	9.65	9.74	9.98	10.26
hf1 (kJ/kg)	232.4	232.7	232.8	233.3	233.6	234.0	234.5	234.9	235.5	235.8	236.6	237.5
hfg1 (kJ/kg)	176.9	176.8	176.7	176.5	176.4	176.2	176.0	175.8	175.5	175.4	175.0	174.6
rhoL2 (kg/m3)	1459	1458	1456	1455	1453	1451	1450	1448	1447	1445	1444	1441
hf2 (kJ/kg)	228.7	229.2	229.6	230.2	230.8	231.5	231.8	232.7	233.2	233.8	234.4	235.4
dh (kJ/kg)	6.09	6.59	6.92	7.26	7.68	7.93	8.35	8.94	9.44	10.11	10.63	11.72
quality	0.01374	0.0174	0.02096	0.02372	0.02778	0.03094	0.0325	0.03841	0.04049	0.04604	0.04818	0.05543
Gp (kg/m2s)	200	200	199	199	199	199	199	198	198	198	198	197
Homogeneous Flow												
rhoH (kg/m3)	442.8	376.4	328.1	301.3	267.4	247.7	240.7	211.6	205.6	185.6	182.1	165.0
HEM Void	0.70	0.74	0.78	0.80	0.82	0.83	0.84	0.86	0.86	0.88	0.88	0.89
HEM Vp (m/s)	0.448	0.527	0.604	0.657	0.740	0.798	0.821	0.933	0.959	1.062	1.081	1.191
Separated Flow												
Corr. Factor	1.002	1.001	1.001	1.001	1.001	1.000	1.000	0.999	0.999	0.998	0.998	0.997
RAD Void	0.33	0.37	0.40	0.44	0.46	0.51	0.51	0.56	0.57	0.61	0.62	0.64
MCA Void	0.31	0.35	0.37	0.38	0.45	0.48	0.48	0.51	0.53	0.56	0.57	0.60
Velocity ratio	4.68	4.96	5.16	5.09	5.30	4.89	4.98	4.87	4.79	4.55	4.50	4.53
U_G (m/s)	0.95	1.07	1.17	1.21	1.32	1.32	1.35	1.45	1.46	1.53	1.54	1.65
U_L (m/s)	0.20	0.21	0.23	0.24	0.25	0.27	0.27	0.30	0.31	0.34	0.34	0.37
rho (kg/m3)	972	916	865	821	781	718	711	647	628	567	555	517
V_EQ (m/s)	0.21	0.22	0.24	0.25	0.27	0.29	0.29	0.32	0.33	0.37	0.38	0.41
Superficial Gas and Liquid Phase Velocities												
U_GS	0.315	0.395	0.473	0.527	0.610	0.669	0.692	0.805	0.831	0.935	0.955	1.065
U_LS	0.136	0.135	0.135	0.134	0.134	0.133	0.133	0.132	0.132	0.131	0.131	0.130
RMS Amplitude (% dia.)												
Srms (%)	1	1.01	1.03	0.99	1.04	1.04	1.05	1.07	1.06	1.04	1.04	1.02
Trms (%)	0.79	0.83	0.86	0.88	0.93	0.96	0.99	1.09	1.09	1.14	1.16	1.16
Frequency Hz												
Strm 1	35.3	35.5	35.8	35.8	36	36.1	36.2	36.2	36.4	36.4	36.5	36.5
Trns 1	35.1	35.4	35.5	35.8	35.8	36.1	36.3	36.3	36.3	36.5	36.5	36.6
Damping Ratio (%)												
Strm 1	3.19	3.11	3.1	3.37	3.17	3.34	2.51	2.78	2.67	2.49	2.36	2.27
Trns 1	2.24	2.57	2.57	2.58	2.13	2.49	1.93	2.01	1.58	1.62	1.53	1.4

Hydrodynamic Mass f_L = 31.8 Hz, fa = 38.1 Hz, m_t = 0.179 kg/m, m_L = 0.078 kg/m

m_h (kg/m)	0.03071	0.02776	0.02545	0.02374	0.02261	0.02038	0.01874	0.01874	0.01765	0.01657	0.01604	0.0155
m_R	0.394	0.356	0.326	0.304	0.290	0.261	0.240	0.240	0.226	0.212	0.206	0.199

Data Sheet for Two-Phase Flow-Induced Vibration — Single Flexible Tube (#5) in a Rigid Tube Array

Exp B03 June 07/96 — Gamma Densitometer Calibration

Light Probe Calibration — SCA — MCA

34.3 V/inch STRM — 25644 -LIQ- — 27621 rho_L = 1474 kg/m3

46 V/inch TRNS — 38269 -GAS- — 42998

Trial #	1	2	3	4	5	6	7	8	9	10	11	12
Q1 (in)												
Q2 (in)	1.1	1.1	1.1	1.1	1.1	1.1	1.1	1.1	1.1	1.1	1.1	1.1
T1d (mV)	2.2	2.24	2.25	2.28	2.31	2.34	2.38	2.4	2.45	2.5	2.55	2.63
T2 (mV)	1.99	2.04	2.08	2.12	2.16	2.2	2.25	2.29	2.33	2.37	2.44	2.52
Power (kW)	4.05	4.3	4.6	4.9	5.2	5.5	5.8	6.1	6.4	6.8	7.1	8.05
N (rpm)	480	480	480	480	480	480	480	480	480	480	480	480
SCA Count	29276	29792	30483	30912	31330	31635	31912	32231	32482	32628	32945	33320
MCA Count	31866	32426	33394	33776	33866	34368	34585	34932	35382	35426	35852	36300
P1 (psi)	8.9	9	9.5	9.8	9.8	10.3	11	11.1	11.7	12	12.9	14
T4 (mV)	1.15	1.13	1.13	1.09	1.09	1.11	1.11	1.07	1.08	1.05	1.06	1.03
T6 (mV)	0.89	0.87	0.87	0.82	0.82	0.82	0.82	0.81	0.8	0.8	0.81	0.79
Qw (inHg)	0.65	0.65	0.65	0.9	0.9	0.9	0.9	1.4	1.4	1.9	1.9	2.5
Calculated Data												
Q (L/s)	0.739	0.739	0.739	0.739	0.739	0.739	0.739	0.739	0.739	0.739	0.739	0.739
Q1 (L/s)	0.505	0.505	0.505	0.505	0.505	0.505	0.505	0.505	0.505	0.505	0.505	0.505
Q2 (L/s)	0.234	0.234	0.234	0.234	0.234	0.234	0.234	0.234	0.234	0.234	0.234	0.234
T1d (C)	36.6	37.2	37.4	37.9	38.4	38.9	39.5	39.9	40.7	41.5	42.4	43.7
T1_corrected (C)	36.8	37.5	37.7	38.2	38.6	39.1	39.8	40.1	41.0	41.8	42.6	43.9
T2 (C)	33.1	33.9	34.6	35.3	35.9	36.6	37.4	38.1	38.7	39.4	40.5	41.9
Fluid Properties												
rhoL1 (kg/m3)	1448	1446	1446	1445	1443	1442	1440	1440	1438	1436	1434	1430
rhoG1 (kg/m3)	8.84	9.01	9.06	9.19	9.33	9.46	9.65	9.74	9.98	10.21	10.46	10.85
hf1 (kJ/kg)	232.8	233.4	233.6	234.0	234.5	234.9	235.5	235.8	236.6	237.3	238.1	239.3
hfg1 (kJ/kg)	176.7	176.4	176.4	176.2	176.0	175.8	175.5	175.4	175.0	174.7	174.4	173.8
rhoL2 (kg/m3)	1457	1455	1453	1452	1450	1448	1446	1445	1443	1442	1439	1435
hf2 (kJ/kg)	229.5	230.2	230.8	231.4	232.0	232.6	233.3	233.9	234.5	235.1	236.2	237.4
Gp (kg/m2s)	248	247	247	247	247	246	246	246	245	245	245	244
Homogeneous Properties												
dh (kJ/kg)	5.38	5.71	6.11	6.52	6.92	7.33	7.74	8.14	8.56	9.10	9.52	10.82
quality	0.01136	0.01412	0.01892	0.02207	0.02524	0.02841	0.03162	0.03566	0.03721	0.03955	0.04371	0.0513
rhoH (kg/m3)	508.2	444.9	361.3	324.8	295.7	272.0	253.1	230.9	227.3	220.2	206.3	185.5
HEM Void	0.65	0.70	0.75	0.78	0.80	0.82	0.83	0.85	0.85	0.85	0.86	0.88
HEM Vp (m/s)	0.484	0.553	0.680	0.756	0.830	0.901	0.968	1.060	1.076	1.108	1.182	1.311
Separated Flow												
Corr. Factor	0.991	0.991	0.990	0.990	0.990	0.989	0.989	0.988	0.988	0.987	0.986	0.985
RAD Void	0.31	0.35	0.41	0.44	0.47	0.50	0.52	0.54	0.56	0.57	0.59	0.62
MCA Void	0.30	0.34	0.41	0.43	0.44	0.47	0.48	0.50	0.53	0.53	0.56	0.58
Velocity ratio	4.22	4.25	4.47	4.49	4.45	4.51	4.55	4.63	4.39	4.39	4.34	4.43
U_G (m/s)	1.03	1.10	1.27	1.34	1.41	1.49	1.56	1.66	1.64	1.67	1.73	1.87
U_L (m/s)	0.24	0.26	0.28	0.30	0.32	0.33	0.34	0.36	0.37	0.38	0.40	0.42
rho (kg/m3)	1004	942	860	811	764	730	700	665	639	625	592	555
V_EQ (m/s)	0.25	0.27	0.29	0.31	0.33	0.35	0.37	0.39	0.40	0.41	0.43	0.47
Superficial Gas and Liquid Phase Velocities												
U_GS	0.318	0.387	0.516	0.593	0.667	0.739	0.806	0.899	0.915	0.949	1.023	1.154
U_LS	0.169	0.169	0.168	0.167	0.167	0.166	0.165	0.165	0.164	0.164	0.163	0.162
RMS Amplitude (% dia.)												
Srms (%)	0.91	0.95	1.02	1.01	0.99	0.99	0.99	1.02	0.99	0.97	1	0.96
Trms (%)	0.72	0.79	0.86	0.94	0.93	0.95	0.98	1.03	1.09	1.08	1.11	1.16
Frequency Hz												
Strm 1	35.2	35.4	35.8	36.1	36.1	36.3	36.3	36.3	36.4	36.5	36.5	36.6
Trms 1	35	35.3	35.6	36	36.1	36.1	36.2	36.3	36.4	36.4	36.6	36.5
Damping Ratio (%)												
Strm 1	3.15	3.09	3.16	2.76	3.15	3.09	2.81	2.7	2.65	2.62	2.58	2.36
Trms 1	2.59	2.43	2.51	1.78	2.18	2.03	1.76	1.92	1.86	1.59	1.42	1.26
Hydrodynamic Mass	f_L = 31.8 Hz, fa = 38.1 Hz, m_t = 0.179 kg/m, m_L = 0.078 kg/m											
m_h (kg/m)	0.03191	0.02693	0.02488	0.02094	0.02038	0.01928	0.01874	0.01819	0.01711	0.01657	0.0155	0.0155
m_R	0.409	0.371	0.319	0.268	0.261	0.247	0.240	0.233	0.219	0.212	0.199	0.199

Data Sheet for Two-Phase Flow-Induced Vibration — Single Flexible Tube (#5) in a Rigid Tube Array

Exp B05 June 13/96 — Gamma Densitometer Calibration

Light Probe Calibration — SCA

86.9 V/inch STRM — 25959 -LIQ- — rho_L = 1479 kg/m3

136 V/inch TRNS — 38861 -GAS-

Trial #	1	2	3	4	5	6	7	8	9	10	11	12
Q1 (in)	0.85	0.85	0.85	0.85	0.85	0.85	0.85	0.85	0.85	0.85	0.85	0.85
Q2 (in)	3.3	3.3	3.3	3.3	3.3	3.3	3.3	3.3	3.3	3.3	3.3	3.3
T1d (mV)	2.3	2.31	2.33	2.35	2.37	2.39	2.42	2.45	2.48	2.51	2.55	2.59
T2 (mV)	2.04	2.06	2.1	2.13	2.16	2.21	2.27	2.31	2.35	2.4	2.45	2.5
Power (kW)	5.05	5.45	5.8	6.1	6.3	6.7	7.05	7.5	8.05	8.6	9.05	9.65
N (rpm)	690	690	690	690	690	690	690	690	690	690	690	690
SCA Count	28455	29052	29669	30347	30678	31237	31947	32444	32821	33207	33535	33646
MCA Count												
P1 (psi)	10	10.3	10.5	10.8	10.9	11	11.5	11.9	12	12.6	13	13.6
T4 (mV)	1.27	1.25	1.25	1.23	1.25	1.25	1.26	1.26	1.22	1.23	1.22	1.22
T6 (mV)	0.89	0.86	0.85	0.86	0.87	0.89	0.89	0.88	0.88	0.88	0.88	0.88
Qw (inHg)	0.8	0.8	0.8	1.1	1.1	1.1	1.4	1.4	1.9	1.9	2.6	2.6
Calculated Data												
Q (L/s)	1.121	1.121	1.121	1.121	1.121	1.121	1.121	1.121	1.121	1.121	1.121	1.121
Q1 (L/s)	0.716	0.716	0.716	0.716	0.716	0.716	0.716	0.716	0.716	0.716	0.716	0.716
Q2 (L/s)	0.405	0.405	0.405	0.405	0.405	0.405	0.405	0.405	0.405	0.405	0.405	0.405
T1d (C)	38.2	38.4	38.7	39.0	39.4	39.7	40.2	40.7	41.2	41.7	42.4	43.0
T1_corrected (C)	38.5	38.6	39.0	39.3	39.6	40.0	40.5	41.0	41.5	42.0	42.6	43.3
T2 (C)	33.9	34.3	34.9	35.4	35.9	36.7	37.7	38.4	39.0	39.9	40.7	41.5
Fluid Properties												
rhoL1 (kg/m3)	1444	1443	1443	1442	1441	1440	1439	1438	1436	1435	1434	1432
rhoG1 (kg/m3)	9.28	9.33	9.42	9.51	9.60	9.69	9.83	9.98	10.12	10.26	10.46	10.65
hf1 (kJ/kg)	234.3	234.5	234.8	235.1	235.4	235.7	236.1	236.6	237.0	237.5	238.1	238.7
hfg1 (kJ/kg)	176.0	176.0	175.8	175.7	175.6	175.4	175.2	175.0	174.8	174.6	174.4	174.1
rhoL2 (kg/m3)	1455	1454	1452	1451	1450	1448	1446	1444	1442	1440	1438	1436
hf2 (kJ/kg)	230.2	230.5	231.1	231.5	232.0	232.7	233.6	234.2	234.8	235.6	236.3	237.1
Gp (kg/m2s)	351	351	350	350	350	349	349	348	348	347	347	346
Homogeneous Properties												
dh (kJ/kg)	4.74	5.12	5.45	5.73	5.93	6.31	6.64	7.07	7.60	8.12	8.56	9.13
quality	0.0035	0.00649	0.01007	0.01253	0.01447	0.0192	0.02368	0.02701	0.0309	0.03566	0.03906	0.04329
rhoH (kg/m3)	936.5	722.5	569.8	499.2	456.3	375.7	323.9	295.4	268.2	241.2	227.0	211.3
HEM Void	0.35	0.50	0.61	0.66	0.69	0.74	0.78	0.80	0.82	0.84	0.85	0.86
HEM Vp (m/s)	0.372	0.482	0.610	0.696	0.761	0.924	1.071	1.173	1.291	1.435	1.523	1.634
Separated Flow												
Corr. Factor	0.988	0.988	0.988	0.987	0.987	0.987	0.986	0.986	0.985	0.985	0.985	0.984
RAD Void	0.20	0.25	0.30	0.36	0.38	0.43	0.48	0.52	0.55	0.57	0.60	0.60
MCA Void												
Velocity ratio	2.22	3.05	3.63	3.49	3.57	3.92	3.84	3.73	3.78	3.85	3.78	4.01
U_G (m/s)	0.67	0.98	1.25	1.30	1.38	1.62	1.75	1.82	1.95	2.11	2.17	2.33
U_L (m/s)	0.30	0.32	0.34	0.37	0.39	0.41	0.46	0.49	0.52	0.55	0.58	0.58
rho (kg/m3)	1160	1087	1012	933	895	831	752	699	659	619	585	575
V_EQ (m/s)	0.30	0.32	0.35	0.38	0.40	0.43	0.47	0.51	0.54	0.58	0.61	0.63
Superficial Gas and Liquid Phase Velocities												
U_GS	0.132	0.244	0.374	0.461	0.527	0.691	0.839	0.943	1.062	1.207	1.295	1.407
U_LS	0.242	0.241	0.240	0.240	0.239	0.238	0.236	0.236	0.235	0.233	0.232	0.231
RMS Amplitude (% dia.)												
Srms (%)	0.9	1.07	1.12	1.23	1.19	1.2	1.24	1.18	1.18	1.17	1.14	1.22
Trms (%)	0.67	0.78	0.81	0.94	0.93	1.05	1.12	1.18	1.36	1.45	1.61	1.66
Frequency Hz												
Strm 1	34.2	34.8	35	35.5	35.8	36	36.1	36.5	36.5	36.6	36.7	36.7
Trms 1	33.9	34.3	34.7	34.8	35.3	35.7	35.6	36.1	36.3	36.5	36.5	36.6
Damping Ratio (%)												
Strm 1	3.68	3.38	3.14		3.28	3.15		3.2	3.03	3.01	2.56	2.35
Trms 1	2.81	2.38	2.66		2.21	2.27		1.68	1.66	1.46	1.24	1.18
Hydrodynamic Mass Calculations	f_L = 31.8 Hz, fa = 38.1 Hz, m_t = 0.179 kg/m, m_L = 0.078 kg/m											
m_h (kg/m)	0.04511	0.03867	0.03494	0.03131	0.0266	0.02317	0.02317	0.01819	0.01711	0.0155	0.01497	0.01444
m_R	0.578	0.496	0.448	0.401	0.341	0.297	0.297	0.233	0.219	0.199	0.192	0.185

Data Sheet for Two-Phase Flow-Induced Vibration **Date: July 10/97**
Test Series C: Exp No. 12 P_atm = 0.102 MPa

Light probe calibration		Upstrm	Bundle	**Gamma densitometer calibration**		
Strm (V/in) =	23.3	6.459	4.061	= LIQ (volts)	1476	kg/m3 (Liq. R-11 density)
Trns (V/in) =	44.3	8.586	5.028	= GAS (volts)	25.0	C (R-11 temperature at calibration time)

Trial No.	**1**	**2**	**3**	**4**	**5**	**6**	**7**	**8**	**9**
Q1 (inHg)	0.65	0.65	0.65	0.65	0.65	0.65	0.65	0.65	0.65
Q2 (inHg)	1.00	0.90	0.90	0.90	0.90	0.90	0.90	0.90	0.90
T1d (mV)	2.12	2.18	2.23	2.28	2.34	2.41	2.46	2.52	2.66
T1u (mV)	2.22	2.24	2.28	2.33	2.36	2.45	2.50	2.56	2.70
T3 (mV)	1.69	1.70	1.74	1.77	1.80	1.84	1.84	1.90	1.98
T2 (mV)	2.04	2.06	2.12	2.17	2.22	2.30	2.35	2.42	2.56
Power (kW)	5.05	5.35	5.70	6.25	6.60	7.10	7.40	8.00	9.00
N (rpm)	520	520	520	520	520	520	520	520	520
GD upstrm (Volts)	7.441	7.626	7.681	7.716	7.767	7.809	7.828	7.877	7.938
GD bundle (Volts)	4.530	4.562	4.586	4.603	4.618	4.632	4.648	4.661	4.684
P1 (psi)	8.40	8.40	8.60	9.50	10.00	11.00	11.80	12.50	14.50
T4 (mV)	1.22	1.20	1.19	1.19	1.19	1.19	1.19	1.19	1.21
T6 (mV)	0.85	0.83	0.83	0.83	0.83	0.83	0.83	0.83	0.83
Qw (inHg)	0.70	0.70	0.80	0.90	1.00	1.20	1.30	1.60	1.60
CALCULATED DATA									
Q (L/s)	0.828	0.828	0.828	0.828	0.828	0.828	0.828	0.828	0.828
Q1 (L/s)U-tube	0.536	0.536	0.536	0.536	0.536	0.536	0.536	0.536	0.536
Q1 (L/s)diff	0.549	0.563	0.563	0.563	0.563	0.563	0.563	0.563	0.563
Q2 (L/s)	0.279	0.265	0.265	0.265	0.265	0.265	0.265	0.265	0.265
T1d (C)	35.3	36.2	37.1	37.9	38.9	40.0	40.9	41.9	44.2
T1u (C)	36.9	37.2	37.9	38.7	39.2	40.7	41.5	42.5	44.8
T1_corrected (C)	35.7	36.5	37.3	38.1	39.0	40.2	41.1	42.0	44.4
T3 (C)	28.2	28.4	29.0	29.5	30.0	30.7	30.7	31.6	32.9
T2 (C)	33.9	34.3	35.3	36.1	36.9	38.2	39.0	40.2	42.5
Physical Properties of R-11									
rho_L1 (kg/m3)	1450	1448	1447	1445	1443	1439	1437	1435	1429
rho_G1 (kg/m3)	8.552	8.759	8.964	9.186	9.418	9.768	10.003	10.291	10.984
rho_L5 (kg/m3)	1455	1454	1452	1450	1448	1444	1442	1439	1434
h_L1 (kJ/kg)	231.8	232.5	233.3	234.0	234.8	235.9	236.7	237.6	239.7
h_LG1 (kJ/kg)	177.1	176.8	176.5	176.2	175.8	175.3	175.0	174.6	173.6
h_L2 (kJ/kg)	230.2	230.5	231.4	232.1	232.9	234.1	234.8	235.9	238.0
Gp (kg/m2s)	246.7	246.6	246.2	245.9	245.5	245.0	244.6	244.1	243.2
HEM void fraction									
dh (kJ/kg)	6.29	6.66	7.11	7.81	8.26	8.90	9.29	10.06	11.37
quality	0.0263	0.02607	0.02973	0.03373	0.03622	0.04034	0.04263	0.048	0.05573
dens (kg/m3)	267	274	251	230	222	208	203	188	174
HEM Void	0.82	0.82	0.83	0.85	0.85	0.86	0.86	0.88	0.88
Separated flow calculations									
Corr. Factor	0.993	0.992	0.992	0.991	0.990	0.989	0.988	0.988	0.986
Rad Void (upstrm)	0.47	0.56	0.58	0.59	0.61	0.63	0.63	0.65	0.67
Rad Void (bundle)	0.48	0.51	0.53	0.54	0.56	0.56	0.58	0.59	0.60
Slip (w.r.t. upstrm)	5.1	3.5	3.6	3.8	3.6	3.7	3.7	3.7	3.7
U_G (m/s)	1.61	1.32	1.41	1.52	1.54	1.61	1.64	1.74	1.83
U_L (m/s)	0.31	0.37	0.39	0.40	0.42	0.44	0.45	0.47	0.49
rho (kg/m3)	762	715	685	664	646	632	613	600	578
Tube vibration response									
Ampl_ST (%Dia)	1.43	1.19	1.15	1.15	1.12	1.13	1.10	1.10	1.06
Ampl_TR (%Dia)	0.90	0.86	0.9	0.96	0.95	0.98	0.96	0.94	0.95
Damp_ST (%)	4.76	3.61	3.55	3.48	3.13	2.56	3.23	2.94	2.98
Damp_TR (%)	3.51	2.86	2.66	2.12	2.29	1.70	2.01	1.75	1.70
Freq_ST (Hz)	37.5	37.5	37.7	37.8	37.8	38.0	38.0	38.0	38.0
Freq_TR (Hz)	37.3	37.7	38.0	37.8	37.8	38.0	38.0	38.0	38.0

Hydrodynamic Mass f_L = 33.6 Hz, fa = 39.7 Hz, m_t = 0.138 kg/m, m_L = 0.0547kg/m

m_h (kg/m)	0.0175	0.01585	0.01382	0.01422	0.01422	0.01262	0.01262	0.01262	0.01262
m_R	0.320	0.290	0.253	0.260	0.260	0.231	0.231	0.231	0.231
M_R (HEM)	0.179	0.184	0.168	0.154	0.148	0.139	0.135	0.125	0.115
M_R (RAD)	0.528	0.443	0.421	0.407	0.386	0.371	0.365	0.347	0.327

Data Sheet for Two-Phase Flow-Induced Vibration **Date: July 11/97**
Test Series C: Exp No. 13 P_atm = 0.102 MPa

Light probe calibration		Upstrm	Bundle	Gamma densitometer calibration
Strm (V/in) =	23.7	6.509	4.087 = LIQ (volts)	1481 kg/m3 (Liq. R-11 density)
Tms (V/in) =	44.9	8.649	5.028 = GAS (volts)	23.0 C (R-11 temperature at calibration time)

Trial No.	1	2	3	4	5	6	7	8	9
Q1 (inHg)	1.30	1.30	1.30	1.30	1.30	1.30	1.30	1.30	1.30
Q2 (inHg)	1.05	1.05	1.05	1.05	1.05	1.05	1.05	1.05	1.05
T1d (mV)	2.08	2.18	2.23	2.28	2.34	2.42	2.53	2.63	2.74
T1u (mV)	2.22	2.24	2.28	2.33	2.38	2.46	2.56	2.65	2.76
T3 (mV)	1.66	1.72	1.77	1.78	1.81	1.87	1.93	1.98	2.04
T2 (mV)	2.03	2.06	2.11	2.17	2.23	2.31	2.41	2.51	2.60
Power (kW)	5.00	5.25	5.80	6.25	6.75	7.40	8.05	8.80	9.65
N (rpm)	645	645	645	645	645	645	645	645	645
GD upstrm (Volts)	7.369	7.416	7.488	7.619	7.648	7.685	7.729	7.766	7.822
GD bundle (Volts)	4.457	4.483	4.506	4.539	4.563	4.581	4.592	4.610	4.636
P1 (psi)	7.90	8.30	8.80	9.50	10.20	11.20	12.70	14.00	15.40
T4 (mV)	1.19	1.21	1.17	1.15	1.13	1.15	1.17	1.19	1.19
T6 (mV)	0.79	0.79	0.79	0.79	0.80	0.82	0.82	0.82	0.82
Qw (inHg)	0.60	0.60	0.80	1.00	1.30	1.40	1.50	1.60	1.80
CALCULATED DATA									
Q (L/s)	1.061	1.061	1.061	1.061	1.061	1.061	1.061	1.061	1.061
Q1 (L/s)U-tube	0.758	0.758	0.758	0.758	0.758	0.758	0.758	0.758	0.758
Q1 (L/s)diff	0.774	0.774	0.774	0.774	0.774	0.774	0.774	0.774	0.774
Q2 (L/s)	0.286	0.286	0.286	0.286	0.286	0.286	0.286	0.286	0.286
T1d (C)	34.6	36.2	37.1	37.9	38.9	40.2	42.0	43.7	45.5
T1u (C)	36.9	37.2	37.9	38.7	39.5	40.9	42.5	44.0	45.8
T_corrected (C)	35.3	36.5	37.3	38.1	39.1	40.4	42.2	43.8	45.6
T3 (C)	27.7	28.7	29.5	29.7	30.2	31.1	32.1	32.9	33.9
T2 (C)	33.8	34.3	35.1	36.1	37.1	38.4	40.0	41.7	43.2
Physical Properties of R-11									
rho_L1 (kg/m3)	1452	1448	1447	1445	1442	1439	1435	1431	1426
rho_G1 (kg/m3)	8.432	8.759	8.964	9.186	9.444	9.814	10.325	10.804	11.364
rho_L2 (kg/m3)	1455	1454	1452	1450	1447	1444	1440	1436	1432
h_L1 (kJ/kg)	231.4	232.5	233.3	234.0	234.9	236.1	237.7	239.1	240.8
h_LG1 (kJ/kg)	177.3	176.8	176.5	176.2	175.8	175.3	174.5	173.9	173.1
h_L2 (kJ/kg)	230.0	230.5	231.2	232.1	233.0	234.2	235.7	237.2	238.6
Gp (kg/m2s)	349.0	348.7	348.3	347.7	347.1	346.3	345.4	344.4	343.5
HEM void fraction									
dh (kJ/kg)	4.40	4.62	5.11	5.52	5.97	6.56	7.16	7.85	8.63
quality	0.01719	0.01454	0.01758	0.02075	0.02359	0.02701	0.02989	0.03419	0.03706
dens (kg/m3)	368	427	379	341	315	292	280	260	254
HEM void	0.75	0.71	0.74	0.77	0.79	C.80	0.81	0.82	0.83
Separated flow calculations									
Corr. Factor	0.991	0.991	0.990	0.989	0.989	0.987	0.986	0.985	0.983
Rad Void (upstrm)	0.41	0.43	0.46	0.52	0.53	0.54	0.56	0.57	0.59
Rad Void (bundle)	0.38	0.40	0.42	0.45	0.48	0.49	0.49	0.51	0.53
Slip (w.r.t. upstrm)	4.4	3.3	3.4	3.1	3.3	3.5	3.4	3.6	3.4
U_G (m/s)	1.75	1.36	1.49	1.52	1.65	1.77	1.80	1.92	1.91
U_L (m/s)	0.40	0.41	0.44	0.49	0.50	0.51	0.52	0.54	0.56
rho (kg/m3)	909	870	838	792	760	739	730	711	680
Tube vibration response									
Ampl_ST (%Dia)	1.43	1.19	1.15	1.15	1.12	1.13	1.10	1.10	1.06
Ampl_TR (%Dia)	0.90	0.86	0.9	0.96	0.95	0.98	0.96	0.94	0.95
Damp_ST (%)	4.76	3.61	3.55	3.48	3.13	2.56	3.23	2.94	2.98
Damp_TR (%)	3.51	2.86	2.66	2.12	2.29	1.70	2.01	1.75	1.70
Freq_ST (Hz)	37.5	37.5	37.7	37.8	37.8	38.0	38.0	38.0	38.0
Freq_TR (Hz)	37.3	37.7	38.0	37.8	37.8	38.0	38.0	38.0	38.0
Hydrodynamic Mass	f_L = 33.6 Hz, fa = 39.7 Hz, m_t = 0.138 kg/m, m_L = 0.0547kg/m								
m_h (kg/m)	0.0175	0.01585	0.01382	0.01422	0.01422	0.01262	0.01262	0.01262	0.01262
m_R	0.320	0.290	0.253	0.260	0.260	0.231	0.231	0.231	0.231
M_R (HEM)	0.249	0.291	0.257	0.231	0.213	0.197	0.189	0.176	0.172
M_R (RAD)	0.594	0.573	0.542	0.484	0.473	0.460	0.445	0.433	0.412

Data Sheet for Two-Phase Flow-Induced Vibration **Date: July 16/97**
Test Series C: Exp No. 14 P_atm = 0.102 MPa

Light probe calibration		Upstrm	Bundle	**Gamma densitometer calibration**				
Strm (V/in) =	21.6	6.508	4.085	= LIQ (volts)	1478	kg/m3 (Liq. R-11 density)		
Trns (V/in) =	42.7	8.727	5.059	= GAS (volts)	24.0	C (R-11 temperature at calibration time)		

Trial No.	**1**	**2**	**3**	**4**	**5**	**6**	**7**	**8**	**9**
Q1 (inHg)	0.25	0.25	0.25	0.25	0.25	0.25	0.25	0.25	0.25
Q2 (inHg)	1.10	1.10	1.10	1.10	1.10	1.10	1.10	1.10	1.10
T1d (mV)	2.17	2.17	2.20	2.25	2.31	2.42	2.53	2.64	2.73
T1u (mV)	2.22	2.22	2.23	2.28	2.34	2.45	2.55	2.66	2.76
T3 (mV)	1.79	1.79	1.81	1.84	1.87	1.95	2.01	2.07	2.11
T2 (mV)	2.01	2.03	2.05	2.13	2.20	2.32	2.43	2.53	2.62
Power (kW)	4.65	4.90	5.10	5.65	6.10	7.00	7.65	8.35	9.20
N (rpm)	430	430	430	430	430	430	430	430	430
GD upstrm (Volts)	7.682	7.745	7.757	7.883	7.954	8.019	8.076	8.066	8.104
GD bundle (Volts)	4.557	4.602	4.607	4.647	4.668	4.688	4.710	4.707	4.724
P1 (psi)	8.40	8.40	8.60	9.40	10.00	11.50	13.00	14.40	15.50
T4 (mV)	1.25	1.22	1.23	1.23	1.21	1.25	1.27	1.25	1.25
T6 (mV)	0.90	0.85	0.85	0.85	0.85	0.85	0.86	0.85	0.85
Qw (inHg)	0.70	0.70	0.70	0.80	1.05	1.10	1.20	1.50	1.80
CALCULATED DATA									
Q (L/s)	0.661	0.661	0.661	0.661	0.661	0.661	0.661	0.661	0.661
Q1 (L/s)U-tube	0.332	0.332	0.332	0.332	0.332	0.332	0.332	0.332	0.332
Q1 (L/s)diff	0.368	0.368	0.368	0.368	0.368	0.368	0.368	0.368	0.368
Q2 (L/s)	0.293	0.293	0.293	0.293	0.293	0.293	0.293	0.293	0.293
T1d (C)	36.1	36.1	36.6	37.4	38.4	40.2	42.0	43.8	45.3
T1u (C)	36.9	36.9	37.1	37.9	38.9	40.7	42.4	44.2	45.8
T_corrected (C)	36.3	36.3	36.7	37.5	38.5	40.3	42.1	43.9	45.5
T3 (C)	29.8	29.8	30.2	30.7	31.1	32.5	33.4	34.4	35.1
T2 (C)	33.4	33.8	34.1	35.4	36.6	38.6	40.4	42.0	43.5
Physical Properties of R-11									
rho_L1 (kg/m3)	1449	1449	1448	1446	1444	1439	1435	1430	1426
rho_G1 (kg/m3)	8.703	8.703	8.808	9.027	9.295	9.801	10.311	10.854	11.328
rho_L2 (kg/m3)	1456	1455	1454	1451	1448	1444	1439	1435	1431
h_L1 (kJ/kg)	232.4	232.4	232.7	233.5	234.4	236.0	237.6	239.3	240.7
h_LG1 (kJ/kg)	176.9	176.9	176.7	176.4	176.0	175.3	174.6	173.8	173.2
h_L2 (kJ/kg)	229.7	230.0	230.3	231.5	232.6	234.4	236.0	237.5	238.9
Gp (kg/m2s)	153.1	153.1	153.0	152.6	152.3	151.8	151.4	150.9	150.5
HEM void fraction									
dh (kJ/kg)	9.32	9.83	10.24	11.37	12.30	14.16	15.52	16.99	18.77
quality	0.03799	0.04253	0.04451	0.05352	0.05975	0.07144	0.07977	0.08766	0.09797
dens (kg/m3)	199	180	175	152	141	126	119	115	108
HEM void	0.87	0.88	0.88	0.90	0.91	0.92	0.92	0.93	0.93
Separated flow calculations									
Corr. Factor	0.992	0.992	0.992	0.991	0.990	0.988	0.987	0.985	0.984
Rad Void (upstrm)	0.54	0.57	0.57	0.62	0.65	0.67	0.69	0.68	0.69
Rad Void (bundle)	0.48	0.52	0.52	0.56	0.58	0.59	0.60	0.59	0.60
Slip (w.r.t. upstrm)	5.6	5.7	5.8	5.5	5.3	5.5	5.4	5.9	6.1
U_G (m/s)	1.24	1.32	1.36	1.46	1.51	1.65	1.70	1.79	1.88
U_L (m/s)	0.22	0.23	0.23	0.26	0.28	0.30	0.31	0.30	0.31
rho (kg/m3)	764	700	694	642	618	599	576	589	572
Tube vibration response									
Ampl_ST (%Dia)	1.43	1.19	1.15	1.15	1.12	1.13	1.10	1.10	1.06
Ampl_TR (%Dia)	0.90	0.86	0.9	0.96	0.95	0.98	0.96	0.94	0.95
Damp_ST (%)	4.76	3.61	3.55	3.48	3.13	2.56	3.23	2.94	2.98
Damp_TR (%)	3.51	2.86	2.66	2.12	2.29	1.70	2.01	1.75	1.70
Freq_ST (Hz)	37.5	37.5	37.7	37.8	37.8	38.0	38.0	38.0	38.0
Freq_TR (Hz)	37.3	37.7	38.0	37.8	37.8	38.0	38.0	38.0	38.0

Hydrodynamic Mass f_L = 33.6 Hz, fa = 39.7 Hz, m_t = 0.138 kg/m, m_L = 0.0547kg/m

m_h (kg/m)	0.0175	0.01585	0.01382	0.01422	0.01422	0.01262	0.01262	0.01262	0.01262
m_R	0.320	0.290	0.253	0.260	0.260	0.231	0.231	0.231	0.231
M_R (HEM)	0.132	0.119	0.115	0.099	0.092	0.081	0.077	0.073	0.068
M_R (RAD)	0.461	0.434	0.430	0.378	0.351	0.329	0.310	0.319	0.308

APPENDIX D

Miscellaneous Tables and Figures

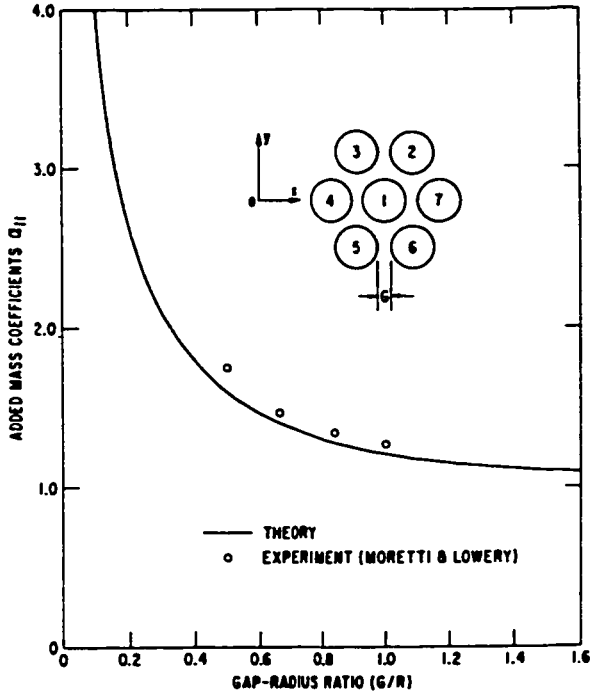

Figure D1 Theoretical prediction and experimental values of self-added mass coefficient for a seven tube bundle with tube #1 flexible and other tubes rigid. Chen (1975).

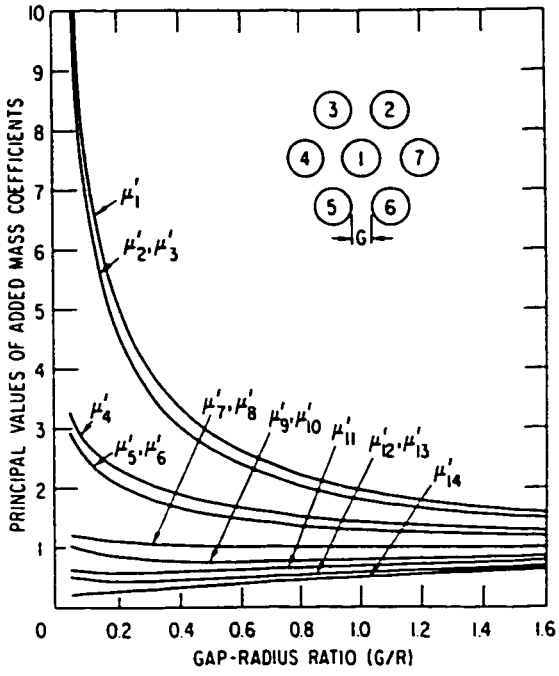

Figure D2 Theoretical prediction of coupled-mode added mass coefficient for a seven tube bundle with all tubes flexible. Chen (1975).

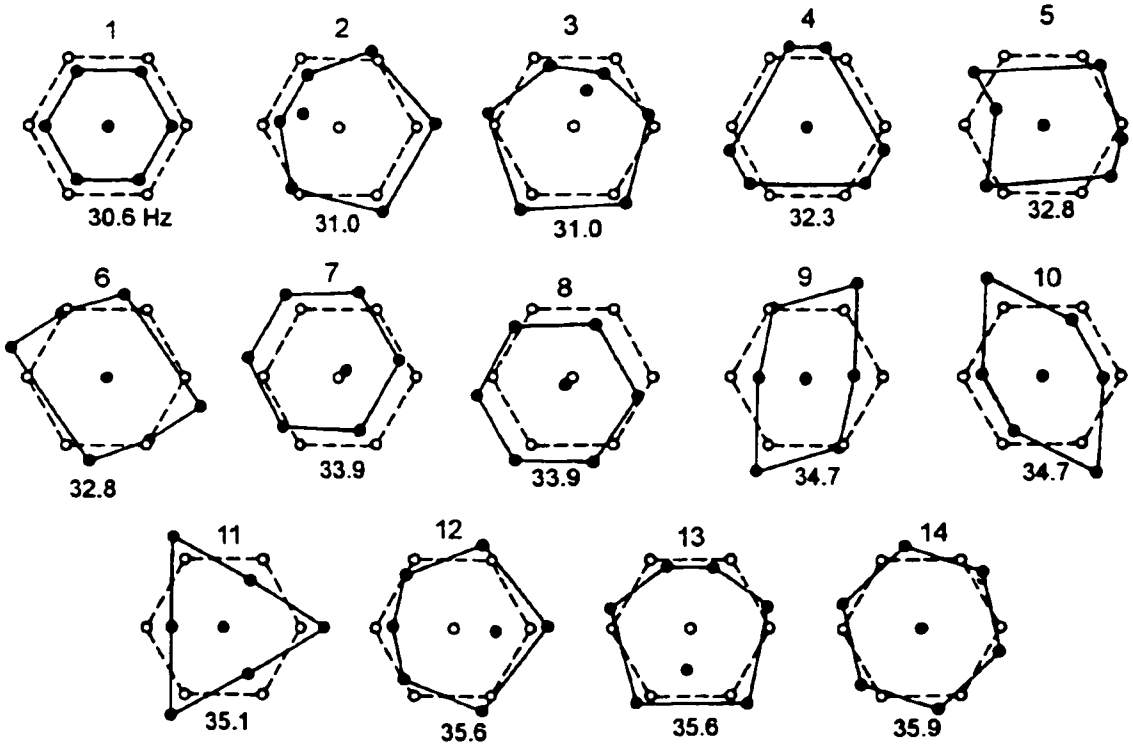

Figure D3 Normal modes of a seven flexible tube bundle, P/D = 1.44 vibrating in a liquid. Adapted from Chen (1975).

Table D1 Thermodynamic Property Table

Refrigerant 11 (Trichlorofluoromethane) Properties of Saturated Liquid and Saturated Vapour.

T (C)	P (kPa)	ρ_F (kg/m^3)	ρ_G (kg/m^3)	h_f (kJ/kg)	h_{fg} (kJ/kg)
10	60.84	1511	3.633	208.77	187.00
12	65.80	1506	3.907	210.53	186.28
14	71.08	1502	4.197	212.31	185.53
16	76.68	1497	4.503	214.08	184.80
18	82.63	1493	4.827	215.87	184.04
20	88.93	1488	5.168	217.65	183.29
22	95.60	1483	5.527	219.44	182.53
24	102.66	1479	5.906	221.23	181.77
26	110.12	1474	6.304	223.03	181.00
28	117.99	1469	6.723	224.83	180.23
30	126.30	1464	7.163	226.63	179.45
32	135.05	1460	7.625	228.44	178.66
34	144.26	1455	8.109	230.25	177.87
36	153.95	1450	8.617	232.06	177.08
38	164.13	1445	9.149	233.88	176.28
40	174.83	1440	9.706	235.70	175.47
42	186.05	1435	10.288	237.52	174.66
44	197.81	1430	10.898	239.35	173.84
46	210.14	1425	11.534	241.18	173.01
48	223.05	1420	12.200	243.01	172.18
50	236.55	1415	12.893	244.85	171.34
52	251.14	1410	13.587	246.69	170.49
54	265.73	1405	14.347	248.53	169.64
56	281.15	1397	15.528	251.30	168.35
58	297.38	1392	16.367	253.15	167.48
60	313.61	1389	16.835	254.08	167.04

Table D2 Chromel-Constantan (E Type) Thermocouple Look-Up Table

Electromotive Potential vs. Temperature.

V (mV)	Temp. (C)	V (mV)	Temp. (C)	V (mV)	Temp. (C)	V (mV)	Temp. (C)
0.00	0.00	1.00	16.83	2.00	33.28	3.00	49.37
0.02	0.34	1.02	17.17	2.02	33.61	3.02	49.68
0.04	0.68	1.04	17.50	2.04	33.93	3.04	50.00
0.06	1.02	1.06	17.83	2.06	34.26	3.06	50.32
0.08	1.36	1.08	18.17	2.08	34.59	3.08	50.63
0.10	1.69	1.10	18.50	2.10	34.92	3.10	50.95
0.12	2.03	1.12	18.83	2.12	35.25	3.12	51.27
0.14	2.37	1.14	19.17	2.14	35.57	3.14	51.59
0.16	2.71	1.16	19.50	2.16	35.90	3.16	51.90
0.18	3.05	1.18	19.83	2.18	36.23	3.18	52.22
0.20	3.39	1.19	20.00	2.20	36.56	3.20	52.54
0.22	3.73	1.20	20.16	2.22	36.89	3.22	52.86
0.24	4.07	1.22	20.49	2.24	37.21	3.24	53.17
0.26	4.41	1.24	20.82	2.26	37.54	3.26	53.49
0.28	4.75	1.26	21.15	2.28	37.87	3.28	53.81
0.30	5.08	1.28	21.48	2.30	38.20	3.30	54.13
0.32	5.42	1.30	21.80	2.32	38.52	3.32	54.44
0.34	5.76	1.32	22.13	2.34	38.85	3.34	54.76
0.36	6.10	1.34	22.46	2.36	39.18	3.36	55.08
0.38	6.44	1.36	22.79	2.38	39.51	3.38	55.40
0.40	6.78	1.38	23.11	2.40	39.84	3.40	55.71
0.42	7.12	1.40	23.44	2.41	40.00	3.42	56.03
0.44	7.46	1.42	23.77	2.42	40.16	3.44	56.35
0.46	7.80	1.44	24.10	2.44	40.48	3.46	56.67
0.48	8.14	1.46	24.43	2.46	40.79	3.48	56.98
0.50	8.47	1.48	24.75	2.48	41.11	3.50	57.30
0.52	8.81	1.50	25.08	2.50	41.43	3.52	57.62
0.54	9.15	1.52	25.41	2.52	41.75	3.54	57.94
0.56	9.49	1.54	25.74	2.54	42.06	3.56	58.25
0.58	9.83	1.56	26.07	2.56	42.38	3.58	58.57
0.59	10.00	1.58	26.39	2.58	42.70	3.60	58.89
0.60	10.17	1.60	26.72	2.60	43.02	3.62	59.21

...continued next page.

Electromotive Potential vs. Temperature (continued)

V (mV)	Temp. (C)	V (mV)	Temp. (C)	V (mV)	Temp. (C)	V (mV)	Temp. (C)
0.62	10.50	1.62	27.05	2.62	43.33	3.64	59.52
0.64	10.83	1.64	27.38	2.64	43.65	3.66	59.84
0.66	11.17	1.66	27.70	2.66	43.97	3.67	60.00
0.68	11.50	1.68	28.03	2.68	44.29	3.68	60.16
0.70	11.83	1.70	28.36	2.70	44.60	3.70	60.48
0.72	12.17	1.72	28.69	2.72	44.92	3.72	60.79
0.74	12.50	1.74	29.02	2.74	45.24	3.74	61.11
0.76	12.83	1.76	29.34	2.76	45.56	3.76	61.43
0.78	13.17	1.78	29.67	2.78	45.87	3.78	61.75
0.80	13.50	1.80	30.00	2.80	46.19	3.80	62.06
0.82	13.83	1.82	30.33	2.82	46.51	3.82	62.38
0.84	14.17	1.84	30.66	2.84	46.83	3.84	62.70
0.86	14.50	1.86	30.98	2.86	47.14	3.86	63.02
0.88	14.83	1.88	31.31	2.88	47.46	3.88	63.33
0.90	15.17	1.90	31.64	2.90	47.78	3.90	63.65
0.92	15.50	1.92	31.97	2.92	48.10	3.92	63.97
0.94	15.83	1.94	32.30	2.94	48.41	3.94	64.29
0.96	16.17	1.96	32.62	2.96	48.73	3.96	64.60
0.98	16.50	1.98	32.95	2.98	49.05	3.98	64.92
1.00	16.83	2.00	33.28	3.00	49.37	4.00	65.24

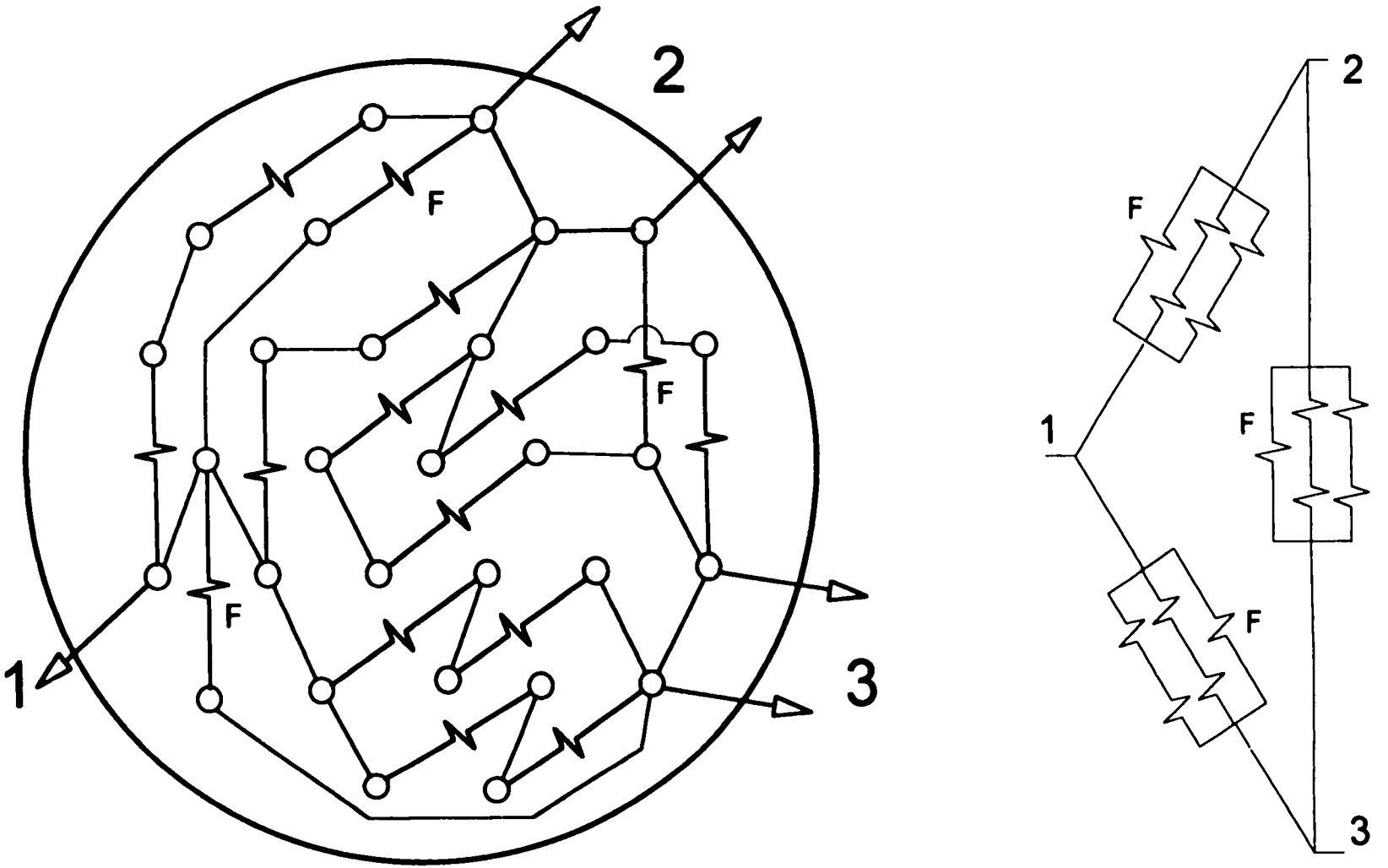

Figure D4 Heater wiring diagram for 19.2 kW maximum. Full power heating elements are denoted "F" while the unlabelled elements are wired for half power.

Table D3 Steam generator data for CANDU nuclear power plant - Pickering A*

Quantity	12
Type	Vertical, integral U-tube in shell heat exchanger and steam separator drum.
Material	Shell: Carbon-silicon steel, Tubes: Monel
O.D. of heat exchanger shell	68.25" (1.73 m)
I.D. of heat exchanger shell	65" (1.65 m)
O.D. of tubing	0.5" (12.7 mm)
Wall thickness of tubing	0.049" (1.24 mm)
O.D. of steam drum	98.375" (2.50 m)
I.D. of steam drum	93.75" (2.38 m)
Height of boiler	559" (14.2 m)
Mass of boiler (dry)	185,000 lb (83,990 kg)
Tube sheet thickness	11.06" (280 mm)
Tubes per boiler	2600
Heat transfer area per boiler	20,000 ft^2 (185822,297 m^2)
Tube side (D_2O) pressure	1270 psig (8853 kPa abs.)
Tube side (D_2O) inlet temperature	560 °F (293 °C)
Steam drum pressure	579 psig (4091 kPa abs.)
Steam drum temperature	485 °F (251 °C)
Steam quality at drum	99.78%
Steam output per boiler	538,250 lb/hr (67.9 kg/s)
Pressure drop through dryers	2.0 psi (13.7 kPa)
Feedwater inlet temperature	340 °F (171 °C)
Feedwater flow	497,416 lb/hr (62.7 kg/s)
Reheater drains flow	40,794 lb/hr (5.2 kg/s)
Recirculation ratio (min.)	8.0
D_2O flow per boiler	5.11×10^6 lb/hr (645 kg/s)

* Source: Atomic Energy of Canada Ltd.

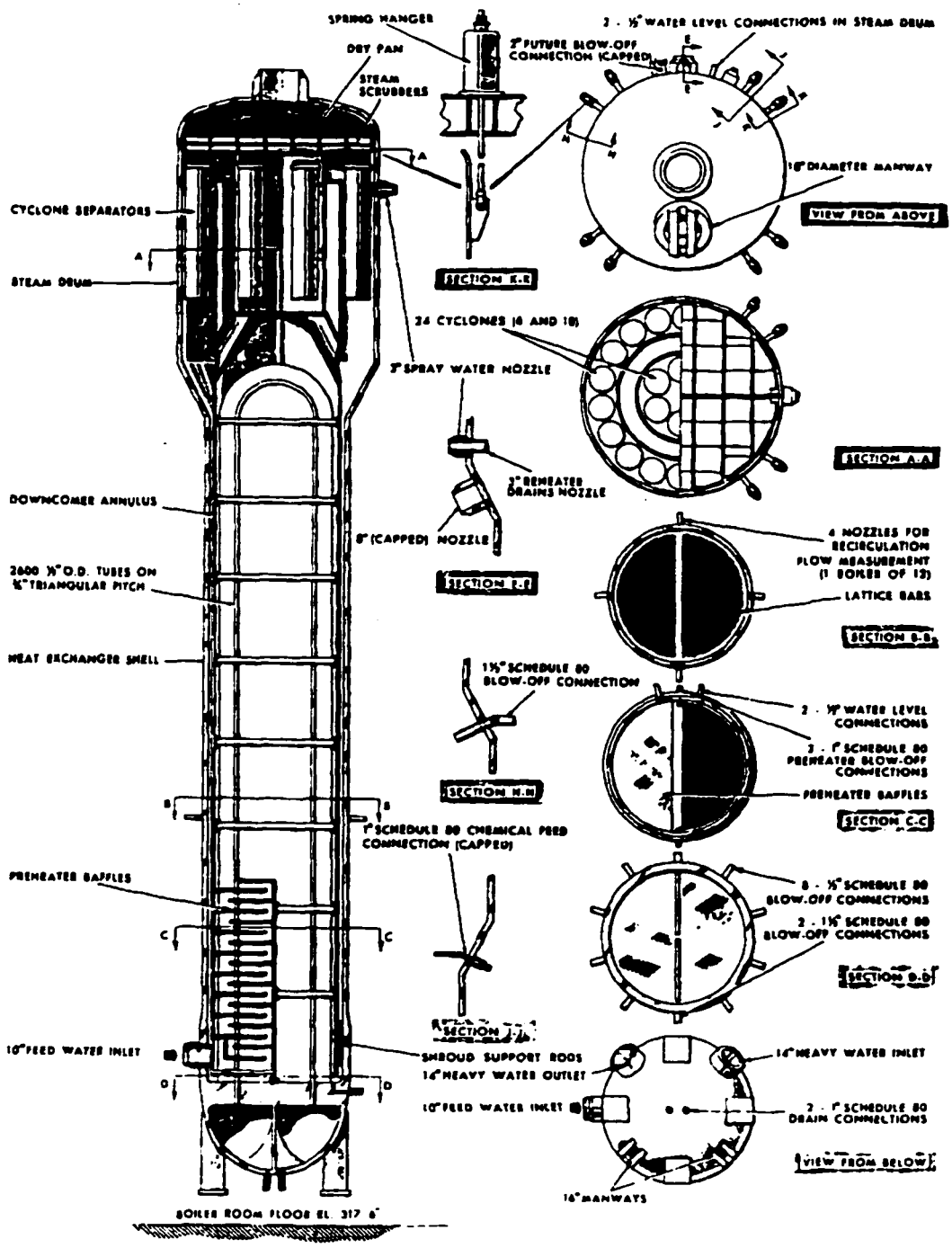

Figure D5 Steam generator details - Pickering "A".
Courtesy: Atomic Energy of Canada Limited.

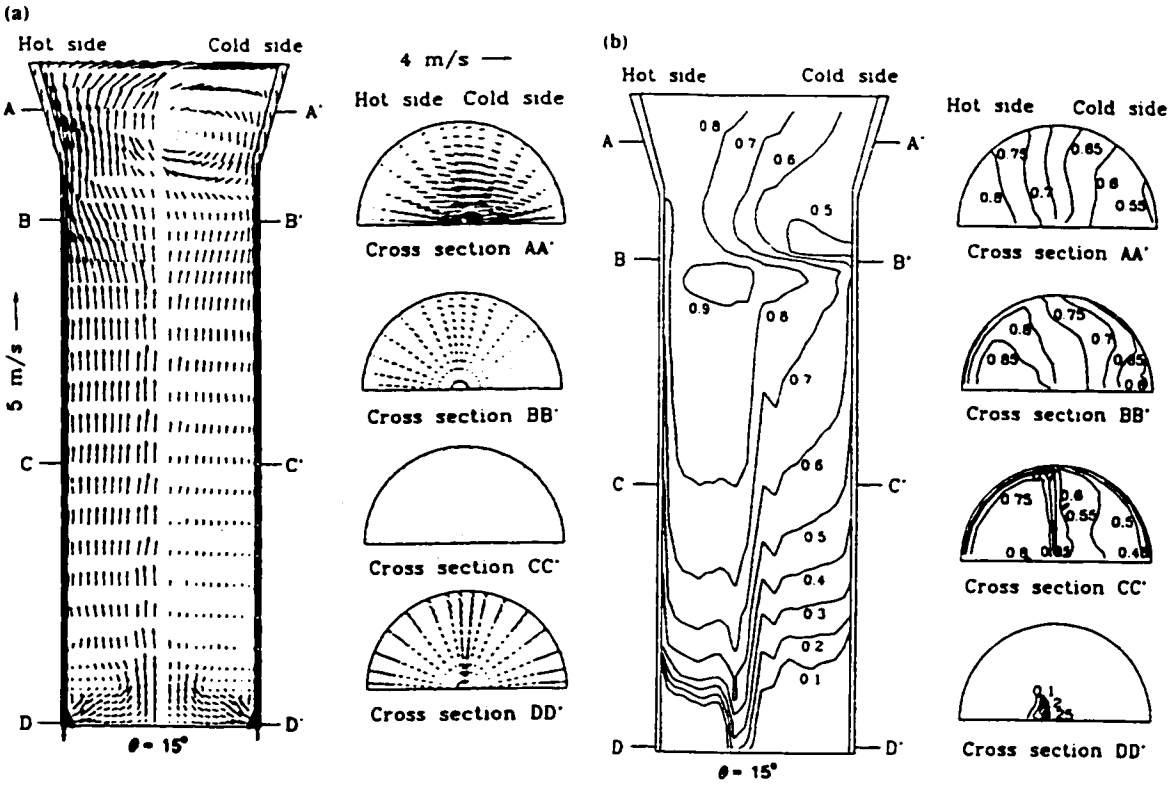

Figure D6 (a) Velocity vectors and, (b) void fraction distributions of mixture in the steam generator as determined by the ATHOS3 computer code. Jo & Shin (1999).

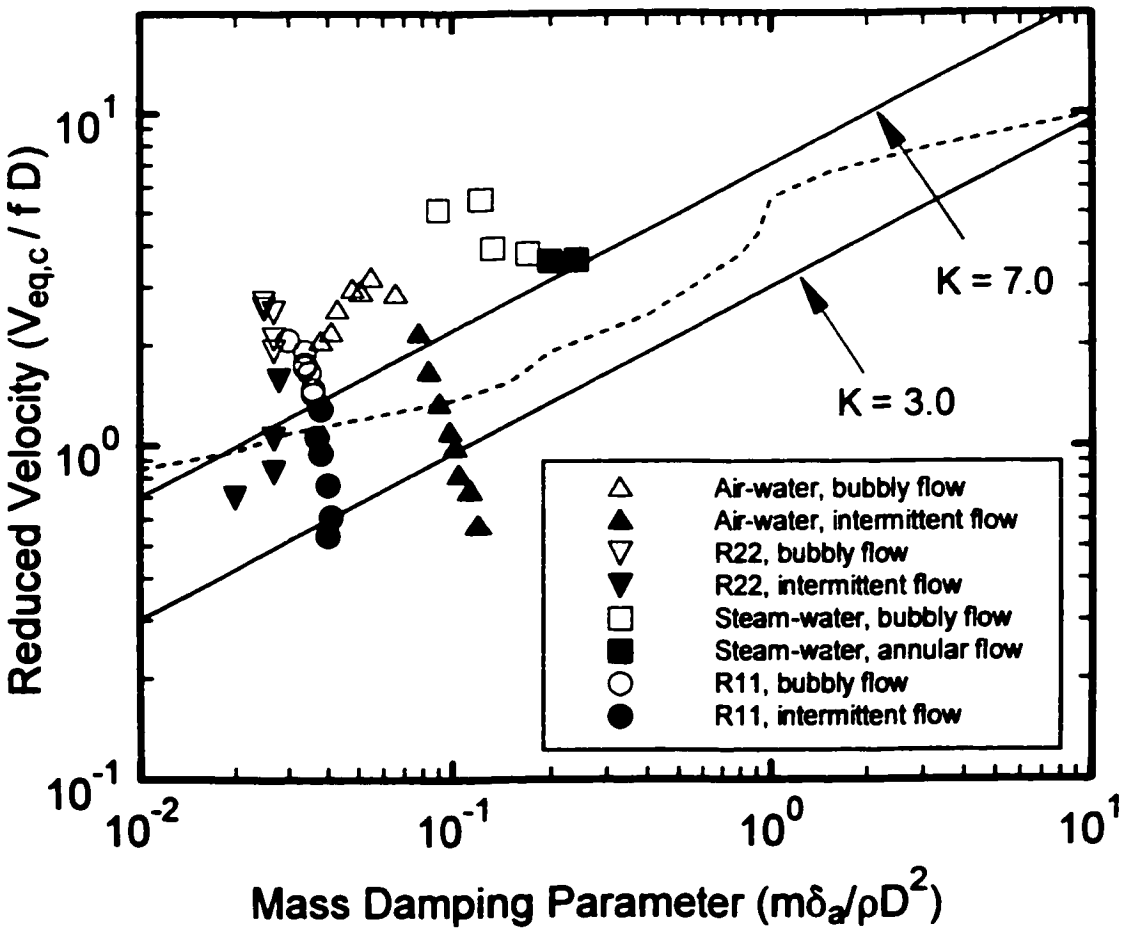

Figure D7 Critical flow velocities for fluidelastic instability of parallel triangular tube arrays in two-phase cross-flow. Data analysis utilizes the void fraction model and in-air damping. ○● Present study in R-11, △▲ Pettigrew *et al.* (1989b) in air-water, ▽▼ Pettigrew *et al.* (1995) in R-22, □■ Axisa *et al.* (1985) in steam-water, ——— Connors' theory, ------- analytical prediction of Li & Weaver (1997).

APPENDIX E

Miscellaneous Computer Software

The following is a description of computer software which was used to analyse data in this thesis. The source code and executable files are located on the CD-rom under the subdirectory /software/. The following extensions indicate which type of file they are:

- *.for - Fortran77 code,
- *.exe - executable code for the DOS operating environment,
- *.mcd - MathCad file,
- *.m - MATLAB "m" file.

ASCTO2D.EXE (ASCTO2D.FOR) is the Fortran program which is needed to convert the ASCII data from the HP Analyzer to a format which can be used as input to 2D.EXE for analysing damping data. Before this program can be executed however, the binary data saved using the HP 35670A analyser (*.DAT) must be converted to ASCII format using the HP Utility file called SDFTOASC.EXE and the following switch, /Y:PRD, must be invoked to obtain units of power spectral density, V_2/Hz. The program is designed to read in all of the data from an axperiment, which may include up to 14 trials. Therefore, a strict naming convention of the data files must be observed for the streamwise and transverse data files, ie., EX?xxyyS.ASC and EX?xxyyT.ASC, where "?" refers to the series letter (ie., A, B, or C etc.) and "xx" refers to the experiment number and "yy" refers to the trial number. Thus EXB0103S.ASC refers to the streamwise (or drag) data of trial number 03 of experiment number 01 of test series "B". The frequency spectra can range from 0 - 50 Hz or 0 - 100 Hz. The program makes this distinction because the output file

The output consists of 2 files: EX?xxyyS.FRQ, EX?xxyyT.FRQ, where each file consists of 2 columns (frequency vs r.m.s. amplitude). Since the output is designed only for damping analysis, conversion to engineering units is not required, and so the units of the output files are volts. ASCTOQP.EXE must read a parameter data file called ASCTOQP.DAT which contains the following data:

1. The lower frequency range of the data (usually 0 Hertz)
2. The upper frequency range of the data (usually 50 or 100 Hertz)
3. The number of frequency lines (usually 400 or 800)
4. The beginning trial number (integer value, usually 1)
5. The ending trial number (integer value no greater than 14)
6. The experiment number (interger value)
7. the experiment call letters (ie., A, B, or C)

This file can be created using the editor in DOS, (invoked by typing: `edit ascto2d.dat`)

REDUCE.EXE (REDUCE.FOR) is a Fortran program designed to take data from an ASCII file and create a new, smaller file with the same name but with a different extension. This file is used primarily for annihilating data points in a file for later FFT analysis. You have the choice of selecting the first x number of points, or you can skip over x number of points when reducing the data points.

LOGDEC2.EXE (LOGDEC2.FOR) is an Fortran program which calculates the logarithmic decrement damping of a single degree of freedom system subjected to an initial displacement. The program output is a number of damping values, which are determined from a number of vibration cycles which the user specifies. This program utilizes an algorithm which fits an envelope curve to the peaks of a steadily decaying amplitude trace. The input data file must consist of a single column of vibration amplitude in ASCII format. Any additional data columns are ignored. The user must prepare a parameter file called LOGDEC.DAT from which the program can read: natural frequency, sampling rate, number of vibration cycles to use for each damping value, number of damping values to calculate, number of header lines to skip, measurement units (text).

RMS.EXE (RMS.FOR) is a Fortran program which calculates the r.m.s. amplitude of a frequency spectra over a desired frequency range of spectral data from the HP analyzer. his program works only for transducers in which the output voltage is proportional to displacement, such as a strain gauge or a displacement transducer (not accelerometers!). The input data must consist of a single column of frequency spectra data in ASCII format in units of power spectral density, V^2/Hz. This can be obtained by converting the standard data format of the HP 35670a analyser using the HP utility file called SDFTOASC.EXE with the "/Y:PRD" switch. The user must prepare a parameter file called RMS.DAT from which the program can read: the frequency range of the data file (low, high), frequency resolution, frequency range of interest (low, high).

RMSACC.EXE (RMSACC.FOR) is a similar to the above program (RMS.EXE) except that it is designed for accelerometer data, where the output voltage is proportional to acceleration and not displacement. This Fortran program calculates the r.m.s. amplitude of a frequency spectra over a desired frequency range of spectral data from the HP analyzer. The same conditions which apply to RMS.EXE also apply to this program.

2D.EXE is the Fortran program supplied by AECL for calculating equivalent viscous damping,ζ, from the frequency spectra of tube vibration. This program prompts for: number of peaks in the frequency spectra, data file of frequency (Hz) vs. r.m.s. amplitude (2 columns and maximum of 800 rows), frequency range in which the peak(s) of interest lie, and finally the "guess" data file whch contains the initial guesses of zero frequency, natural frequency and damping ratio. The amplitude units should be linear units and not squared units (ASCTO2D.EXE takes care of this). Specific instructions for using this program are given below.

Instructions for using 2D.EXE

2D.EXE is the program developed by AECL for the purpose of determining an equivalent damping ratio (ζ) from the amplitude vs. frequency graph. This program is specifically designed to deal with the two-peak phenomenon that appears in many frequency spectra of tube vibration in single and two phase flow. This program will calculate the natural frequency (f_n) and equivalent damping ratio (ζ) of each peak separately.

1) When the program is executed, the first thing it asks for is how many peaks are to be analyzed. If your data file contains two peaks, they can be analyzed both at once, or they can be analyzed separately.

2) The second input is the name of the data file. this file should be in ASCII format, and should consist of two columns and a maximum of 800 rows (1st column is frequency in Hz, 2nd column is amplitude in arbitrary units). The two elements in each row must be separated by at least one space. Make sure the amplitude is in linear units (either peak or RMS) and not squared units, which is what you get from a *.sdf output files from the HP35670A portable analyzer, regardless of the display state.

3. The program will then ask for a frequency range in which the peaks in question lie. If you chose initially to analyze two peaks, then you must specify a range which contains these two peaks. For example, in Figure 1 on the opposite page, an acceptable range to analyze the two peaks (f_{n1} = 22.6 Hz, f_{n2} = 23.8 Hz) would be say 21.7 Hz to 25 Hz. However, if you initially chose to analyze only one peak, then you must specify a range which includes only one of the peaks. For example, in Figure E1 below, an acceptable range to analyze the first peak at f_{n1} = 22.6 Hz would be say 21.7 Hz and 23.3 Hz. An acceptable range to analyze the second peak at f_{n2} = 23.8 Hz would be say 23.3 Hz to 25 Hz.

4. The final thing required is to specify the name of the "guess" data file, in which the guess parameters are located. This file, in ASCII format, must consist of a single column of 3 or 6 values for analysing 1 or 2 peaks respectively.

An example data file for analysing the first peak in Figure 1 is,

```
0.01    ; frequency at zero amplitude
22.4    ; estimate of natural frequency
0.003   ; estimate of damping ratio
```

An example data file for analysing both peaks in Figure 1 is,

```
0.01    ; frequency at zero amplitude
22.4    ; estimate of natural frequency of first peak
0.003   ; estimate of damping ratio of first peak
0.1     ; frequency at zero amplitude
23.6    ; estimate of natural frequency of second peak
0.001   ; estimate of damping ratio of second peak
```

Hints on using 2D.EXE

1. It is important to choose the appropriate guess values in order for the program to converge to a solution. These initial guess parameters are required to completely define the curve, since it consists of amplitude frequency and damping values. The first parameter is the frequency at which the

amplitude is near zero. It is not crucial to guess this parameter accurately, since the program will converge quite nicely even if the guess value is way off.

2. The second parameter is P2 = natural frequency estimate. It is important to be within roughly 1.5 % of the actual natural frequency to obtain convergence.

3. The third parameter is P3 = damping ratio estimate. A more generous allowance is allowed for error in this "guesstimate" to obtain convergence. It is usually best to low-ball this estimate, since over-estimates will generally diverge.

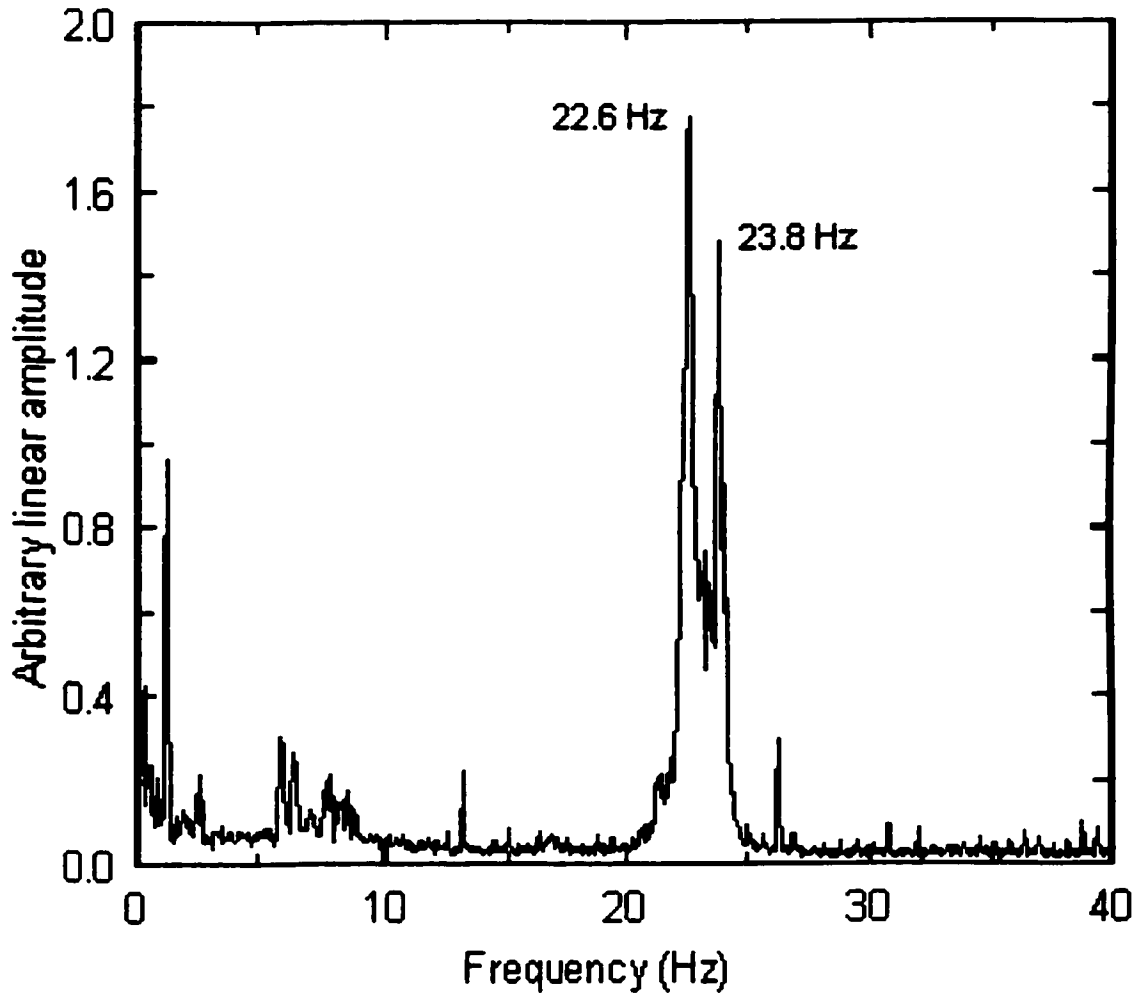

Figure E1 Sample frequency spectra with two closely spaced peaks.

MathCad Documents

The following files, with "*.mcd" filename extensions, were designed within MathCad Version 8 Professional, which is the software needed to open them. These files are miscellaneous and were not essential to the data analysis for this thesis.

J_accept.mcd is a MathCad file which computes the joint acceptance of random excitation of a cantilevered tube in cross-flow. The calculation is performed using both the classical formula and the approximation suggested by Axisa *et al.* (1990), and the comparison is made. This file allows the user to vary the input parameters of the tube and correlation length in order to determine how well the approximate formula agrees with the actual formula for joint acceptance.

Turbbuff.mcd is a MathCad file which computes the r.m.s. amplitude response of a cantilevered tube due to two-phase cross-flow turbulence buffeting. The method proposed by deLangre and Villard (1998) is used to compute an upper bound of the dimensionless excitation forces, which was determined from an analysis of the available experimental data. The program computes the fluid properties for Refrigerant 11 from the temperature, but the program can be modified to include any fluid.The user must input the parameters of the tube such as diameter, modulus of elasticity, length etc. The user must also input fluid conditions such as void fraction, mass flux, an estimation of correlation length.

Damping.mcd is a MathCad file which is a sample calculation for the normalized two-phase damping component of the R-11 data, which was presented in Chapter 9. This file can also serve as a template for determining the normalized two-phase damping for other fluids and other flow conditions. The calculation methodology follows the method of Pettigrew *et al.* (1994) which includes a surface tension scaling factor. However, in a latter paper by Pettigrew and Taylor (1997) the surface tension term was not used since they deemed it incorrect. Hence, the calculation for damping is repeated with the surface tension term omitted.

Matlab Documents

The following files, with "*.m" filename extensions, were designed within student edition of Matlab, Version 5. These files are in ASCII format so any text editor can open them for viewing. The codes written in these files are similar to C language but they are designed to run exclusively in Matlab version 5 or higher. These files are miscellaneous and were not essential to the data analysis for this thesis.

BPF.m is a Matlab file which applies a band pass filter to a amplitude vs. time trace. The user must prepare two input files (in ASCII format). The first file is a parameter file (with a ".m" filename extension) which contains the following parameter data: Sample frequency; low frequency to filter off; high frequency to filter off; ripple (usually about 0.1); and attenuation per decade (usually 30 to 40dB/decade). A sample of such a file is given as follows: 200, 30, 50, 0.1, 40, (note that each value should start on a new line) which indicates a 200 Hz sample rate, a bandpass frequency range of 30

to 50 Hz, a passband ripple of 0.1 and 40 dB attenuation per decade in the filtered range. The second input file is the amplitude vs. time trace of a vibrating system (with an "*.prn" filename extension), which can also be a amplitude decay trace since this is what the program was originally designed for.

Logdec.m in a Matlab file which calculates the logarithmic decrement damping of a single degree of freedom oscillator. Note that **bpf.m** must be run before this program in order to filter off any other modes than the one desired for damping determination. This program performs a least squares curve fit to the peaks of an amplitude decay trace, and that logarithmic decrement damping is determined from this fit. The user must prepare one input file (in ASCII format with a ".m" filename extension) which contains the following parameter data: Natural frequency; number of data points to use for each curve fit; number of damping values to calculate; units. Thus a parameter file with the following data: 39.5; 20; 5; 10.3, indicates that the natural frequency of the signal is 39.5 Hz, 20 vibration peaks are to be used for each curve fit; 5 damping values are to be calculated (thus the input data file must be at least 100 cycles in length); and the data values must be multiplied by 10.3 in order to obtain the desired engineering units (usually to convert from volts to mm of displacement).

Appendix F

R-11 Temperature Correction

The determination of flow quality in the main sub-loop is sensitive to the location of the temperature measurement, because as the flow travels vertically upward, there is a constantly changing hydrostatic head. Shown in Figure F1 are the thermocouple locations relative to the tube bundle location. It was revealed in the experiments of Test series "C" that temperature *T1d* (downstream of the tube bundle) was always lower than *T1u* (upstream of the tube bundle). This temperature difference was also revealed by thermocouples located inside the tubes of tube bundle #4, indicated by T_{t4} and T_{t7}, where the latter always gave a slightly higher temperature for the R-11. This phenomenon is readily explained by examining the pressure-enthalpy diagram shown in Figure F2. When the two-phase flow travels upward from thermocouple *T1u* to *T1d*, the enthalpy remains roughly constant since there is negligible heat or work transfer to or from the fluid, but the pressure is not constant. Following a vertical line drawn in the two-phase region of the P-E diagram of Figure F2, it is clear that the temperature and density of the flow decreases while quality increases. Thus, to accurately determine the fluid properties in the vicinity of the tube bundle, it is important to use a temperature measurement that is made as close to the centerline of the bundle as possible.

The pressure drop, ΔP, and temperature drop, ΔT, of the R-11 from thermocouples *T1u* to *T1d* can be determined theoretically as follow,

$$\Delta P = \rho_{TP} g \Delta y , \qquad \textbf{(F1)}$$

where ρ_{TP} is the two-phase density of the flow, g is the gravitational constant, and Δy is the change in height between the two thermocouples ($\Delta y = 427$ mm). Examination of the R-11 property table reveals a pressure to temperature gradient (in the range of 40°C) as follows,

$$dP/dT = 0.0087 + 1.138\times10^{4}\,T\,. \qquad \textbf{(F2)}$$

Thus, the temperature drop from thermocouple Tlu to Tld is predicted as follows,

$$\Delta T = \frac{dP}{(\frac{dP}{dT})|_{Tlu}}\,. \qquad \textbf{(F3)}$$

However, the outcome of equations (F2) and (F3) were much smaller than the actual difference measured in selected data sets, which was likely due to the added pressure drop of the flow homogenizer, tube bundle as well as the small amount of heat transfer from the test section to the room.

In order to obtain more accurate determinations of quality, a correction factor has been applied to some of the previous data sets in which thermocouple Tlu was not available, namely test series "M", "A" and the first eleven experiments of test series "B". This was done through an analysis of some test series "C" data, in which both thermocouples, Tlu and Tld were utilized as well as the in-tube thermocouples T_{t4} and T_{t7} located in tubes 4 and 7 respectively. The temperature at the bundle centerline was interpolated between measurements of Tlu and Tld as follows,

$$Tl_{corrected} = Tlu - C\,(Tlu - Tld)\,, \qquad \textbf{(F4)}$$

where the expected value of C was about 0.71 based upon the distance between the bundle centerline and the two thermocouples. Analysis of data from test series C indicated that equation (F4) predicted well the temperature inside the bundle as indicated by the thermocouples T_{t4} and T_{t7}. Hence, equation (F4) with C = 0.71 was used to determine a corrected temperature, $Tl_{corrected}$, in the bundle for tesct series C data. In these earlier experiments where only the downstream thermocouple, Tld, was available, another means was employed to correct for the temperature in the bundle. It was found from a further analysis of test series C data that the average temperature difference between Tld and Tlu was about 0.9°C. This temperature difference seemed to be unaffected by mass flux or flow quality over the range that was tested. Thus, to correct for temperature in the bundle in the previous

experiments in which only the downstream thermocouple, *T1d*, was available, 0.26°C was subtracted from the measurement at *T1d*, which is 29% of 0.9°C, which is roughly the proportion of distance between the bundle centerline and thermocouple *T1d*. It must be remembered that while there was little effect of mass flux and flow quality on the difference between temperatures *T1d* and *T1u*, there was a significant effect of flow uniformity. In those experimental trials in which non-uniform flow conditions were present, in which there occurred significant downward liquid reflux, there was a significantly larger temperature difference between the two thermocouple temperature measurements. It is likely that *T1d* gave a lower temperature reading during these occurrences because the liquid down-flow, which usually occurred at the left side in Figure F1, was cooler than the upward two-phase flow. In most of the cases where significant non-uniform flow was present, the data was deemed unsuitable for analysis and hence no temperature correction was attempted.

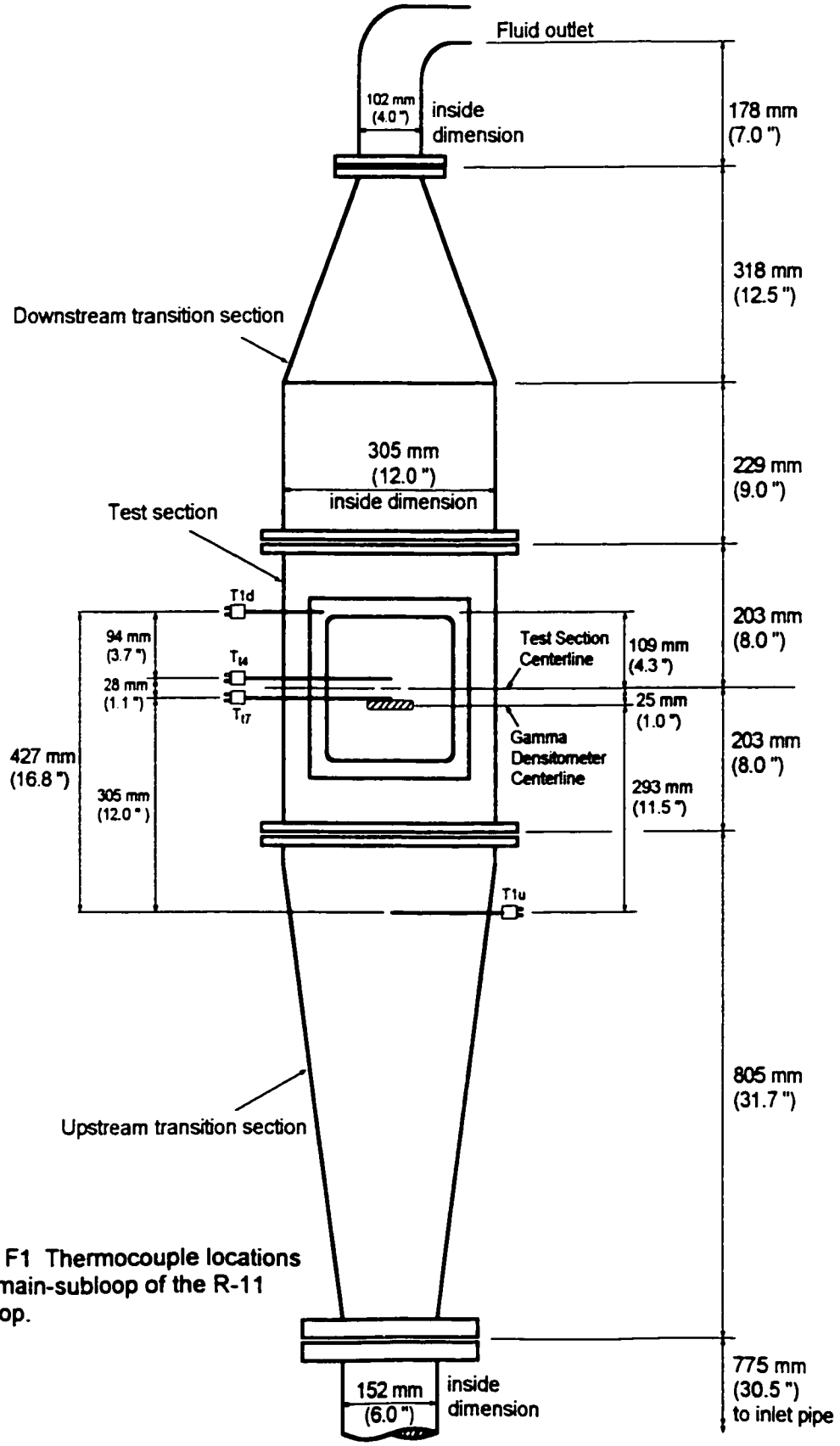

Figure F1 Thermocouple locations in the main-subloop of the R-11 flow loop.

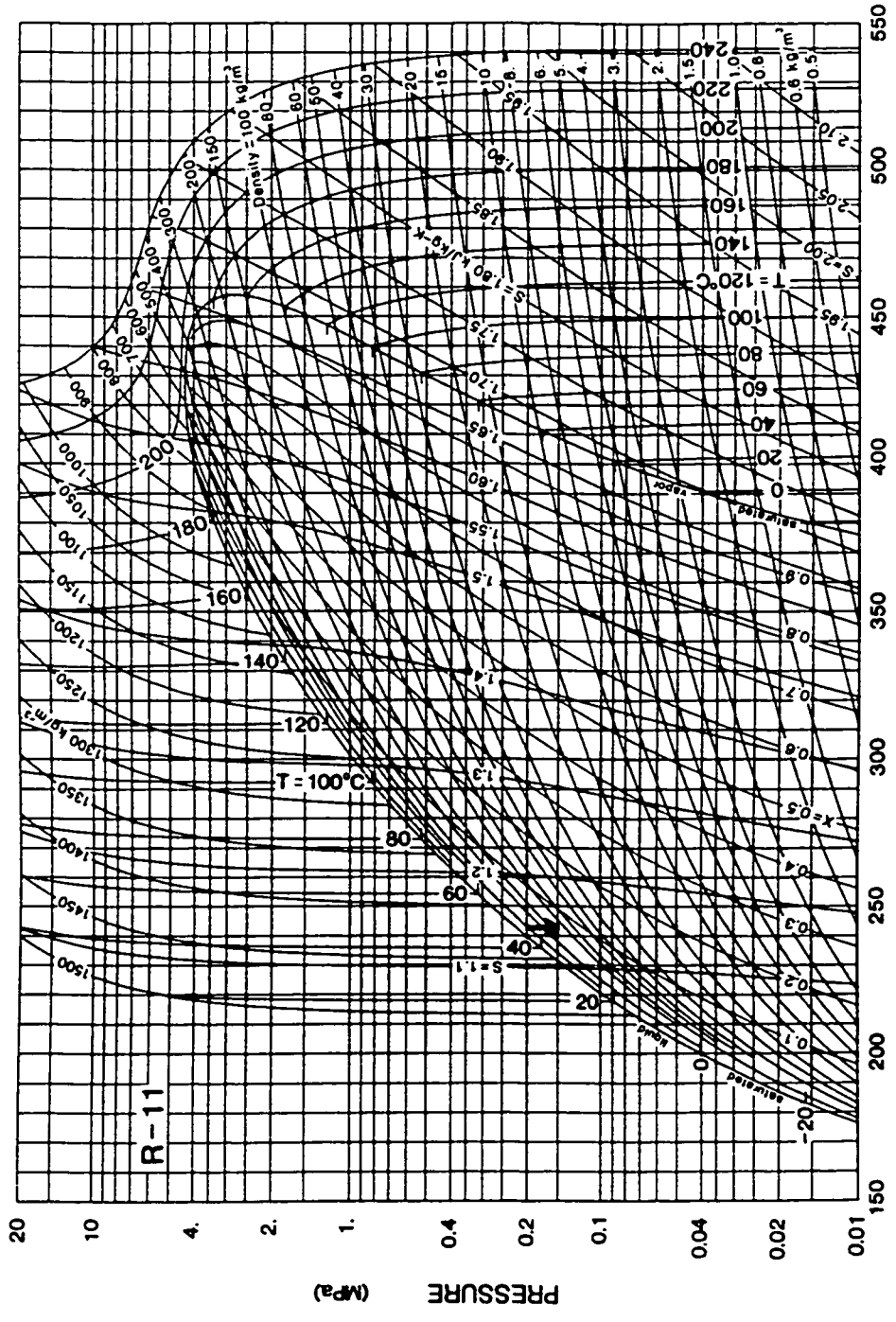

Figure F2 Pressure-Enthalpy for Refrigerant R-11. The small downward pointing arrow indicates roughly (slightly exaggerated) the change in fluid property as the flow travels upward in the test section from thermocouple T1u to T1d.

Appendix G

CD-rom Contents

The CD-rom in the back cover contains much of the text and figures of this thesis. The text of the thesis and most of the tables are stored in Wordperfect version 8 format in separate files for each chapter. Most of the figures were generated by AXUM software or by TurboCad 2D/3D software while others are scanned images stored as bitmap files. Some of the relevant data files are stored in Quattro Pro format. The table below indicates the software needed to access the various files stored on the CD-rom. In most cases, the title of each file clearly indicates the contents so that a detailed listing is not required.

Table G1 Filename extensions of data stored on CD-rom.

Type of File	Filename Extensions[1]	Software Needed to Access Files[2]
Text	*.wpd	Wordperfect version 6,7, or 8.
Figures	*.axg, *.axd *.tcw *.bmp, *.tif	Axum version 4 or 5. TurboCad version 3. Any graphics or photo software.
Data	*.wb2	Quattro Pro version 6, 7, or 8.
Software	*.exe *.for *.m *.mcd	MS-DOS version 5 or higher. Any FORTRAN 87 compiler. Matlab version 5 or higher. MathCad version 8 or higher.

1. Can be lower or upper case letters.

2. Wordperfect and Quattro Pro are registered trademarks of Corel Corporation Ltd.
   Axum and MathCad are registered trademarks of MathSoft Inc.
   TurboCad is a registered trademark of IMSI Inc.
   MS-DOS is a registered trademark of Microsoft Corporation Ltd.
   Matlab is a registered trademark of The Math Works Inc.